

ADVANCED COUPLED THM ANALYSIS IN GEOMECHANICS

A Dissertation

by

AJAY SESHADRI SHASTRI

Submitted to the Office of Graduate and Professional Studies of
Texas A&M University
in partial fulfillment of the requirements for the degree of

DOCTOR OF PHILOSOPHY

Chair of Committee, Marcelo Sanchez
Committee Members, Jean Louis Briaud
Charles Aubeny
Maria Barrufet
Head of Department, Robin Autenrieth

August 2014

Major Subject: Civil Engineering

Copyright 2014 Ajay Seshadri Shastri

ABSTRACT

This dissertation is aimed at advancing current understating and modeling of problems involving the complex soils systems. A wide range of problems are tackled here including those in: frozen soils; gas hydrate bearing sediments and compressed air energy systems. The soils considered here are affected by changes in temperature fluid pressures and mechanical stresses which would also result in phase change of the constituents in the pore structure. The research conducted here encompasses fundamental; experimental; constitutive and numerical modeling employing the use of coupled formulations. The environmental variables affecting the soil in each case are identified, new or enhanced theoretical formulations and constitutive laws are presented. Particular emphasis is placed on the mechanical constitutive equations, as they are especially important in geotechnical engineering. The formulations presented here are validated against a number of laboratory experiments and case histories that illustrate the relevance and implications of the developments described for geotechnical engineering practice.

ACKNOWLEDGEMENTS

I would like to gratefully acknowledge the support from of my advisor Dr. Marcelo Sanchez, for being a guide, mentor over the course of the last four years. His perseverance and dedication to the field of engineering has been a source of inspiration for me. Finally, his patience for putting with the many problems that I brought to him each week is remarkable. I would also like to my committee members and faculty of the geotechnical engineering here at Texas A&M, whose vast knowledge and support has helped me on the road to become a better engineer.

I also wish to acknowledge my friends, particularly those in my office Dr. Madhuri Murali, Dr. Congpu Yao, Dr. Ryan Beemer, and Dr. Francisco Grajales who help me come up with some very inspired ideas. I would finally like to thank my family, for their invaluable support and unwavering belief during this period.

TABLE OF CONTENTS

	Page
ABSTRACT	ii
ACKNOWLEDGEMENT	iii
LIST OF FIGURES	vii
LIST OF TABLES	xvi
1 INTRODUCTION.....	1
1.1 Methodology	2
1.1.1 Background on THM coupled phenomena	3
1.1.2 Existing THM formulation and numerical code	6
1.2 Scope and original components of this research	13
1.2.1 Behavior of frozen soils	14
1.2.2 Behavior of hydrate bearing sediments	19
1.2.3 Behavior of compressed air energy storage systems	24
1.3 Objectives and associated activities toward achieving them	28
1.3.1 Frozen soils	30
1.3.2 Hydrate bearing sediments	31
1.3.3 Compressed air energy storage systems	32
1.4 Organization of the dissertation	33
2 BEHAVIOUR AND CONSTITUTIVE MODELING OF FROZEN SOILS.....	36
2.1 Introduction	36
2.2 Effect of ice on the behavior of frozen soils	41
2.3 Unfrozen water in frozen soils	47
2.4 Effect of unfrozen water on flow behavior of frozen soils.....	55
2.5 Modeling heat and mass transfer in frozen soils	59
2.5.1 Existing flow models.....	59
2.5.2 Hydraulic behavior of frozen soils.....	60
2.6 Mechanical behavior of frozen soils	65
2.6.1 Existing mechanical models for frozen soils	66
2.6.2 Volumetric and deviatoric behavior of frozen soils	70
2.6.3 Modified BBM for frozen soils.....	74
2.7 THM framework of frozen soil	79

3 APPLICATION CASES INVOLVING FROZEN SOILS	82
3.1 Introduction	82
3.2 Flow modeling in frozen soils	83
3.3 Model validation for natural soils	90
3.3.1 Description of experimental work	91
3.3.2 Hydrostatic tests	95
3.3.3 Uniaxial tests	97
3.3.4 Triaxial tests	99
3.3.5 Constitutive modeling of natural samples	101
3.4 Reconstituted samples of frozen soils	113
3.4.1 Description of experimental work	113
3.4.2 Numerical modeling of reconstituted frozen soils	115
3.5 Case studies	119
3.5.1 Case I: Pipeline collapse	119
3.5.2 Case II: Foundation failure	129
4 CYCLIC FREEZE THAW BEHAVIOR OF SOILS	136
4.1 Introduction	136
4.2 Background	137
4.3 Experimental procedure	145
4.3.1 Test setup	145
4.3.2 Results of the experimental campaign	153
4.4 Model formulation	156
4.4.1 Freezing interaction curve	162
4.4.2 Thawing interaction curve	163
5 BEHAVIOR OF HYDRATE BEARING SEDIMENTS	166
5.1 Introduction	166
5.2 Background	168
5.2.1 Morphology of gas hydrate	170
5.2.2 Behavior of HBS	174
5.3 Constitutive modeling of HBS	177
5.3.1 Numerical simulation	192
5.4 Validation of the proposed model	196
5.4.1 Description of experimental work	196
5.4.2 Numerical modeling	199
5.4.3 Gas production	206

6 ANALYSIS OF COMPRESSED AIR ENERGY STORAGE SYSTEMS	211
6.1 Introduction	211
6.2 Background information	212
6.2.1 Potential of CAES	213
6.2.2 CAES operation	215
6.3 Types of CAES.....	216
6.3.1 CAES in salt and hard rock formations.....	217
6.3.2 Porous rock	221
6.4 Numerical approach to the case study.....	227
6.5 Numerical analyses	233
6.5.1 THM analyses of CAES storage imposing air pressure.....	233
6.5.2 HM analyses of CAES system imposing air flow rate.....	244
7 SUMMARY AND SCOPE FOR FURTHER WORK.....	255
7.1 Summary	255
7.2 Conclusions and scope for future work.....	256
7.3 Concluding remarks	261
REFERENCES.....	262
APPENDIX.....	275
A.1 Balance equations.....	275
A.2 Constitutive equations	276
A.2.1 Mechanical constitutive model.....	276
A.2.2 Thermal constitutive model.....	280
A.2.3 Hydraulic constitutive model	282
A.3 Equilibrium restrictions.....	286
A.3.1 Equilibrium restrictions.....	286
A.3.2 Phase physical properties	287

LIST OF FIGURES

	Page
Figure 1.1 Schematic representation of the porous medium considered in the analyses a) Soil structure and b) Associated phase diagram	3
Figure 1.2 Schematic representation of the porous medium showing the main THM phenomena in and their mutual interactions (Sanchez, 2010).....	4
Figure 1.3 Possible ways to solve coupled THM problems in CODE_BRIGHT (Sanchez, 2010)	12
Figure 1.4 Distribution of permafrost and average maximum extent of seasonally and intermittently frozen ground in the Northern Hemisphere (Rekacewicz, 2005)	15
Figure 1.5 Large settlement observed in residential homes in Dawson City, Yukon (Varani, 2000).	16
Figure 1.6 a) Schematic representation of the frozen soils with the 3 phases and 2 species considered in this dissertation b) associated phase diagram.	18
Figure 1.7 Stability zone of methane hydrates in marine sediments (Sanchez, 2010)	20
Figure 1.8 a) USGS study showing distribution of carbon in the earth; b) typical problems associated with dissociation of methane hydrates from sediments (Sanchez, 2010)	21
Figure 1.9 Schematic representation of the hydrate bearing sediments with the 5 phases and 3 species a) Soil structure b) Associated phase diagram (Sanchez, 2010).....	23
Figure 1.10 Graph showing wind capacity around the entire world (Calontiw, 2013).....	26
Figure 2.1 Infrastrure failures in permafrost regions a) Building Failure due to thaw settlement (Romanovsky, 2003) b) Road failure (Turchett, 2010) c) Rock fall due to glacial slope failure (Schoeneich et al., 2011) d). Excessive railroad distortion (Turchett, 2010).....	37
Figure 2.2 Construction of a frozen core dam (Nuna Logistics, 2014).	38
Figure 2.3 Ground freezing for sinking shafts (Moretrench, 2011).	39

Figure 2.4 Frozen soil barrier system at Oak Ridge National Laboratory (Johnson et al., 2000)	40
Figure 2.5 Phase Diagram of Water (Cmglee, 2013)	42
Figure 2.6 Different formation types of ice a) Granular Ice b) Columnar-grained ice with c-axis in vertical plane c) Columnar-grained ice with random orientation of c-axis d) Columnar-grained ice with horizontal c-axis (Sinha 1989).	44
Figure 2.7 Temperature dependence of ice elastic properties (Sinha, 1989)	45
Figure 2.8 Effect of strain rate and temperature on strength of ice (Schulson, 2004).	46
Figure 2.9 Volume Temperature diagram of water	47
Figure 2.10 Schematic representation of frozen soils (melting may induce a significant changes of the soil structure)	48
Figure 2.11 Results of the PNMR (Tice et al., 1988)	50
Figure 2.12 Piston cylinder model (results modified after Everett, 1961)	51
Figure 2.13. Schematic of an open and a closed system transitioning from unfrozen to frozen state.	54
Figure 2.14 Schematic representation of a frozen soil profile	57
Figure 2.15 Flow rate vs temperature in frozen soils	58
Figure 2.16 Schematic representation of unsaturated and frozen soils.	61
Figure 2.17 Degree of saturation vs temperature for the Tice model	62
Figure 2.18 Typical van Genuchten retention curve for different values of P_0 and λ	63
Figure 2.19 Schematic of the frozen soil (Yusufuku and Springman, 1999)	68
Figure 2.20 Results of an idealized hydrostatic test	70
Figure 2.21 Volumetric behavior of reconstituted frozen soils: a) Reconstituted frozensamples, b) Natural frozen soils.	71

Figure 2.22 Variation of the stress strain behavior of reconstituted soils: a) Effect of temperature, and b) Effect of confining pressure	72
Figure 2.23 Variation of strength with temperature	73
Figure 2.24 Idealized isotropic behavior of frozen soils	75
Figure 2.25 Idealized Yield Surface	78
Figure 2.26 Idealized thawing-collapse stress path	79
Figure 3.1 Temperature distribution along the length of the different samples	84
Figure 3.2 Variation of the flux across Mongolia Silt Samples 1 and 2.....	86
Figure 3.3 Model details a) Finite Element Mesh b) Schematic representation of the boundary conditions	87
Figure 3.4 Soil Behavior Characteristics a) Retention curve for Mongolia silt and Lanzhou sand b) Liquid Relative Permeability	88
Figure 3.5 Comparison of flow rates between model and test data for a) Mongolia Silt b) Lanzhou sand sample.....	89
Figure 3.6 Flow rates from simulation for a) Change in water content b) Change in temperature gradient.....	90
Figure 3.7 Schematic of low temperature testing pressure vessel and frozen sample configuration to be used for the axisymmetric testing series (Lee et al., 2002).	93
Figure 3.8 High Pressure Low Temperature Pressure Vessel with external cooling system to be used for axisymmetric compression and extension testing (Lee et al., 2002).	94
Figure 3.9 Isotropic behavior of frozen soils.....	96
Figure 3.10 Variation of apparent pre-consolidation pressure with temperature	97
Figure 3.11 Unconfined stress-strain behavior	98
Figure 3.12 Variation of strength with temperature	98
Figure 3.13 Variation of the stress strain behavior of natural soils at different temperatures under different confining pressures	100

Figure 3.14 Variation of the stress strain behavior of natural with confining pressure at temperatures of -10 °C	101
Figure 3.15 Projection of yield surface on mean stress suction plane a) LC curve b) p-s curve.....	103
Figure 3.16 Mesh used in the study.....	104
Figure 3.17 Boundary condition for a) Isotropic tests b) Unconfined tests c) Triaxial tests	105
Figure 3.18 Results of the simulation of hydrostatic tests at a) temperature -6°C b) temperature -10°C c) temperature -25°C	106
Figure 3.19 Comparison of model and experimental results of the unconfined test at temperature-5 °C	107
Figure 3.20 Comparison of model and experimental results of the unconfined test at temperature-10 °C	108
Figure 3.21 Comparison of model and experimental results of the unconfined test at temperature-24 °C	108
Figure 3.22. Comparison of model and experimental results of the confined test	110
Figure 3.23 Results of experiment conducted at a) Different temperatures b) Confining pressures	115
Figure 3.24. Projection of yield surface on a) The p_n -s plane: LC curve b) Projection of yield surface on the p_n -s plane: ps curve	116
Figure 3.25 Comparison of experimental and model results at a) 0.1 MPa confining pressure	117
Figure 3.26 Comparison of experimental and model results at 5.5 MPa confining pressure	118
Figure 3.27 Comparison of experimental and model results at a) -10°C b) -6°C c) -10°C d) -15 °C	120
Figure 3.28 Cross-section of the pipeline showing varying degrees of settlement with time.....	122
Figure 3.29 Vertical settlement and temperature variation in the pipeline with time.....	123

Figure 3.30 Numerical simulation of the pipeline a) Geometry b) Finite element mesh	124
Figure 3.31 Contour of temperature variation at steady state condition (initial temperature was -5°C).....	125
Figure 3.32 Contour of settlement at the end of heating.	126
Figure 3.33 Typical stress path a) isotropic behavior b) variation in p-s plane.....	128
Figure 3.34 Induced settlement below the center of the pipeline at different temperatures.	129
Figure 3.35 Administrative Service Combine building of the Kadykchanskaya mine in the Magadan region of the former USSR constructed in 1967 .	130
Figure 3.36 Numerical simulation of the foundation a) Boundary conditions	131
Figure 3.37. Contour of temperature variation at steady state condition (initial temperature was -10°C).....	132
Figure 3.38. Contour of displacements at the end of heating.	133
Figure 3.39 Typical stress path a) isotropic behavior b) variation in p-s plane.....	134
Figure 3.40. Variation of settlement with temperature at two different positions (center and edge) in the foundation.....	135
Figure 4.1 Porous structure rearrangement in the soil a) Distribution of micro and macropores for clayey silt soil b) Rearrgangment of particles due to freezing of micropore	139
Figure 4.2 Results of permeability test post thawing a) Battleford till and Regina clay samples b)Bentonite-Ottawa sand mixtures (Wong and Haug 1991).....	140
Figure 4.3 Variation of voids ratio with number of freeze-thaw cycles for soils of different densities.	142
Figure 4.4 Behavior of soils subjected Freeze-thaw cycles based on arrangement....	143
Figure 4.5 Test results a)Variation in the height of sample S10 with time and load b) Change in voids ratio after the freeze-thaw cycles (Konrad, 2010) ..	144
Figure 4.6 Experimental setup a) Experimental cell b) Base Pedestal c) Plunger with porous stone	146

Figure 4.7 LVDT used for the experiment	147
Figure 4.8 Experimental setup a) Picture of the set-up used in this research, b) Scheme showing the main components of the proposed setup	148
Figure 4.9 Environmental chamber used to simulate the freeze-thaw tests	149
Figure 4.10 CSZ touch screen controller	150
Figure 4.11 Temperature imposed during each freeze-thaw cycle	152
Figure 4.12 Variation of voids ratio with the freeze cycles for a) OC samples b) NC soils	154
Figure 4.13 Variation of voids ratio for high density samples at high and low OCRs.	155
Figure 4.14 Schematic of volumetric changes during freeze-thaw cycle for dense and loose soils	159
Figure 4.15 Schematic representation LC curves during freezing and thawing	161
Figure 4.16 Freezing Interaction Function	162
Figure 4.17 Thawing Interaction Function	163
Figure 4.18 Combined freezing and thawing interaction functions	164
Figure 5.1 Distribution of methane hydrates (Zeimusu, 2008)	167
Figure 5.2 Schematic Pressure–Temperature equilibrium curves for methane–water system for hydrate formation	169
Figure 5.3 Hydrate habit in the pore space a) Pore filling b) Load bearing and c) Bonding material (Waite et al., 2009)	171
Figure 5.4 Triaxial tests conducted on HBS of different hydrate concentration a) Deviatoric stress q vs. axial strain (ϵ_a) b) Volumetric strain vs. axial strain c) Compressive strength vs. hydrate concentration (Masui et al., 2008)	176
Figure 5.5 Structure of HBS a) Granular structure b) Phase diagram	179
Figure 5.6 Schematic representation of stress distribution a) in the HBS system b) Stress distribution for lower hydrate concentrations c) Stress distribution for higher hydrate concentrations	190

Figure 5.7 Results of hydrate formation by cooling a) Schematic of stress path b) Stress path and heat flow observed plotted along phase boundaries c) Retention curve d) Phase saturation of hydrates, water (liquid), gas and ice	194
Figure 5.8 Results of hydrate formation by heating a) Schematic of stress path b) Stress path and heat flow observed plotted along phase boundaries c) Retention curve d) Phase saturation of hydrates, water (liquid), gas and ice	195
Figure 5.9 Instrumentation of the tests for sample 21C-02E (Yun et al., 2010)	198
Figure 5.10 Results of controlled depressurization showing variation of a) Fluid pressure b) Temperature c) Gas Production (Yun et al., 2010).....	199
Figure 5.11 Results of hydrate formation by heating a) Schematic of stress path b) Stress path and heat flow observed plotted along phase boundaries c) Gas produced d) Phase saturation of hydrates, water (liquid), gas and ice	200
Figure 5.12 Numerical simulation of depressurization experiment a) Geometry b) Mesh	203
Figure 5.13 Results of the simulation compared to experimental results a) Pressure vs time b) Stress path with respect to the PT phase diagram c) Amount of gas generated with time d) Temperature of the specimen with time.....	205
Figure 5.14 Finite element mesh used for the gas production	206
Figure 5.15 Initial conditions imposed	207
Figure 5.16 Modeling result of the depressurization	208
Figure 5.17 Modeling result of the heating	210
Figure 6.1 Onshore wind resource and population density of the U.S. (NREL, 2002).....	215
Figure 6.2 Schematic of CAES power plant.....	216
Figure 6.3 Existing CAES power plants a) Huntroff, Germany (Mohmeyer and Schard, 2001) b) McIntosh power plant. Alabama, U.S.A. (Epcinc, 2009)	218

Figure 6.4 Rendering of the proposed CAES in hard rock in Norton, Ohio (OPSB, 2001)	219
Figure 6.5 CAES storage facility in aquifer.	222
Figure 6.6 Schematic of Gas Storage (Succar and Williams, 2009)	223
Figure 6.7 Distribution of the properties of the sandstone with depth.	229
Figure 6.8 Results of the main constitutive laws used in this study a) Variation of the porosity with permeability b) Water retention curve c) Relative permeability of water and gas	230
Figure 6.9 Geometry, initial and boundary conditions: a) Geometry and adopted finite element mesh b) Initial stresses and mechanical boundary conditions c) Initial liquid pressure and imposed air pressure during the air-bubble formation stage.	235
Figure 6.10 Variations of the daily demand and applied load a) Typical demand of energy (Kushnir et al., 2012) b) Applied gas pressure to match the demand	236
Figure 6.11 Computed gas flow rate.....	237
Figure 6.12 Domain used in the contour plots.....	239
Figure 6.13 Results of THM modeling with uniform porosity) Air pressure b) Air saturation	239
Figure 6.14 Results of THM modeling with uniform porosity) Temperature b) Vertical Stress	240
Figure 6.15 Results of THM modeling of short correlation a) Air pressure b) Air saturation c) Porosity distribution	242
Figure 6.16 Results of THM modeling of long correlation a) Air pressure b) Air saturation c) Porosity distribution	243
Figure 6.17 Impact of heterogeneities a) Cumulative air inflow b) Cumulative water production.....	244
Figure 6.18 Geometry, initial and boundary conditions: a) Initial stresses and mechanical boundary conditions b) Initial liquid pressure and imposed air pressure during the air-bubble formation stage c) Air saturation of the end of air-bubble formation and imposed cyclic air flow-rate.	245

Figure 6.19 Variations in the applied load.....	246
Figure 6.20 Evolution of gas pressure for the uniform case.....	247
Figure 6.21 Adopted geometry and domain used in the contour plots.....	248
Figure 6.22. Results of modeling with uniform porosity a) Air pressure b) Air saturation	249
Figure 6.23 Results of modeling with uniform porosity a) Horizontal Stress b) Vertical Stress c) Porosity.....	250
Figure 6.24 Evolution of the gas pressures for the long and short correlations	251
Figure 6.25 Results of modeling of short correlation a) Air pressure b) Air saturation c) Porosity distribution.....	252
Figure 6.26 Results of modeling of long correlation a) Air pressure b) Air saturation c) Porosity distribution.....	253
Figure 6.27 Liquid flow in the aquifer a) Cumulative air flow intake during the one year period of air injection at constant pressure (i.e. formation of air-bubble) b)Cumulative water production during the subsequent three years of compression/decompression cycles.....	254

LIST OF TABLES

	Page
Table 3.1 Properties of soil samples used on the experiment	84
Table 3.2 Grain size distribution for the soil samples (Xu et al., 1999).....	85
Table 3.3 Model parameters.....	87
Table 3.4 Laboratory constitutive testing of Alaskan frozen soil	94
Table 3.5 Model parameters.....	102
Table 3.6 Model Parameters used in modeling reconstituted samples	116
Table 4.1 Results of the consolidation test prior to freeze-thaw cycles	153
Table 4.2 Results of the consolidation test prior to freeze-thaw cycles	155
Table 6.1 Costs for various energy storage options (Sucaar and Williams, 2008)	214
Table 6.2 Summary of constitutive laws and equilibrium restrictions.....	231

1 INTRODUCTION

The range of problems that geotechnical engineers face has increased in complexity and scope. This complexity generally arises from the interaction between the soil and the environment. Such problems are dealt by progressively upgrading classical soil mechanics formulations to incorporate the effects of new phenomena and new variables on soil behavior. The range of problems considered in this dissertation range from, analyzing geotechnical problems involving very low temperatures in permafrost settings (frozen soils), studying the coupled multi-physics interactions associated with hydrate bearing sediments (HBS) behavior; to the analysis of the compressed air energy storage (CAES) systems.

The problems considered here are given particularly high importance as ever increasing population and a rapidly increasing demand for space and fuel alternatives require engineers to explore frontiers of technology. This has increased the range of problems encountered by geotechnical engineers with demands for efficient and safer infrastructures in more complex and challenging environments. The soils related to problems suggested are referred to as ‘problematic soils’. However, in this context it is worth quoting Dr. P. R. Vaughan, who once wrote: “Classical soil mechanics has evolved around a few simplified models which do not fit the properties of most real soils sufficiently for useful and safe predictions to be made . . . Since we cannot change the soil to fit the soil mechanics, perhaps we should change the soil mechanics to fit the soil. The theory which fails to fit their behavior is problematic, not the soil.” (Vaughan, 1999).

In each of the applications presented in this dissertation the causes of the environmental variables are identified, enhanced theoretical formulations are proposed and new or extended constitutive laws are presented. Particular emphasis is placed on the mechanical constitutive equations, as they are especially important in geotechnical engineering. The dissertation includes summary accounts of a number of case histories that illustrate the relevance and implications of the developments described for geotechnical engineering practice. This dissertation is aimed at advancing current understanding and modeling of problems involving complex soils systems. The research encompasses fundamental; experimental and constitutive and numerical modeling. The soils are characterized by the fact that perturbations from given P-T (Pressure-Temperature) equilibrium conditions may lead to a phase transformation (from solid to fluid, or vice versa), triggering a number of coupled THMG (Thermo-Hydraulic-Mechanical and Geochemical) phenomena.

1.1 METHODOLOGY

The dissertation follows a consistent methodology where the importance of studying a particular problem is identified, the gaps in the current knowledge are recognized, the new developments to fill these gaps are described in detail and the corresponding validations of the proposed models are presented and discussed. In the following section a background of the main THM phenomena and mutual interactions anticipated in porous media is introduced, alongside with the adopted mathematical formulation and computer code adopted in this research.

1.1.1 Background on THM coupled phenomena

All the developments presented in this dissertation are within the framework of coupled THM and chemical phenomena in porous media. The starting point was the fully coupled THM framework originally developed by Olivella et al. (1994) and modified later on by different researches (e.g. Guimarães et al., 2006; Sanchez et al., 2008, 2012). In this original multiphase/multispecies approach it was assumed that water (w) is the main component of the liquid phase (l), and water is also present in the gas phase (g) as water vapor. Another assumption is that dry air (a) is the main component of the gas phase, and that air is also present in the liquid phase as dissolved air. The solid phase was composed by minerals only. Figure 1.1a) presents a schematic representation of the porous medium considered in this formulation and Figure 1.1b) the associated phase diagram showing the three phases and three species considered in this formulation.

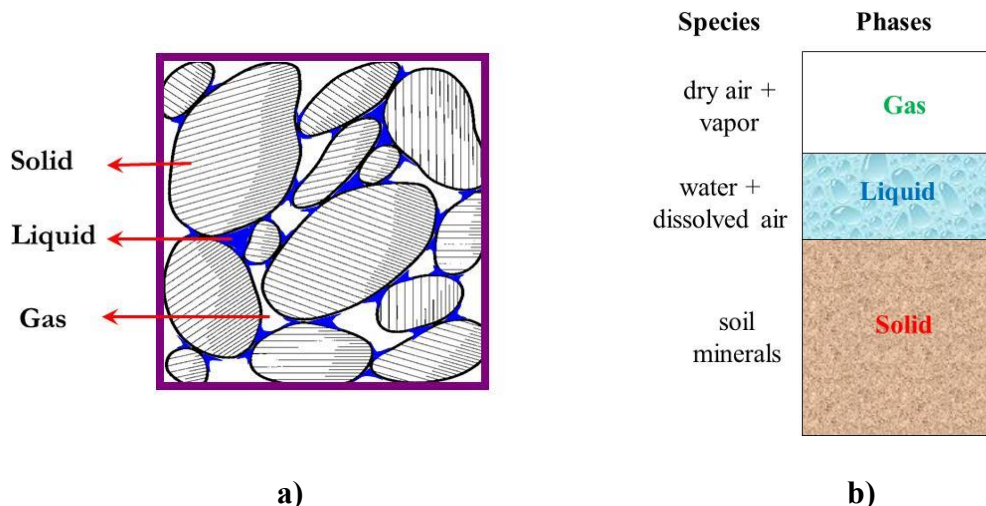


Figure 1.1 Schematic representation of the porous medium considered in the analyses a) Soil structure and b) Associated phase diagram

Figure 1.2 schematically illustrates the main physical phenomena (and their mutual interactions) that takes place in a porous medium subjected to simultaneous THM perturbations.

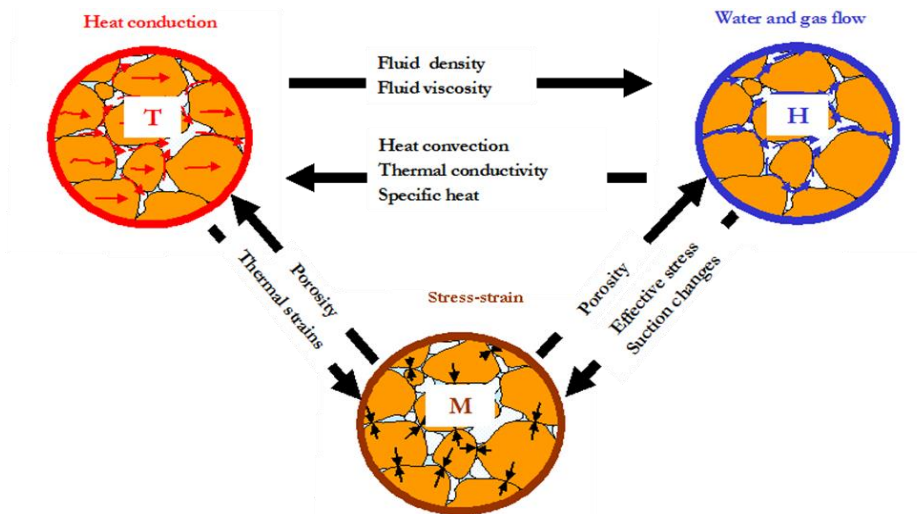


Figure 1.2 Schematic representation of the porous medium showing the main THM phenomena in and their mutual interactions (Sanchez, 2010)

Within the thermal phenomena (T), heat storage is assumed to be proportional to temperature. This is strongly affected by hydraulic phenomena, via fluid flow (i.e. liquid and gas movements change the amount of water and air present in the porous medium); and by the mechanical problem, via porosity changes (which modify the amount of space left for fluids). Phase changes also modify heat storage through the latent heat of vapor. Heat conduction is driven by temperature gradients (through Fourier’s law). Thermal conductivity (the main soil property associated with heat conduction) depends on: the partial saturation of the phases (which are mainly controlled by liquid and gas

flow) and porosity variations (which is related to stress/strain changes). Heat transport in the fluid phases by heat advection (i.e. liquid and gas mass flows) is other relevant phenomenon related to the thermal problem.

Within the hydraulic phenomena (H), water storage is affected by the thermal problem through the dependence of liquid and vapor density on temperature. Phase change modifies the amount of water in liquid and gas phases. Water storage also depends on hydraulic phenomena via the dependence of liquid density on liquid pressure and vapor density on fluid pressures. Water storage is also affected by the mechanical problem, as porosity changes modify the space available for the flow of liquid and gas. Liquid water transfer is mainly controlled by liquid pressure gradients through Darcy's law. Hydraulic conductivity, the main soil property associated with fluid flow, is mainly affected by liquid viscosity (that diminishes with temperature); porosity changes (controlled by the mechanical problem); and the degree of saturation (which varies with temperature in unsaturated conditions due to thermal expansion and phase changes). Furthermore, pore water pressure increases with temperature in saturated and quasi-saturated conditions, and liquid density variation with temperature gives rise to convective flow. Water vapor transfer is mainly controlled by gradients of vapor concentration, i.e. vapor diffusion (through Fick's law) and vapor advection, controlled by gas flow. Vapor diffusion depends mainly on the degree of saturation and porosity changes. Similar processes and couplings govern the air storage, gaseous air transfer and dissolved air transfer.

Within the mechanical phenomena (M), the mechanical constitutive law establishes the relation between stresses and strains. Temperature field affect the mechanical problem via the thermal expansion/contraction of materials, and the dependence of the constitutive law on temperature. Hydraulic phenomena affect the mechanical field by the dependence of effective stresses on liquid pressure (for the saturated conditions); or by the dependence of net (or average stress) on average fluid pressures (when the porous medium is not fully saturated). In unsaturated conditions the constitutive laws also depend on suction (i.e. difference between gas and liquid pressures).

From the previous description, it is evidenced the increase activity when coupled THM phenomena takes place in a porous media, particularly when simultaneous heating and hydration occur. Similar couplings and interactions can be anticipated when the chemical problem come into play.

1.1.2 Existing THM formulation and numerical code

A macroscopic approach developed in the context of the continuum theory for porous media has been adopted in this dissertation taking into account the main following phenomena (Olivella et al., 1994):

- Heat transport: heat conduction; heat advection (liquid water and water vapor); phase changes.
- Water flow: liquid phase advection; water vapor diffusion.
- Air flow: gas phase; air solution in water; dissolved air diffusion.

- Mechanical behavior: thermal expansion of materials; behavior of soil and rocks dependent on stresses, suction and temperature

These THM phenomena were incorporated in a coupled formulation consisting of 3 main set of equations (Olivella et al., 1994):

- 1) balance equations;
- 2) constitutive equations; and
- 3) equilibrium restrictions.

The mass balance of water, air and solid are established. The formulation also includes: the momentum balance for the whole medium; the equation for internal energy balance. The balances of momentum for fluid phases and dissolved species are reduced to constitutive laws: Darcy's law and Fick's law. The main unknowns (state variables) related to these equations are: solid displacements, \mathbf{u} (three spatial directions, associated with the momentum balance); liquid pressure P_l (associated with the mass balance water); gas pressure P_g (associated with the mass balance of air); and temperature T (associated with balance of internal energy). More details can be found elsewhere (Olivella et al., 1994 and Olivella et al., 1996)

A fundamental part of the formulation is the set of constitutive laws and equilibrium restrictions. The constitutive equations establish the link between the state variables, or unknowns, and the dependent variables (e.g. S_l , S_g ; σ , advective flow of liquid and gas, etc.). Below the main aspects of these three main parts of the basic formulation are presented, more details can be found in the Appendix.

Balance equations

To establish the mass balance equations a compositional approach is adopted. This approach consists of balancing the species (mineral, water and air). The phase change terms do not appear explicitly, when equilibrium is assumed. In the notation, the subscript is used to identify the phase (s for solid, l for liquid and g for gas) and the superscript indicates the species: 'w' for water and 'a' for air. No symbol is attributed to the mineral species, because it has been assumed that it coincides with the solid phase. The main balance equations are presented in the following paragraphs.

Balance of mass of water

$$\frac{\partial}{\partial t}(\theta_l^w S_l \phi + \theta_g^w S_g \phi) + \nabla \cdot (\mathbf{j}_l^w + \mathbf{j}_g^w) = f^w \quad (1.1)$$

where, θ_l^w and θ_g^w are the masses of water per unit volume of liquid and gas phase respectively. ϕ is the porosity and S_α is the volumetric fraction of pore volume occupied by the alpha phase ($\alpha=l,g$). \mathbf{j}_l^w and \mathbf{j}_g^w denote the total mass fluxes of water in the liquid and gas phases with respect to a fixed reference system. f^w is the external mass supply of water per unit volume of medium.

Balance of mass of air

$$\frac{\partial}{\partial t}(\theta_l^a S_l \phi + \theta_g^a S_g \phi) + \nabla \cdot (\mathbf{j}_l^a + \mathbf{j}_g^a) = f^a \quad (1.2)$$

where, θ_l^a and θ_g^a are the masses of air per unit volume of liquid and gas phase respectively. \mathbf{j}_l^a and \mathbf{j}_g^a denote the total mass fluxes of air in the liquid and gas phases with respect to a fixed reference system. f^a is the external mass supply of air per unit volume of medium. Note that dry air is considered as a single species in spite of the fact

that it is a mixture of gasses. The gaseous phase is assumed as a mixture of air and water vapor.

Balance of a conservative species

The basic version of the original formulation can deal with the presence of a single conservative chemical specie dissolved in the liquid phase. An extension to the code to reactive transport problems was done by Guimarães (2002), full details about this THMC version of the formulation can be found elsewhere (e.g. Guimarães et al., 2006; Guimarães et al., 2009).

Balance of internal energy

$$\frac{\partial}{\partial t} [E_s \rho_s (1-\phi)] + \frac{\partial}{\partial t} (E_l \rho_l S_l \phi + E_g \rho_g S_g \phi) + \nabla \cdot (\mathbf{i}_c + \mathbf{j}_{E_s} + \mathbf{j}_{E_l} + \mathbf{j}_{E_g}) = f^E \quad (1.3)$$

The balance of energy has been expressed in terms of internal energy where, E_s is the solid specific internal energy, E_l and E_g are specific internal energies corresponding to the liquid and gas phases respectively. ρ_l and ρ_g are the liquid and gas phase densities of the medium. f^E is the energy supply per unit volume of medium. The most important processes for energy transfer in a porous medium have been considered in equation (1.3), which are: conduction, advection and phase change. \mathbf{i}_c is the conductive heat flux. \mathbf{j}_s , \mathbf{j}_{E_l} and \mathbf{j}_{E_g} are the energy fluxes due to the motion of phase. A thermal equilibrium between the phases has been assumed, therefore the temperature is the same for the phases. This also implies a single equation of total energy is required

Balance of mass of solid

$$\frac{\partial}{\partial t}(\rho_s (1-\phi)) + \nabla \cdot (\rho_s (1-\phi) \dot{\mathbf{u}}) = 0 \quad (1.4)$$

where, $\dot{\mathbf{u}}$ is the solid velocity vector. The variation of porosities in terms of changes in solid density and volumetric deformation of the soil skeleton is obtained from equation (1.4).

Constitutive equations

The constitutive equations establish the link between the unknowns and the dependent variables. There are several categories of dependent variables depending on the complexity with which they are related to the unknowns. The governing equations are finally written in terms of the unknowns when the constitutive equations are substituted in the balance equations. The basic constitutive laws are divided in three main groups, namely: thermal, hydraulic and mechanical. In spite of this distinction between the three basic components of the problem, the constitutive equations provide in fact the links that couple the various phenomena considered in the formulation. The general expressions of the constitutive laws for the thermal, hydraulic and mechanical problems are presented in the Appendix.

Equilibrium restrictions

It is assumed that phase changes are rapid in relation to the characteristic times typical of this problem. Therefore, they can be considered to be in local equilibrium, giving rise to a set of equilibrium restrictions that must be satisfied at all times. Equilibrium restrictions are given for the concentration of water vapor in gas phase and

for the concentration of dissolved air in liquid phase. The respective equations are presented in the Appendix.

Computer code

The numerical solver that integrates the three set of equations quoted above is the CODE_BRIGHT (Olivella et al; 1996). It is a finite element code designed to solve thermo-hydro-mechanical problems in geological media. One unknown (state variable) is associated with each of the balance equations presented. The unknowns are obtained by solving the system of PDE's (Partial Differential Equations) numerically in a coupled way. The state variables are: solid velocity, \mathbf{u} (one, two or three spatial directions); liquid pressure, P_l ; gas pressure, P_g ; and temperature T . From state variables, dependent variables are calculated using the constitutive equations or the equilibrium restrictions. Strains are defined in terms of displacements. Small strains and small strain rates are assumed for solid deformation. Additionally, advective terms due to solid displacement are neglected after the formulation is transformed in terms of material derivatives (in fact, material derivatives are approximated as eulerian time derivatives).

Figure 1.3 presents a scheme showing the different alternatives that CODE_BRIGHT offers to solve problems in geological media. It can for example to solve the uncoupled thermal, or hydraulic or mechanical problem. It can also be possible to couple pairs of them or to solve the fully THM coupled problem. The software GiD (gidhome.com, 2014) has been adopted to perform the pre-process associated with the preparation of the finite element model (i.e. preparation of the geometry, mesh,

boundary conditions, etc.), GiD is also used for the post-processing of the CODE_BRIGHT numerical outputs.

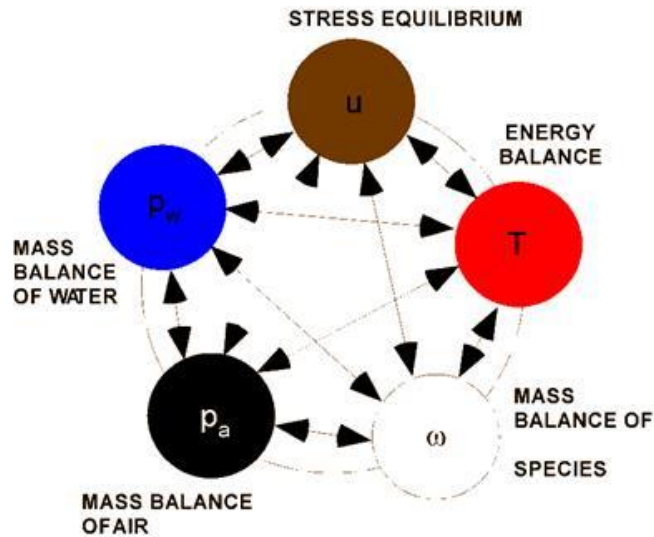


Figure 1.3 Possible ways to solve coupled THM problems in CODE_BRIGHT (Sanchez, 2010)

The numerical approach can be viewed as divided in two parts: spatial and temporal discretization. Galerkin finite element method is used for the spatial discretization while finite differences are used for the temporal discretization. The discretization in time is linear and an implicit scheme is used. Finally, since the problems presented here are non-linear, the Newton-Raphson method is adopted as the iterative scheme. The numerical code has a wide library of elements including segments, triangles, quadrilaterals, tetrahedrons, triangular prisms and quadrilateral prisms. Linear interpolation functions and, for some elements, quadratic interpolation functions are available. Analytical or numerical integration is used depending on element type. For the

mechanical problem, selective integration is used for quadrilateral and quadrilateral prisms (this means that the volumetric part is integrated with a reduced integration of 1 point). The program has a scheme for the automatic discretization of time. Reduction of time increment may be caused by excessive variation of unknowns per iteration or by excessive number of iterations to reach convergence or if the correction is larger than in the previous iteration. Convergence criteria are established in terms of forces or flows and of state variables.

Regarding the boundary conditions of the mechanical problem, forces and displacement rate can be enforced in any spatial direction and at any node. In the hydraulic problem, mass flow rate of water and dry gas can be prescribed at any node, and liquid/gas pressure can be also enforced at any node. For the thermal problem, heat flow and temperature can be prescribed at any node of the mesh. This code has been extensively used in the simulation of complex coupled geomechanical applications and it has been validated in a number of projects and benchmarks (e.g. Gens; 2009; Sanchez et al., 2008).

1.2 SCOPE AND ORIGINAL COMPONENTS OF THIS RESEARCH

This dissertation focuses on the study of different geomechanical problems related to characterizing the behavior hydrate bearing sediments. The initial review of hydrates revealed that the existing models in the literature do not consider the formation and effects of ice on the behavior of hydrate bearing sediments during the hydrate dissociation (an endothermic process). Therefore to better understand these effects, an investigation into the behaviors of frozen and freezing soils was undertaken. This

investigation involved analyzing and simulating the mechanical and hydraulic behaviors of frozen soils at varying temperatures and volumetric changes which occur during the freeze and thaw cycles. The research refocused on the response of hydrate bearing sediments utilizing the experience obtained during the modeling of the frozen soil behavior.

A significant challenge is posed in storing of the gas released from the HBS. One possible solution is storing of this gas in underground caver/ aquifers. These systems are also utilized for load balancing i.e process of using excess electrical energy during low demand periods for release as demand rises. A study is made into the working of such a storage based in aquifer has been made here. This would involve storage of gas/air compressed at high pressure in geological media during low energy demand periods and the decompression of this air to generate electricity during peak energy demand periods.

To summarize the main topics of research are:

- Frozen soil;
- Hydrate bearing sediments (HBS), and;
- Underground energy storage.

More details about these topics and the motivations for the research presented in this dissertation is introduced in the following paragraphs

1.2.1 Behavior of frozen soils

Permafrost or cryotic soil can be defined as a soil that for two or more years is at or below the freezing point of water 0 °C (32 °F). Figure 1.4 shows the distribution of permafrost and average maximum extent of seasonally and intermittently frozen ground

in the Northern Hemisphere (Varani, 2000). The blue regions correspond to seasonally frozen ground, and it refers to those areas where soil is frozen for 15 days or more per year. The pink regions correspond to intermittently frozen ground, and it refers to areas where the soil is frozen for fewer than 15 days per year. The solid line indicates the average maximum extent of the seasonal snow cover (Rekacewicz, 2005). Permafrost occupies about 22.79 million km² or 23.9 % of the exposed land surface. On average, the maximum extent of seasonally frozen ground is about 55 million km² or 55 % of the total land area (Rekacewicz, 2005).

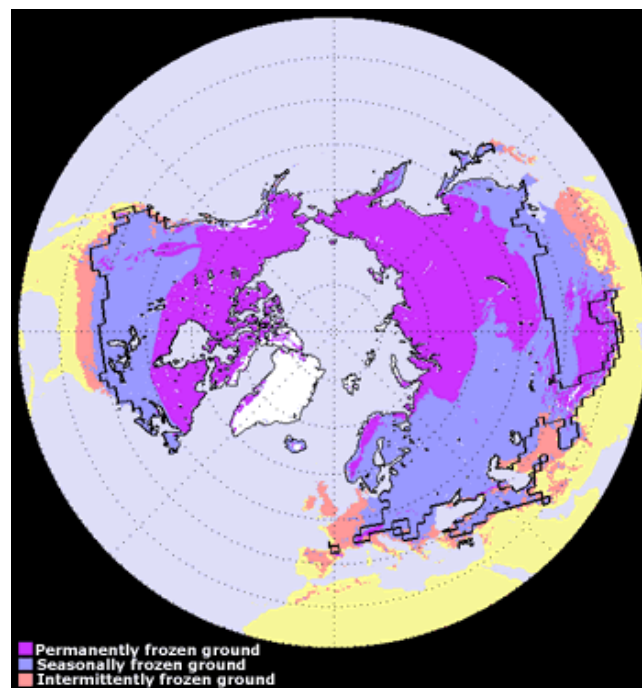


Figure 1.4 Distribution of permafrost and average maximum extent of seasonally and intermittently frozen ground in the Northern Hemisphere (Rekacewicz, 2005)

Over the past decade there has been a peaked interest in exploring the frozen regions of the planet due to the abundance of fuel sources especially near the Polar Regions. The development of infrastructure in these regions necessitates a clear understanding of the behavior of frozen soils. Phase changes in the constituents of the soil in the pore structure affect mechanical, hydraulic, thermal behaviors based on the conditions to which they are subjected to Frozen soil behavior has been a subject of much discussion over the past century beginning with works made by Taber (1929). A large number of papers have been published later on covering several subjects associated with frozen soils. However, there are still some features of frozen soils behavior that still need more research. One of them is the large settlements observed in residence and other civil infrastructure on frozen soils. Figure 1.5 present a typical settlement problem observed in foundations constructed in frozen soils.



Figure 1.5 Large settlement observed in residential homes in Dawson City, Yukon (Varani, 2000)

To predict the kind of behavior observed in Figure 1.5, a model needs incorporate basic evolution laws able to simulate the changes in soil stiffness and strength associated with the thawing of frozen soils. Nishimuara et al. (2009) proposed the extension of the Barcelona Basic Model (BBM) to deal with problems involving cryogenic temperatures. This framework seemed capable of simulating this kind of behavior. However, this has not been proved or validated against experimental data yet. This was exactly the first objectives of this dissertation, that is, to check the ability of this model to simulate the volumetric collapse compression observed in frozen soils subjected to thawing.

Experimental data related to mechanical tests (both unconfined and triaxial tests) on reconstituted samples was used for this endeavor. Furthermore, thanks to a collaboration with Sandia National Laboratories it was possible to access to high quality data associated with triaxial tests on natural frozen samples. This experimental campaign involved isotropic, unconfined and triaxial tests at under zero centigrade temperatures and it was instrumental to comprehensive validation of the proposed mechanical model. The validation of the model has been very successful and, as far as this candidate knows, this constitutes an original piece of research as there is not a similar work in the literature validating a constitutive mechanical model for frozen soils able to explain the increase of stiffness, and strength with decreasing freezing temperatures observed in frozen soils using a unique and consistent framework.

As the final goal is to model actual boundary value problems involving frozen soils, the formulation presented in Section 1.1 was adapted for the case of frozen soils.

For the sake of the simplicity it was assumed that the no gas was present in the frozen soils, i.e. only three phases were considered, namely: liquid, ice and solid; and only two species were considered: water and soil minerals (i.e. no dry air). This can be a considered a valid assumption for most of the engineering problems involving frozen soils. Figure 1.6a) present a schematic representation of the conceptual model adopted in this dissertation to represent the frozen soils and figure 1.6b) the associated phase diagram.

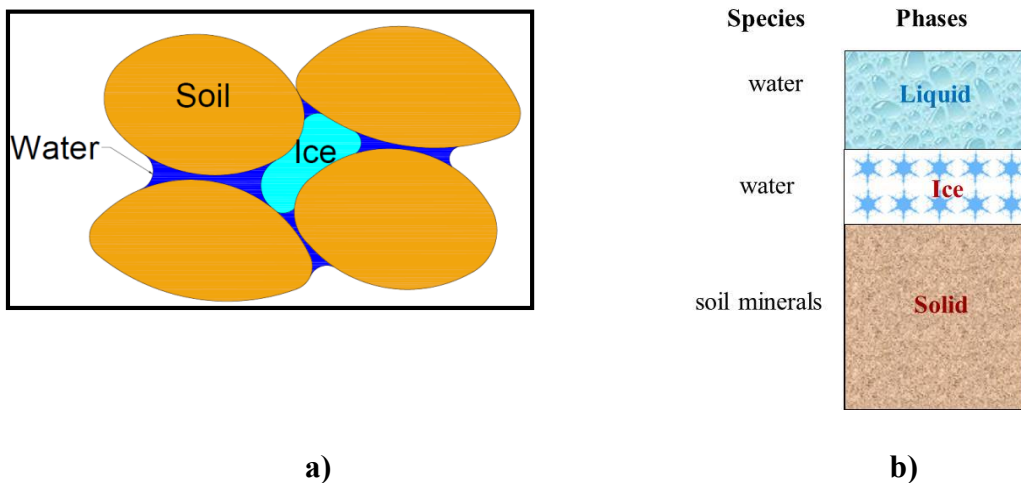


Figure 1.6 a) Schematic representation of the frozen soils with the 3 phases and 2 species considered in this dissertation b) associated phase diagram

The mathematical formulation was modified to incorporate the ‘liquid-water to solid-ice’ phase change. This was contemplated in the mass balance of water (i.e. equation 1.1) and also in the balance of internal energy (i.e. equation 1.3) accounting for the impact of this phase transformation on internal energy through the latent heat associated with the phase change liquid-water to ice (and the reverse one).

CODE_BRIGHT was used to model geotechnical cases involving foundations with problems in frozen soils. The two cases analyzed were reported in the literature and the observed problems were related to large settlements observed in these structures after thawing. The proposed models were able to reproduce the problems observed of these foundations and also to provide a physical explanation for the reported problems. This is also an original contribution of this dissertation, as no similar work explaining the large settlements associated with frozen soil melting has been published in the open literature.

Another problem that needs further research is the behavior of soils subjected to cycles of freezing and thawing. The literature review revealed that the experimental data associated with the cyclic behavior of soils subjected to freeze and thaw is sparse with no actual analytical/numerical models to simulate this behavior. In this dissertation, both experimental investigation and modeling have been performed to advance current state of the art in this subject. The experiments performed in this dissertation have allowed gaining a better understanding on the effect of freeze/thaw cycles on fined grain soils. The proposed model has been able to explain satisfactorily the main trends observed in soils subjected to freeze/thaw cycles. This also constitutes a novel contribution of this dissertation.

1.2.2 Behavior of hydrate bearing sediments

Methyl-hydrates constitute methane molecules encapsulated inside the crystal structure of water. Methane hydrates form under condition of high pressure (P) and low temperature (T), common in permafrost settings and in deep marine sediments (>500 m).

The stability of methane depends on pressure and temperature. Figure 1.7 presents a schematic representation of the stability zone for hydrates formed in marine sediments.

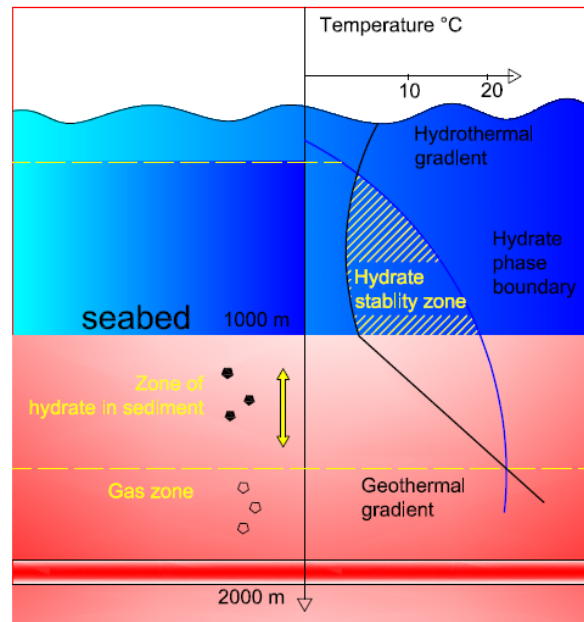


Figure 1.7 Stability zone of methane hydrates in marine sediments (Sanchez, 2010)

Methane hydrate soil is highly compacted (stable) under deposit conditions and is likely to behave as a bonded sedimentary soil. However, if stability conditions are altered (by e.g. increasing temperature or decreasing temperature), very large volume expansion upon dissociation are anticipated (e.g. 1 m³ of methane hydrate can release 164 m³ of methane gas and 0.87 m³ of water). Such a large volume expansion would develop high fluid pressure and large fluid flux. Dissociation is an endothermic process, so important changes in the temperature field are also anticipated. Therefore, hydrate dissociation will trigger strongly coupled THM and chemical changes in the sediments.

Huge opportunities and problems are associated with methane hydrate in soils. The reserve of energy in the form of methane hydrate is perhaps the biggest one in our planet. For example Figure 1.8a) present the results of an study performed from USGS showing that methane hydrates contain more carbon than all the world's other fossil resources combined. The economical extraction of the hydrates from sediments would be a crucial step in solving the impending energy crisis (Sloan, 1998; Rutqvist and Moridis, 2007). However hydrates are also a source of problems. For example, hydrate dissociation causes borehole instability, blowouts, foundation failures, affect submarine infrastructure, and trigger large-scale submarine slope failures (Kayen and Lee, 1991; Jamaluddin et al., 1991; Briaud and Chaouch, 1997; Chatti et al., 2005). The escape of methane into the atmosphere would also exacerbate greenhouse effects and contribute to global warming (Dickens et al., 1997). Figure 1.8b) presents some typical problems associated with hydrate dissociation.

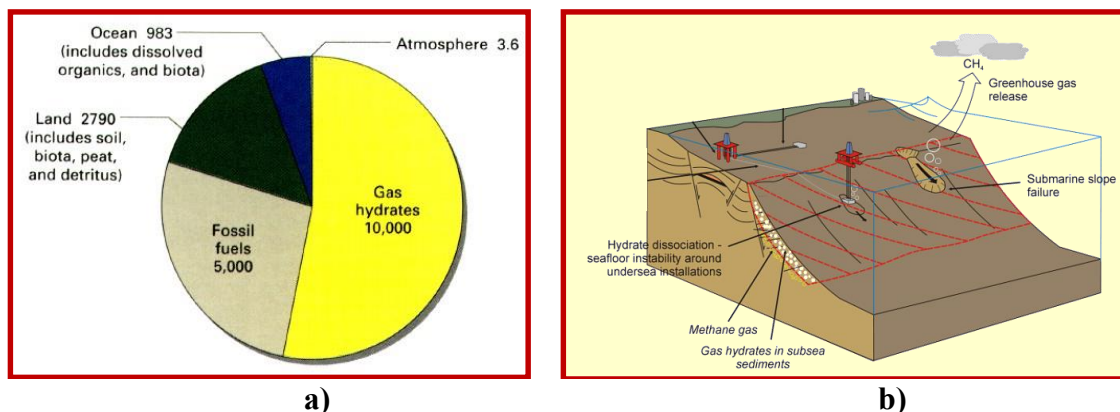


Figure 1.8 a) USGS study showing distribution of carbon in the earth; b) typical problems associated with dissociation of methane hydrates from sediments (Sanchez, 2010)

Experimental study of HBS is hindered by two main reasons, the very low solubility of methane in water (which make very difficult to reconstruct samples in the laboratory), and the difficulty to extract undisturbed samples from the field (heating and depressurization during core extraction are very difficult to prevent with standard sampling technique). Therefore, numerical modeling is crucial in order to advance the current understanding of this complex material.

The THM formulation presented in Section 1.1 was extended by Sanchez et al. (2014) to deal with problems involving gas hydrates. The basic formulation was extended to include the species and additional phases necessary to model gas hydrate behavior. Figure 1.9a) presents the conceptual model adopted for hydrates and Figure 1.9b) the corresponding phase diagram with the three species considered (i.e. methane, water and sediment minerals) and the five species (i.e. gas, liquid, hydrate, ice and solid). Methane is the main component of the gas phase, it can also be found in the hydrate and in liquid phase as a dissolved gas. Water is the main component of the liquid and ice phase and it can also be found in the hydrate phase and in the gas phase as vapor.

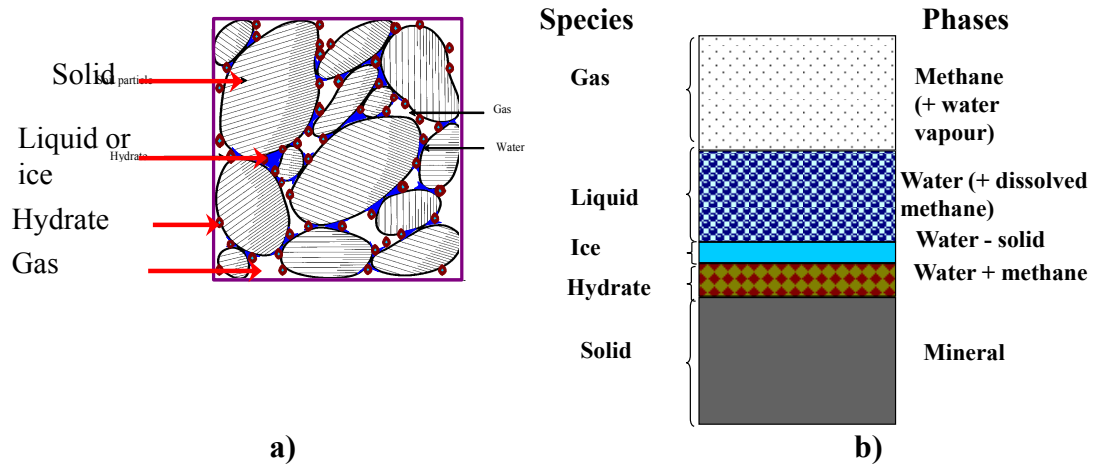


Figure 1.9 Schematic representation of the hydrate bearing sediments with the 5 phases and 3 species a) Soil structure b) Associated phase diagram (Sanchez, 2010)

This thesis has contributed to a better understanding and modeling of HBS by incorporating the effect of subzero temperatures in the analyses. In addition the effect of chemical stimulation on hydrate dissociation has been incorporated into the modeling of HBS by establishing a dependence of the phase boundary (hydrate-methane) on water salinity. These two aspects (i.e. behavior of HBS at freezing temperatures and effect of water salinity on hydrate dissociation) has been instrumental to model the scaled gas production test performed in the laboratory under controlled conditions on a natural HBS from India extracted by means of one state of art pressurized core device developed at Georgia Institute of Technology by Yun et al., (2010).

The undisturbed samples with the HBS were subjected then to a depressurization test under controlled conditions in the laboratory with sensors located in different positions to measure the temperature and sediments properties changes during the

depressurization. Freezing temperatures were observed during the test. This experiment was modeled in this dissertation and very satisfactory agreements between model predictions and observation were achieved. Also, large scale problems, mimicking actual production scenarios were modeled in this dissertation considering different techniques to induce hydrate dissociation, namely: heating, depressurization and chemical stimulation.

The original component of this research are various, perhaps the more relevant one has been the incorporation of the ice formation on the modeling of HBS. No other simulation involving this feature of HBS was published report. In this line the modeling of the scaled gas production experiment was not performed before. It is also worth to mention that this has been the first attempt to model problems involving HBS using a truly coupled THMC formulation. Previous work in this area adopted staggered approaches based generally in the coupling of different codes (to solve the different physics) with generally one direction coupling (Rutqvist and Moridis, 2007). This is not recommendable in highly coupled problems, as the one reported in this section involving the dissociation of HBS,

1.2.3 Behavior of compressed air energy storage systems

With a focus on different forms of energies suggested in the previous topic, the behavior of alternate energy storage is also examined in this dissertation. The desire for energy independence requires the re-evaluation of conventional and unconventional sources of energy; and also to explore how energy storage can help to balance out periods of peak energy production with those periods of maximum energy demand.

Renewable sources have been considered as more viable and sustainable alternatives to current energy generating strategies. Wind energy constitutes a vital part of this discussion. Even with the variability of wind resources it would be enough to satisfy the current energy requirements of the world several times over (Succar and Williams, 2009). Figure 1.10 shows how fast the wind energy sector has progressed in the last few years; playing nowadays a significant role in the energy market. A more recent study has shown that wind developers had set a new record for installations in 2013, with a total worldwide capacity exceeding 330,000 megawatts. Wind farms generate carbon-free electricity in more than 80 countries, 24 of which have at least 1,000 megawatts. At the European level of consumption, the world's operating wind turbines could satisfy the residential electricity needs of 450 million people. In the U.S. new wind electricity generating capacity was added in 2012 than any other generation technology, including natural gas—a record 13,100 megawatts. The United States remains second; China is ahead with 60,000 total megawatts of wind capacity; which is enough to power more than 14 million U.S. homes.



Figure 1.10 Graph showing wind capacity around the entire world (Calontiw, 2013)

However imbalances between the periods of energy requirements respect to the ones of energy production are a hindrance to become it in a truly economical alternative. This can be overcome by developing a temporary storage of the produced energy at peak generation time, so that it then can be released in times of maximum energy demands. Air storage systems provide one solution to this problem; the idea is to compress air and stored it in the underground. This air is compressed by utilizing the electricity produced during peak energy generation periods and is then decompressed to produce electricity during periods of high energy requirements. The effects of the decompression may be magnified by burning this decompressed air along with natural gas or coal to have higher

volumetric expansions giving greater yields of electricity. Only certain geologies (like cavern and mines) have been historically utilized for CAES systems.

The initial idea was to store the compressed air in pre-excavated caverns in salt or hard rocks. In fact the two CAES plants currently operating in the world are based on this concept. A lined is generally required to prevent the leakage of the air to the host formation. A drawback of this technique is the relatively high cost associated with the construction of underground facility. For example, the cost of production for a CAES plant in: salt-rock is around 2 \$/kWh while in a hard-rock is around 30 \$/kWh. A new concept based on the storage of compressed air in a porous-rock (i.e. aquifers) has been recently proposed. This concept has a number of advantages, as for example: it is not necessary to excavate the cavern (and the associated lined), it is quite easy to extend the capacity of a plant (i.e. simply more wells need to be installed), and there are plenty of aquifers that can be used in this kind of project. The main advantage of this type of project is the relatively low cost, around 0.11 \$/kWh.

The air storage in aquifers is performed in two stages: i) first air is injected at a constant pressure to desaturate the host rock and form the so called 'air bubble'; ii) then the air bubble is utilized for daily operations by cyclic compression and decompression of the stored air based on the demand requirements.

Challenges associated with this type of problems is that cyclic compression and decompression of air within the reservoir will lead to significant changes in temperature, liquid and gas saturations and mechanical stresses. Therefore, coupled THM analyses are necessary for a realistic prediction of the short and long term behavior of this kind of

projects. Heterogeneity of the host rock will heavily influence the behavior of the CAES system.

One of the goals of this dissertation has been to gain a better understanding of the operation of this kind of system. In this context, an actual field investigation aimed at exploring the feasibility of a CAES plant in a porous rock in Dallas, Iowa, was used in this project to investigate some key factors associated with the design of this kind of system, amongst others: possible air injection rates based on maximum and minimum reservoir pressures; operational maximum and minimum air pressure associated with a given (operational) air injection rate; time necessary to develop the air bubble; changes in temperature, pressures, porosity and stresses induced in the host rock by the cycles of compression and decompression; effect of rock heterogeneity on CAES system performance; development of fingering effects during CAES operation.

These numerical analyses have contributed to a better understanding of the operation of a CAES system in aquifers. It is also a truly original contribution of this dissertation, as not a work has been reported in the literature associated with design of a CAES plant in porous rock. The use of actual data from a real project also represents a plus of the numerical analyses performed in this research, as the particular analysis of the CAES plant in Dallas has not published yet

1.3 OBJECTIVES AND ASSOCIATED ACTIVITIES TOWARD ACHIEVING THEM

The particular research objectives organized according to the three main topics described in Section 1.2 are summarized first below. The main activities developed in this dissertation to achieve these objectives are introduced afterward

Frozen soils:

- To develop and validate a suitable constitutive model for describing the mechanical behavior of frozen soils including the main interaction between the fluid-pressure temperature and mechanical fields.
- To improve the current understanding on the effects of freeze-thaw cycles on soils by performing laboratory tests and developing a constitutive modeling that incorporate this feature of soil.
- To implement the general model for frozen soils in a coupled THM framework to simulate actual geotechnical problems of practical interests.
- To develop and validate a suitable constitutive model for describing the mechanical behavior of frozen soils including the main interaction between the fluid-pressure temperature and mechanical fields.
- To improve the current understanding on the effects of freeze-thaw cycles on soils by performing laboratory tests and developing a constitutive modeling that incorporate this feature of soil.
- To implement the general model for frozen soils in a coupled THM framework to simulate actual geotechnical problems of practical interests.

Hydrate bearing sediments:

- To develop and validate a numerical framework model for HBS incorporating the effect of fabric change during dissociation
- To discuss current strategies to extract methane from HBS.

Compressed air energy storage systems:

- To understand and simulate the behaviors of CAES systems in aquifers
- To understanding the heterogeneities and their impact on the performance in these storages.

An executive summary for the different problems has been made here and the detailed description of each of the topic has been described in the respective sections.

1.3.1 Frozen soils

Over the past decade there has been a peaked interest in exploring the frozen regions of the planet due to the abundance of fuel sources especially near the Polar Regions. Development of infrastructure in these regions necessitate a clear understanding of the behavior of frozen soils. Phase changes in the constituents of the soil in the pore structure affect mechanical, hydraulic, thermal behaviors based on the conditions to which they are subjected to.

Frozen soil behavior has been a subject of much discussion over the past century beginning with works made by Taber (1929). Therefore, an exhaustive review of the behavior has been conducted and detailed in section 2. The section also includes different frameworks for simulating this behavior. A numerical model (Nishimuara et al., 2009) was found to be suitable in capturing several key components of frozen soil behaviors. The validation of this model was lacking in the original work and has been performed in Section 3 for different soil sample both natural and reconstituted. This validation has been performed with a focus on the mechanical and hydraulic behaviors in

response to changing environmental conditions such as temperatures. The model also has been extended to several field studies made in frozen soils to understand collapse behavior of frozen soils.

The framework suggested by Nishimura et al. (2009) does not account of effects of cyclic freeze and thaw on soil behavior. After the review of the existing literature, it was perceived that the available experimental information is lacking. Therefore an experimental campaign is undertaken to study the impact of the freeze-thaw cycles. Combining this experimental information with existing literature, a constitutive mechanical framework is suggested extending the one proposed by Nishimura et al. (2009) to account for this behavior. This experimental campaign, and the constitutive framework has been detailed in Section 4.

1.3.2 Hydrate bearing sediments

Methyl-hydrates constitute methane molecules encapsulated inside the crystal structure of water. Methane hydrates form under condition of high pressure (P) and low temperature (T), common in permafrost settings and in deep marine sediments (>500 m). These hydrates in soils exist forming the Hydrate Bearing Sediments (HBS). Economical extraction of the hydrates from sediments would be a crucial step in solving the impending energy crisis (Sloan, 1998; Rutqvist and Moridis, 2007). The dissociation of these hydrates are also known to cause borehole instability, blowouts, foundation failures, and trigger large-scale submarine slope failures (Kayen and Lee, 1991; Jamaluddin et al., 1991; Briaud and Chaouch, 1997; Chatti et al., 2005). The escape of methane into the atmosphere would also exacerbate greenhouse effects and contribute to global warming

(Dickens et al., 1997). Experimental study of HBS is hindered by the very low solubility of methane in water and sampling difficulties during core extraction. Therefore numerical modeling is crucial in order to advance the current understanding of these. The work presented in Section 5 examines the validity of a previously proposed numerical framework (Sanchez et al., 2014) with a focus on the behavior of HBS during production of the natural gas by techniques such as depressurization, heating and chemical stimulation.

1.3.3 Compressed air energy storage systems

With a focus on alternate forms energies suggested in the previous topic, the behavior of alternate energy storage is also examined in this dissertation. The desire for energy independence, a need to re-evaluate the conventional sources of energy and energy storage is required. Sustainable and renewable sources have been considered as more viable alternatives to current energy generating strategies. Wind energy form a vital part in this discussion. Even with the variability of wind resources it would be enough to satisfy as the current energy requirements of the world several times over (Succar and Williams, 2009). However, imbalances in periods of requirement to energy production is a hindrance to it being a economical alternative. This is overcome by utilizing a temporary storage of the produced energy is required, so that it can be released in times of peak energy demands. Air storage systems provides one solution to this problem Air is compressed and stored in underground caverns or aquifers. This air is compressed is by utilizing the electricity produced during peak energy generation periods and is then decompressed to produce electricity during periods of high energy

requirements. The effects of the decompression may be magnified by burning this decompressed air along with natural gas or coal to have higher volumetric expansions giving greater yields of electricity. Only certain geologies (like cavern and mines) have been historically utilized for CAES systems. The concept of locating a storage system inside an aquifer is being considered. The storage is performed by desaturating the aquifer host rock by forming an ‘air bubble’. The air bubble is then utilized for daily operations by cyclic compression and decompression of the stored air based on the demand. The constant compression and decompression of air within the reservoir would lead to changes in temperature, liquid and gas saturations and mechanical stresses. Heterogeneity of the host rock heavily influences the behavior of the CAES. A case study has been undertaken described in Section 6 to study of a proposed a CAES facility considering the effects of the heterogeneity. The recommendations and the scope for carrying out future work has been outlined in Section 7.

1.4 ORGANIZATION OF THE DISSERTATION

The first Section of this dissertation is advocated to introduce the research performed. Section 2 is related to the behavior of frozen soils, An exhaustive review of the behavior of this kind of soil is in the Section 2. This section also includes different frameworks for simulating this behavior. A numerical model (Nishimuara et al., 2009) was found to be suitable for capturing several key features of frozen soil behaviors. The validation of this model for frozen soils is presented in Section 3. Different type of soil samples (i.e. natural and reconstituted) were used in the model validation. The validation focused on the mechanical and hydraulic behaviors in response to changing

environmental conditions mainly controlled for fluctuation of subzero temperatures. The model was then applied to study several field real cases associated with foundations in frozen soils. The major objective is to understand collapse compression behavior of frozen soils upon thawing.

The framework presented in Section 3 does not account for the effects of cyclic freeze and thaw on soil behavior. After the review of the existing literature, it was perceived that the available experimental information is lacking. Therefore an experimental campaign was undertaken to study the impact of the freeze-thaw cycles. Combining this experimental information with existing literature, a constitutive mechanical framework is suggested extending the model for frozen soils proposed in Section 2 to account for this cyclic behavior. The experimental campaign and the associated constitutive model are detailed in Section 4.

The work presented in Section 5 examines the validity of a recently proposed numerical framework for HBS proposed by Sanchez et al. (2014). The main focus is on the behavior of HBS at low temperature and during production of the methane gas by the implementation of possible dissociation techniques, such as: depressurization, heating and chemical stimulation.

Section 6 is related to the analyses of CAES project in porous rock. A general introduction to this problem is presented in this Section. The numerical models proposed to analyze the CAES project at Dallas site are also presented in this Section in detail. The effect of heterogeneity of the host rock on CAES performance is also discussed in

Section 6. The recommendations and the scope for carrying out future work have been outlined in Section 7.

2 BEHAVIOUR AND CONSTITUTIVE MODELING OF FROZEN SOILS

2.1 INTRODUCTION

A substantial portion (24%) of the northern hemisphere is covered under permafrost (Andersland and Ladanyi, 2004). Permafrost is usually defined as the soil which is frozen for more than two consecutive years. The extent of permafrost thickness depends on the season but usually varies from 0.3 to 4m. Because of the extensive amount of land under these conditions it is crucial to have an understanding on the behavior of these frozen soils.

Constructions in regions of permafrost have always posed a significant challenge. Engineering properties of the soils such as strength, stiffness, flow and volumetric behaviors change drastically with changes in temperature. The study of these soils is also important due to the recent discovery of fossil fuels, such as petroleum and gas hydrates near the Arctic Circle. Resource and transport development for these areas requires the performance of major engineering works. Engineering problems that persist in these regions include, amongst others, distress of foundations due to thawing leading to cracking of the super structure (Figure 2.1a); differential movements caused in roads and other infrastructure due to thaw weakening (Figure 2.1b); glacial and periglacial slope failures causing landslides (Figure 2.1c); and railroad distortion due to heaving of the soil (Figure 2.1d). The possible effects of climate change on frozen regions have increased the interest on the study of frozen soils (Parry et al., 2007). These problems are generally observed in soil which undergoes large changes in volume during thawing. The assumption in this work is that significant rearrangement of the soil structure

induced during heating are the main responsible of these problems. A large focus of this chapter and Section 3 is to understand and replicate this behavior typically observed in frozen soils.



a)



b)



c)



d)

Figure 2.1 Infrastructure failures in permafrost regions a) Building Failure due to thaw settlement (Romanovsky, 2003) b) Road failure (Turchett, 2010) c) Rock fall due to glacial slope failure (Schoeneich et al., 2011) d). Excessive railroad distortion (Turchett, 2010)

Frozen soil mechanics also finds its application in construction of ice core dams (Figure 2.2). Frozen soils have a very low permeability which makes them an excellent

core material in permafrost regions. To maintain the freezing temperatures in the dam thermosyphons are placed in the dam to take the heat out. A majority of these dams have been constructed in and around the regions of Alaska, Canada and Russia.



Figure 2.2 Construction of a frozen core dam (Nuna Logistics, 2014)

Other applications include artificial ground freezing, where the ground is frozen by circulating a cryogenic fluid around the area to be treated (Figure 2.3). This has been extensively used for sinking shafts and constructing tunnels (Moretrench, 2011). More recently this technique has been used in preservation of building foundation of historically significant buildings.



Figure 2.3 Ground freezing for sinking shafts (Moretrench, 2011)

Frozen soils have also been used as barriers for waste containment (Figure 2.4) in Canada and the USA. They have been historically used to prevent the seepage of low level radioactive waste into the ground water (DOE, 1999). Recently, there has also been a proposal to utilize cryotic soils to contain nuclear waste near the Fukushima nuclear plant facility (Kiger, 2013).



Figure 2.4 Frozen soil barrier system at Oak Ridge National Laboratory (Johnson et al., 2000)

Understanding the behavior of soils subjected to freezing temperature would require in depth knowledge on the processes of freezing, melting, water migration and deformation under loading, freeze thaw behavior and creep. The study and modeling of the soil behavior under these conditions have been studied for the past 100 years. The initial literature review suggested that research on creep and partially frozen soils are extensive while large gaps exist in the mechanical and hydraulic description of frozen soils. The work done during this dissertation is concentrates on the Hydro-Mechanical (HM) behavior of frozen soils.

Substantive experimental and analytical studies have been undertaken to understand the complex behavior of these soils. On the experimental front, extensive studies have been performed on reconstituted and natural frozen soils to understand its behavior. Approaches towards modeling vary based on the application and the

phenomena studied. A good example of this would be Yusufuku and Springman, 1999 considered frozen soil as a composite ice-soil material in order to quantify the elastic properties such as Young's Modulus and Poisson's ratio of frozen soils whereas, Michalowski and Zhu, (2006) in trying to capture frost heaving utilized the concept of a porosity rate function based on changes of the pore space during freezing and thawing.

This section addresses the behavior of frozen soils in the proceeding sections followed by a brief description of previous analytical models developed to explain this behavior. The framework based on critical state mechanics utilizing a two stress variable concept was developed by Nishmura et al. (2009) whose details are briefly discussed.

2.2 EFFECT OF ICE ON THE BEHAVIOR OF FROZEN SOILS

When the temperature drops below the freezing point, the water in the pore space may freeze to form ice depending on a number of factors, amongst others, freezing temperature, pore size, pressure and type of soil. The formation of the ice is generally accepted to have a huge impact affecting the mechanical and hydraulic behavior of frozen soil. It is therefore vital to understand the behavior of ice when studying frozen soils.

The type of ice depends mainly on the pressure and temperature at which the ice is formed. Figure 2.5 shows the different types of ice in the Pressure-Temperature (PT) diagram for the water. The most predominant ice found in soils in the biosphere is the type 'Ice I_h'. It is generally formed between pressures of 1Pa to 100 MPa and temperature between 0°C and -120°C. This is the only formation type considered in this

study as most engineering problems fall within these confines of pressure and temperature.

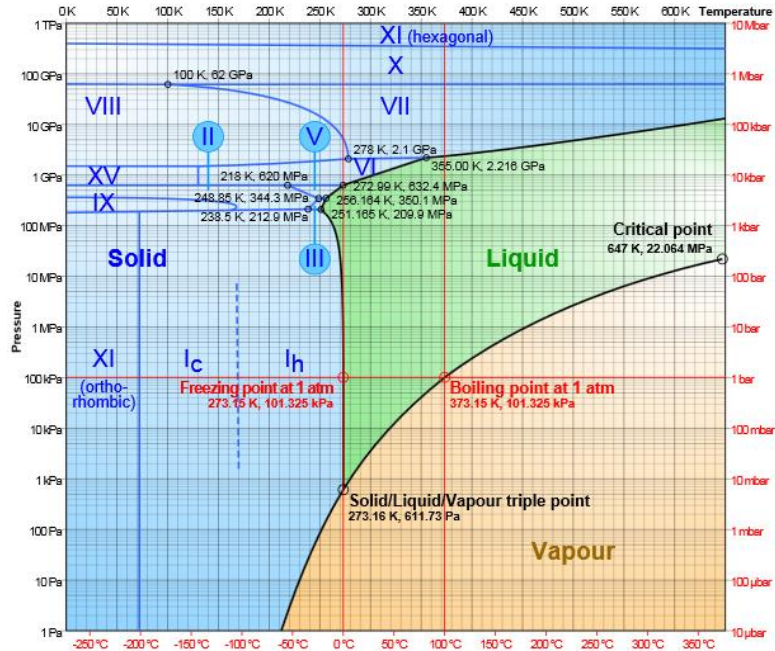


Figure 2.5 Phase Diagram of Water (Cmglee, 2013)

Figure 2.6 a) to d) shows some of the different microstructure types of ice. The orientation of ‘c-axis’ or the axis of crystallographic symmetry is a common term used to distinguish between the formation types. Granular ice (Figure 2.6 a) is a common form of ice produced by freezing water saturated ice particles or snow. Columnar-grained ice with c-axis in vertical plane (Figure 2.6b) is ice formed on relatively calm conditions and grain sizes of the ice particles are generally larger than the granular ice. Columnar-grained ice with random orientation of c-axis (Figure 2.6 c) is generally found in glacial ice or Arctic sea ice (Weeks, 1998). Columnar-grained ice with horizontal c-

axis (Figure 2.6 d) is common feature of landfast sea ice. All naturally occurring ice is generally composed of these basic microstructure types. For example, sheet ice is formed from consolidation of pancake ice or congelation of grease ice which are formed from granular ice in rough and calm oceans respectively (NSIDC, 2014). Details on the different of formation of ice and their behavior are described in greater detail in a number of publication as for example: Sinha, (1989), Schulson, (2004), Michel and Ramseier, (1971) Weeks, (1998).

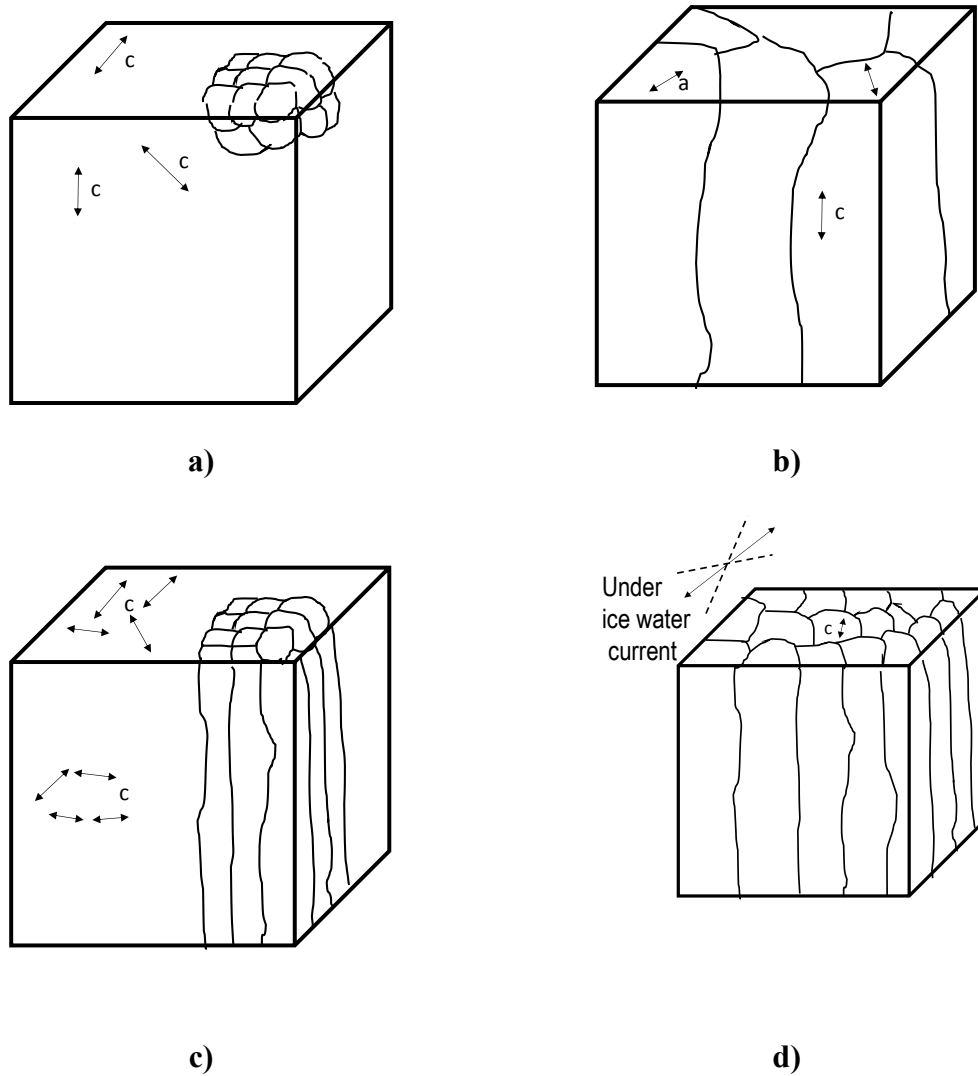


Figure 2.6 Different formation types of ice a) Granular Ice b) Columnar-grained ice with c-axis in vertical plane c) Columnar-grained ice with random orientation of c-axis d) Columnar-grained ice with horizontal c-axis (Sinha 1989)

The stiffness of ice depends on the formation type, strain rate of testing, and the salinity of the freezing water. The Young's Modulus of ice tested in various forms (i.e. granular or otherwise) ranges between 9 and 11 GPa, and it is slightly influenced by the variation of temperature in the range 0 to -50 °C. For example, Figure 2.7 shows

variation of the Young Modulus (E), shear modulus (G) and Poisson ration (ν) obtained by Sinha (1989) for temperatures ranging from 0 to -50 °C. As it can be observed the impact of freezing temperature on elastic properties is not very significant.

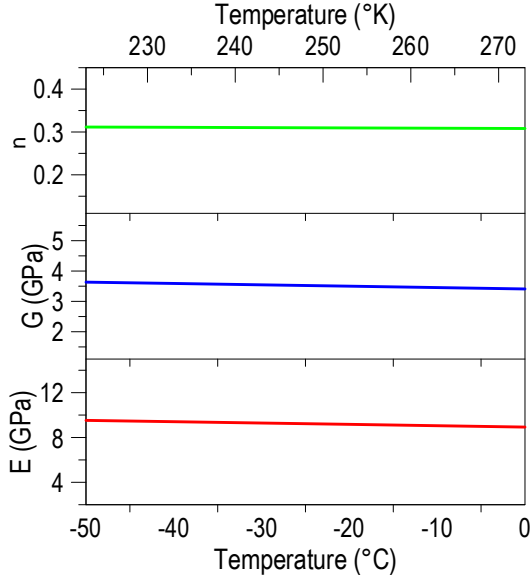


Figure 2.7 Temperature dependence of ice elastic properties (Sinha, 1989)

Similar behavior was observed by other researches, as for example: Yasufuku and Springman, (1999); Hawkes and Mellor (1972); Mellor and Cole (1982). The variation in the strength of ice tested at different temperatures and different strain rates is shown in Figure 2.8 (Schulson, 2004). It can be seen that the strain rate has a significant effect on the strength, while the impact of temperature is marginal (as discussed above). It has also been observed that the strength of ice depend on the confining pressure and ice type.

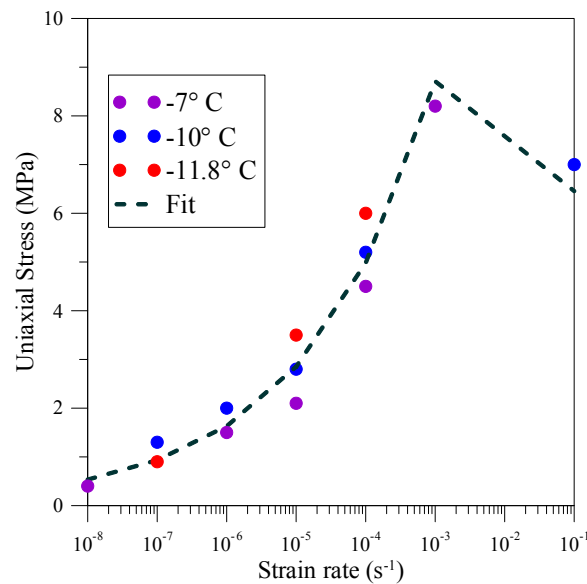


Figure 2.8 Effect of strain rate and temperature on strength of ice (Schulson, 2004)

The volumetric behavior of ice also plays a unique role in influencing frozen soil behavior. When the temperature of water is nears the freezing point, the density of water starts to decrease and at around 4°C reaches its peak of 1001 Kg/m³ (Wagner et al.,

2002). Below this temperature it remains fairly constant until 0°C when there is a phase transformation to ice increasing the volume to about 9% (Wagner et al., 2002) and reducing the density to 991 Kg/m³. Further cooling reduces the volume again but it is negligibly small. A schematic showing the volume change with respect to temperature is presented in Figure 2.9.

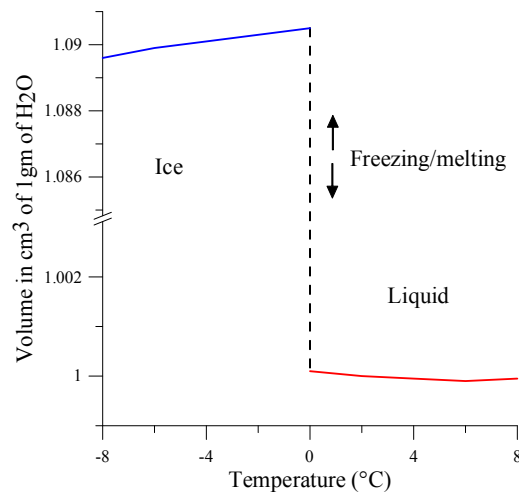


Figure 2.9 Volume Temperature diagram of water

2.3 UNFROZEN WATER IN FROZEN SOILS

The primary motivations for the study of frozen soils stemmed from the problems associated with heaving. It was originally thought that the volume changes observed when soils froze were primarily due to the volumetric expansion of water during its phase change to ice. However, the observed volumetric strains greatly differed from the expected ones and that the soils continued to heave if they had access to free

water. These observations demanded a revision in this theory. Taber, (1929) explained that not all the pore water present in the soil freezes when the temperature reduces below the freezing point of water and termed this as ‘unfrozen water’. A schematic of the frozen soils soil with unfrozen water is shown in Figure 2.10. The presence of this unfrozen water was mainly attributed to a capillary action of the pore spaces in the soils. Beskow, (1935) observed that larger pores freeze at higher temperatures when compared to smaller one.

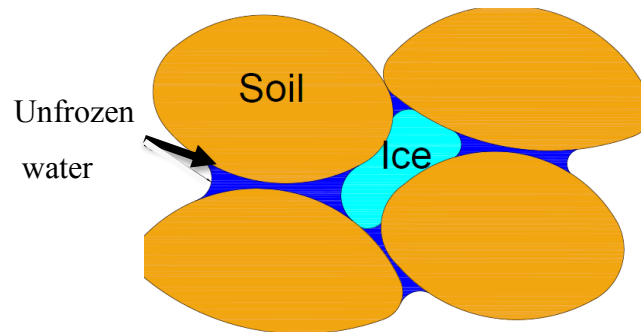


Figure 2.10 Schematic representation of frozen soils (melting may induce a significant changes of the soil structure)

The soils are assumed to be fully saturated with water prior to freezing. When the temperature falls below freezing temperature, the pore space would be occupied by the ice and the unfrozen water, therefore the degree of saturation of ice S_i is given by,

$$S_i = 1 - S_l \quad (2.1)$$

where, s_i is the degree of ice saturation and s_w is the degree of unfrozen water saturation.

Various techniques have been developed to study the existence of unfrozen water in frozen soils. Tice et al, (1988), demonstrated the existence of unfrozen water in Alaskan silt using a Pulse Nuclear Magnetic Resonance (PNMR) technique. The PNMR technique is a common scientific method used in the study of isotopes and has found it applications in medicine, chemistry, quantum computing as well as petroleum industry (Andrew, 2009). The technique relies on the phenomena where a nuclei in a magnetic field absorbs and re-emits a unique electromagnetic radiation. Based on this emitted radiation the different constituents are determined. The soil particles used in the study by Tice were of a fairly large size (D_{30} ranging between 0.022 and 0.004). Unfrozen water in undisturbed samples and remolded samples are shown in Figure 2.11. The unfrozen water content is as high as 23% in remolded samples and as much as 10% in undisturbed samples. Details of the experiment are provided in greater expanse in Tice et al., (1988).

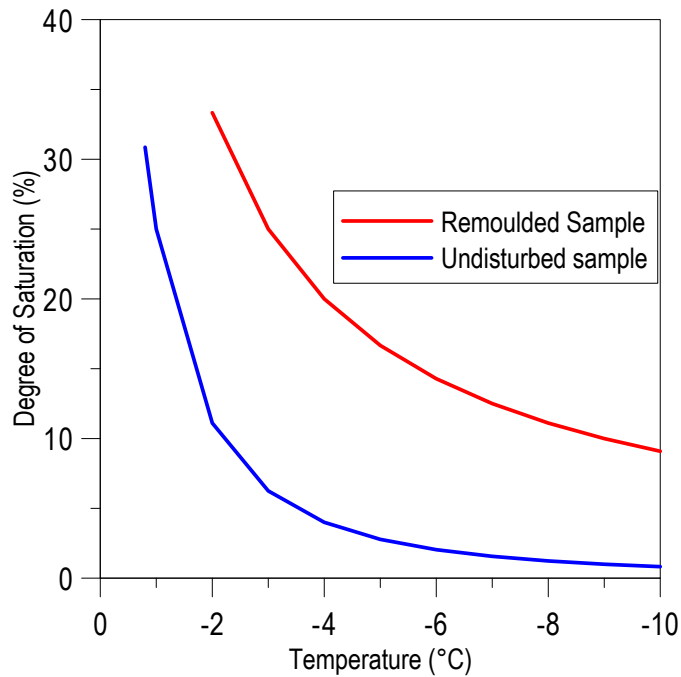


Figure 2.11 Results of the PNMR (Tice et al., 1988)

Other methods such as the dilatometer technique (Pusch, 1978), cation exchange (Tice et al., 1976), electron microscope (White, 1999), were also developed to demonstrate the presence of unfrozen water in frozen soils. These techniques concentrated mainly on clays where the unfrozen water influences the microstructure behavior. The effect of this phenomenon on the macroscopic behavior of frozen soils is explained in greater detail in Section 4.

The experimental evidence clearly suggests that the ice and unfrozen water coexist and, at a given temperature, a thermodynamic equilibrium is established between these two phases. One way of visualizing this concept was introduced by Everett (1961) using the ‘Piston-cylinder’ model of ice growth shown in Figure 2.12.

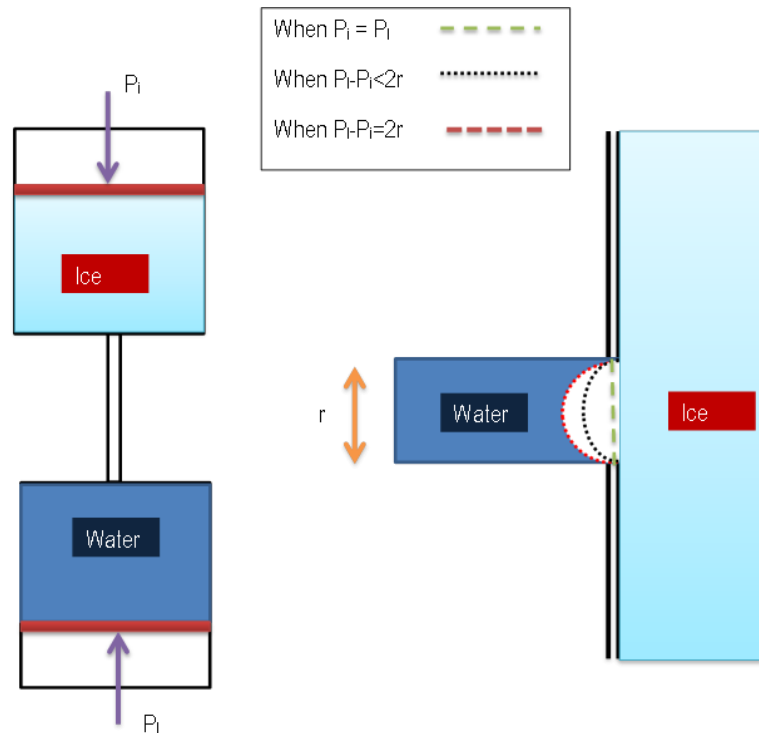


Figure 2.12 Piston cylinder model (results modified after Everett, 1961)

Everett's model consisted of two cylinders connected by a singular pipe representing the pore capillary. Initially both pistons are filled with water. The temperature is lowered in the top piston to cause the nucleation of ice. The ice formation induces an increase in the piston height of the top cylinder due to the volumetric changes in the ice. If the pressure of the ice and the liquid are equal then, the interface between them is planar and the ice does not propagate along the capillary. If there is a difference in the pressure, then either the water from the bottom piston moves up along the capillary and freezes in the top piston increasing the height of the piston, causing frost heave, or the ice from the top piston grows along the capillary. Everett related the

surface area of the interface formed between the ice and water phases using a thermodynamic relation shown in equation (2.2).

$$P_i - P_l = \psi_{sl} \left(\frac{dA_r}{dV} \right) \quad (2.2)$$

where, ψ_{sl} is the interfacial tension between the two phases, A_r is the surface of the interface and V is the volume of the ice crystal. Note that for a hemispherical surface the ratio dA_r/dV is equal to two divided by the radius (r) of the capillary (i.e. $(dA_r/dV) = 2/r$). This relationship is an important milestone in establishing a connection between the liquid and ice pressures and the radius of the pore capillary. This relationship was used in later models for unfrozen water in frozen soils (e.g. Arenson and Springman 2005, Miller et al, 1975, Multon et al, 2010, Michalowski and Zhu, 2006). The model proposed by Everett however does not consider the effects of the adsorbed water and osmotic pressures, which was eventually overcome by the models proposed by Loch (1978) and Miller (1978). Loch redefines the chemical potential as the Gibbs free energy per unit mass of a substance shown in equation (2.3).

$$\eta_l d\mu_l = -SdT + VdP - \eta_s d\mu_s \quad (2.3)$$

Where, η is the mass of the substance, S is the entropy, μ is the chemical potential, V , P and T refer to the volume pressure and temperature of the substance respectively, the subscripts l and s refer to water and soil mineral respectively. The equation was then effectively reduced to the form shown in equation (2.4).

$$P_i = \frac{\rho_i}{\rho_l} P_l - \rho_i \left(\frac{\Delta T}{T_0} \right) \quad (2.4)$$

where, l is the latent fusion of heat, T_0 is the reference temperature of freezing. This equation is generally termed as the generalized Clausius Clapeyron equation and is used widely in studies involving cryotic soils. The difference between the ice and the liquid pressure (i.e. P_i and P_l , respectively) is termed as the ‘cryogenic suction’ (s_c), as follows:

$$s_c = P_i - P_l \quad (2.5)$$

Cryogenic suction is defined in the positive range only. Unfrozen water affects several properties such as the strength, stiffness, volumetric changes (such as heaving and thawing), the hydraulic conductivity and the thermal conductivity of frozen soils. The amount of unfrozen water is influenced by several factors, as for example temperature, the pore size, the type of soils and the access to free water. Based on the access to the free water, soil systems are classified in to main categories: open and closed systems. Soils which have access to free unfrozen water are termed as open systems and those with no access to such water are called closed systems. Schematics of closed and open systems are shown in Figure 2.13.

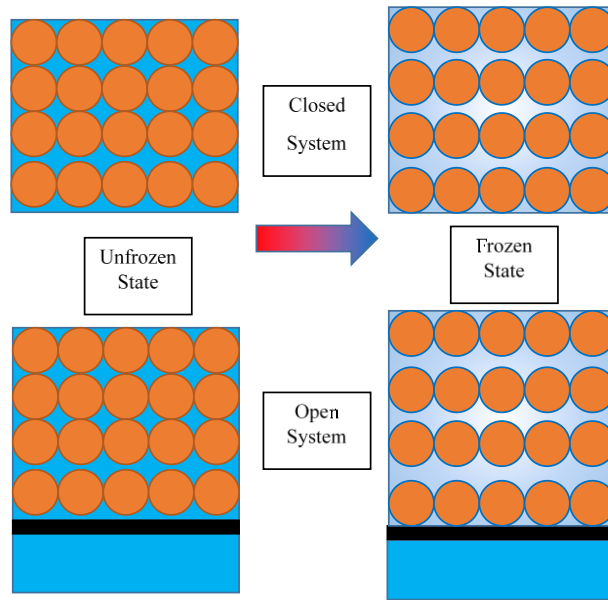


Figure 2.13. Schematic of an open and a closed system transitioning from unfrozen to frozen state

Both the closed and open systems exhibit a volumetric increase of the soil when frozen. The expansion is referred to as heaving of the soil. Heaving causes the rearrangement of the soil skeleton and affects several important properties. This expansion exhibited by the closed system is generally lower than the open system. Open systems expand beyond the 9%, usually associated during the phase change. Similar to the piston case described above the soils here continue to absorb the free unfrozen water. It has also been observed (Konrad and Shen 1996; Konrad and Morgenstern, 1980) that there are formations of ice lenses in these open systems. An ice lens is formed when interconnected pores freeze forming a sheet of ice within the soil. Ice lenses tend to grow with reduction in temperature and induce cracks within the soil structure. Upon thawing the ice melts creating gaps and increasing the porosity of the soil. This process leads to

an irrecoverable increase in the permeability of the soil and it could also weaken the soil structure.

In contrast, the amount of expansion in closed systems is directly related to the amount of frozen water existing in the soil at that particular temperature. Ice lenses are generally not formed in closed systems. Closed systems form a vital part of this study as their behavior dominates the response of fully frozen soils as well as soils with no access to free water.

2.4 EFFECT OF UNFROZEN WATER ON FLOW BEHAVIOR OF FROZEN SOILS

A schematic representation of a frozen ground is presented in Figure 2.14. The ground surface has a linear increasing temperature gradient with depth with the lowest temperature at the top. At the top of the unfrozen zone (i.e. the contact between the unfrozen one and the partially frozen zone) the temperature is assumed to be 0°C. Three distinct zones are identified for these soils:

- i) The frozen zone, where the soil is completely frozen and is completely saturated with ice;
- ii) The unfrozen zone, where the soil is completely unfrozen and;
- iii) The partially frozen zone where the unfrozen water exists at subzero temperature.

The distribution of the ice pressure in the frozen zone can be assumed to be hydrostatic in nature as described in Konrad and Duquennoi, (1993). Gens et al. (2010) however, theorized that the ice and liquid pressures are due to a thermodynamic

equilibrium rather than a hydrostatic distribution of pressure. The ice pressure at the top of the soil layer is assumed to be zero and the corresponding liquid pressure is calculated based on the Clausius Clapeyron (equation 2.3). The liquid pressure is reduced linearly to zero from the top of the soil to the center of the unfrozen soil layer. The ice pressure for the remaining length is calculated using equation (2.3) based on the temperature at the corresponding length. The degree of saturation of ice is calculated based on the ice and liquid pressure and the prevalent temperature using a 'retention curve'. Different forms of the retention curve are discussed in section 2.6. The amount of unfrozen water is assumed to occupy the remaining pore space left in the soil. The probable distribution of the liquid pressure, ice pressure, and liquid and ice saturations resulting from these assumptions are also presented in Figure 2.14.

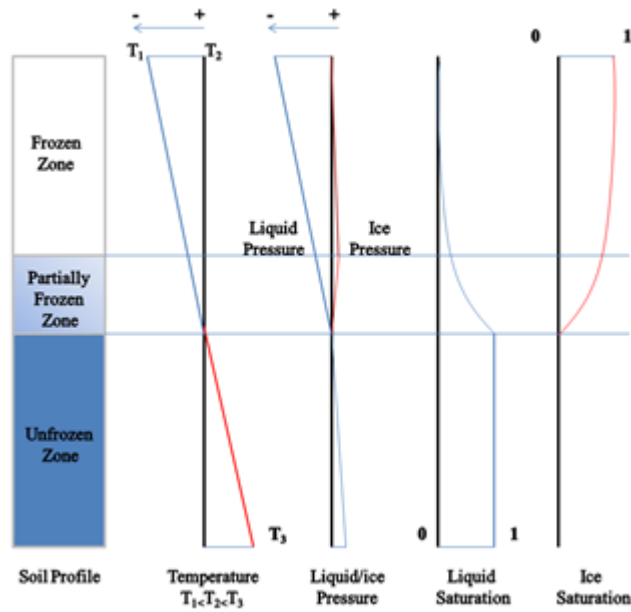


Figure 2.14 Schematic representation of a frozen soil profile

The permeability of silty loam soil of marine origin was tested at different temperatures below the freezing point by Ishizake et al. (1985). The reduction of temperature increases the amount of water in frozen state, and thereby occupying more of the pore space effectively reducing the flow of the unfrozen water and therefore the coefficient of permeability of the soil.

Xu et al. (1999) conducted a series of experiments in closed systems where the soils were subjected to freezing temperatures at one end of the specimen while keeping the other end above the freezing temperature. The pattern of the water migrations under these conditions observed for a typical soil specimen is shown in Figure 2.15. When the soil was close to the freezing point (i.e. 0°C) the maximum water flux was observed at the center, and it was also detected that the fluxes dropped down at the hot and the cold

ends of the sample. The cryogenic suction at the hot end is equal to zero and increases with depth due to the temperature calculated using equation (2.5). The difference in this potential causes the water to flow from hot end to the colder region of the soil column which is marked by the increase in flux between the 0 and 7 cm. The reduction in the water flux in the colder regions (height 7-15 cm) of the sample is due to the drop in permeability and the decreases in the amount of unfrozen water at these temperatures. The water migration patterns exhibited in frozen soils are similar to the ones observed in unsaturated where changes in flow can be expressed using a generalized form of Darcy's law.

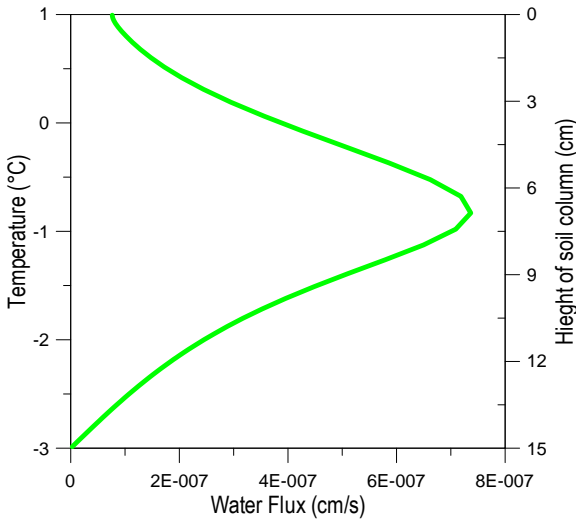


Figure 2.15 Flow rate vs temperature in frozen soils

2.5 MODELING HEAT AND MASS TRANSFER IN FROZEN SOILS

2.5.1 Existing flow models

Several different types of models have been developed for simulating the mass and heat transfer focused on freezing and thawing of soils. Most of them can be classified as thermo-hydro (TH) coupled models. They can be divided into three wide and streams as:

- i. Rigid-ice models (e.g.; Gilpin, 1980; O'Neill and Miller, 1985; Nixon, 1991; Nakano, 1997).
- ii. Hydrodynamic models (e.g. Harlan, 1973; Guymon and Luthin, 1974; Jame and Norum, 1980; Newman and Wilson, 1997; Hansson et al., 2004; Hansson and Lundin, 2006).
- iii. Segregation potential model (Konrad and Morgenstern, 1980, 1981, 1984).

The rigid-ice model predicted freeze-thaw deformations using the concept of ice lenses but does not consider the expansion or contraction of the soil skeleton (e.g.; Gilpin, 1980; O'Neill and Miller, 1985; Nixon, 1991; Nakano, 1997). The process of regelation is also described by Miller (1978), as the one in which there is movement of ice with the soil throughout the process of melting, transport and refreezing. In this process of movement it displaces the soil grain before refreezing. This concept was used to account for the heat transfer during ice formation.

The hydrodynamic model proposed by Harlan, (1973) assumes that hydraulic conductivity of a partially frozen soil depends on the energy state of the soil-water-ice

system, similar to the soil-water-air system in unsaturated soils. The mass transfer in the soil system by conceptualizing the ice as sink/source where water can be added or removed from storage based on temperature and energy of the system.

The segregation potential model developed by Konrad and Morgenstern, (1980) introduces the concept of the segregation pressure. This segregation potential depends on the following main variables: temperature, overburden pressure and the size of the capillary. This model is able to predict the formation and separation of ice lenses. The process of formation and separation of ice lens increases the expansion beyond the 9% and is referred to as secondary heave.

2.5.2 Hydraulic behavior of frozen soils

The literature review on frozen soil behavior presented in Section 2.3.1 suggests that there is a strong similarity between the behaviors of frozen soils and unsaturated soils. The matric suction formed between the water and air phases in unsaturated soil can be replaced by the cryogenic suction occurring in frozen soils. The schematic of the representation of the phases is represented in Figure 2.16. The following sections present the typical constitutive models used to describe the ability of frozen soils to retain unfrozen water in the pore space; and also the models used to describe the flow of unfrozen water in saturated soils.

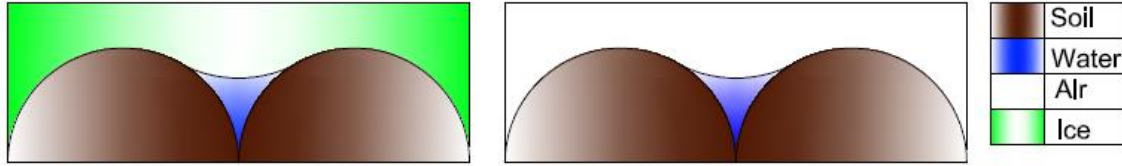


Figure 2.16 Schematic representation of unsaturated and frozen soils

Retention of unfrozen water in frozen soils

The frozen soil is assumed to consist of three phases, namely: liquid (unfrozen) water, ice (i.e. frozen water), and solid (consisting of the soil mineral). In soils subjected to atmospheric conditions the amount of unfrozen water depends mainly on the existing temperature, the type of soil and pore structure of the soil.

One of the first models proposed to account for the amount of unfrozen water in frozen soils was proposed by Tice et al. (1976). Tice' model relates degree of saturation of liquid water with the freezing temperature by means of the following equation.

$$S_l = (1 - (T - T_0))^\alpha \quad (2.6)$$

where, S_l is the degree of saturation of unfrozen water,

T_0 is the reference freezing temperature at the reference pressure. For soils at atmospheric conditions is equal to 273.15 °K), and

α is a parameter that depend on the pore structure (Tice et al., 1976).

The variation in the degree of saturation of the unfrozen water versus temperature for different values of α obtained from equation (2.5) is presented in Figure

2.17. The lower values of α would represent fine grained soils where the amount of unfrozen water is high even at very low temperatures.

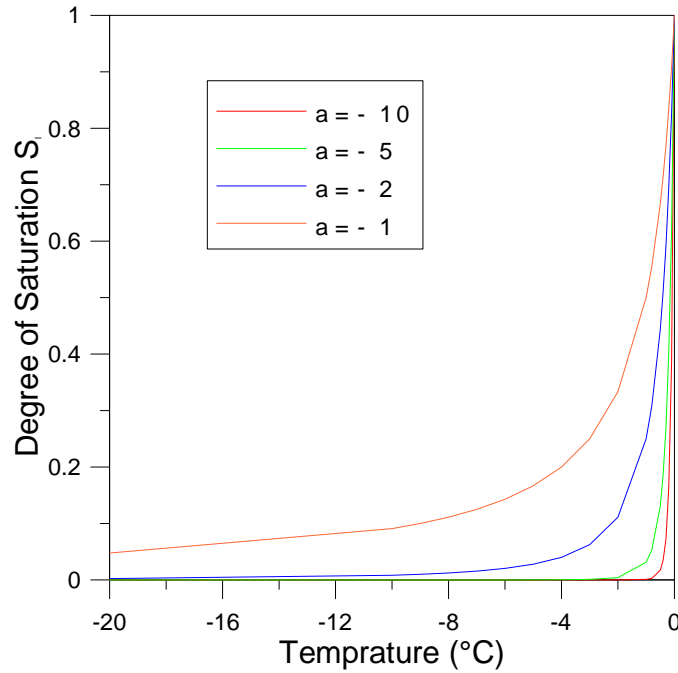


Figure 2.17 Degree of saturation vs temperature for the Tice model

An alternative approach to model the amount of unfrozen water in frozen soils was suggested by Nishimura et al. (2009). It is based on the water retention curve typically used in unsaturated soil mechanics. They adopted the equation proposed by van Genuchten to model the water retention phenomenon in soils (van Genuchten, 1980). This equation can be written in terms of the liquid degree of saturation and cryogenic suction as follows:

$$S_l = \left(1 + \left(\frac{P_i - P_l}{P_o} \right)^{\frac{1}{1-\lambda}} \right)^{-\lambda} \quad (2.7)$$

where, P_o and λ are parameters which depend on the porosity of the soil. Details about the modeling of unsaturated soil behavior can be found elsewhere (e.g. Fredlund and Rahardjo 1993 Gens and Alonso, 1988; Sanchez et al., 2009, Briaud, 2013)

Combining equations (2.6) and (2.3) it is possible to express the liquid degree of saturation in terms of the freezing temperature, resembling Tice's model:

$$S_l = \left(1 + \left(\frac{-\left(1 - \frac{\rho_i}{\rho_l} P\right) P_l - \rho_l l \ln\left(\frac{T}{T_0}\right)_i}{P} \right)^{\frac{1}{1-\lambda}} \right)^{-\lambda} \quad (2.8)$$

Figure 2.18 shows a typical retention curve for different values of P_o and λ .

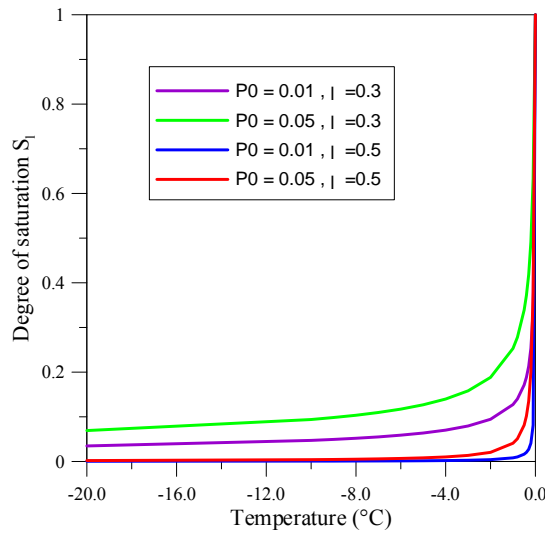


Figure 2.18 Typical van Genuchten retention curve for different values of P_0 and λ

Darcy's law

The generalized Darcy's law is an extension developed to overcome some of the limitations of Darcy's law such as considering unsaturated flow, changes in pore structure, heterogeneities and anisotropy in soil behavior. Equation (2.9) represents the generalized Darcy's law adopted for the flow of unfrozen water in the pore space. Because ice is rigid, only the flow of the unfrozen water is considered.

$$q = \frac{k_{rl}}{\mu_l} \mathbf{k} (\nabla P_l - \rho_l \mathbf{g}) \quad (2.9)$$

where, q is the flux of the water flux, \mathbf{k} is intrinsic permeability matrix, k_r is the relative permeability of the soil for water, μ_l is the viscosity of the water, ∇P is the gradient of the liquid pressure and \mathbf{g} is the gravity vector (0,0,-g)

Relative permeability

The relative permeability is the ratio of the effective permeability of that phase to the absolute permeability. Similar to unsaturated soils the relative permeability depends on the degree of saturation of that phase. The relative permeability derived from the van Genuchten is given by:

$$k_r = \sqrt{s_l} \left[1 - \left(1 - s_l^{1/\lambda} \right)^\lambda \right]^2 \quad (2.10)$$

Alternatively it can be calculated using the power law given by

$$k_r = A S^\beta \quad (2.11)$$

where, A and β are model parameters

Fourier's law and thermal conductivity

Fourier's law is employed in the above equation for calculating the conductive heat flux. Fourier's law is given by

$$i_c = \lambda \nabla T \quad (2.12)$$

where, i_c is the conductive heat flux and λ is the overall thermal conductivity

The thermal conductivity is calculated by using the geometric mean (Cote and Konrad, 2005),

$$\lambda = \lambda_s^{1-\phi} \lambda_l^{S_l \phi} \lambda_i^{(1-S_l)\phi} \quad (2.13)$$

where, λ is the overall thermal conductivity of the soil mass, the subscript s denotes the mineral phase.

2.6 MECHANICAL BEHAVIOR OF FROZEN SOILS

The importance in understanding the mechanical behavior of frozen soils for geotechnical engineers cannot be overemphasized. Construction of buildings and other infrastructure depend on the strength, the stiffness and the compressibility of the natural soil. This section presents first the existing models to describe the mechanical behavior of frozen soils. Afterwards, the focus is on discussing some of the limitations of the existing models to describe key aspect of frozen soil behavior and also presenting the most relevant data from laboratory experiments used in this dissertation to validate a recent model for unfrozen soils.

2.6.1 Existing mechanical models for frozen soils

The drive towards developing mechanical models for understanding frozen soil behavior stems from design of foundations in these soils. The effect of creep of ice was considered as the main controlling factor in the design. A large number of creep models have been developed for describing this feature of frozen soil behavior (Andersland and Ladanyi, 2004; Sayles, 1973) and has been extensively used in the design guidelines for frozen soil (Ladanyi and Johnston, 1974; Nixon 1978; Jessberger, 1981). Other contributions have been focused on the study of the distress in thaw weakened pavements (e.g. Shoop et al., 2008).

Mechanical constitutive models combining uncoupled thermo-mechanical have also been proposed (e.g. Nixon, 1990). This kind of approaches represented a step forward respect to previous ones, however experimental studies have shown that there is a direct correlation and strong coupling between the mechanical and the thermal behavior of frozen soils described above.

More recent frameworks have incorporated in the modeling changes in pore space to reproduce typical features of frozen soils. For example Michalowski and Zhu, (2006), incorporated a new parameter; which was coined as the ‘porosity rate function’ which allowed to correlate the changes in freezing temperatures with the volumetric deformation though the following equation.

$$\dot{n} = \dot{n}_m \left(\frac{T - T_0}{T_m} \right) e^{1 - (T - T_0)/T_m} \quad (2.14)$$

where, \dot{n}_m is the maximum porosity growth rate for a given soil, T is the current temperature and T_m is the temperature where the maximum porosity rate occurs

This model however does not consider plastic mechanical behaviors of frozen soils soil. Other approaches considered the frozen soils as a composite material, consisting of a granular ice matrix with inclusions of sand particle (Yusufuku and Springman, 1999). A schematic view of the mixture is shown in Figure 2.19

The stresses acting in the frozen soils are split between the ice and the soil skeleton, based on both: the ice content; and the stiffness of ice and soil. The strains in the soil would be calculated based on the Young's modulus and the Poisson's ratio. The effect of changing temperatures is factored into the model by modifying the elastic properties based on a linear relationship between the Young's modulus and the poison's ratio and the prevalent temperature.

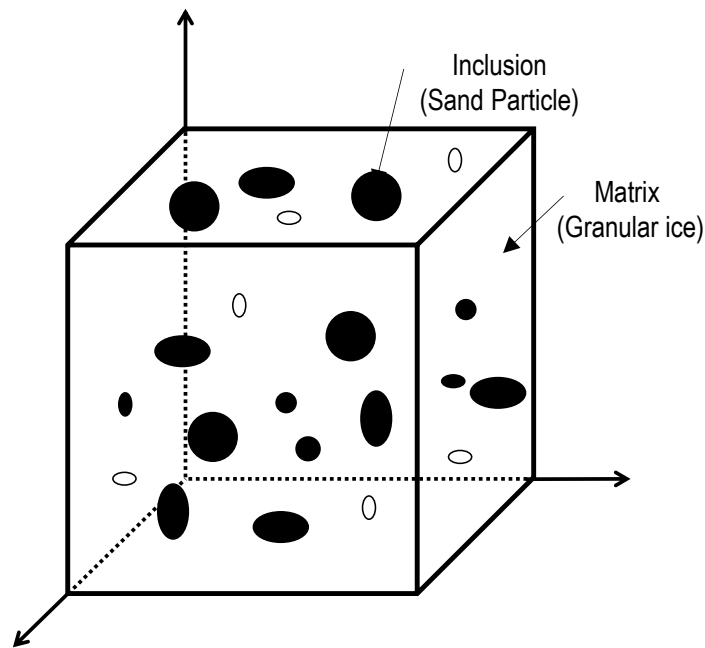


Figure 2.19 Schematic of the frozen soil (Yusufuku and Springman, 1999)

A new concept to model the behavior of frozen soils was proposed by Nishimura et al. (2009). They suggested adapting the Barcelona Basic Model (BBM) to simulate the mechanical behavior of frozen soils and also the incorporation of the cryonic suction as an additional stress variable. The BBM is the most popular constitutive law for modeling the behavior of unsaturated soils. This model extends the Cam-Clay model to the unsaturated conditions and adopts two stress variables: net stress (i.e. total stress minus air pressure) and matric suction (i.e. excess of air pressure over the liquid pressure). The BBM has been applied in many areas of geotechnical engineering, including modeling of barriers for nuclear waste disposal (Gens et al., 1998, Sanchez et

al., 2012), subsidence problems (Menin et al., 2008). The BBM framework is presented in detail in Section 2.6.3 and Appendix I.

In the work by Nishimura et al. (2009) the BBM was proposed as a proper framework to describe the behavior of frozen soils, but this model was not validated against experimental data. It is also true that this model inherits the limitations of the BBM to reproduce some features of soil behavior that are relevant for frozen soils. As for example, the cumulated plastic behavior observed in frozen soils subjected to freezing/thawing cycles. One of the aims of this dissertation is to improve the current modeling approaches to simulate the behavior of frozen soils, including the irreversible cumulative deformations observed during cycles of freeze and thaw. The starting point of the proposed approach is the BBM. The first step was to validate the extended BBM to deal with subzero temperatures. For this endeavor, an extensive search of the experimental data was undertaken. Based on these laboratory tests, the model was validated for a wide range of temperatures and confinement conditions, involving both reconstituted and natural samples. This piece of research is presented in detail in Section 3. Once the extended model was validated to deal with the monotonic decrease (or increase) of freezing temperatures, the model was then extended to handle the effect of thaw/freeze cycles. This enhanced model is presented in Section 4. In the following section background information about the mechanical behavior of frozen soils is briefly introduced. Afterwards, the mathematical framework of the BBM extended to subzero temperatures is introduced.

2.6.2 Volumetric and deviatoric behavior of frozen soils

Figure 2.20 shows a typical response of a soil subjected to isotropic loading in terms of void ratio and mean effective stress. Soils behave elastically for stresses lower than the pre-consolidation pressure, and its volumetric behavior is controlled by the over-consolidate line (also known as unloading/reloading curve) as pressure delimits. Once stresses reach the pre-consolidation pressure, the volumetric behavior is controlled by the virgin consolidation line, and an elasto-plastic behavior of the soil is anticipated during yielding.

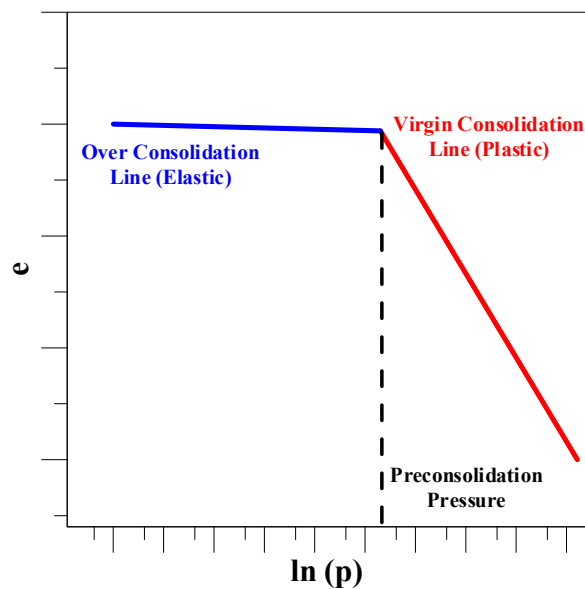
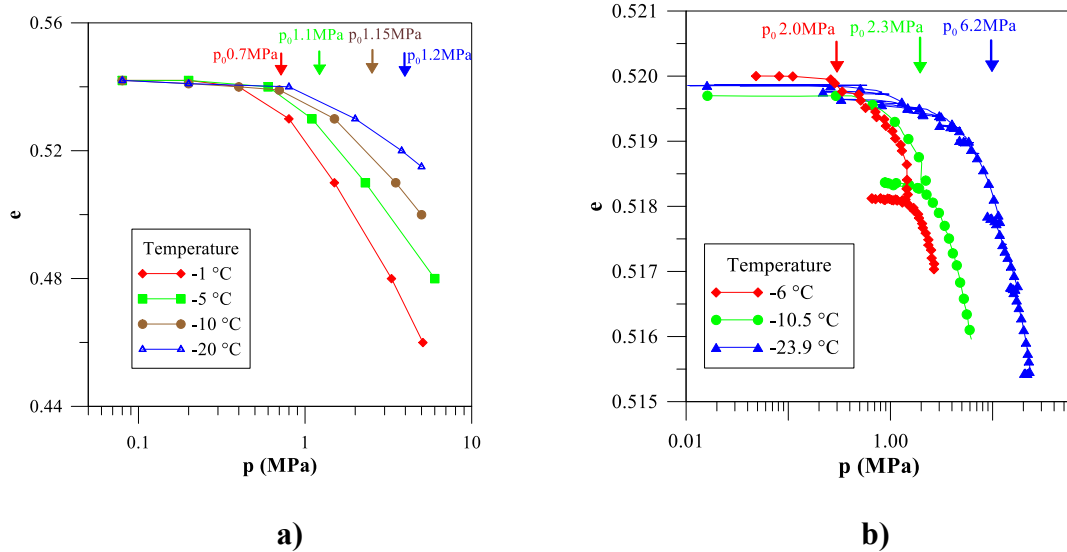


Figure 2.20 Results of an idealized hydrostatic test

The isotropic behavior of frozen soils at different subzero temperatures were studied in the laboratory using both: reconstituted frozen samples (Qi et al., 2010) and natural frozen soils (Lee et al., 2009). Figure 2.21 a) shows the results of the isotropic

tests on reconstituted samples for temperatures varying from $-1\text{ }^{\circ}\text{C}$ to $-20\text{ }^{\circ}\text{C}$. Figure 2.21 b) presents the results associated with natural frozen samples for temperatures ranging from $-6\text{ }^{\circ}\text{C}$ to $-23.9\text{ }^{\circ}\text{C}$.



a) **b)**
Figure 2.21 Volumetric behavior of reconstituted frozen soils: a) Reconstituted frozen samples, b) Natural frozen soils

In both set of tests it can be observed that the values of the pre-consolidation pressures (identified with arrows) tend to increase with the decrease of temperature. This behavior is associated with an increase of the elastic domain. These results also indicate that the elastic slope of the over-consolidated line is practically no affected by the temperature changes. However, the virgin consolidation slope shows a distinct pattern, it decreases with a decrease in temperature. This implies soil stiffening with the reduction of the temperature.

The deviatoric behavior of the frozen soil was explored by means of unconfined and triaxial tests. As it is usual in these types of tests, the soil is sheared by applying a progressively increasing axial load on cylindrical samples under confined conditions (triaxial compression test) or without confinement. Figure 2.22 a) shows the variation of the deviatoric stress with strain for unconfined triaxial test conducted on reconstituted samples of frozen soils by Parmeswaran and Jones (1981). It can be observed that both the stiffness of the soil and the maximum deviatoric stress increases with the decrease of temperature. Parmeswaran, (1980) explored the effect of confinement on the behavior of frozen soils by testing reconstituted frozen samples in a triaxial device. Figure 2.22 b) presents the main results of the experimental campaign. It can be observed that, as in other soils, the maximum deviatoric stress increase with the cell pressure.

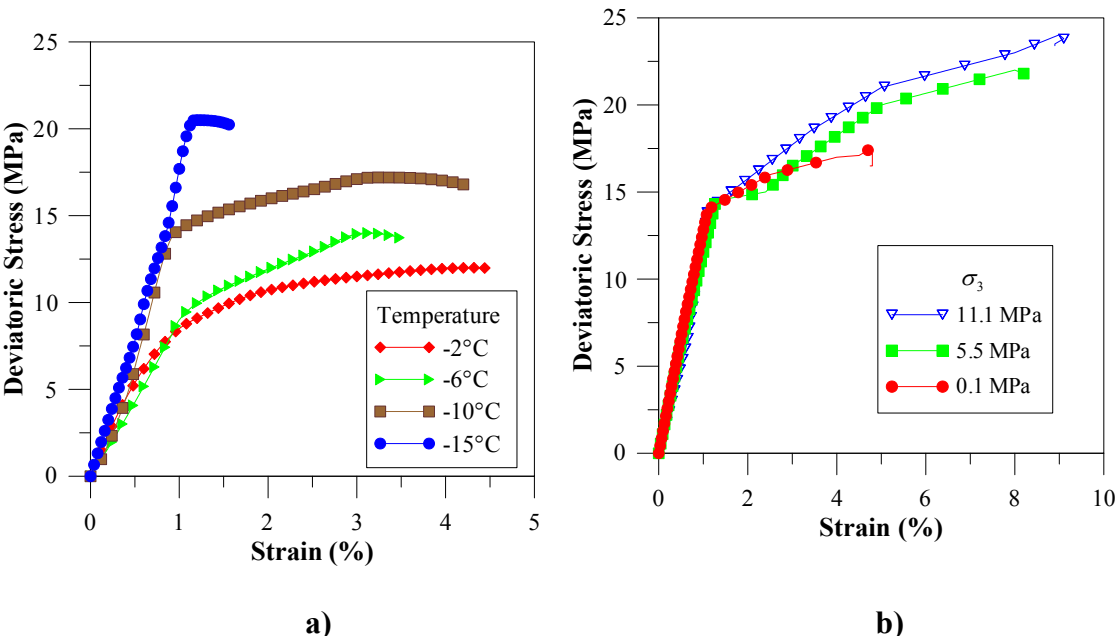
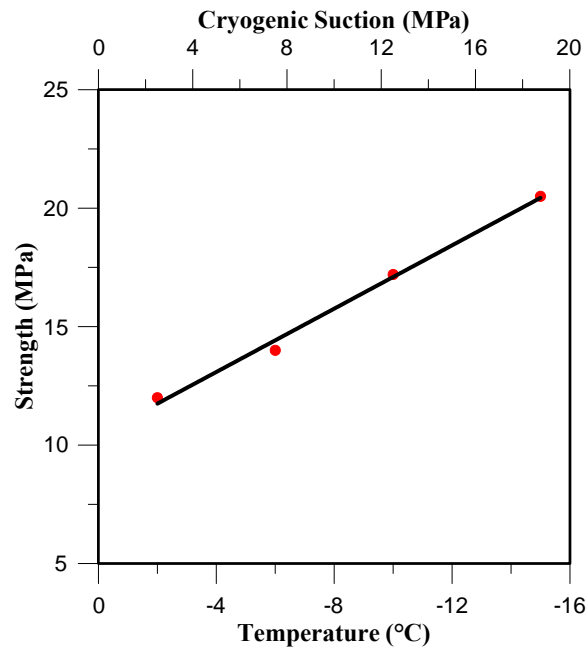


Figure 2.22 Variation of the stress strain behavior of reconstituted soils: a) Effect of temperature, and b) Effect of confining pressure

Figure 2.23 shows the variation of the maximum deviatoric stress with the freezing temperature in the experiments conducted by Parmeswaran and Jones (1981). There is a linear rise in the strength of the soil with the decrease of temperature.

The main effects of cryogenic temperatures on mechanical behavior of frozen soils (i.e. impact of suction on strength, stiffness and pre-consolidation pressure) resemble the influence of matric suction on unsaturated soils. This is why it has been proposed to adapt the BBM to deal with subzero temperatures. The modification of the code is explained in the next section.



c)

Figure 2.23 Variation of strength with temperature

2.6.3 Modified BBM for frozen soils

As mentioned above the BBM adopts two stress variables to describe the behavior of unsaturated soils, namely: net stress and cryogenic suction. For the case of frozen soils these two variables are replaced by the: a modified net stress and the cryogenic suction. The modified definition adopted for the net stress (σ_n) used for frozen soils is as follows:

$$\sigma_n = \sigma - \max(p_l, p_i, 0) \quad (2.15)$$

The definition for cryogenic suction used in the modeling is a slightly variation of equation (2.4), as follows:

$$s_c = \max(P_i - P_l; 0) \quad (2.16)$$

As in the original BBM, the basic idea behind this framework is to extend a well know model for saturated soils, and isothermal conditions, to deal with the typical features of frozen soils behavior discussed in the previous section, amongst others, increase of the preconsolidation pressure with the decrease of temperature, stiffening of the material in the normal consolidation range with the reduction of temperature, and increment of the soil strength with the decrease of temperature. The adopted ‘reference’ elastoplastic framework is the Cam-clay model. However, any proper critical state model for saturated conditions can be adopted as the reference framework.

The developments presented in this section assume that the soil is it is saturated at the freezing point of water. Based on the results presented in Figure 2.24 it is possible

to sketch the idealized isotropic tests conducted at different temperature presented in Figure 2.24.

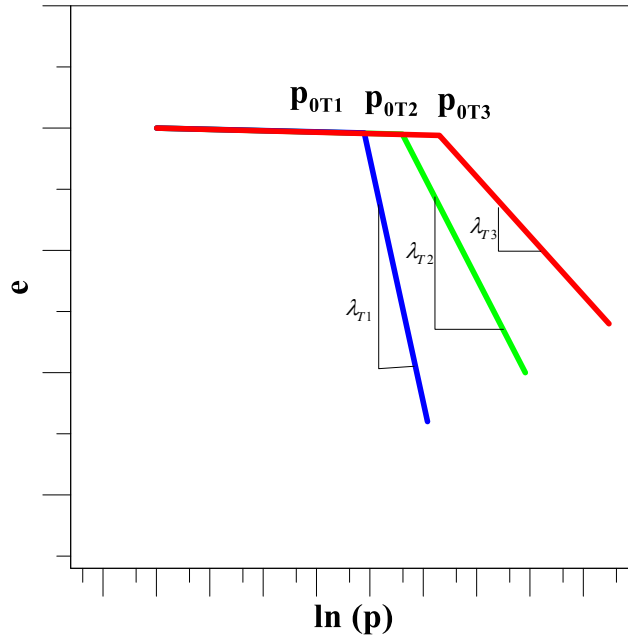


Figure 2.24 Idealized isotropic behavior of frozen soils

The curve here denotes the variation in the behavior of the soil at temperatures T_1 , T_2 and T_3 , where, $T_1 > T_2 > T_3$. The changes in slopes of the three curves mark the transition of the soil behavior from elastic to plastic state. The elastic slopes for all three temperatures remain unchanged and characterized by a single value of stiffness K . It can also be observed that there is a significant increase in soil stiffness for plastics states ($\lambda_{r1}, \lambda_{r2}, \lambda_{r3}$). The change in slope after the pre-consolidation pressure is indicative of the increased stiffness with decreasing temperatures. The apparent preconsolidation pressures (points P_{0T1} , P_{0T2} , P_{0T3}) are considered as yield points beyond which

irreversible deformations occur in the soil. As observed in the laboratory for reconstituted and natural frozen samples, there is an increase in the elastic domain with the decrease of temperature. Note that, through the Clausius-Clapeyron equation (2.3) and equation (2.4), the cryogenic suction is directly related to subzero temperatures. The combination of the cryonic suction and net stress causing yielding results in a yield curve in the $p_n - s_c$ plane that delimit elastic behavior from plastic response of frozen soils. This curve is termed in the context of the BBM as the Loading-Collapse (LC) curve. Yielding of the soil is caused either by increasing net stress or suction decrease (i.e. thawing for this problem, which is associated with a decrease of the cryonic suction).

The expression for the LC proposed by Alonso et al. (1990) is described by equation (2.17),

$$p_0 = p^c \left(\frac{p_0^*}{p^c} \right)^{\frac{\lambda_0 - \kappa}{\lambda_s - \kappa}} \quad (2.17)$$

where

$$\lambda_s = \lambda_0 \left[r + (1-r) \exp(-\beta s_c) \right] \quad (2.18)$$

p_0 is the mean net yield stress, λ_s is the slope of consolidation curve at a given cryogenic suction s_c , p^c is the reference pressure, β is the rate of stiffness increase with suction and r defines asymptotic maximum stiffness

To extend this into deviatoric plane, the yield surface of the ellipse of the modified cam clay is adopted. The equation of the yield surface is given by equation (2.19).

$$F = \left[p_n - \left(\frac{p_{n0} - ks}{2} \right) \right]^2 + \frac{q^2}{M^2} - \left(\frac{p_{n0} - ks}{2} \right)^2 \quad (2.19)$$

and the flow rule is dictated by equation (2.20).

$$\frac{d\varepsilon_s^p}{d\varepsilon_v^p} = \frac{2q\alpha}{M^2(2p + p_s + p_0)} \quad (2.20)$$

where M is the slope of the critical state line, k is the parameter describing the increase in cohesion due to suction, α is the parameter related to the non-associative flow rule (Alonso et al., 1990) and q is the deviatoric stress given by

$$q = \sqrt{\left(\frac{3}{2} s_{ij} s_{ij} \right)}, \quad s_{ij} = \sigma_{ij} - p\delta_{ij}$$

In consistency with the modified Cam-clay model, the plastic strains ε_v^p are determined using equation (2.21).

$$d\varepsilon_v^p = \frac{\lambda_0 - \kappa}{(1+e)} \frac{dp_0^*}{p_0^*} \quad (2.21)$$

where, λ_0 is the slope of the saturated (suction, $s = 0$) virgin consolidation curve, κ is the slope of the unloading and reloading line, p_0^* is the apparent preconsolidation pressure at saturation and e is the voids ratio

A three dimensional representation of the yield surface accounting for the features described above is shown in Figure 2.25.

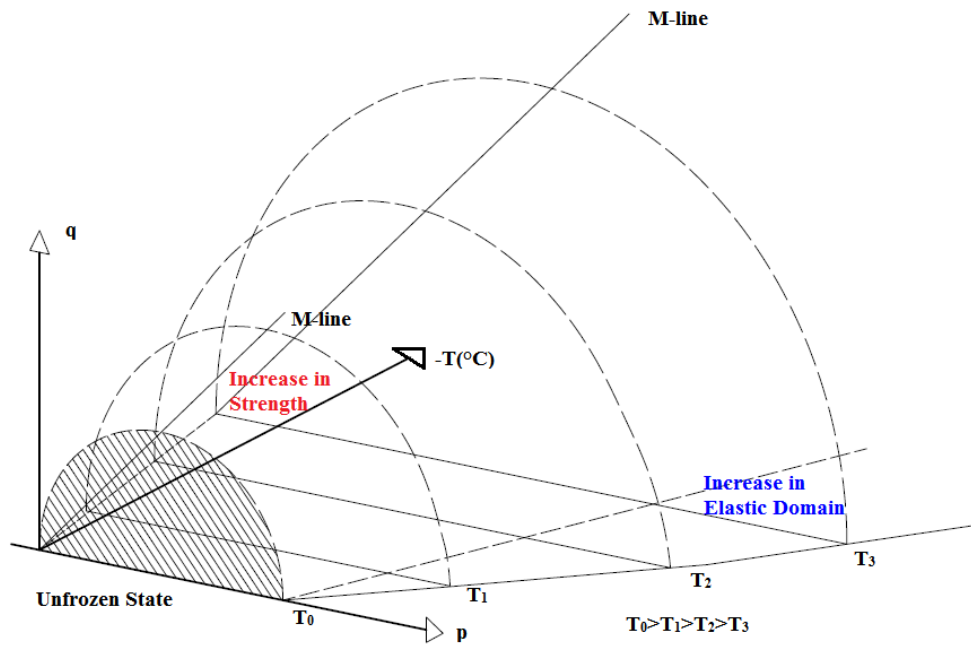


Figure 2.25 Idealized Yield Surface

Large volume changes observed in the laboratory and field can be attributed to the important re-arrangements in the soil structure that take place during soil melting. The change in stiffness along the virgin consolidation curve for varying temperatures will lead to a collapse compression behavior observed when the temperature rises under constant loading (Figure 2.26).

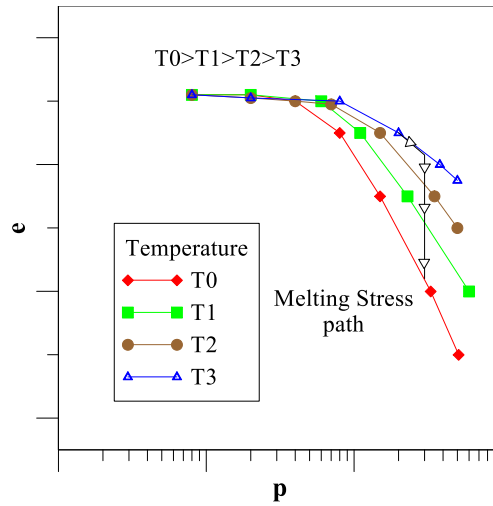


Figure 2.26 Idealized thawing-collapse stress path

2.7 THM FRAMEWORK OF FROZEN SOIL

Over the past decade there has been a consistent effort to consider all the relevant processes and integrate them in a single model. Some of the THM frameworks that have been developed include Coussy, 2005; Thomas et al., (2009); Nishimura et al., (2009); Liu and Yu, (2011); Multon et al. (2010).

The models proposed by Thomas et al., (2009) and Liu and Yu (2011) considered an elastic mechanical model coupled to TH model. Thomas et al., (2009) utilized the Tice equation (equation 2.6) to describe relation between the amount of unfrozen water and the temperature. A segregation pressure relation was also defined to understand formation of new ice lenses. Multon et al. (2010) proposed a framework based on the radius of the pore required to cause freezing at the specified temperature. This model

used an elastic framework to describe the mechanical behavior of the soil based on Biot's approach (Biot, 1941) to modeling stresses.

Nishimura et al., (2009) utilized the constitutive laws presented in sections 2.5.2 and 2.7.3 are now integrated into a formal framework to consider all behavior of the soil with changing temperature, fluid pressures and mechanical loads. Details of the formulation are presented in Appendix II.

The mass of the unfrozen water is $\rho_l S_l \phi$ and for the ice $\rho_i S_i \phi$, where ϕ is the porosity; ρ_l, S_l and ρ_i, S_i are the density and degrees of liquid and ice saturation respectively. The mass conservation of pore water is expressed as

$$\frac{\partial}{\partial t}(\rho_l S_l \phi + \rho_i S_i \phi) + \nabla \cdot (\rho_l q_l) = f^w \quad (2.22)$$

where, q_l is the liquid water flux vector and f^w is the sink/source term of mass.

The energy conservation equation is written as

$$\frac{\partial}{\partial t} [e_s \rho_s (1 - \phi) + e_l \rho_l S_l (\phi) + e_i \rho_i S_i (\phi)] + \nabla \cdot (-\lambda \nabla T + j_l^e) = f^e \quad (2.23)$$

where, e_s, e_l and e_i are the specific internal energy of solid soil minerals, liquid water and ice respectively; j_l^e is the advective term of heat flux and f^e is the sink/ production term of energy. The specific internal energies, e_s, e_l and e_i , are

$$\begin{aligned} e_s &= c_s T \\ e_l &= c_l T \end{aligned} \quad (2.24)$$

$$\text{and} \quad e_i = -l + c_i T \quad (2.25)$$

where, c_s, c_l and c_i are the specific heats for solid soil mineral, liquid water and ice respectively and l is the latent heat of fusion. It can be noted that the specific internal

energy of the ice contains an additional term that represents the latent heat term. The thermal consequences of phase changes which take place from due to freezing/melting of water are therefore taken into account in a straightforward way.

The mechanical equilibrium is then written as

$$\nabla \cdot \boldsymbol{\sigma} + \mathbf{b} = 0 \quad (2.26)$$

where, $\boldsymbol{\sigma}$ are the total stresses and \mathbf{b} are the body forces.

The model proposed here is implemented in the finite element program CODE_BRIGHT (Olivella et al., 1996). CODE_BRIGHT is numerical tool developed for solving complex multiphysics problems pertaining to porous media. The validation of this model is performed in the next section.

3 APPLICATION CASES INVOLVING FROZEN SOILS

3.1 INTRODUCTION

The application of numerical approach presented in the previous section to problems involving unfrozen soils is presented in this section. Both, the flow and the mechanical models are analyzed independently using test data published in the open literature. Section 3.2 presents the analysis related to the flow of the unfrozen water under changing subzero temperatures. The experimental data published by Xu et al. (1999) involving a variety of frozen soils is inspected and used to explore the ability of the flow model to simulate this problem. The mechanical constitutive model for frozen soils presented in Section 2 is validated in Sections 3.3 and 3.4. As explained in Section 2, the extension of the BBM to frozen soils was first proposed by Nishumura et al. (2009). However they didn't validate the model against experimental data. One prime objective of this dissertation was to check the ability of the proposed model to describe the behavior of soils subjected to cryonic temperatures by comparing model predictions against already published experimental data for frozen soils.

A natural soil from the Yukon air base in Alaska is studied. Soils samples from this site were tested at the Sandia National Laboratories. The details of the experimental setup and the validations of the proposed mode for this natural soil are described in the Section 3.3. The details of the experiment conducted on reconstituted sample are presented in Parmeswaran (1980) and Parmeswaran and Jones (1981). The experimental data from these publications is used in Section 3.4 to validate the proposed model. Once the model was validated, it was then used to study different real engineering problems

involving subzero temperatures. Two cases are presented in Section 3.5. One of them is related to the failure of the foundation of an administrative building in the region of Magadan, in Russia. The second case analyzed in this Section is associated with a pipeline collapse in the Inuvik region of Canada.

3.2 FLOW MODELING IN FROZEN SOILS

The mechanism of frost heave of soils found in regions around Northern China was investigated by Xu et al. (1999). The experimental setup studied in that work was designed to study on the migration of water in freezing soils for a closed system. Two different soil types, namely Inner Mongolia Clayey Silt and Remolded Lanzhou Sand were used in this research. Different Mongolia silt samples were chosen based on the values of fines and salinity content. The specimens were first air dried and mixed with distilled water to reach the desired water content. After consolidations for up to three days, the soil columns were then cut down to the desired lengths to be used for testing (i.e. 12 cm for the Lanzhou samples and 15 cm for the Mongolia Silt samples). The samples were then placed in a constant temperature chamber. Thermo-couples were fixed at every 2 cm along the wall of the soil box. Plates at the top and the bottom of the sample were used to control the temperature of the sample. The temperature gradient established along the soil specimens is shown in Figure 3.1.

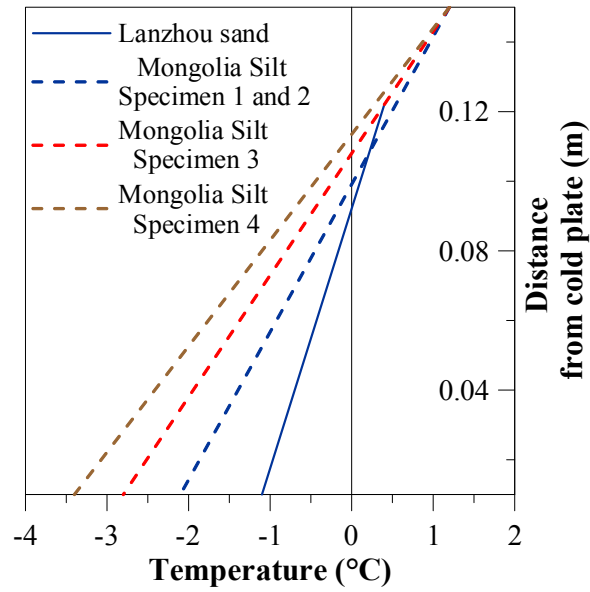


Figure 3.1 Temperature distribution along the length of the different samples

The properties of the Mongolia silt and the Lanzhou samples are listed in Table 3.1. The Mongolia Silt specimens 3 and 4 had the similar temperature gradients although they were prepared with different initial water content. Specimens 1 and 2 had different initial water content with the same temperature gradient.

Table 3.1 Properties of soil samples used on the experiment

Property	Mongolia Silt Specimen 1	Mongolia Silt Specimen 2	Mongolia Silt Specimen 3	Mongolia Silt Specimen 4	Lanzhou Sand
Dry density ρ_d (g/cm ³)	1.56	1.56	1.56	1.56	1.52
Initial Water Content (%)	25.71	18.57	23.38	23.38	15.99
Temperature Gradient grad θ (°C/cm)	0.16	0.16	0.20	0.26	0.13
Specific Gravity	2.71	2.71	2.71	2.71	2.64

The grain size distribution for the different soil specimens as reported during the experiments are provided in Table 3.2.

Table 3.2 Grain Size distribution for the soil samples (Xu et al., 1999)

Sample Number	Soil	Grain Size distribution		
		>0.05 mm	0.05-0.005 mm	<0.005 mm
1	Inner Mongolia clayey silt	29.5	47.0	23.5
2		20.7	55.5	23.8
3		8.0	46.8	45.2
4		20.8	64.8	14.4
5	Lanzhou Sand	85.2	14.8	

The final water content of the sample was determined at different depths along the length of the sample. The movement of the unfrozen water was determined using the changes in the water content. Typical results associated with the tests performed on Mongolian Silt samples 1 and 2 are shown in Figure 3.2 below.

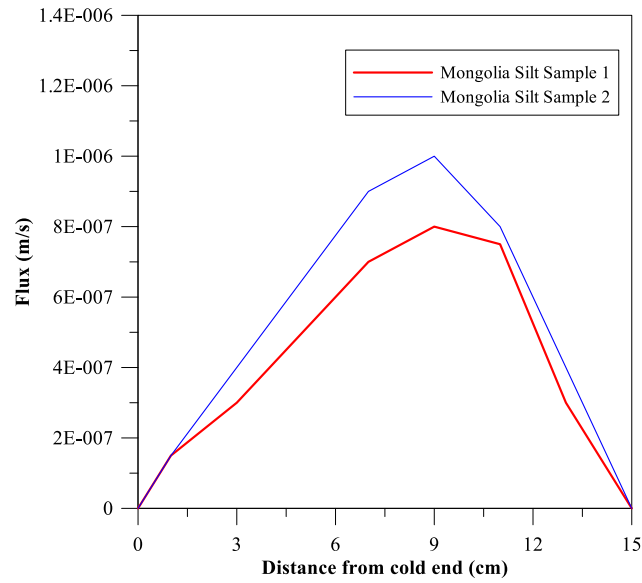
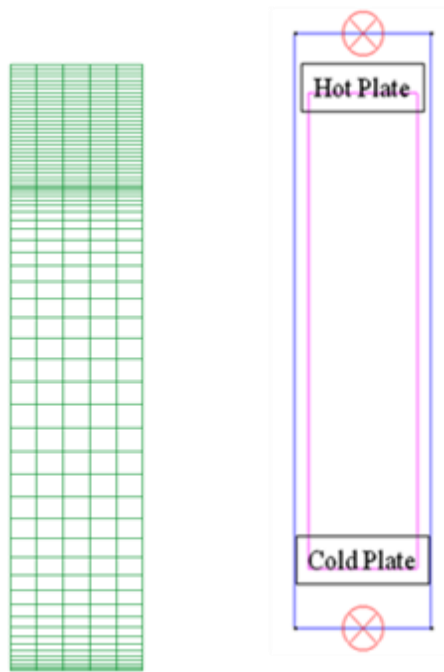


Figure 3.2 Variation of the flux across Mongolia Silt Samples 1 and 2

Figure 3.3 presents a schematic representation of the geometry boundary conditions and mesh (366 elements for the case of the Lanzhou sand) used in the numerical analyses.



a) b)

Figure 3.3 Model details a) Finite Element Mesh b) Schematic representation of the boundary conditions

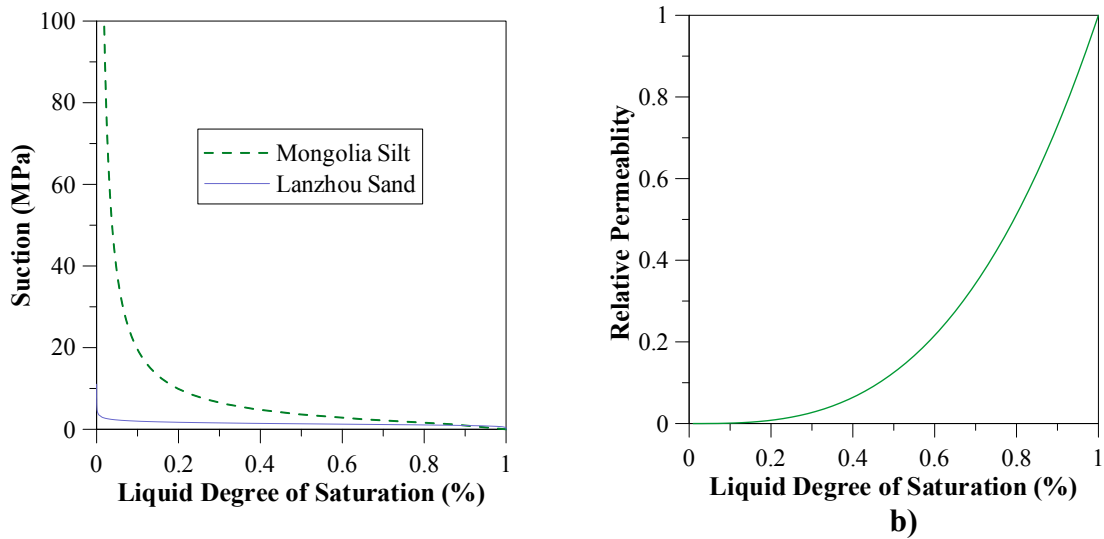
Table 3.3 presents the parameters adopted for the retention curve (equation 2.6), and relative permeability (equation 2.10). The parameters were back calculated from the experiments.

Table 3.3 Model Parameters

Equation	Parameters	Silt	Lanzhou Sand
	Designation		
Retention Curve	P (MPa)	4.2	1.3
	λ	0.63	0.84
Relative Permeability	λ	3	3

The retention curve for Lanzhou sand and Mongolia silt are shown in Figure 3.4

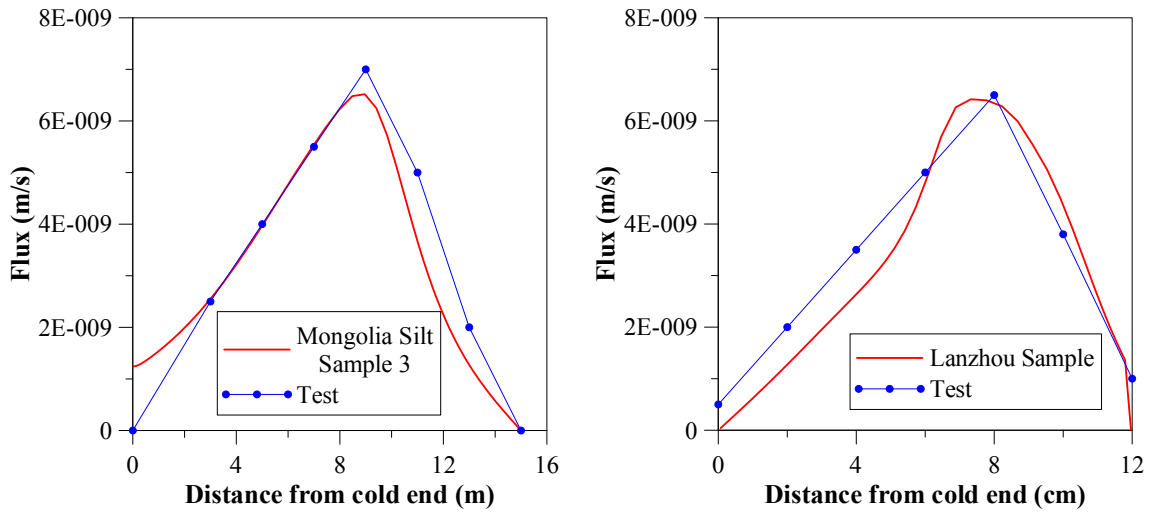
a). The variation of the degree of saturation with the relative permeability is presented in Figure 3.4 b).



a)

Figure 3.4 Soil Behavior Characteristics a) Retention curve for Mongolia silt and Lanzhou sand b) Liquid Relative Permeability

The comparison of the flux across the samples for the model and test data is shown in Figure 3.5 a) and b) for the silt and Lanzhou sand samples respectively. It can be seen that the model manages to capture the main tendencies observed in those tests in terms of the flow rate.



a) **b)**
Figure 3.5 Comparison of flow rates between model and test data for a) Mongolia Silt b) Lanzhou sand sample

The effect of water content and temperature on Mongolian silt soil samples are shown in Figure 3.6 a) and b) respectively. It can be observed that flow rates are higher for the sample with higher water content and is attributed to the porosity of the sample. The porosity of the sample 1 is 0.40 and that of sample 2 is 0.32. This increase in porosity facilitates for easy water flow resulting in an increased flux.

The flow rate is greater for the sample with the lower temperature gradient (i.e. Sample 3) when compared against the sample with the higher temperature gradient (i.e. Sample 4). The temperature gradient results in different end temperatures of the sample. The decrease in flow rate is attributed to the formation of a greater fraction of ice, thereby reducing the degree of water saturation in the soil. The drop in the degree of saturation reduces the relative permeability and lowers the flow rate

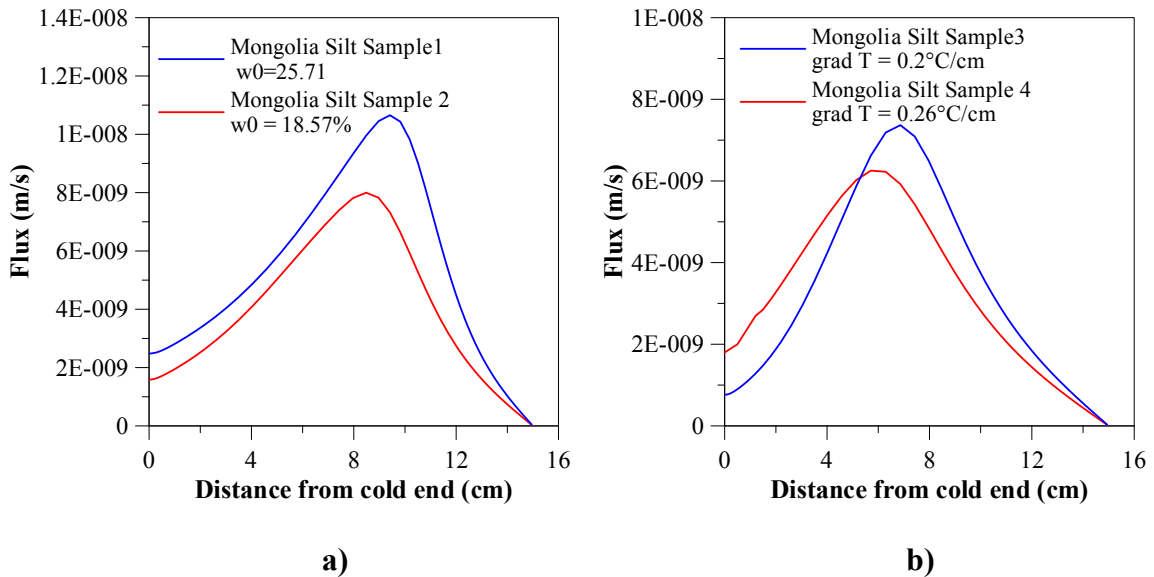


Figure 3.6 Flow rates from simulation for a) Change in water content b) Change in temperature gradient

3.3 MODEL VALIDATION FOR NATURAL SOILS

This section is advocated to explore the capabilities of the mechanical constitutive model to simulate the behavior of natural frozen soils. It should be noted for all the modeling efforts attempted here a uniform procedure was adopted to calculate the liquid and ice pressures described in Section 2.4. The ice pressure determined from either of the two methodologies prescribed in Section 2.4 is found to be extremely small at the surface of the soil. Therefore the ice pressure is assumed to be zero, the liquid pressure is now calculated based on the prevailing temperature based on the Clausius-Clapeyron equation (Equation 2.4). The liquid pressure would therefore be negative for all temperatures below the freezing point. The suction is now calculated as the difference between the ice and liquid pressure. The net pressure is calculated based on Equation

2.15. The mean net stress would be referred as mean stress due to these assumptions. The experimental campaign for the natural soils is presented first, followed by the main experimental results and modeling outputs.

3.3.1 Description of experimental work

The soil samples used in this study were obtained from the Yukon Test Range at Eielson Air Force Base in Alaska. The samples were extracted from a depth ranging from 0.2m to 0.8m below the ground surface. The extracted cores were transported to the Sandia National Laboratories, where they were stored at -10°C. High pressure water jets were used to cut the samples from the cores and a spring loaded V block apparatus was used to mount the end caps on the sample. The soil characterization revealed that most samples had low density ($<1\text{gm/cm}^3$) above 0.3m depth and were of higher density below the 0.3m. The water content of the samples varied from 34% to 85% with most samples having a water content around 40%. For the unconsolidated sand experiments, coring using a water-jet cutting technique will be used (Lee et al., 2002) while consolidated cores will be prepared by coring using a diamond drill bit. Right cylinders fabricated according to ASTM-D4543 (“Standard Practice for Preparing Rock Core Specimens and Determining Dimensional and Shape Tolerances) will be prepared either with a diamond wire saw cooled with liquid nitrogen or with a special spring-loaded V-block holder to affix 316 stainless steel or Inconel end caps to the samples. The slight pressure applied by the V-block will ensure right cylinders via pressure melting (Lee et al., 2002). Individual cores so prepared will be jacketed with neoprene sleeves, which remain flexible under the cold temperatures of interest (down to minus 20 °C). Up to

twelve piezoelectric acoustic velocity pins will be affixed to the sample using low temperature epoxy to enable both p- and s-wave velocity determination during the testing and also to record onset of plastic straining via acoustic emissions. A special multiplexer apparatus has been in use at SNL to permit near-simultaneous recording of ultrasonics and acoustics during triaxial testing.

Testing procedures in the laboratory include routine sample unloading during plastic yielding to determine modulus degradation, and to compare dynamic and static elastic compliance during testing. The cold temperatures and concomitant piston-seal friction require use of internal load cells and we have two designed load cells for operation under these conditions (Lee et al., 2002; 2004). The instrumented sample and pressure vessel configuration for testing is shown below in Figure 3.7. This includes up to twelve coaxial feed-throughs for acoustic/ultrasonic measurements and two internal LVDT's, designed for cold temperature conditions, for horizontal and lateral displacement measurements. An internal Inconel sheathed thermocouple will be used to determine sample temperature during testing.

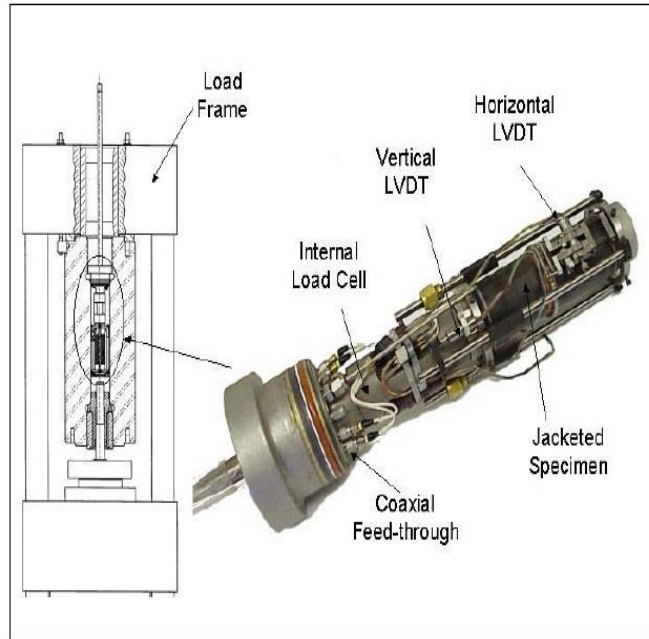


Figure 3.7 Schematic of low temperature testing pressure vessel and frozen sample configuration to be used for the axisymmetric testing series (Lee et al., 2002)

A unique pressure vessel with external cooling system based on liquid nitrogen circulation (Figure 3.8). The assembled vessel will then be placed into a 1.9 MN servo-controlled load frame with MTS controlling.



Figure 3.8 High Pressure Low Temperature Pressure Vessel with external cooling system to be used for axisymmetric compression and extension testing (Lee et al., 2002)

The mechanical properties of this soil were estimated performing several quasi static tests under controlled conditions. Table 3.4 presents the various tests conducted under varying temperatures and confinements. Brief details of the tests model here are presented below. A detailed report of all the experiments conducted in the testing program is presented in Lee et al. (2002).

Table 3.4 Laboratory constitutive testing of Alaskan frozen soil

Test Type	Temperature range of testing (° C)	No. of Tests Conducted	Test Control
Hydrostatic compression	-6 to -25.6° C	17	Pressure control 0.03 MPa/s
Uniaxial compression	-4.7 to 23.7° C	9	Strain control 10^{-4} to 10^{-1}
Deviatoric compression	-6 to -26° C	45	Strain control 10^{-4}

3.3.2 Hydrostatic tests

Cylindrical specimens, prepared following the ASTM D4543 were used to measure the frozen soil bulk modulus (K). After the specimens were jacketed in a neoprene jacket and instrumented with LVDT's, the assembly was inserted in the HPLT test cell. The push rod, used for applying the axial load to the specimen, was pulled back so as not to apply any deviatoric stress to the specimens. The confining pressure, P , was increased all around the specimen to apply all three principal stresses ($\sigma_1 = \sigma_2 = \sigma_3 = P$; where $\sigma_1, \sigma_2, \sigma_3$ are the maximum, intermediate and minimum principal stresses, respectively). The pressure was measured with the pressure transducer connected to the HPLT test cell and the axial and lateral displacements were measured with the vertical and horizontal LVDT's, respectively. The variation of the hydrostatic behavior of the samples in terms of the volumetric behavior captured using voids ratio ' e ' vs mean stress, ' p ' for different temperatures is shown in Figure 3.9

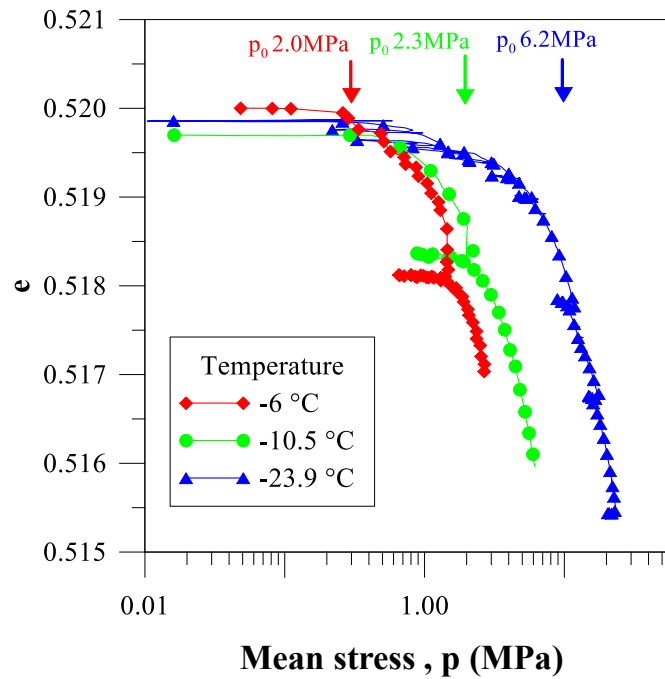


Figure 3.9 Isotropic behavior of frozen soils

The variation of the pre-consolidation pressure with cryonic suction (and freezing temperatures) is shown in Figure 3.9. It can be clearly seen that there is increase in virgin consolidation slope and the pre-consolidation pressures with the increase of the cryonic suction; as explained in Section 2.

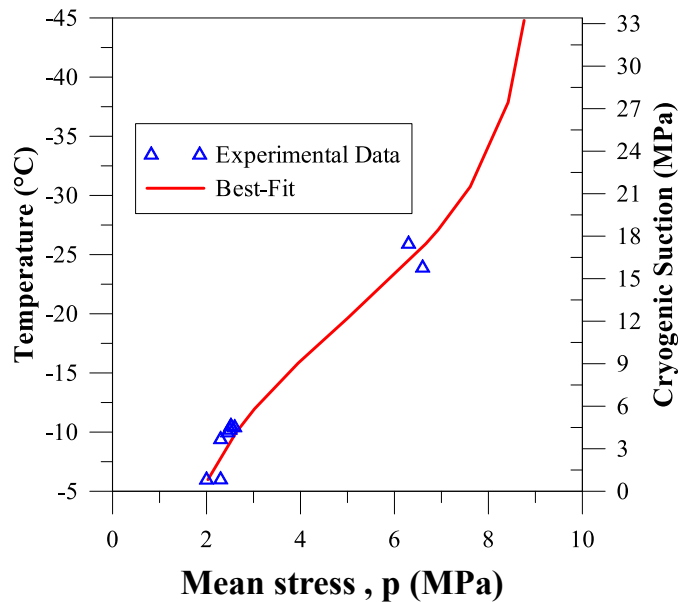


Figure 3.10 Variation of apparent pre-consolidation pressure with temperature

3.3.3 Uniaxial tests

Uniaxial compression tests were conducted in a 0.1 MN servo-controlled loading machine. The prepared specimens were loaded at a constant displacement rate of 10^{-3} mm/s which corresponds to a strain rate of 10^{-5} /s. The axial and lateral deformations were measured by means of the axial and the circumferential LVDT's, respectively. The instrumented specimens were placed between the upper and lower cylindrical end-caps having the same diameter. The specimens were loaded until the 5 or 6% of axial strain was reached. The responses of the frozen samples at different temperature in terms of deviatoric stress versus strain are shown in Figure 3.11.

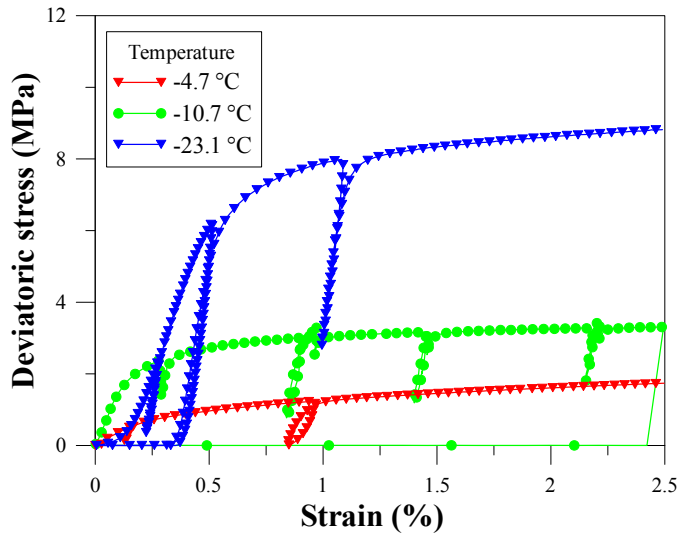


Figure 3.11 Unconfined stress-strain behavior

The shear strength of soils under unconfined conditions tends to increase with a decrease in the testing temperature, as seen in Figure 3.12.

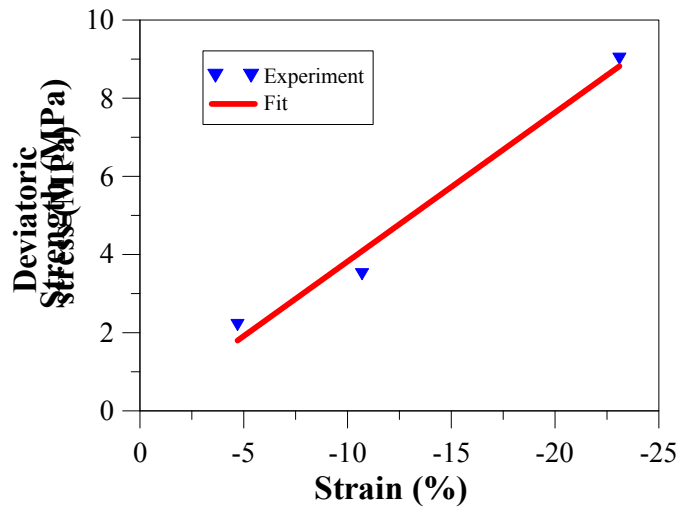


Figure 3.12 Variation of strength with temperature

3.3.4 Triaxial tests

To populate the necessary database for the deformational behavior of the Alaskan frozen soil under deviatoric stress conditions, a series of triaxial tests was conducted under different temperatures and confining pressure conditions. The sample preparation procedures and test equipment for the triaxial tests were identical to those used for the hydrostatic compression tests. After the specimen assembly was placed in the HPLT vessel, hydraulic pressure was applied to a predetermined level of confining pressure. After the confining pressure, P , was stabilized, the specimen was loaded axially at a constant axial strain rate of 10^{-5} /s to create the deviatoric stress condition.

The confining pressure was measured with a pressure transducer connected to the HPLT vessel and the axial and lateral displacements were measured with the internal LVDT's. Figure 3.13 show the effects of temperature and confining pressure on the strength of the natural soil from Alaska. The effect of freezing temperature on soils strength is very noticeable. As explained in Section 2, the increase of ice strength with the decrease of temperature is practically insignificant, so the increase of strength can be mainly attributed to the cryogenic suction on soil structure.

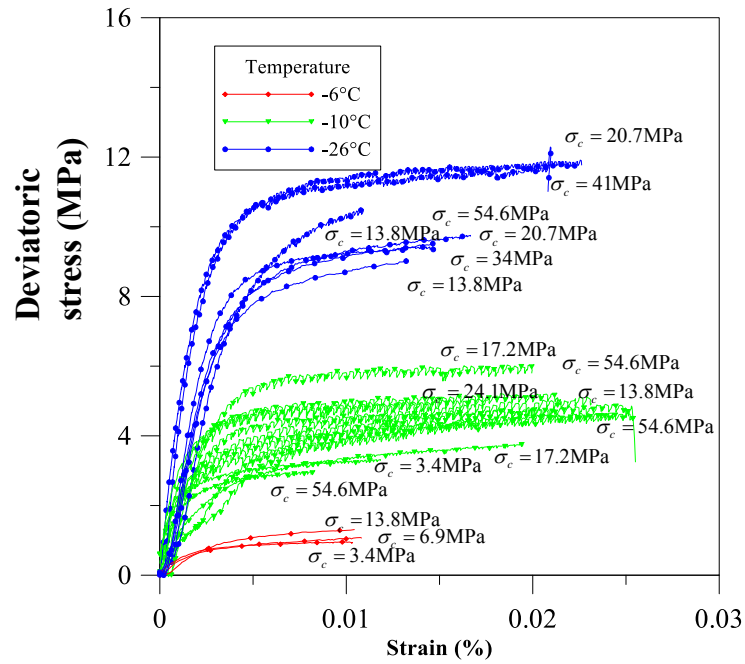


Figure 3.13 Variation of the stress strain behavior of natural soils at different temperatures under different confining pressures

The behavior of this soil respect to the confining pressure is the expected one, i.e. and increase of the strength with increase of confining pressure. Figure 3.14 shows the behavior under different confining pressures at a temperature of -10°C. However this effect is not very relevant in this case.

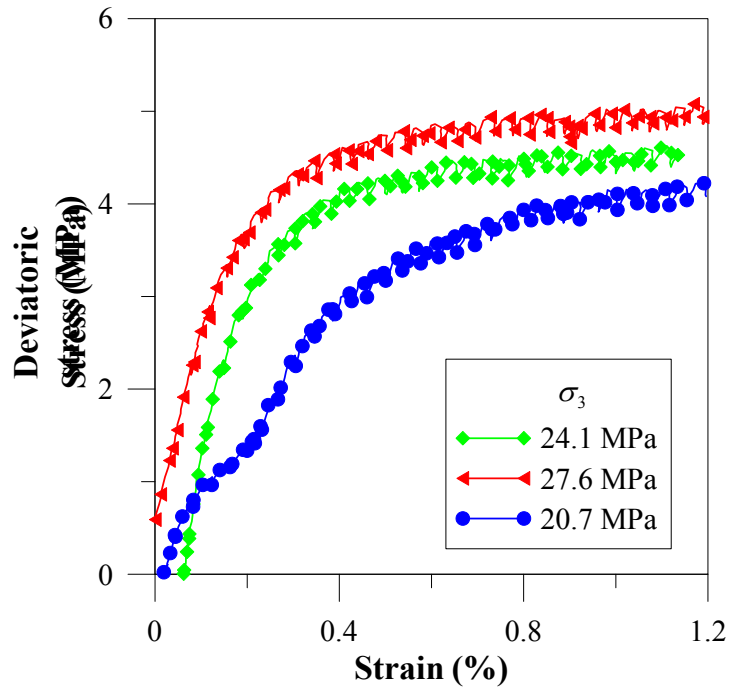


Figure 3.14 Variation of the stress strain behavior of natural with confining pressure at temperatures of -10 °C

3.3.5 Constitutive modeling of natural samples

Model parameters used in the simulation of natural samples are listed in Table 3.1. The preconsolidation pressures for the hydrostatic tests are determined using Casagrande's method. The preconsolidation pressures of the hydrostatic tests at various temperatures are now utilized in determining the parameters β and r used in the LC-curve. The parameters for the 'ps' was back calculated based on the experimental results.

Table 3.5 Model Parameters

Parameter	Value
Mass Density of Water, ρ_l (Kg/m ³)	1000
Mass Density of Ice, ρ_i (Kg/m ³)	910
Mass Density of Ice, ρ_s (Kg/m ³)	1740
Initial Porosity, ϕ_0	.532
Poisson's ratio, ν	0.35
Specific Latent Heat of Fusion, (KJ/Kg)	334
β	1.4
r	0.75
p_c (MPa)	0.1

The p_s curve and the LC curve of the yield surface is shown in Figure 3.15 a) and Figure 3.15 b) respectively. Note that Alonso et al. (1990) proposed a linear relationship for p_s , in this work it was found that a cubic equation is more appropriate for frozen soils.

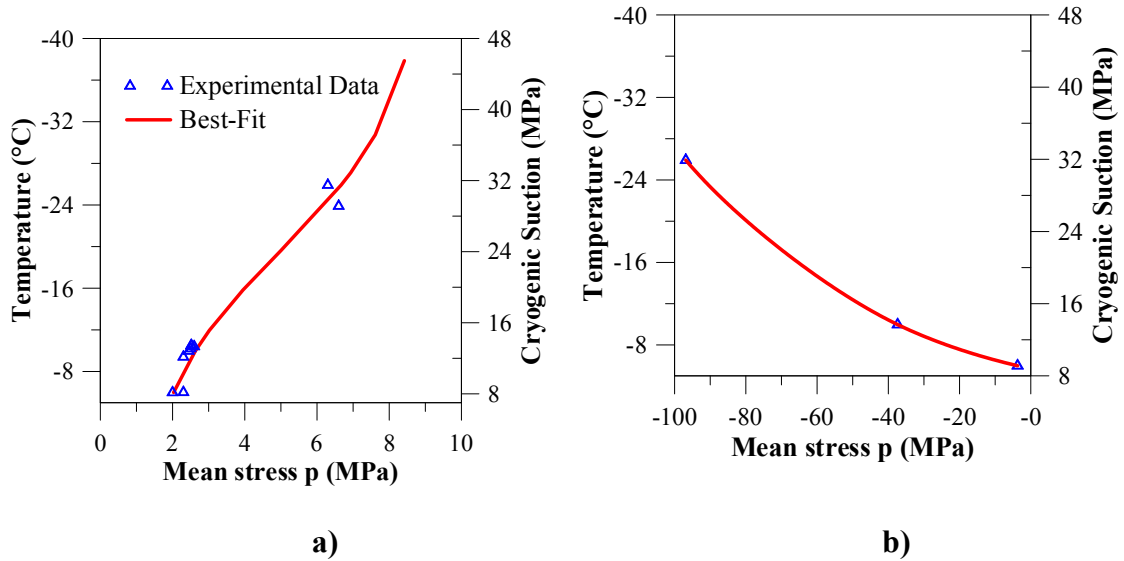


Figure 3.15 Projection of yield surface on mean stress suction plane a) LC curve b) p-s curve

Figure 3.16 presents the mesh used in the study it consisted of 121 nodes and 100 elements. The number of elements were determined from an extensive sensitivity analysis.

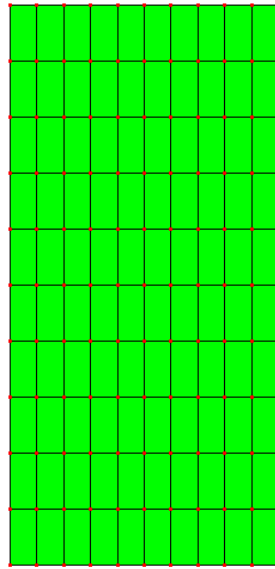
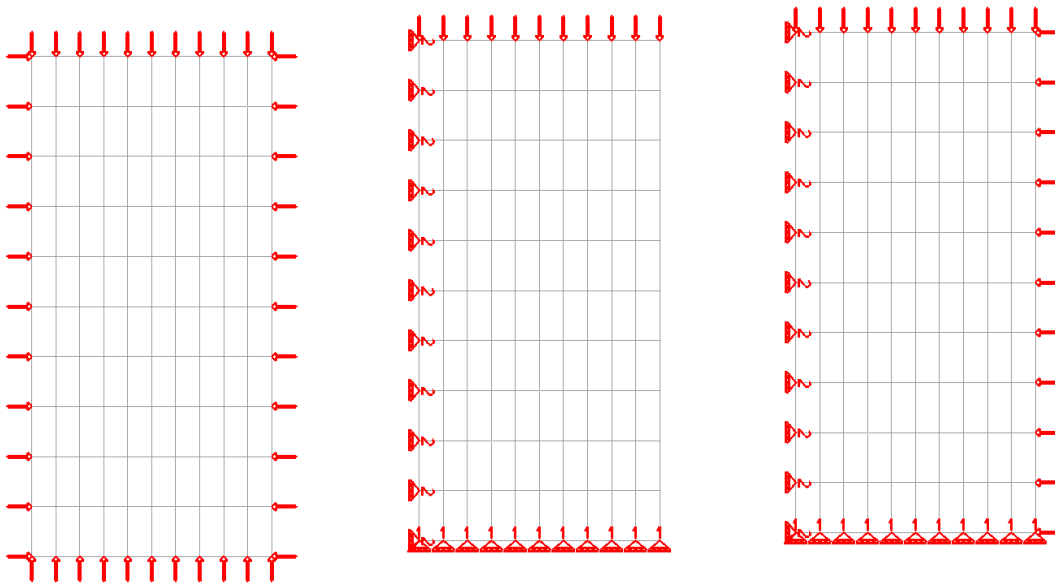


Figure 3.16 Mesh used in the study

Depending on the test being modeled the boundary conditions were modified. The boundary conditions used for the different used for the tests are shown in Figure 3.17.



a)
b)
c)
Figure 3.17 Boundary condition for a) Isotropic tests b) Unconfined tests c) Triaxial tests

Isotropic compression tests

Figure 3.18 a) to Figure 3.18 c) presents the main results comparing the model outputs against the experimental data for the isotropic tests are seen in. The model is able to reproduce quite well both, i) the observed increase in the apparent pre-consolidation with the decrease of temperature, and ii) also the stiffening of the frozen soil as the testing temperature reduces. The elastic slope remained unchanged in the three tests.

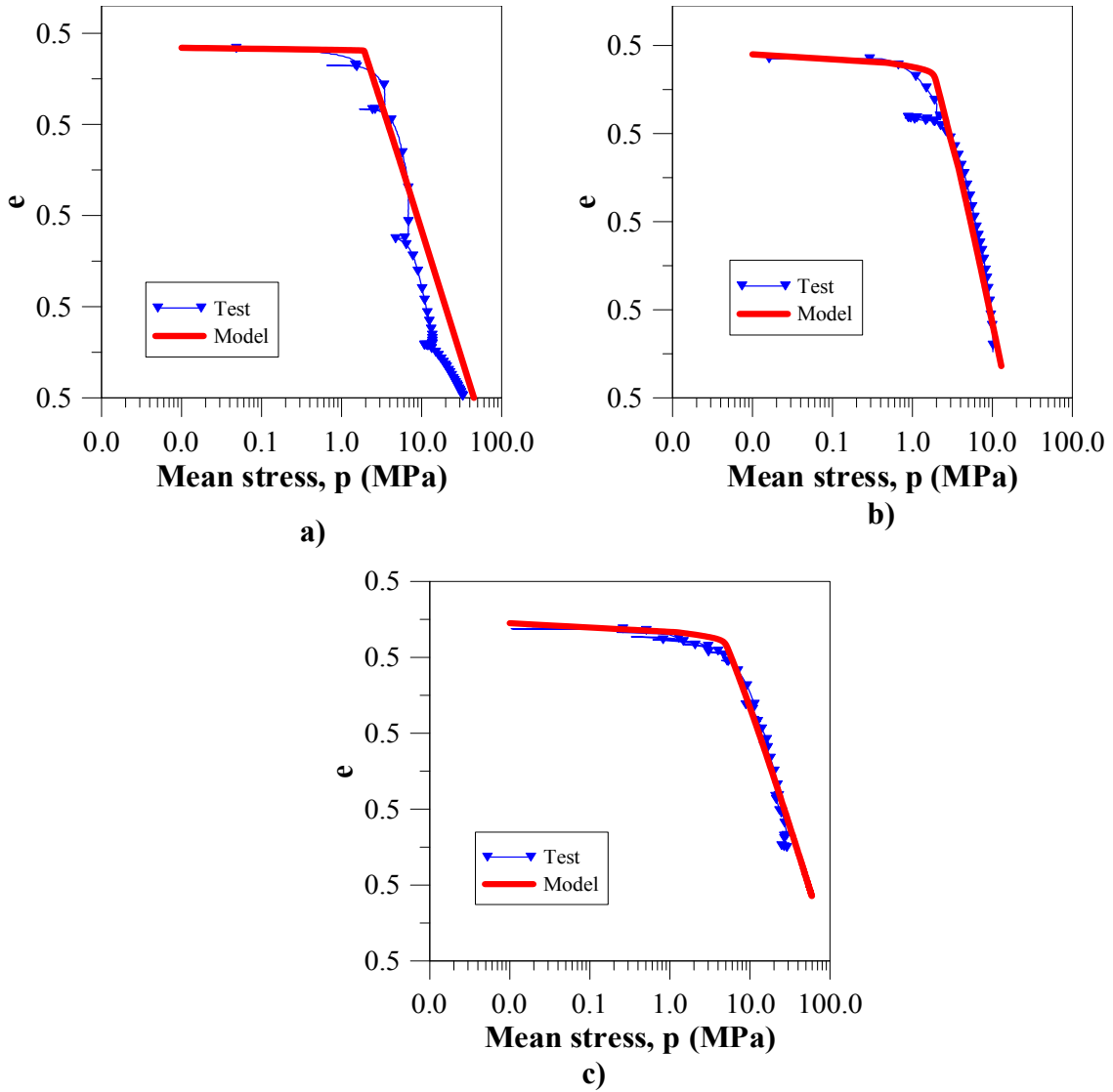


Figure 3.18 Results of the simulation of hydrostatic tests at a) temperature -6°C b) temperature -10°C c) temperature -25°C

Unconfined compression tests

The next step in the model validation was to explore the ability of the proposed model to reproduce the increase in the frozen soil strength observed in the unconfined experiments when the testing temperature was reduced. Three tests conducted at 3 different temperatures were selected for the simulations. The comparison of the

deviatoric stress versus the axial strain between the experiment and the model results are as shown in Figure 3.19, Figure 3.20 and Figure 3.21 for temperatures -5 °C, -10 °C and -24 °C respectively.

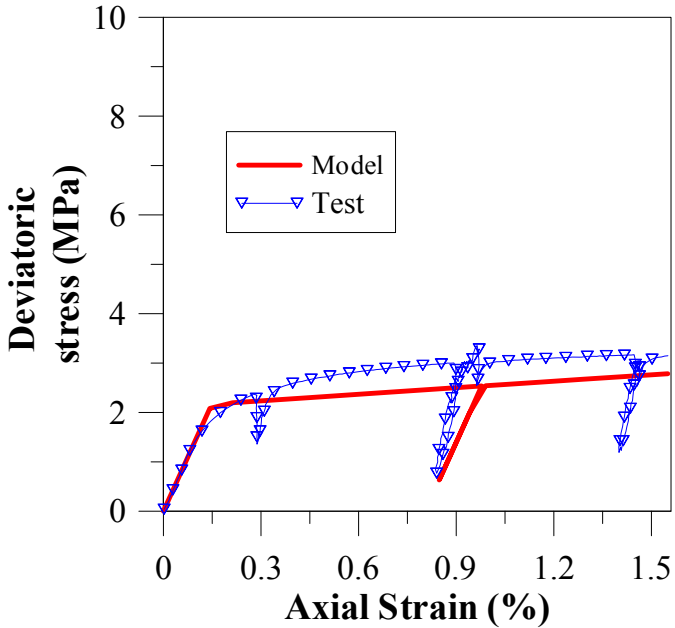


Figure 3.19 Comparison of model and experimental results of the unconfined test at temperature-5 °C

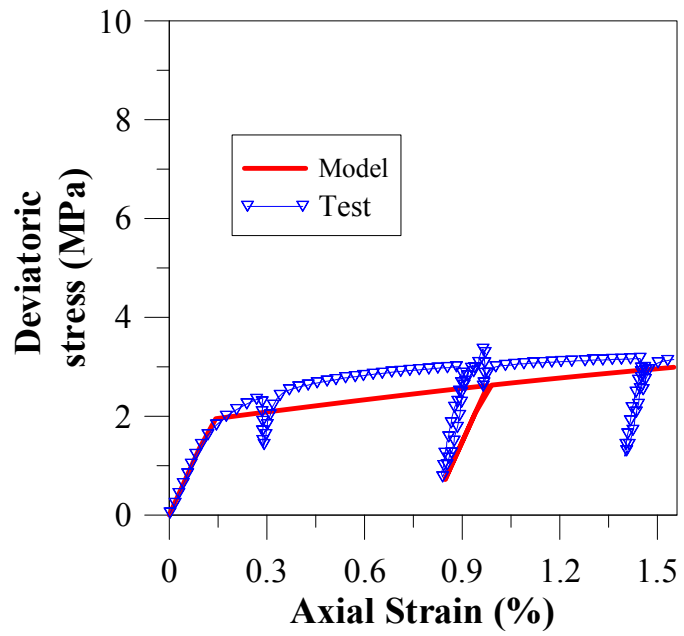


Figure 3.20 Comparison of model and experimental results of the unconfined test at temperature-10 °C

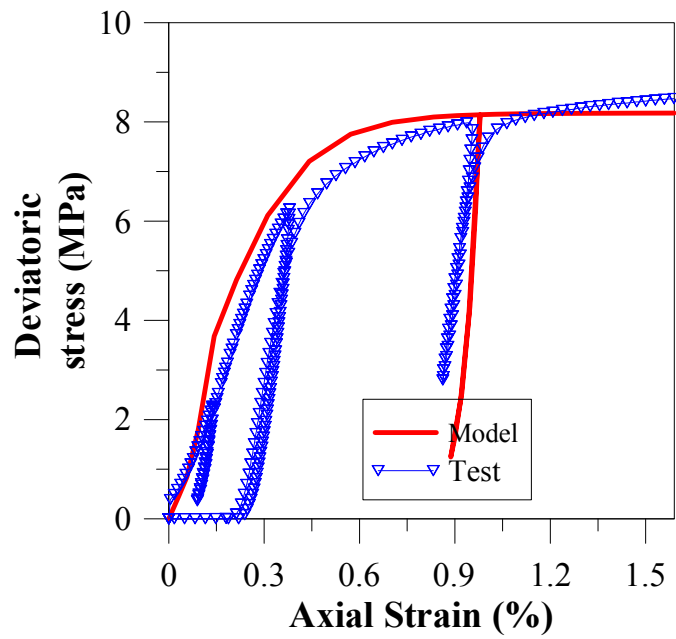


Figure 3.21 Comparison of model and experimental results of the unconfined test at temperature-24 °C

It can be observed that the model is able to capture correctly the observed experimental behavior. The experimental results show that a higher strength is predicted at lower temperatures which the model is able to accomplish. There is also an increase in stiffness of the material that is quite well reproduced by the model. The model also capture quite well the behavior observed during unloading and reloading.

Triaxial compression tests

To investigate the effect of temperature on frozen soil behavior three sets of triaxial tests were simulated at three different temperatures: -6, -10 and -26 °C. The main comparisons between model and experiments are performed in terms of deviatoric stress against axial strain and also in terms of volumetric deformation in terms of axial strain. The main modeling results are shown in Figure 3.22 a) through i) for the three temperatures quoted above.

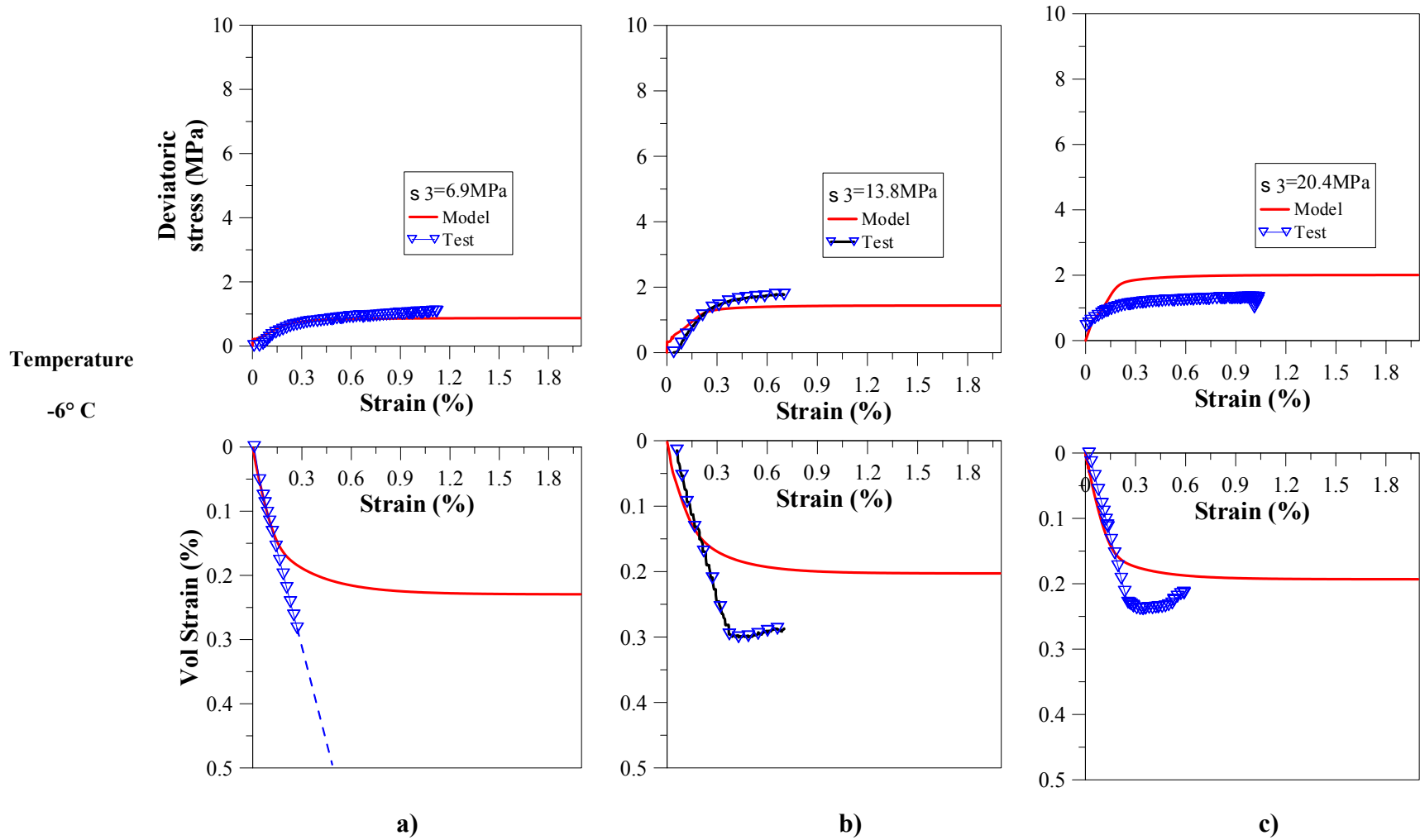


Figure 3.22. Comparison of model and experimental results of the confined test

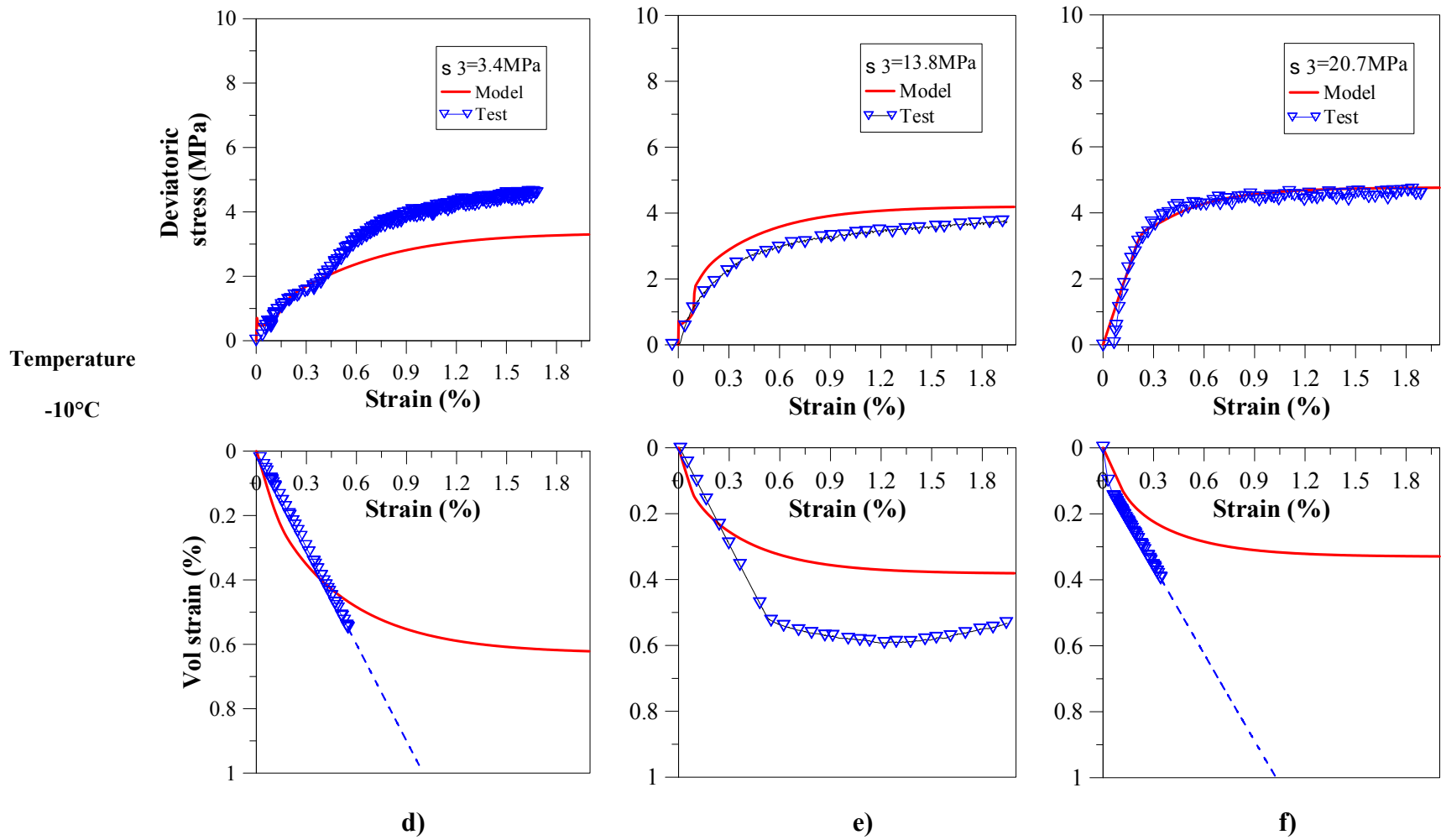


Figure 3.22. Continued

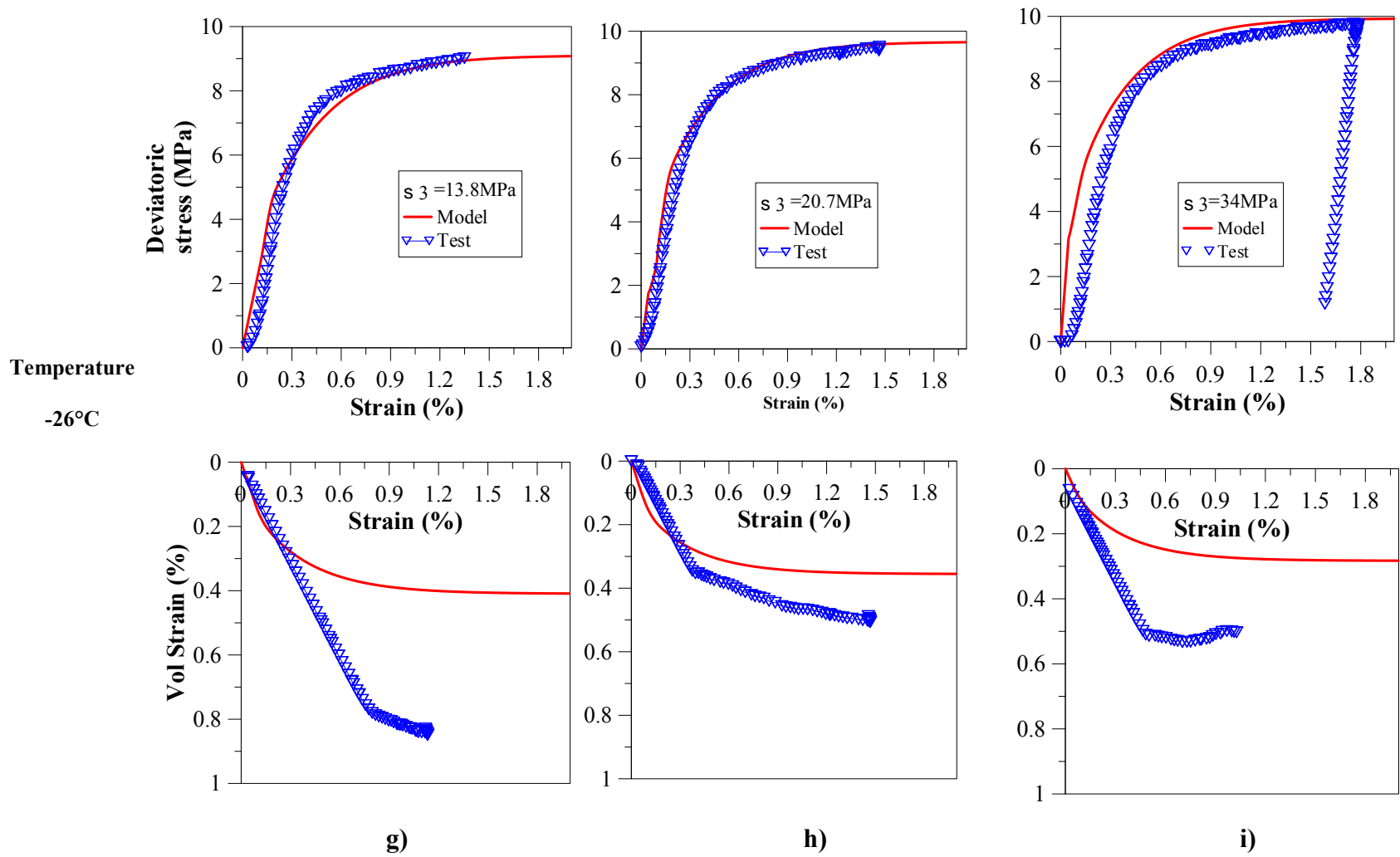


Figure 3.22. Continued

It can be seen that the model properly captures the main tendencies of the frozen soils observed in the experiments at the different temperatures. In some cases the model predict well and other ones the model over and under predict the stresses observed in the experiments. Overall, the results obtained in terms of maximum deviatoric stress and stiffness can be considered very satisfactory. The results in terms of volumetric deformation are sometimes very good, but in other occasion volumetric strains are underestimated. It is important to bear in mind that frozen soils are quite incompressible and therefore volumetric deformations are very difficult to measure in the lab. In fact, these are the only tests reporting the changes in volumetric strain during the deviatoric loading. A number of factors can affect the readings related to the measurements of volumetric strain.

3.4 RECONSTITUTED SAMPLES OF FROZEN SOILS

This section is related to the performance of the mechanical constitutive model when analyzing the behavior of reconstituted frozen soil samples. The main reported in the literature are presented first. Afterwards, the main experimental and modeling results are discussed.

3.4.1 Description of experimental work

The experimental data studied in this section correspond to the work conducted by Parmeswaran (1980) in ‘Ottawa sand’ by exploring the behavior of frozen samples under different cryogenic temperatures subjected to unconfined compression loads. The tests reported by Parmeswaran and Jones (1981) performed on frozen samples of the same Ottawa sand at different subzero temperatures and confining pressure. . Frozen

samples made up from Ottawa sand were prepared at a maximum dry density of 1700 Kg m⁻³ and an initial water content of 14%. The cylindrical samples were prepared using the Plexiglass mould. The sand was then saturated with distilled water and frozen up to a temperature of -6° C. The procedure recommended by Baker (1976) was followed. The final specimens used in the confined tests were 54 mm in diameter and 108 mm height, while the ones used in unconfined tests were of the same diameter but 127 mm height.

The final gravimetric water content of 20 % was recorded. The samples for the unconfined tests were tested at desired strain rates before they were frozen. A kerosene bath was used to maintain the temperature of the sample at the desired temperature and was monitored using a thermocouple. The confined tests were conducted at a constant temperature of -10° C and a strain rate of $7.7 \times 10^{-5} \text{ s}^{-1}$. The confining pressure was applied using Dow Corning silicone fluid 200. The specimens adopted in this dissertation to validate the proposed model for frozen soils were such that they have a strain rate close to $7.7 \times 10^{-5} \text{ s}^{-1}$. The variation of the deviatoric stress vs strain for the various temperatures and confining pressures are presented in Figure 3.23 a) and b).

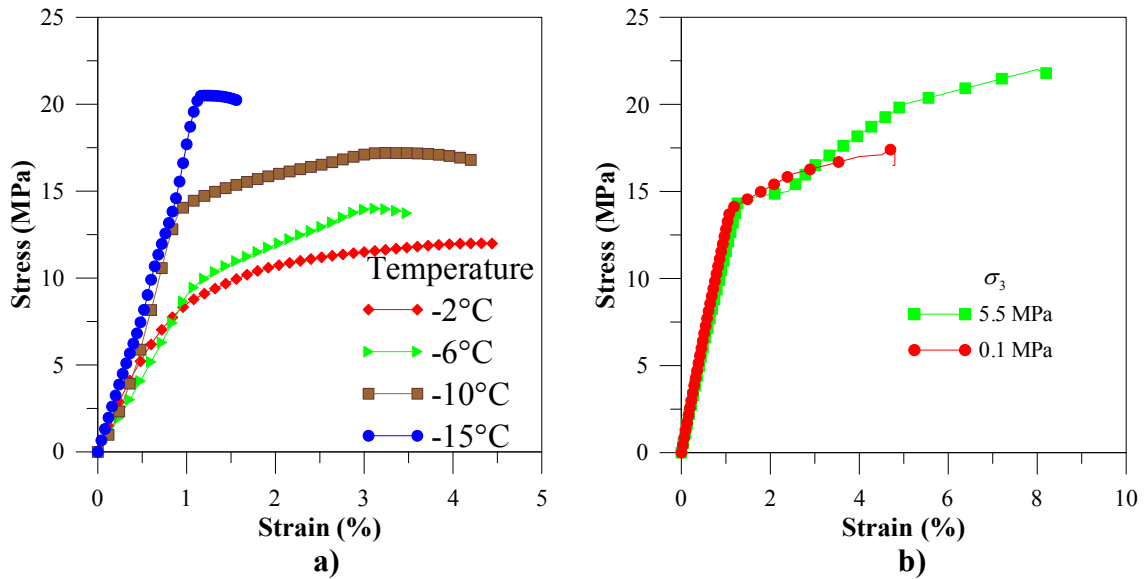


Figure 3.23 Results of experiment conducted at a) Different temperatures b) Confining pressures

3.4.2 Numerical modeling of reconstituted frozen soils

The numerical modeling procedure adopted for the reconstituted soils is similar to that adopted in Section 3.3.5. The boundary conditions were chosen appropriately depending on the tests. Figure 3.24 a) and b) present with symbols the main experimental data in the mean stress suction plane (ps plane) obtained from the experimental campaign. The adopted model is presented with lines. The preconsolidation pressure of the sample was not available in the experimental detail therefore the parameters for the LC curve were back calculated. An initial porosity of 0.3 as specified in the experiments.

It can be seen that both the strength and apparent pre-consolidation pressure of the frozen soil increase with the increase of cryogenic suction.

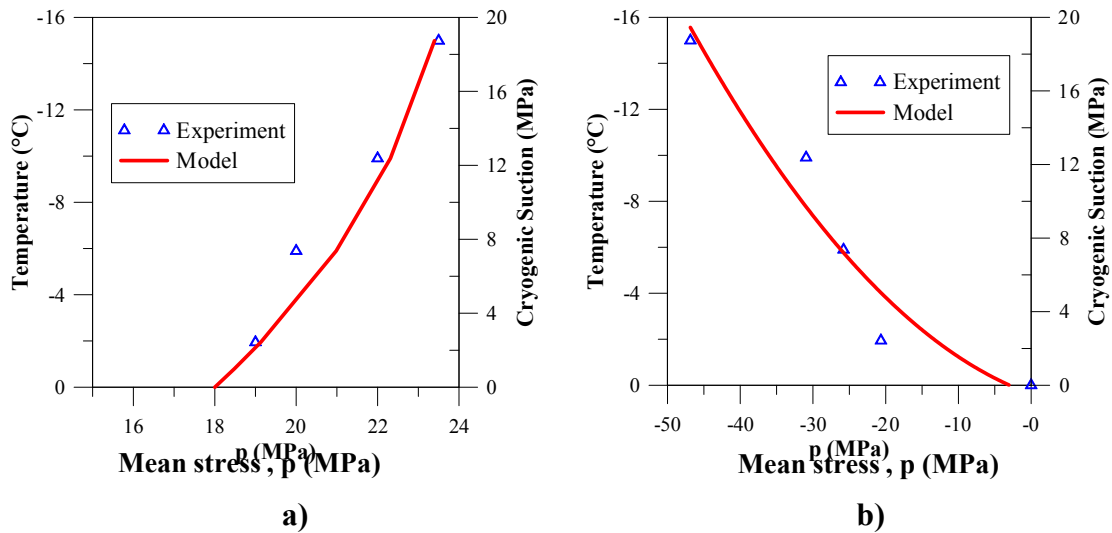


Figure 3.24. Projection of yield surface on a) The p_n - s plane: LC curve b) Projection of yield surface on the p_n - s plane: ps curve

The parameters used for the model are listed in Table 3.6.

Table 3.6 Model Parameters used in modeling reconstituted samples

Parameter	Value
β (MPa ⁻¹)	0.095
r	0.9
M	0.38
ν	0.35
p_c (MPa)	0.1
Initial porosity	0.3

Triaxial compression tests

Triaxial tests at a constant temperature of -10° C and at three different confining stresses (i.e. 0.1, 5.5 and 11.1 MPa) were selected to study the effect of the confining stress on frozen soils. As expected, the strength of the frozen soil slightly increases with

the confinement. The results for 0.1 and 5.5 MPa are presented in Figure 3.25 and Figure 3.26. Experimental and model results are very close.

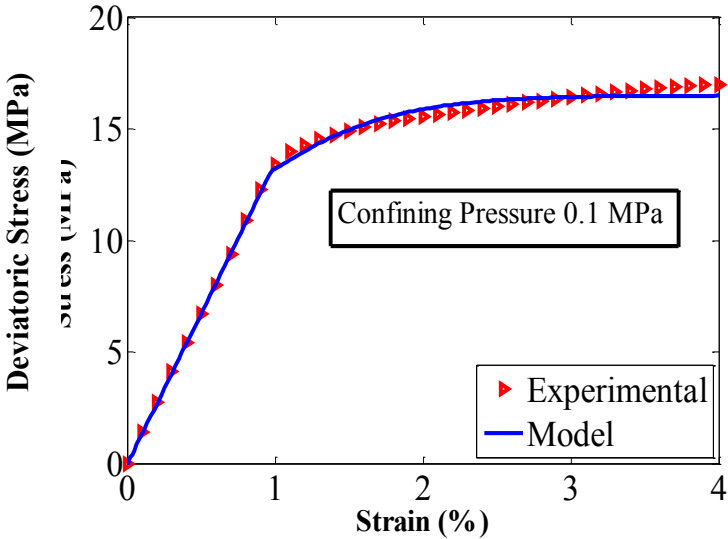


Figure 3.25 Comparison of experimental and model results at a) 0.1 MPa confining pressure

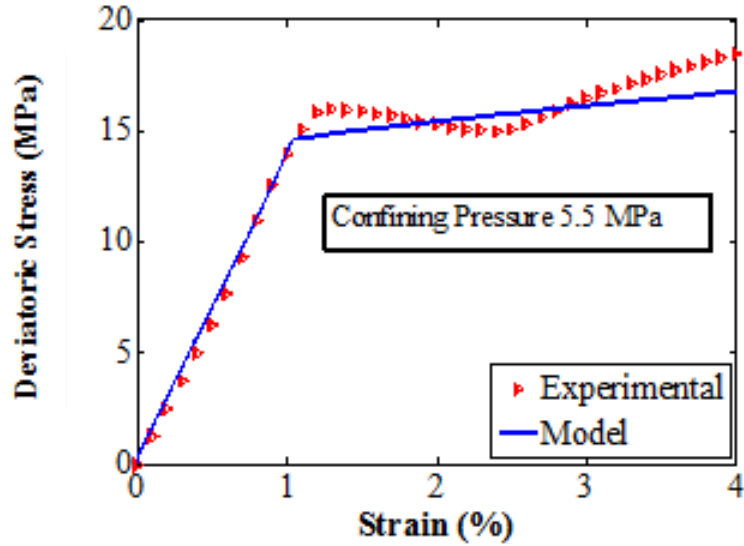


Figure 3.26 Comparison of experimental and model results at 5.5 MPa confining pressure

Unconfined test

Unconfined tests at four different temperatures were selected to study the mechanical behavior of frozen soils, at -2 °C, -6 °C, -10 °C and -15 °C temperature. The comparisons between experimental and model results in term of deviatoric stress and axial strain for these temperatures are presented in Figure 3.27 a), b), c) and d) respectively. Also in these analyses shown that the proposed model is able to capture the main patterns of behavior observed in the experiments. In the unconfined tests, strain hardening control the plastic behavior at low cryogenic suctions; while a marked softening prevails at high cryogenic suctions (i.e. at lower temperatures). The model was able to reproduce both qualitatively and quantitatively well the main tendencies observed in these experiments.

3.5 CASE STUDIES

3.5.1 Case I: Pipeline collapse

One of the key aspects of the proposed model is its ability to replicate the plastic compact compression collapse behavior observed in frozen soils upon thawing. Thaw related failures are very important for structures constructed in the arctic regions of the world. It was observed historically that pipelines constructed in the region of Northern Canada were seen to suffer problems of excessive settlement. These settlements are observed to be common in ice rich soils (Hanna et al., 1983). A full-scale experimental study conducted by Watson et al. (1973) in the Inuvik region of Canada revealed several important aspects related to pipeline designs in this region.

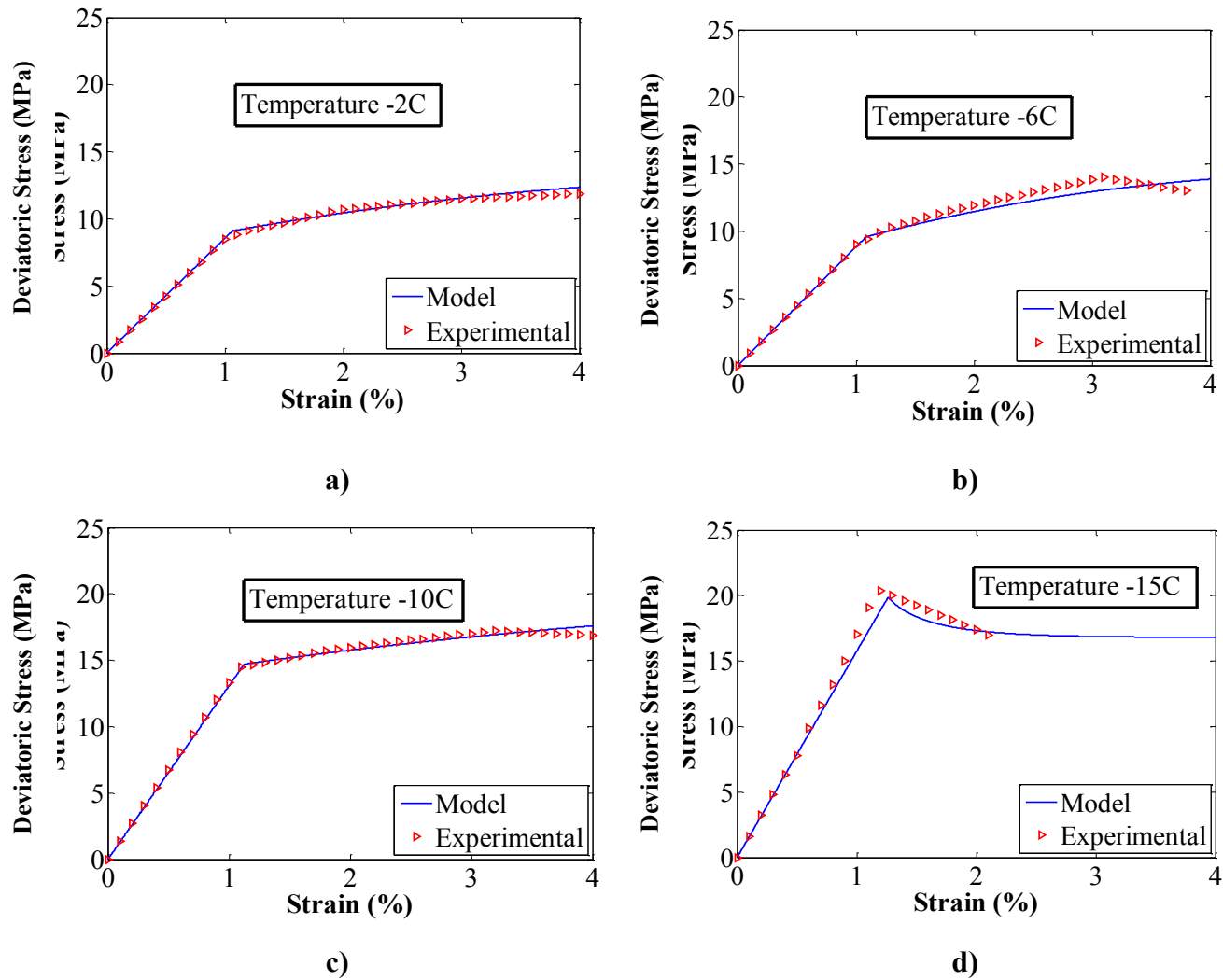


Figure 3.27 Comparison of experimental and model results at a) -10°C b) -6°C c) -10°C d) -15 °C

The work presented here focuses on the behavior of a permafrost soil acting as a foundation for a pipeline carrying oil. The pipeline test section is 27 m long with a diameter of 0.61 m and carried oil at 71 °C. The field observations of the soil around the pipeline were carried out between July 1971 and January 1972. The temperatures, pore pressures and settlement of the foundation were studied along different sections of the pipe. The details of the instrumentation of the pipelines are presented in Watson et al., (1973). The pipeline was buried at location adjacent to an existing oil circulation facility. The average temperature of the ground was recorded at -5°C in July and increased to about 13 °C during the circulation of the oil over a period of six months. The pipeline experienced large settlements within the first two months of the operation, with vertical displacements as high as 2 m. The cross section of the pipeline and the settlements observed during the course of the period of study are shown in Figure 3.28. The description of the different soil layers and the instrumentation used is also detailed in Figure 3.28.

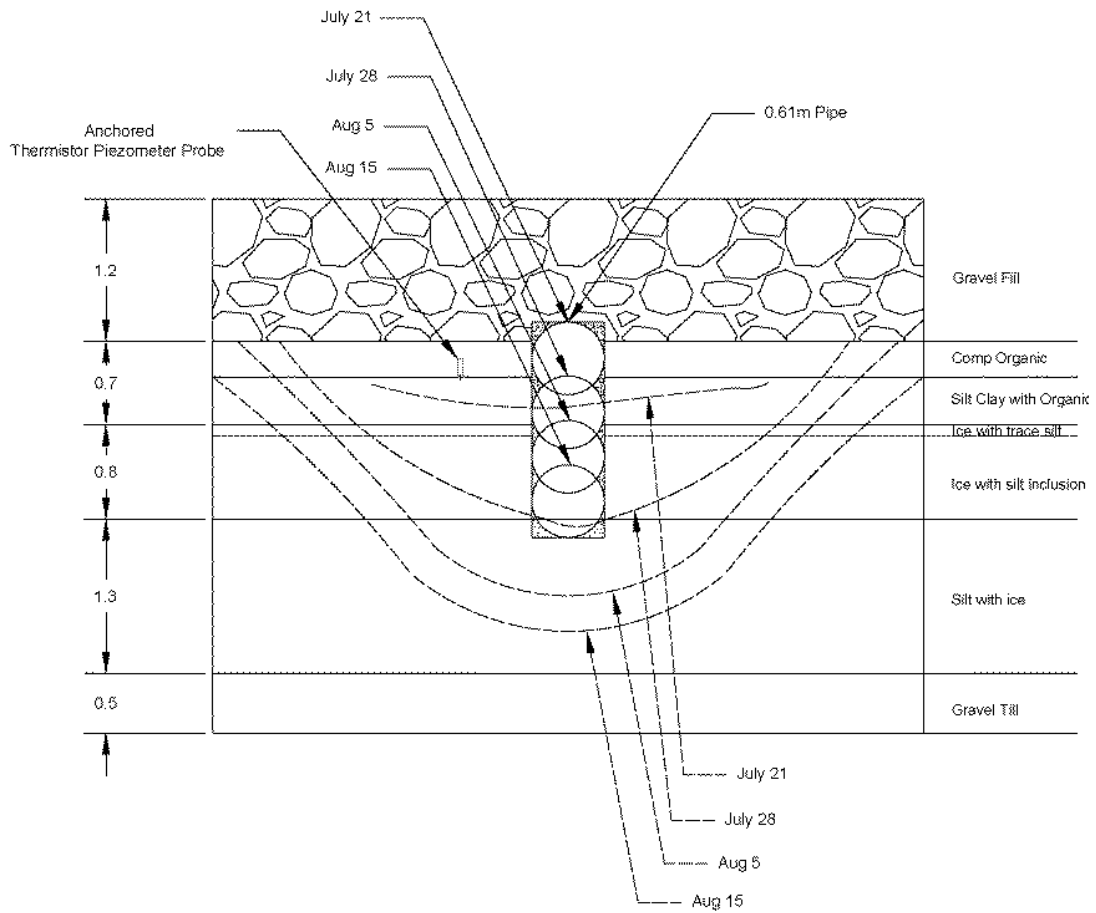


Figure 3.28 Cross-section of the pipeline showing varying degrees of settlement with time

The corresponding temperatures and settlement measure for these times are listed in Figure 3.29. It can be seen that large deformations are observed when the temperature surrounding the pipe increase leading to melting of the soil. This pattern of deformation is similar to the collapse behavior described by in the model in Section 2.9.

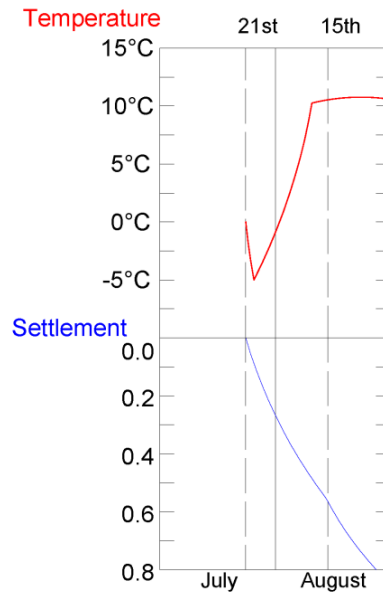


Figure 3.29 Vertical settlement and temperature variation in the pipeline with time

The large deformations observed in the short span indicate that the failure may be related to a volumetric compression collapse mechanism triggered by the increase in temperature in the ground once the pipeline starts the operation. The proposed model is able to capture this feature of frozen soil behavior.

An idealized geometry of this problem is proposed in this Section to perform a numerical analysis aimed at explaining the observed behavior using the formulation presented in Section 2. Figure 3.20 a) presents the adopted 2D plane deformation domain, with the pipeline symmetrically located at the ground level. In this figure, the arrows down indicate the uniform distributed load applied to model the effect of the gravel fill placed on above the ground level (see Figure 3.28). The mesh and the other boundary conditions adopted in this problem are shown in Figure 3.30 b). The vertical

deformation are restricted at the bottom boundary and the horizontal deformation is restricted for the side boundaries. Only half the pipeline was inserted into the soil in field. A semicircular gap was introduced into the mesh to replicate this geometry. Both mechanical and temperature loads were applied to this niche during the simulation. Because the amount of deformation expected was high a large boundary was considered to prevent any influence of the boundary on the final results.

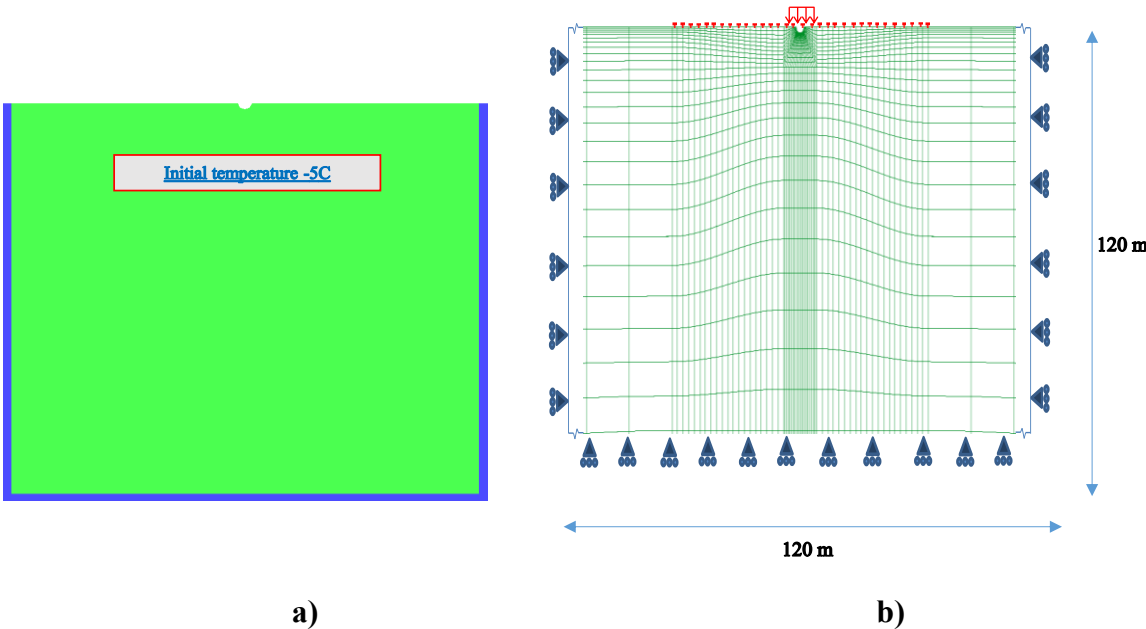


Figure 3.30 Numerical simulation of the pipeline a) Geometry b) Finite element mesh

An initial temperature of -5°C was established in and around the boundary. Temperature of -5°C was maintained at the boundaries of the analyzed domain. The soil was then loaded based on the stress due to pipe. A porosity of 0.4 was adopted based on the conditions described in Watson et al. (1973). The temperature was then increased gradually up to reach 0°C around the pipe. The duration of this analysis was 16 days

and represented the actual period of time observed in the site, starting on July 21st, 1971 and finished on August 5th, 1971 when the temperature reached 0 °C. The model parameter adopted in the study of natural soil presented in Table 3.35 has been used in for this case study.

The distribution of temperature across the studied domain is presented in Figure 3.31. The domain closest to pipe is inspected as this region was understood to have the greatest impact of the deformation. A quite uniform variation of temperature is observed at the end of the heating.

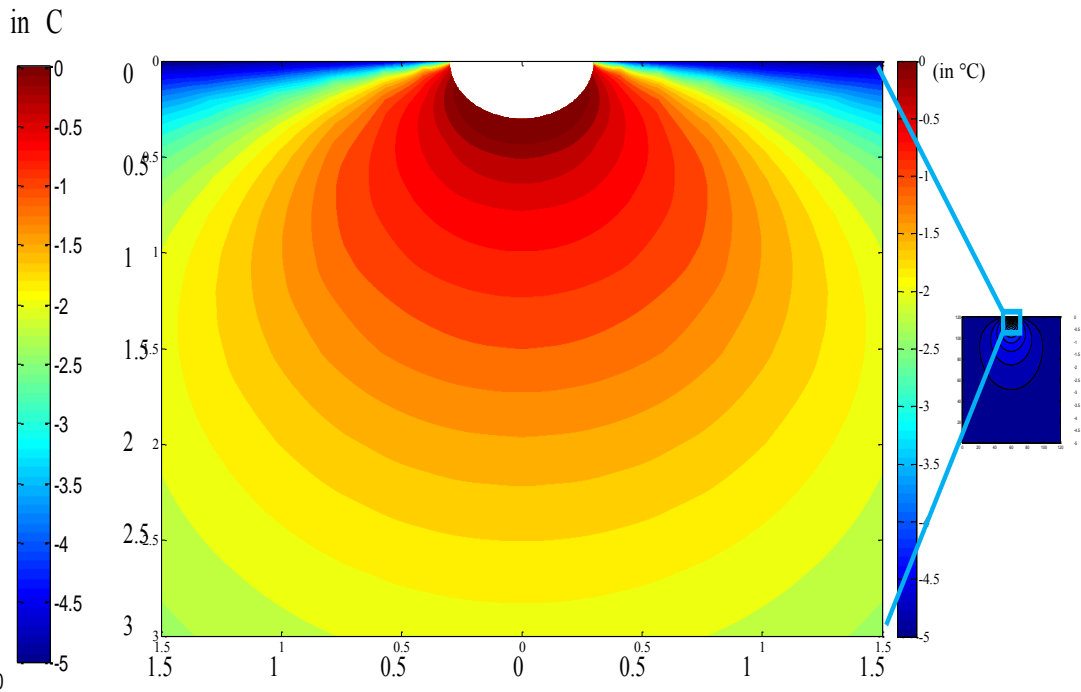


Figure 3.31 Contour of temperature variation at steady state condition (initial temperature was -5°C)

The distribution of the displacement at steady state conditions is displayed in the form of contours in Figure 3.32. As in the case of the Figure 3.31 the relevant domain is zoomed into. It is observed that the highest displacement is near the pipe. The amount of soil deformation attenuates rapidly and is consistent with the temperature imposed on the soil.

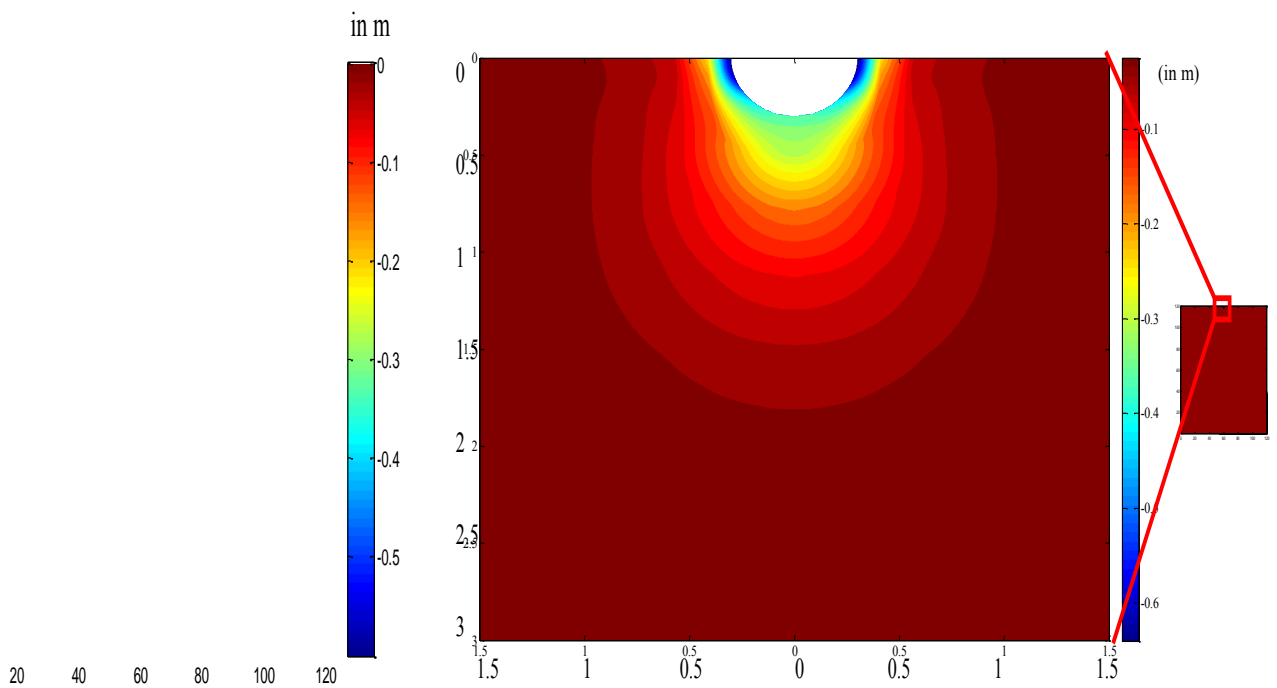


Figure 3.32 Contour of settlement at the end of heating.

It is also interesting to study the stress path followed by some points of the frozen soil subjected to thawing. The changes in void ratio induced by the variation of the mean stress are presented in Figure 3.33 a). Figure 3.33 b) shows the associated stress path in the mean stress vs cryogenic suction plane. Before any construction is started, the frozen

soil is over consolidated due to the effect of the cryogenic suction (point A). The path A-B corresponds to the loading at the initial freezing temperature (i.e. -10°C in this problem) associated with construction of the pipe. Therefore; the compressibility of the frozen soils is controlled by the elastic slope (κ). During the loading process, the stresses may eventually reach the apparent pre-consolidation pressure (p_0), identified as point B in Figure 3.21. As it is well known, beyond this inflexion point B, much larger deformations are predicted because the soil compressibility is controlled now by the virgin compression line (λ_v). The plastic yielding induced by stress increment is indicated by the enlargement of the yield surface in Figure 3.33 b). As shown in Figure 3.33 a), the unfrozen soil condition is associated with a lower pre-consolidation pressure and a higher plastic slope. The heating related to the start of the pipeline operation is associated with the stress path C-D. This is because the compressibility of the melted soil will be controlled by the λ coefficient associated with the thawed temperature (0°C was assumed in this case). The thawing results in a volumetric collapse compression related to the change of void ratio during path C-D (see Figure 3.21 a).

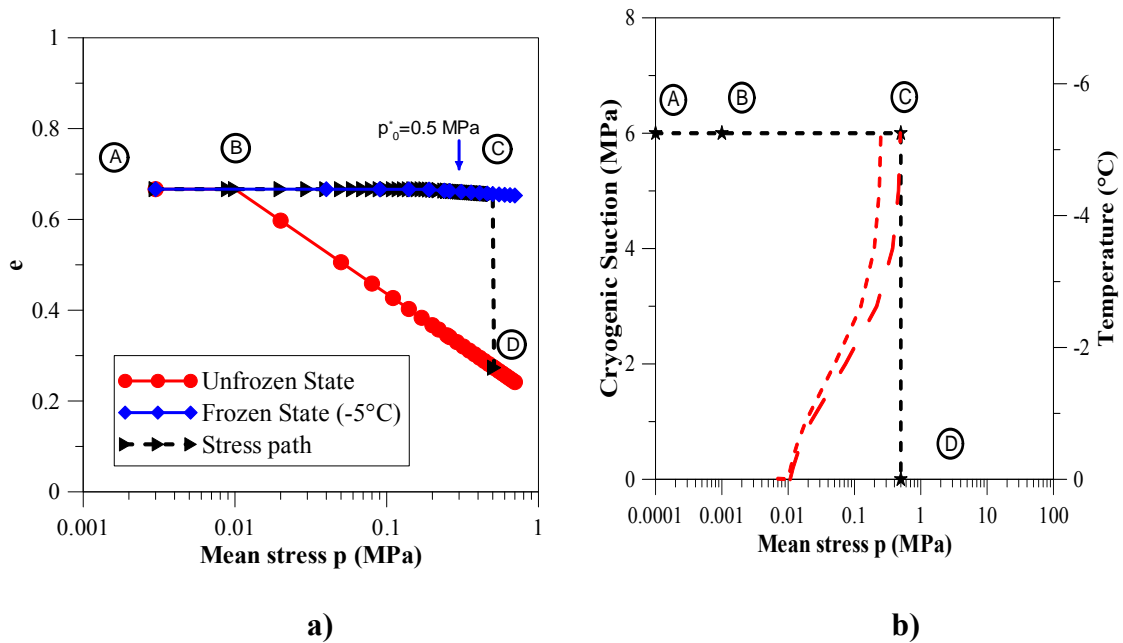


Figure 3.33 Typical stress path a) isotropic behavior b) variation in p-s plane

The loading and thawing paths described above lead to calculate vertical deformation of the ground in the vicinity of the pipeline. In Figure 3.34 the predicted displacements below the center of the pipeline are plotted against the temperature. .

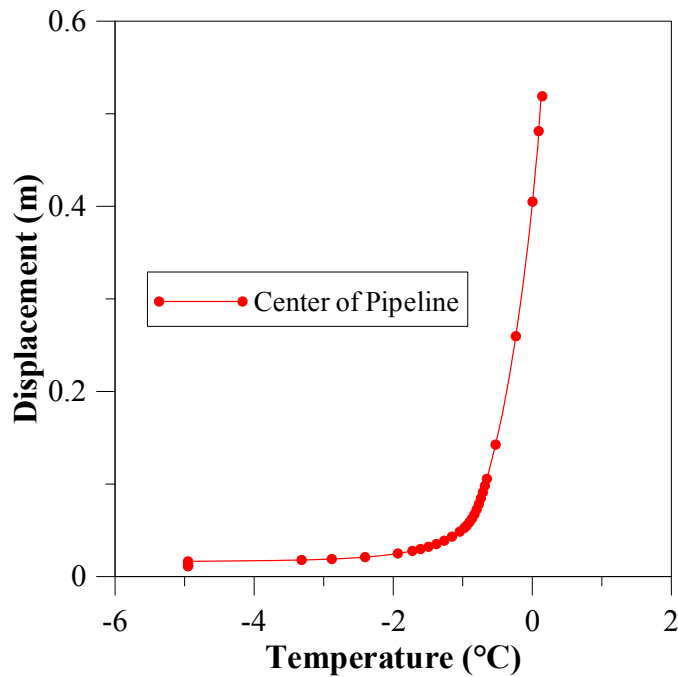


Figure 3.34 Induced settlement below the center of the pipeline at different temperatures

Thaw related failures are very important for structures constructed in the arctic regions of the world. Thaw failures were also observed in other engineering problems, as for example the cases in which engineers favored constructions in concrete over wood (e.g. Goldman, 2002). The next section present the damage upon thawing of the administrative building constructed in in Siberia (Russia), based on the discussion by Zhukov (1991).

3.5.2 Case II: Foundation failure

This section details the failure of an Administrative Service Combine building of the Kadykchanskaya mine in the Magadan region of the former USSR constructed in 1967 (Zhukov, 1990). The foundation trench for the building was excavated and left

uncovered for six years before the foundation was constructed. Therefore, the foundation was constructed on an ice covered soil base. Large settlements with the associated cracks (Figure 3.35) were observed in the building after starting the usage of utilities (Zhukov, 1990).

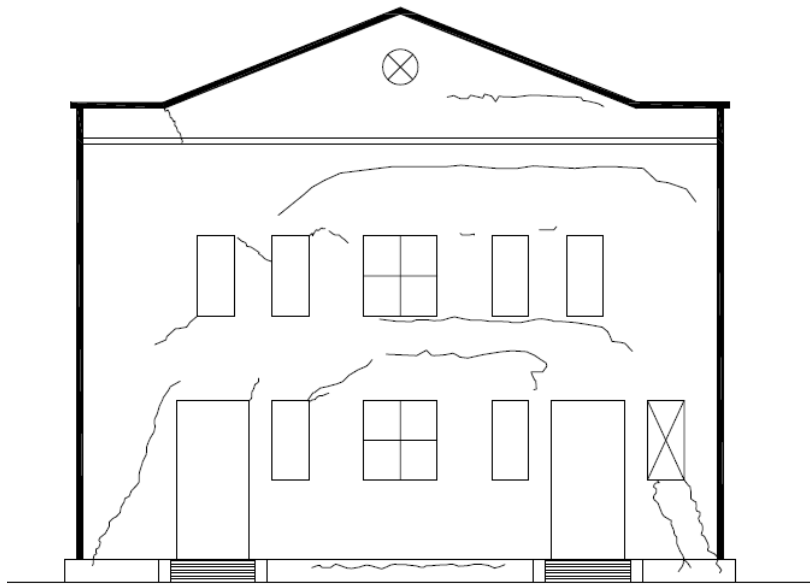
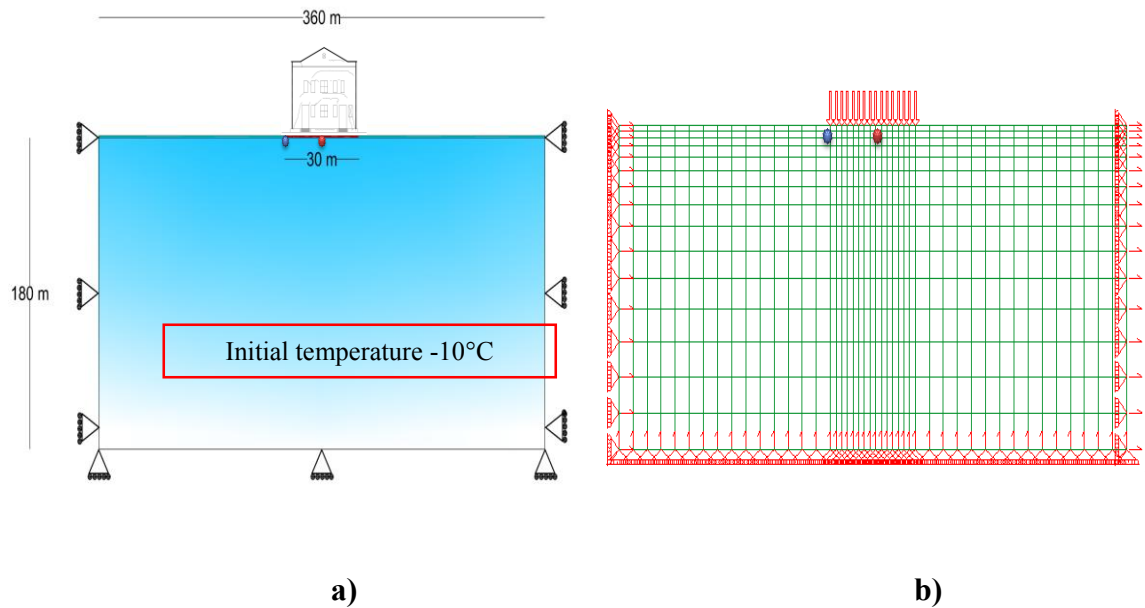


Figure 3.35 Administrative Service Combine building of the Kadykchanskaya mine in the Magadan region of the former USSR constructed in 1967

To explore the capability of the proposed approach to describe this kind of problem a model was developed aimed at mimicking the conditions observed in this building. The boundary conditions adopted for this problem and the corresponding mesh are shown in Figure 3.36 a) and b) respectively.



**Figure 3.36 Numerical simulation of the foundation a) Boundary conditions
b) Finite element mesh**

An initial temperature of $-10\text{ }^{\circ}\text{C}$ was established throughout the whole domain was assumed. This assumption has made based on the available weather data for this region. After applying these initial conditions, the stresses associated with the construction of the building were imposed. A uniform stress 30m long equal to 4 MPa was applied at the center of the adopted domain to simulate the load due to the building. Temperature of $-10\text{ }^{\circ}\text{C}$ was maintained at the boundaries of the analyzed domain. The soil was then thawed by increasing the temperature of the foundation. The behavior of the ground was analyzed for a period of thawing 1000 hours. As information on the soil behavior of this region is scarce, the parameters used in the study of reconstituted soil listed in Table 3.6 has been adopted here

The contour of temperature across the whole domain, at the end of the analysis, is presented in Figure 3.37. As expected, the higher temperature (i.e. 0 °C) is predicted below the foundation, the temperature decreases when moving away from the foundation, reaching the lower temperature at the boundaries.

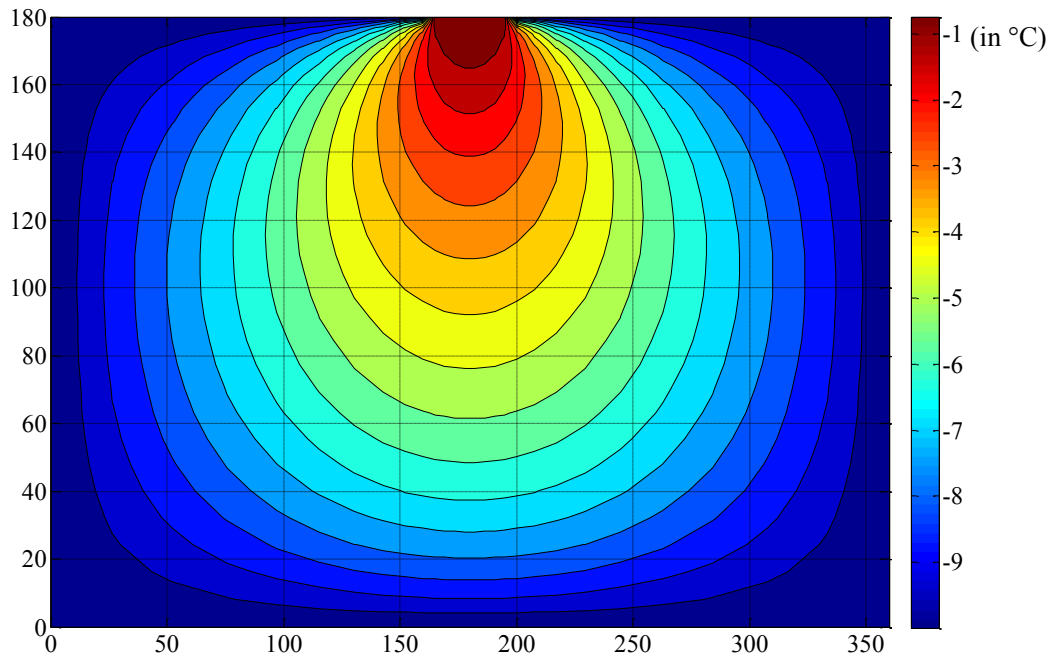


Figure 3.37. Contour of temperature variation at steady state condition (initial temperature was -10 °C)

The variation of the mechanical properties with temperature leads to deformations of the ground. Figure 3.38 shows the displacement fields predicted by the model at the end of the analysis. It can be seen that the highest amount of settlement takes place just below the foundation. It can also be observed that the center of the

foundation undergoes a greater amount of settlement than at the edge of the foundation leading to the differential settlement.

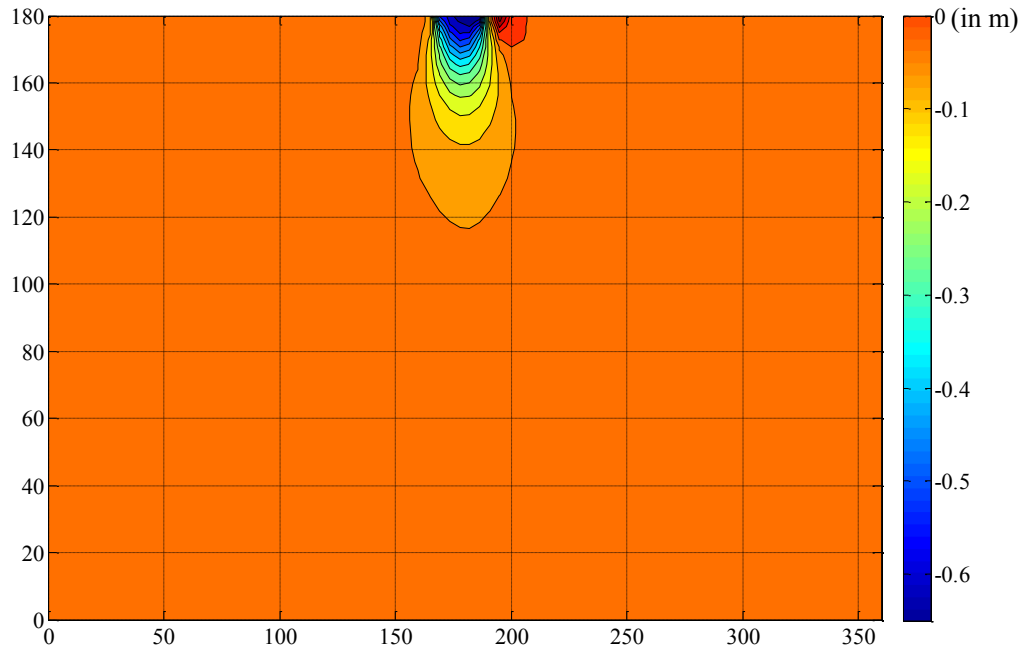


Figure 3.38. Contour of displacements at the end of heating

To assist the interpretation of the results presented in Figure 3.37 the stress path will be inspected in some detail. The predicted changes of void ratio in terms of ' $\ln(p)$ ' are presented in Figure 3.39 a) and Figure 3.39 b) presents a typical stress path in the plane 'mean stress' 'cryogenic suction' followed by the soil below foundation during loading (i.e. building construction) and thawing (i.e. building heating). In those plots, the point A correspond the initial pre-consolidated conditions of the soil below construction.

The path A-B is associated with the increase of stresses during the construction of the building at -10°C . The loading path may reach at some point the apparent pre-consolidation pressure (p_{s0}) identified as B. The maximum load C corresponds to the end of the construction. The settlements observed during construction are controlled by the elastic slope (κ) between A and B and by elasto-plastic gradient λ_s beyond B. The plastic yielding is associated with the enlargement of the yield surface in Figure 3.39 b). It is also observed that the unfrozen soil (red circles in Figure 3.39 a) has a lower pre-consolidation pressure and higher a plastic slope than the frozen soil. During thawing the soil move from point C to D (i.e. the soil will lie on the compression line associated with the current temperature). This thawing path C-D induces a volumetric compression at constant mean stress.

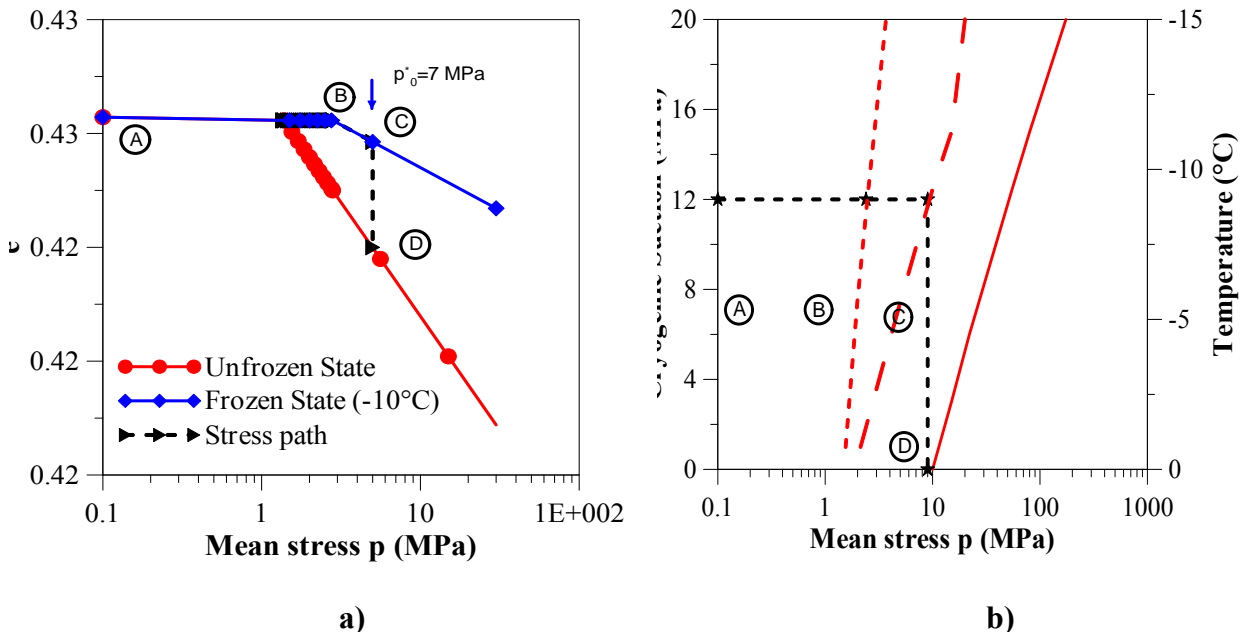


Figure 3.39 Typical stress path a) isotropic behavior b) variation in p-s plane

Finally, the settlements at the center and edge of the foundation are plotted against the temperature in Figure 3.40. The differential settlement predicted by the model explains the cracks observed in the building after heating.

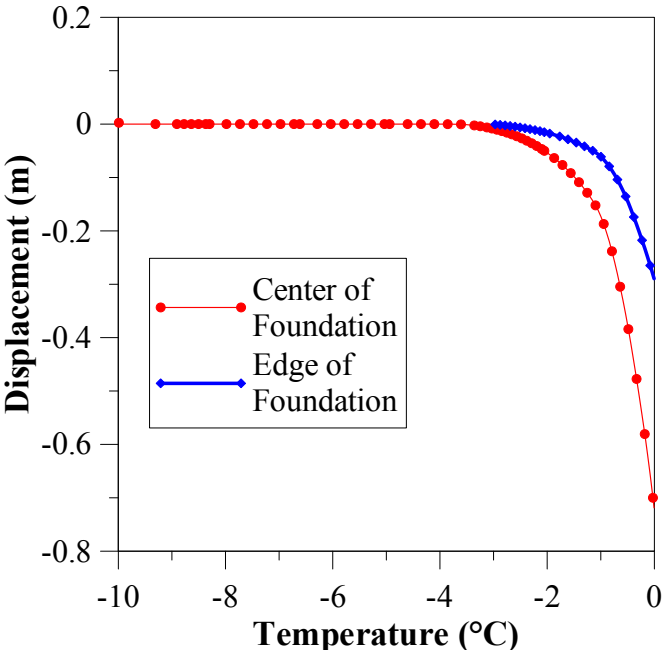


Figure 3.40. Variation of settlement with temperature at two different positions (center and edge) in the foundation

4 CYCLIC FREEZE THAW BEHAVIOR OF SOILS

4.1 INTRODUCTION

In cold regions soils are generally subjected to cyclic freeze-thaw due to seasonal variations in temperature. During this process they undergo several changes affecting various physical properties of the soil, directly impacting in turn in many infrastructure projects in these areas. The effect of freeze-thaw cycles also gains importance recently due to growing interest in geotechnical techniques based on the artificial and temporal freezing of the ground. The temporal freezing of soils is becoming common technique to improve temporally the properties of the ground (e.g. to enlarge a foundation). The behavior after thawing is also relevant in this kind of application. A large number of applications where the cyclic freeze-thaw behavior is relevant have been discussed in section 2.1.

The behavior of frozen soils and the numerical model to describe this behavior was detailed in Section 2. The validation of this model presented in Section 3 proved that this was an appropriate model for reproducing the behavior of frozen soils. However the model fails to account for major changes which take place in the soil during cyclic freeze-thaw. This is a serious drawback of the model as the understanding of the freeze-thaw behavior is crucial in solving most engineering problems related to frozen soils.

This section concentrates on factors affecting the microstructural changes and its impact on the overall behavior during the freeze-thaw cycles. The background on the behavior of these soils under these conditions is presented in section 4.2. An experimental campaign was performed in this dissertation to increment the existing

laboratory data reported in the literature. The details of the experimental campaign are presented in Section 4.3. Also a constitutive model is proposed to reproduce the mechanical behavior of frozen soils subjected to thaw/freeze cycles.

4.2 BACKGROUND

A major contribution towards understanding of the behavior of freeze thaw effects was presented by Chamberlain and Gow, (1979). Freeze-thaw experiments were conducted on fine grained soils to understand the changes in the permeability of the soil. The soil samples were frozen uniaxially with a free access to water (open system) and then subjected to consolidation. The samples were composed of materials with Plasticity Index (PI) ranging 0 to 20. The soil specimens were prepared in the form of a slurry by mixing soil to about twice the liquid limit. Samples were frozen to temperatures of -10 °C from bottom up with free access to water to the top. A frost penetration rate of 5 mm/h was used. Upon completion of freezing, the samples were thawed at temperatures of 22 °C with free access to water.

The soil was then subjected to falling head permeability tests. Freeze/thaw cycles was repeated until no changes in void ratio were observed. Thin section samples were extracted to examine the cracks occurring due to the ice lens formation. It was observed that the freezing and thawing caused significant structural changes in consolidated clay slurries and caused large increases in vertical permeability. The increase was greatest for the soil specimen with the largest plasticity index and, in general, the increase was smaller at the highest applied stress levels. Soils with higher clay particles, displayed increased permeability after the cycles.

Konard (1988) conducted a similar set of experiments on clayey silt obtained from Calgary, Canada. The samples were consolidated and then allowed to rebound to 50 kPa with OCRs (Over-Consolidation Ratio) of 2, 4, 6 and 8. The samples were frozen from the bottom up with a free access to water. The freezing temperature at the bottom was -2°C while the temperature at the top was maintained at 2°C . X-ray photographs were taken of the frozen sample to observe the ice lens formed during this process. Samples were subjected from three to four freeze thaw cycles. Each freeze-thaw cycle was followed up with by reconsolidating the sample to 50 kPa. At the end of the freeze-thaw consolidation cycle, hydraulic conductivity tests were conducted in a triaxial cell. Similar to Chamberlain and Gow (1979), the hydraulic conductivity of the thawed samples increased and the increase was greatest with samples having the highest OCR values. Based on these observations, Konrad (1989) theorized that soil structure was composed of two distinct pore regions consisting of micropores and macropores. The macropores consisted of pore spaces formed between larger particles of the soil where ice formation occurs at higher temperatures. The micropores consist of spaces between the clay grains which were harder to completely freeze despite of the temperature falling well the freezing range due to capillary effects. Figure 4.1 a) shows the distinction between macro and micropores for a clayey silt. The freezing of the micropores brings about a rearrangement of the fine grained particles due to the expansion of water. These deformations are observed to cause the plastic deformation when the soil thaws. The rearrangement caused due to the freezing of the micropore is shown in Figure 4.1 b).

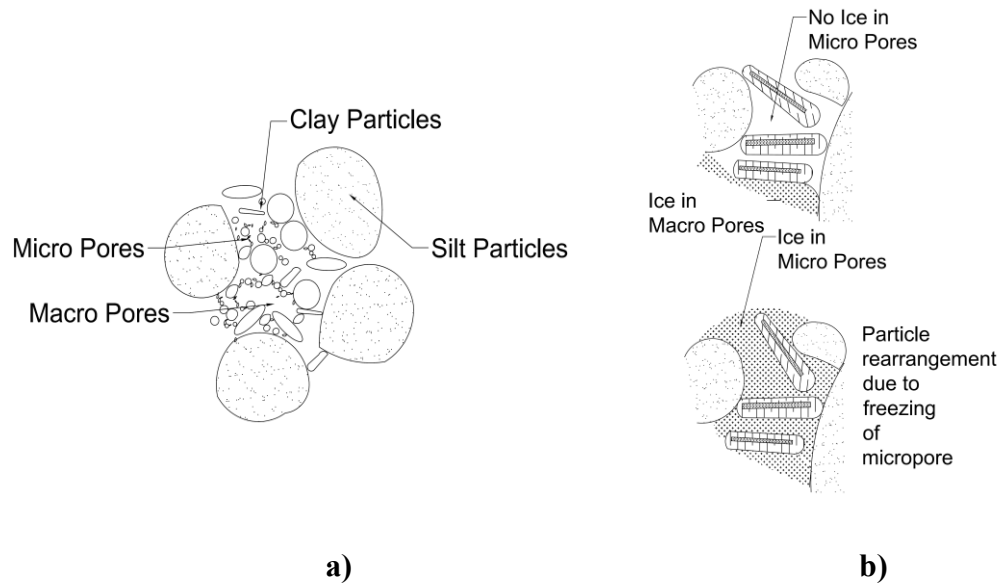


Figure 4.1 Porous structure rearrangement in the soil a) Distribution of micro and macropores for clayey silt soil b) Rearrangement of particles due to freezing of micropore

These changes in permeability were also observed in closed systems with no access to free water (Konrad 2010; Paudel and Wang, 2010; Konrad and Samson, 2000; Haug and Wong, 1991). Of particular interest is the work conducted by Haug and Wong 1991, where the hydraulic conductivity tests on fine grained soil at the end of each freeze-thaw cycle was measured. The soil samples consisted of Regina clay; Battleford till; and a Bentonite-Ottawa sand mixtures with varying proportions of clay (amount of Bentonite varied from 4.5-20%). The samples were compacted according to ASTM D698 specifications in a proctor mold, 2% above the optimum moisture content. The soil samples were then consolidated to an effective vertical stress of 17.2 kPa after which the freeze-thaw tests with the freezing temperatures of $-20\text{ }^{\circ}\text{C}$ were initiated.

Permeability tests were conducted post thawing for each specimen until the change in permeability was less than $0.02E^{-7}$ cm/s. The tests showed two distinct patterns. The Regina clay and till samples exhibited an increase in permeability with each freeze-thaw cycles and the bentonite-sand mixture exhibited a drop in permeability. These results can be seen in Figure 4.2 a) and b).

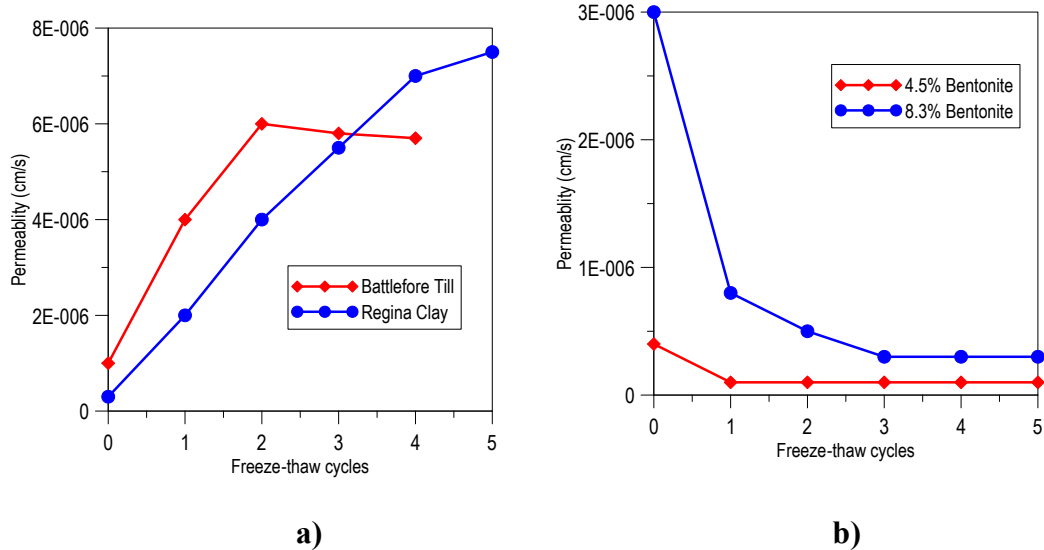


Figure 4.2 Results of permeability test post thawing a) Battleford till and Regina clay samples b) Bentonite-Ottawa sand mixtures (Wong and Haug 1991)

Although there was no direct measurement in the voids ratio, the change in permeability indicates a change in the soil structure with each freeze-thaw cycle. The decrease in permeability of the Bentonite-Ottawa sand mixture indicates that there is a drop in voids ratio and that the soil structure is densifying. While, the voids ratio in the Regina clay and the till samples is increasing marked by the increase in permeability.

Furthermore, the rate of decrease or increase in void ratio reduces with each passing freeze-thaw cycle until a stable structure is attained.

The changes in the voids ratio were better explored in the experiments conducted by Viklander, (1999). Fine grained till with particle size less than 20 mm were compacted to a wide range of densities. Permeameter cells of varying sizes composed of either PVC or Plexiglass were used in the experiment. Samples were frozen from bottom up by insulating the sides and the top of the cell used in the experiment. Deformation and temperature reading were measured by using LVDTs (Linear variable differential transformers) and thermocouples within the cells. The change in permeability and voids ratio of the specimen was measure at the end of every thaw cycle. It was established that the soils subjected to cyclic freeze-thaw experienced different behaviors based on the state of particle arrangement. Figure 4.3 shows the variation of the voids ratio obtained during testing. The soils with higher initial voids ratio, ' e_0 ' are low density soils and the ones with lower initial voids ratio are high density soils. Compressive behavior was observed in those soil samples with lower density (loose soils) and expansion was observed in high density (dense) soils.

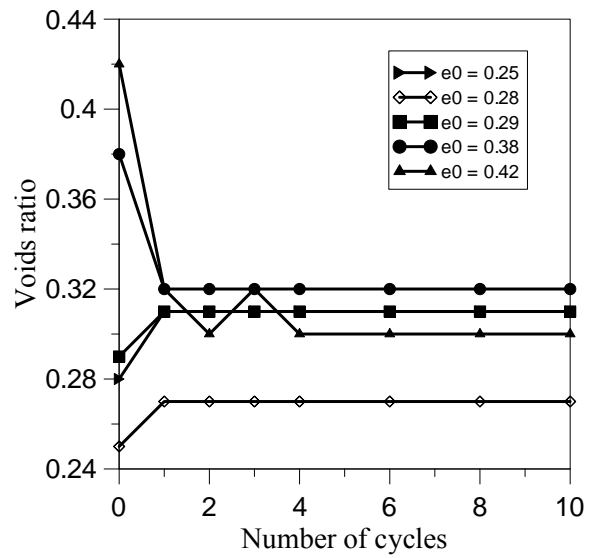


Figure 4.3 Variation of voids ratio with number of freeze-thaw cycles for soils of different densities

The soils upon approached a “residual” voids ratio after a few cycles beyond which there was no significant changes in volume. A schematic of this phenomenon is represented Figure 4.4.

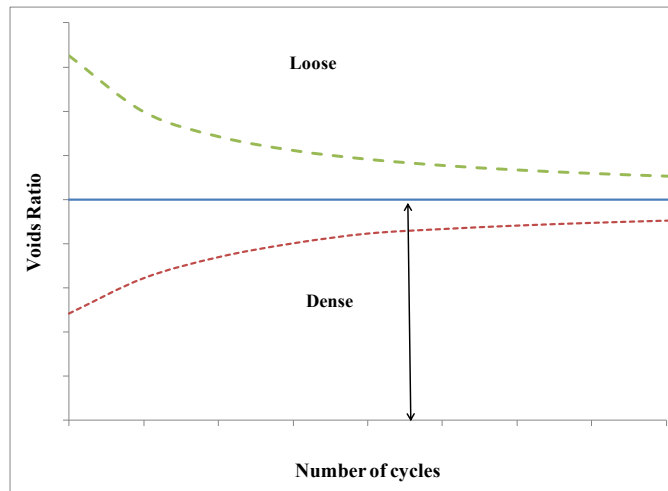


Figure 4.4 Behavior of soils subjected Freeze-thaw cycles based on arrangement

A similar set of experiments was conducted by Konrad (2010) on glacial till samples from Quebec, Canada. Samples were either consolidated or compacted. The consolidated samples were prepared by mixing the soils to about 1.2 times the liquid limit followed by consolidation and freeze-thaw tests. The compacted samples were initially mixed with water content of about 9% and then compacted manually. The compaction process was followed by applying a 20 kPa vertical stress and a constant head permeability test. These samples were then subjected to a 40 kPa of vertical stress after which they were subjected to freeze-thaw cycles. Constant head permeability tests were conducted on the samples before and after all the freeze-thaw cycles.

The variation in the height of one of the sample with the changes in the load and freeze-thaw cycles is shown in Figure 4.5 a). The volume change which occurs at the end of freeze thaw cycles is indicated in Figure 4.5 b).

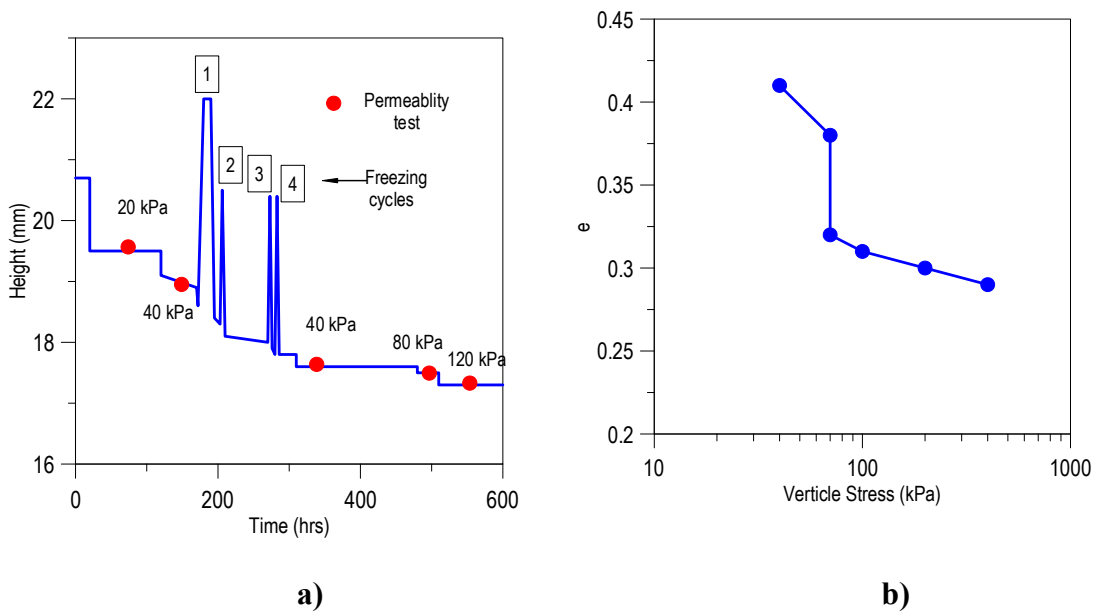


Figure 4.5 Test results a) Variation in the height of sample S10 with time and load b) Change in voids ratio after the freeze-thaw cycles (Konrad, 2010)

The results of the experiments conducted by Konrad is consistent with the behavior of the soil seen in the experiments conducted by Viklander (1999). The soils exhibited a compressive behavior after the first few freeze-thaw cycles and approached a residual value of the voids ratio after a few cycles. Theories on frozen soil expansion presented in Section 2 were largely confined to an elastic expansion of the ice occurring due to the phase change. An elastic response would imply that the overall change in the volume would be zero at the end of the freeze-thaw cycle contrary to the findings in these experiments. The change in voids ratio occurring in the soil is irreversible (plastic) in nature and it approaches a residual value with an increase in the number of cycles of freeze-thaw. This behavior is well documented in sands and silts (coarser soils), however

there is little information available on fine grained soils such as clays. An experimental procedure is developed as part of this dissertation and is presented in Section 4.3 to better understand this behavior in clays. A constitutive model has been proposed for modeling the cyclic freeze-thaw behavior to include these plastic behaviors and is validated in Section 4.4 and 4.5 respectively.

4.3 EXPERIMENTAL PROCEDURE

The behavior of soils subjected to freeze-thaw cycles adds a complex dimension into the behavior of frozen soils. The experimental information associated with the effect of freeze-thaw cycles is limited in the literature, particularly for fine grained soils. An experimental campaign is proposed herein to investigate the effect of freeze-thaw cycles on volume change for clays consolidated at different stresses. The behavior of a Normally Consolidated (NC) sample and an Over Consolidated (OC) sample with an OCR of 3 has been examined here.

4.3.1 Test setup

The test setup of a graduated brass cylinder of diameter 1.5” and a height of 5” mounted on top of a porous stone (

Figure 4.6 a). Inside this cell, the samples were prepared at the desired water content. A plunger with a porous stone at the end of it is inserted on top of the sample (

Figure 4.6 c). The target surcharge load in the form of dead weights was applied via an accessory. The soil was allowed to consolidate under this load. The cylinder has a provision for an outlet at a height of 1.5” so as to allow for drainage from the top of the sample. The setup is mounted on top of a custom pedestal base (

Figure 4.6 b) prepared using a 3D printer at the department of Aerospace at Texas A&M University. To accommodate for drainage, the pedestal is designed to have 2 openings through them. At both ends, top and bottom, the drainage conditions of the sample can be fully controlled.

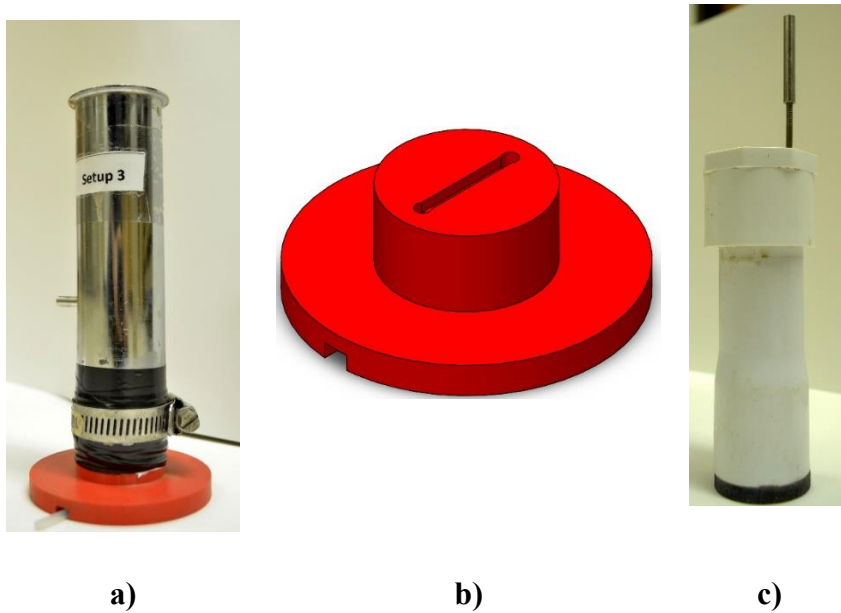


Figure 4.6 Experimental setup a) Experimental cell b) Base Pedestal c) Plunger with porous stone

A LVDT is used to measure the vertical displacement of the sample. The LVDTs used here is a model identify as SE-750-500 (Figure 4.7). This LVDT is specially designed to operate in the sub-zero temperature ranges. The travel length of the LVDT is 0.5" (12.7 mm) with a Full Scale Output (FSO) of ± 10 V. The linearity error of the LVDT is $< 0.25\%$ of FSO. The operational range of temperature of LVDT is between -

20 °C to 70 °C. The core of the LVDT is mounted on the plunger using a cap which is attached to the top of the plunger as shown in Figure 4.6 c.

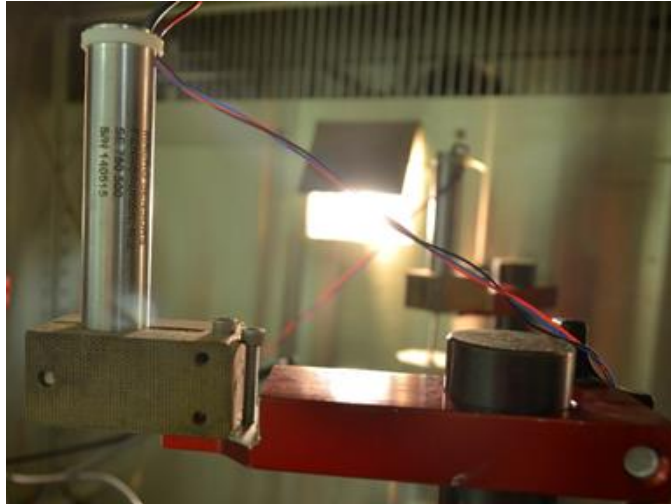
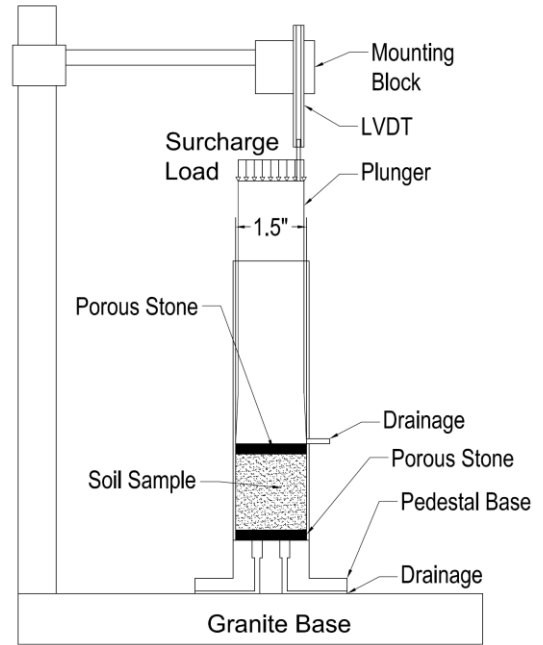


Figure 4.7 LVDT used for the experiment

The experimental setup is placed on granite stand with an anodized aluminum mount for the LVDT. The assembled experimental setup and a schematic of the experiment are shown in Figure 4.8 a) and Figure 4.8 b) respectively.

The freeze-thaw cycles was performed under controlled conditions inside an environmental chamber (Figure 4.9). The environmental chamber used here was a CSZ P500-8Z with a capacity of 64 cu. ft. It has a temperature range from -50°C to 120°C with the ability to modify the humidity inside the chamber from 0 to 100%. It also has an in built thermocouple for measuring the temperature of the test samples inside the chamber. The chamber is well insulated so to maintain the desired test conditions.



a)

b)

Figure 4.8 Experimental setup a) Picture of the set-up used in this research, b) Scheme showing the main components of the proposed setup



Figure 4.9 Environmental chamber used to simulate the freeze-thaw tests

It is also equipped with a touch screen controller (Figure 4.10). The touch screen has options to set the temperature of the chamber, humidity of the chamber directly, as well as controlling the temperature based on a desired thermocouple reading. Predefined profiles can be programmed into the controller to modify the temperature and humidity at any desired time.



Figure 4.10 CSZ touch screen controller

The displacement data was recorded at 5 seconds intervals to ensure that all the deformations during the experiment were captured. The information obtained from the LVDT is read into a database using a LABVIEW program developed to record the deformations. Reduction of the data is performed using a MATLAB program. The experimental setup was calibrated using an aluminum cylinder in place of the soil to compute the coefficient of thermal expansion of the test cell and the base.

The material chosen for testing is known by its commercial name as ‘Red-art Clay’ (Al_2O_3 (15.51%), SiO_2 (64.95%), Fe_2O_3 (7.05%)). This clay is a low plasticity, low shrinkage, clay usually bright red in color and is used in pottery. The Liquid Limit (LL) and plastic limit was determined as 41 and 25 respectively. The plasticity index (PI) of the soil was about 16. The samples were prepared using two different techniques to obtain soil of low and high densities. The low density samples were obtained by mixing dry clay with water to about 1.3 times the LL using an industrial mixer. The mixture

was then pumped into the test cell, and care was taken to ensure that there was no air voids formed.

The samples were consolidated under a 120 kPa of vertical stress using a static load applied using the laboratory weights placed on top of the plunger. The samples were connected to a source of water to ensure the saturation through the process of consolidation. The displacement during the process of consolidation was recorded using a dial gauge. Following 24 hours of loading, one of the samples was unloaded to a vertical stress of 40 kPa, to obtain an OCR of 3. The other sample was maintained at the same stress. The unloading was done for 24 hours and the final heights of the specimens were recorded before loading them into the environmental chamber where the freeze-thaw experiments were conducted.

The high density samples were obtained using a pug-mill system. The pug-mill employed here was the Peter Pugger VPM-9 Power Wedger. The soil specimen is loaded into the chamber of the pug-mill and mixed with water to achieve the desired water content. The pugger is also equipped with a vacuum pump to deair the specimen during the process of mixing. The vacuum pressure of about 2.5 MPa (25 bars) is applied on the specimen to achieve a triaxial B value close to 0.94. The samples are unloaded from the pugger in the form of three inch diameter logs which are cut and loaded in the test setup described earlier. The samples here were consolidated to 80 kPa for a period of 24 hours. After the loading period, one of the samples was unloaded to a vertical stress of 40 kPa, to obtain an OCR of 2, the sample here is designated as high stress sample (HS). The other sample was unloaded to a stress of 0.50 kPa and is designated as low stress sample

(LS). The stress was reduced drastically here to understand the behavior of heavily over consolidated sample.

The temperature cycle for both set of samples are maintained to be the same. A minimum temperature of $-5\text{ }^{\circ}\text{C}$ was maintained for the freezing cycles and a temperature of $5\text{ }^{\circ}\text{C}$ was maintained during the thawing cycles for about 23.5 hours. The change from the freezing to thawing cycles was performed in 1.5 hours by applying a uniform temperature ramp. This process ensures that each freeze-thaw cycle would last about 48 hours. The variation of the applied temperature during each freeze-thaw cycle is shown in Figure 4.11.

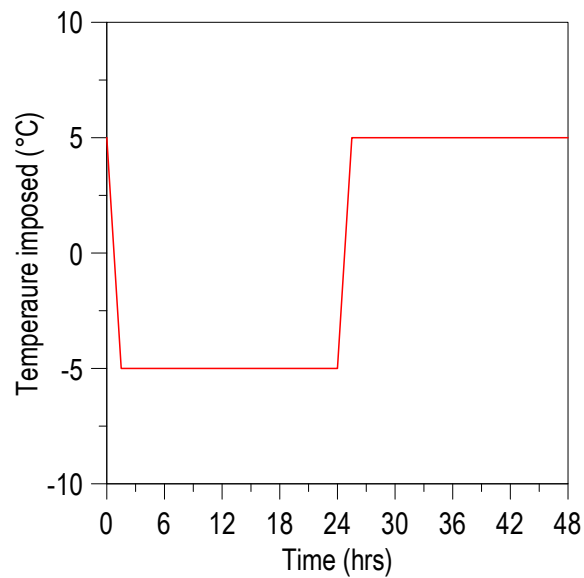


Figure 4.11 Temperature imposed during each freeze-thaw cycle

4.3.2 Results of the experimental campaign

The low density samples were prepared at a water content of 54.5% leading to voids ratio of 1.46 prior to consolidation. After the initial consolidation under the designated 120 kPa load, the samples attained a voids ratio of 1.08. The OC samples were then unloaded for 24 hours and maintained at a vertical stress of 40 kPa. The final voids ratio of the OC specimen was 1.06. These results are summarized in Table 4.1

Table 4.1 Results of the consolidation test prior to freeze-thaw cycles

Property	Value	
	OC sample	NC Sample
Water content of the sample prior to consolidation (%)	54.5	
Void ratio prior to consolidation	1.46	
Void ratio after initial loading	1.08	
Final voids ratio after consolidation	1.06	1.08

The freeze thaw-cycles were conducted until difference in the volume change observed between subsequent thaw cycles for both the samples was less than 0.1 %.

The combined freeze-thaw response of the soils is shown in Figure 4.12 a) and b). The voids ratio at the freeze cycles are indicated by the blue points and the ones at the thaw cycles are indicated by the red points.

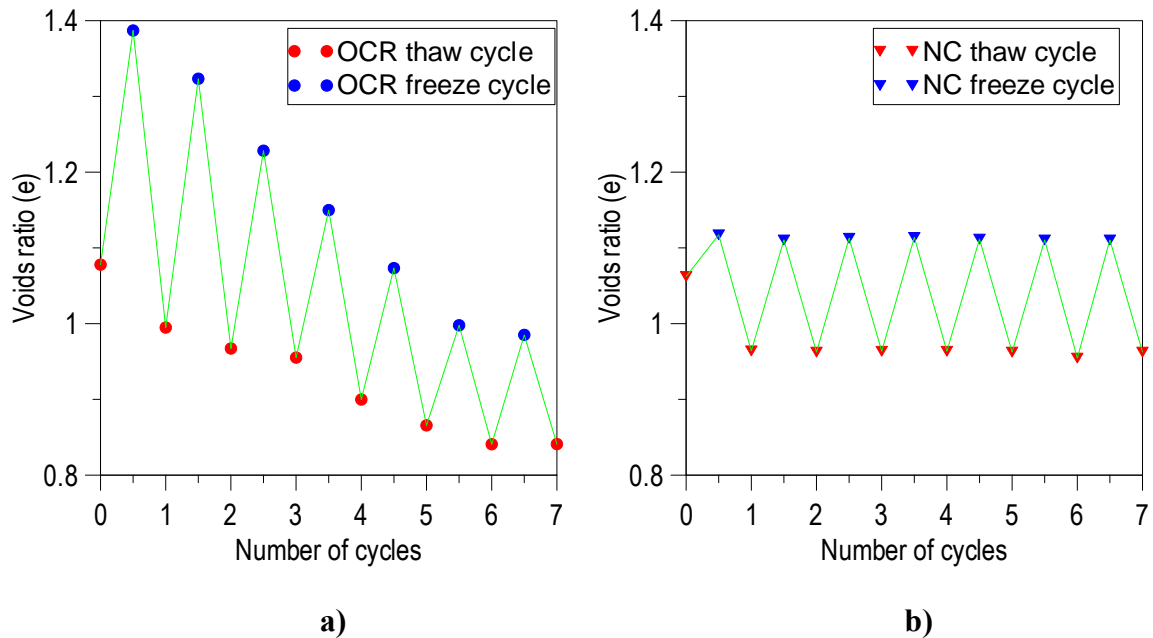


Figure 4.12 Variation of voids ratio with the freeze cycles for a) OC samples b) NC soils

The experimental results show very interesting trends with respect to the behavior of the soil. Both the NC and OC samples exhibit an irrecoverable reduction in volume after cycles. The NC soil displays a consistent trend of similar amount of deformation in the each of the freeze-thaw cycles after the first cycle. The OC soils samples show a constant reduction in the volume for first 6 cycles before achieving a constant freezing and thawing volume on the 7th cycle. It should be noted that both OC and the NC samples start at nearly identical voids ratio and water content. The properties of the high density samples are listed in Table 4.2.

Table 4.2 Results of the consolidation test prior to freeze-thaw cycles

Property	Value	
	HS sample	LS Sample
Water content of the sample prior to consolidation (%)	32.45	
Void ratio prior to consolidation	0.82	
Void ratio after initial loading	0.59	
Stress during 1 st stage of consolidation	80 kPa	
Stress during 2 nd stage consolidation	40 kPa	0.5 kPa
Final voids ratio after consolidation	0.64	0.6

The combined freeze-thaw response of the high density samples is shown in Figure 4.13. The voids ratio at the freeze cycles are indicated by the blue points and the ones at the thaw cycles are indicated by the red points.

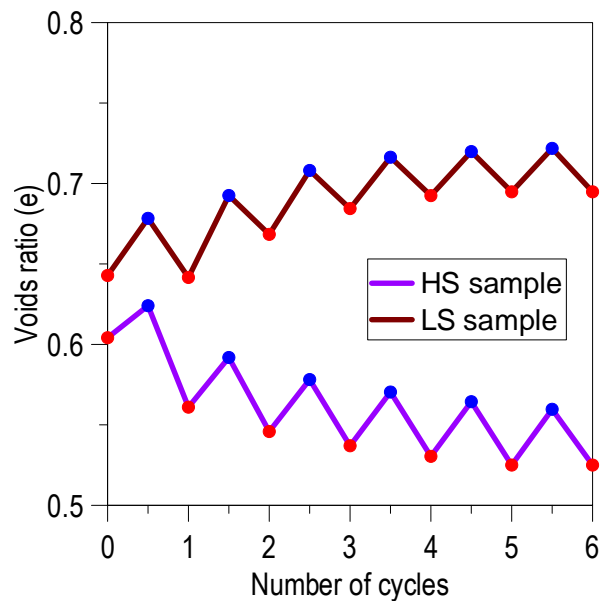


Figure 4.13 Variation of voids ratio for high density samples at high and low OCRs

Both the high density samples exhibit an irrecoverable reduction in volume after cycles. The HS sample is seen to collapse greatly during the first cycle after which there is lesser reduction in volume in each subsequent cycle. The LS sample displays an expansive behavior during the first two cycles beyond which there is small increase in the voids ratio. The change in volume at the end of each cycle is less than 0.1% beyond the 4th cycle for both the samples. The LS and the HS are seen to behave similar to the sand samples of high and low densities respectively described in Section 4.2.

These observations are now used to propose a constitutive mechanical model to describe the changes taking place in the soil during the freeze-thaw cycles. The details of this constitutive model are presented in Section 4.4

4.4 MODEL FORMULATION

The expansive clay model (Gens and Alonso, 1992) is a well-established model (Sanchez et al., 2010 and Sanchez et al., 2005) for reproducing the cyclic wetting and drying in clays. The model accounts for plastic deformation of the soil within the yield surface due to the phenomenon of expansion of the clay mineral. Drawing inspirations from the expansive clay model, a model for freeze thaw behavior of soils is proposed here.

To model the strains occurring in the soil an additive decomposition of strain is considered, as the sum of the elastic and plastic strains

$$\dot{\epsilon}^T = \dot{\epsilon}^{el} + \dot{\epsilon}^P \quad (4.1)$$

The elastic deformations can further be decomposed into contributions of ice formation $(\dot{\epsilon})_i$, suction $(\dot{\epsilon})_s$, mechanical $(\dot{\epsilon})_p$, and thermal $(\dot{\epsilon})_T$ actions described by,

$$\dot{\epsilon}^{el} = (\dot{\epsilon})_p + (\dot{\epsilon})_s + (\dot{\epsilon})_T + (\dot{\epsilon})_i \quad (4.2)$$

The elastic strains during the ice formation or melting is about 9% of the water involved in the phase change, as described in Section 2. The change in the elastic volumetric strain in soil due to ice formation $(\dot{\epsilon}_v)_i$ is assumed to be entirely due to the formation or dissolution of the ice. Therefore, this depends on the change in the degree of saturation of ice. The volumetric strain can be estimated by;

$$(\dot{\epsilon}_v)_i = \dot{S}_i * \epsilon_v^i \quad (4.3)$$

where, ϵ_v^i is the expansion of ice due to phase transformation which is 0.09.

The influence of the deformation due to suction and temperatures are considered to be negligible at this stage, however these can be incorporated if deemed necessary.

The plastic strains due to the ice formation are estimated based on the current value of the stresses with respect to the yield surface. It is understood that loose soils have an initial open structure this cause rearrangement of particles when they are frozen (Figure 4.14). This rearrangement is mostly expansive in nature. Upon thawing, the unstable rearrangement undergoes a collapse densifying the soil at the end of the cycle. The current state of the material which is relatively denser than before undergoes lesser change in volume on the subsequent freeze thaw cycle, this process continues until the residual volume is reached. Dense soils on the other hand exhibit a reversal in this

behavior (Figure 4.14). These soils on freezing expand, however on the thaw cycle are unable to recover the initial state, this process continues with an increase in the number of cycles until it reaches the residual volume. The cyclic behavior is seen to be irreversible and is therefore considered to be plastic in nature.

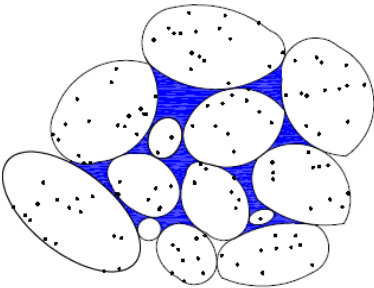
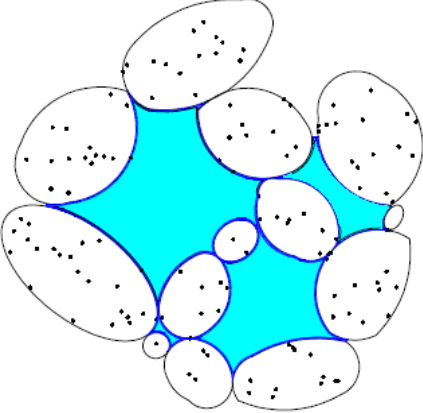
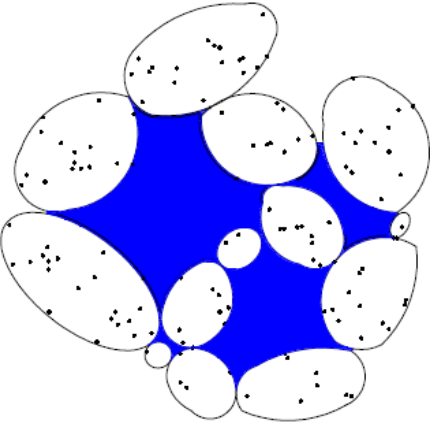
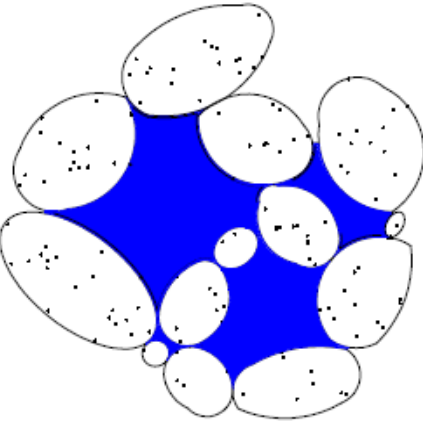
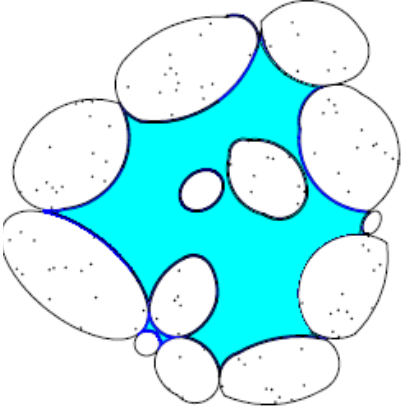
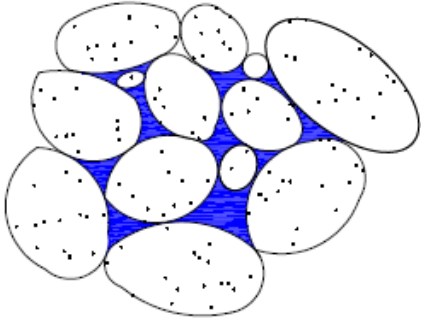
Type of soil	Original state	Frozen state	Thawed state
Dense soils			
Loose soils			

Figure 4.14 Schematic of volumetric changes during freeze-thaw cycle for dense and loose soils

The literature review and experiments conducted in the section 4.2 and section 4.3 reveal the strong correlation between the preconsolidation pressure and the current state of stress. This concept is used to describe the state of soil. The term p/p_0 , defines the ratio of the current mean stress acting on the soil to the current preconsolidation pressure. This ratio describes the openness of the soil structure, a low p/p_0 indicates a dense structure and a high p/p_0 describes a loose soil. As described in Section 2, the preconsolidation pressure at a given cryogenic suction defines the mean stress beyond which the soil behavior is plastic in nature. The variation of this preconsolidation pressure with the cryogenic section defines the yield surface and this curve in suction-mean stress plane forms the LC curve.

When a soil freezes, due to the increase in cryogenic suction the apparent preconsolidation pressure increases based on the LC curve. To account for the plastic strain during the process of freezing the overall size of the yield surface is reduced by moving the LC curve. This reduction in the yield surface induces an expansion which is irrecoverable. When thawing occurs, the cryogenic suction reduces accompanied by an enlargement of the yield surface leading to compressive plastic strains. A schematic of this process is described in Figure 4.15.

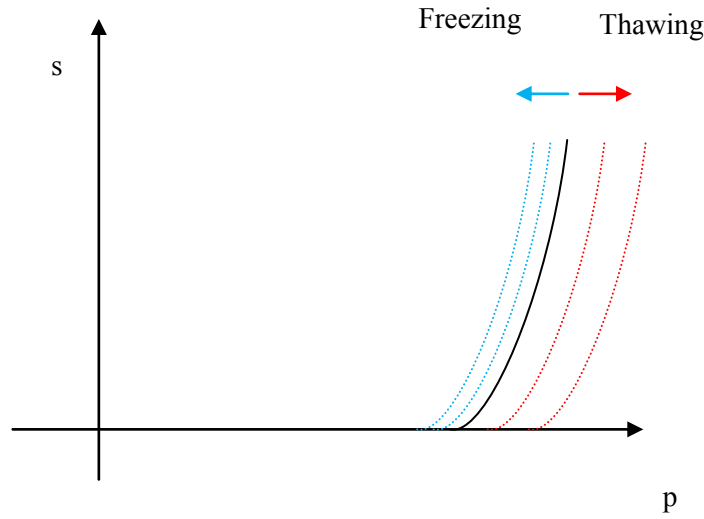


Figure 4.15 Schematic representation LC curves during freezing and thawing

The term $(\dot{\epsilon}_v^p)_{i \rightarrow M}$ which defines the plastic strains due to formation of ice originating from the movement of the yield surface is now incorporated. This plastic strain is related to the expansion/contraction due to formation/melting of the ice using an interaction function defined as

$$f = \frac{(\dot{\epsilon}_v^p)_{i \rightarrow M}}{(\dot{\epsilon}_v)_i} \quad (4.4)$$

The plastic strains which occur on crossing the yield surface are accounted using the flow rule used for the BBM. The process of freezing and thawing and the state of the material interaction functions attain different forms. These interaction functions for the freezing curve is presented in section 4.4.1 and for the thawing curve in 4.4.2.

4.4.1 Freezing interaction curve

During the process of freezing, the water in the soil expands into causing negative (i.e. expansion) elastic volumetric strains. The plastic strains resulting from this are also expansive in nature and therefore is negative. This in turn makes interaction function ' f ' to have a positive value. Figure 4.16 shows the interaction curve during freezing. For a dense soil the freezing starts at point A due to the low value of p/p_0 and moves towards B owing to reduction in density thereby increasing the ratio p/p_0 . Loose soils show a similar behavior starting at point C and moving towards point D. Because dense soils have a tendency to accumulate larger amounts of plastic strain during freezing compared to loose soils the interaction function value at A is larger than at C.

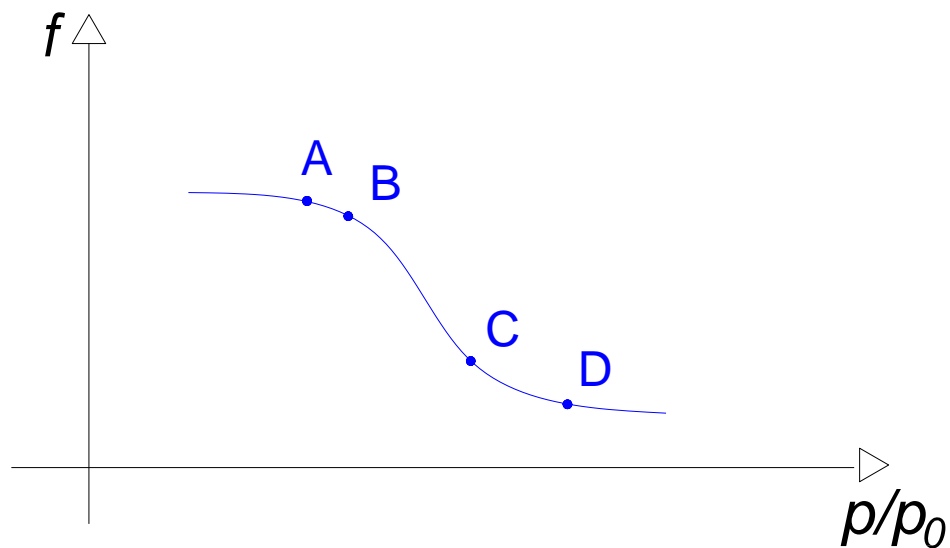


Figure 4.16 Freezing Interaction Function

4.4.2 Thawing interaction curve

The interaction function for the thawing remains positive throughout the process due to positive nature of elastic and plastic contractions brought about during the melting. There is an increase in density during the thaw and therefore there is reduction in the ratio p/p_0 . The amount of plastic strains accumulated for a loose soil is higher than that of a dense soil and the interaction functions follow suit. This difference in behavior compared to freezing requires the thawing curve to be distinct. Figure 4.17 shows the interaction function during the process of thawing. For a loose soil the interaction functions traces the path E-F and for a dense soil the passes through the point G and H.

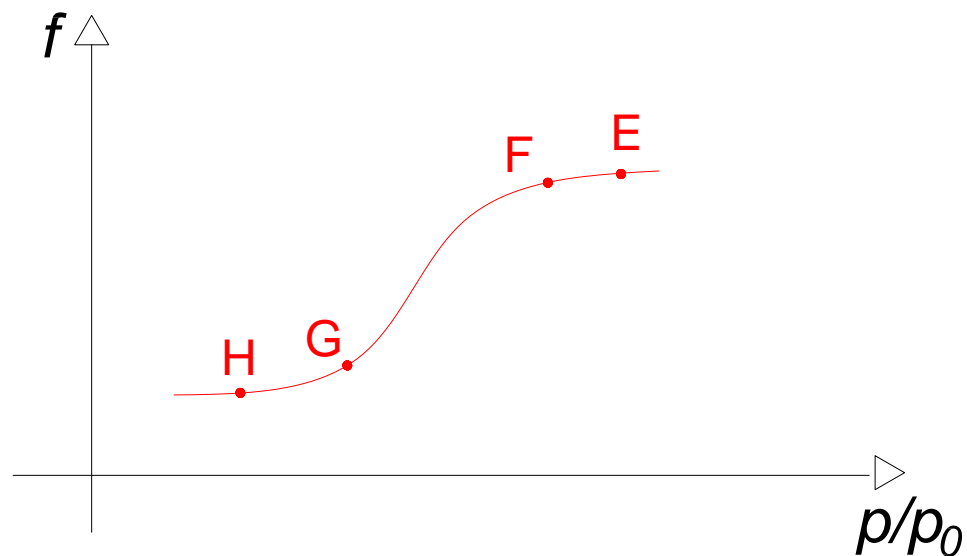


Figure 4.17 Thawing Interaction Function

To capture the complete freeze-thaw behavior the two curves are merged together as shown in Figure 4.18.

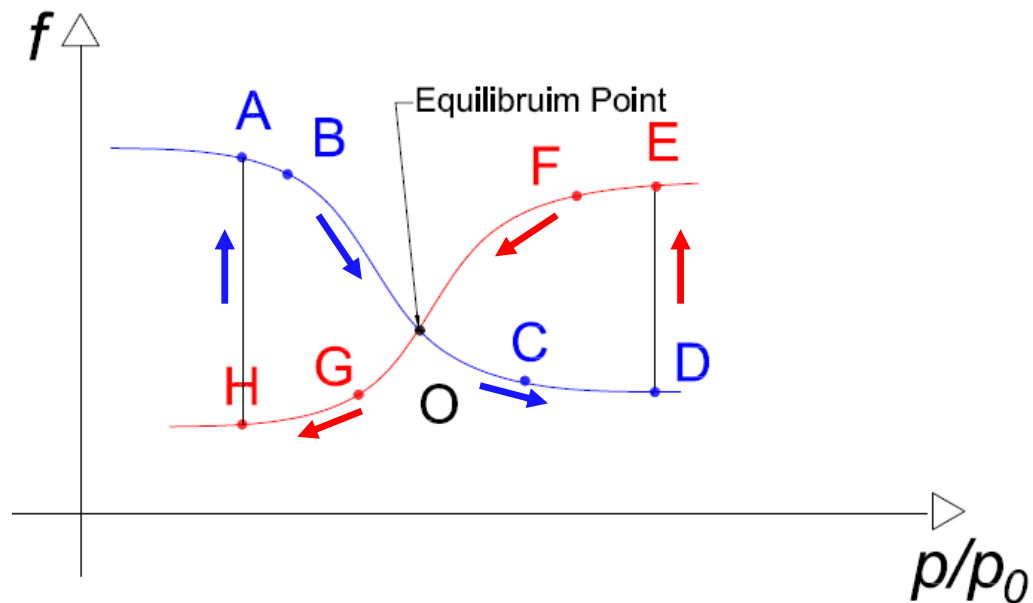


Figure 4.18 Combined freezing and thawing interaction functions

The total amount of plastic strain which occurs during the each freezing process is calculated by summing the plastic strain calculated by tracing the freezing interaction function. A similar procedure is followed to estimate the plastic strain which occur during the thawing. The total amount of plastic strains therefore is the summation of the plastic strains which occur during freezing and thawing. In order to establish the residual state of the material an equilibrium point 'O' is introduced. This point signifies the intersection of the two interaction curves. When the soil reaches a residual state, the amount of negative plastic strains occurring during the freezing would be equal to the amount of positive plastic strain which occur during thawing. The equilibrium point signifies the location around which the summation of these two plastic strains would

result in a net zero plastic strain. It should be noted the interaction diagram may not be unique for a given soil state.

5 BEHAVIOR OF HYDRATE BEARING SEDIMENTS

5.1 INTRODUCTION

In addition to large reserves of petroleum existing in the polar regions of earth there is also an abundance of frozen natural gas in the form methyl-hydrates forming the so called Hydrate Bearing Sediments (HBS). Significant deposits of methane clathrate have also been found under sediments on the ocean floors of Earth (Hoffman, 2006). Methane hydrate, is a solid clathrate compound in which a methane is trapped within a crystal structure of water. Economical extraction of the hydrates from sediments and the construction of the required infrastructure in these regions necessitate a clear understanding of the behavior of frozen soils and the hydrate bearing sediments. These soils pose a unique problem as its behavior is strongly influenced by the constituents present in the pore structure. Phase changes in these constituents are brought by mechanical, hydraulic, thermal and geochemical conditions to which they are subjected to. Hydrate bearing sediments (HBS) are quite common in permafrost regions (e.g. Alaska) and submarine sediments. HBS play a critical role in the evolution of various natural processes in those environments. HBS can become a valuable energy resource as large reserves are expected worldwide (Sloan, 1998; Rutqvist and Moridis, 2007). Figure 5.1 shows the some of the possible sites where gas hydrates were recovered.

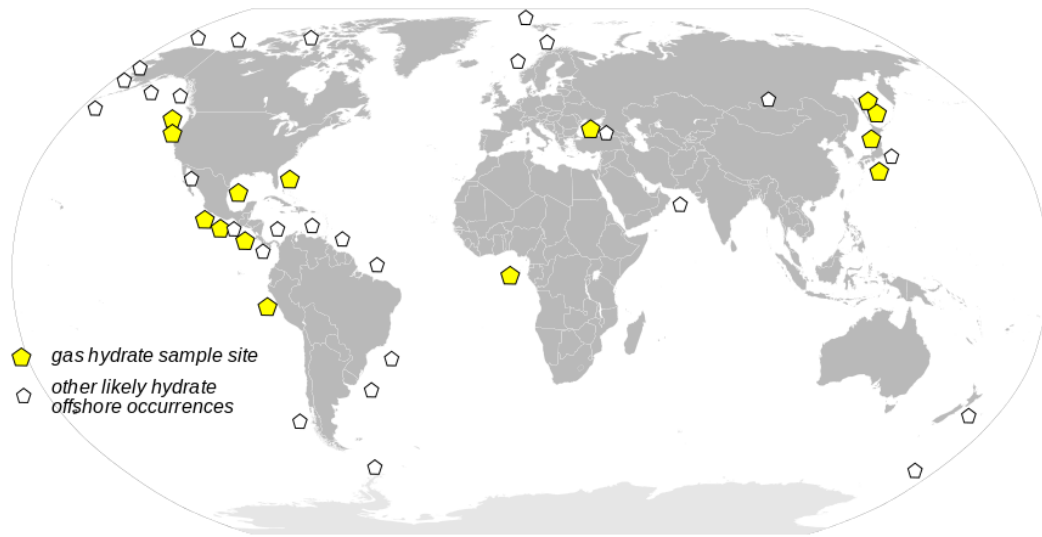


Figure 5.1 Distribution of methane hydrates (Zeimusu, 2008)

Gas hydrates are stable (solid) under certain P-T (Pressure-Temperature) conditions. However, if those conditions change they may dissociate, affecting the behavior of HBS. Hydrate dissociation can be triggered by either increase in temperature (heating), decrease in fluid pressure (depressurization) or changes in pore fluid chemistry (chemical stimulation). Hydrate dissociation is accompanied by very large volume changes. Such pronounced expansion of the pore fluid within the sediment will cause either large fluid flux, if free draining conditions prevail; or high fluid pressure, if the rate of dissociation is faster than the rate of fluid pressure dissipation. In intermediate drainage conditions, the excess pore fluid pressure will depend on the initial volume fraction of the phases, the rate of dissociation relative to the rate of mass transport, heat diffusion, and sediment compliance. In turn, changes in fluid pressure will alter the effective stress, hence the stiffness, strength and dilatancy of the sediment.

Hydrate dissociation can also cause borehole instability, blowouts, foundation failures, and trigger large-scale submarine slope failures (Kayen and Lee, 1991; Jamaluddin et al., 1991; Briaud and Chaouch, 1997; Chatti et al., 2005). The escape of methane into the atmosphere would also exacerbate greenhouse effects and contribute to global warming (Dickens et al., 1997).

The issues discussed above suggest the need of a thorough understanding of the behavior of hydrate bearing sediments and related processes. Unfortunately, the experimental study of hydrate bearing sediments in the laboratory has been hindered by the very low solubility of methane in water and inherent sampling difficulties associated to depressurization and heating during core extraction. Numerical modeling is crucial in order to advance the current understanding of hydrate bearing sediments and to investigate production strategies and their corresponding implications. However, modeling is also affected by the complex behavior of hydrate bearing sediments. The work presented in this section focuses on validating one such previously proposed numerical framework (Sanchez et al., 2014). This validation has been performed with an emphasis on the behavior of HBS during production of the natural gas by techniques such as depressurization, heating and chemical stimulation.

5.2 BACKGROUND

Gas hydrates are solid compounds made of water clustered around low molecular weight gases. All gases can form hydrates under certain pressures and temperatures conditions. Methane hydrates form under condition of high pressure (P) and low temperature (T), common in permafrost settings and in deep marine sediments (>500 m).

Figure 5.2 presents a schematic P-T diagram, with the phase boundaries of the different phases, associated with methane hydrate. The existence of gas hydrates in nature was proven in the 1960s (Makogon, 1965, 1966). Natural gas hydrates are metastable materials, where the formation and dissociation depend on the pressure, temperature, gas composition, water salinity and the characteristics of the porous medium in which they were formed (Makogon, 2010).

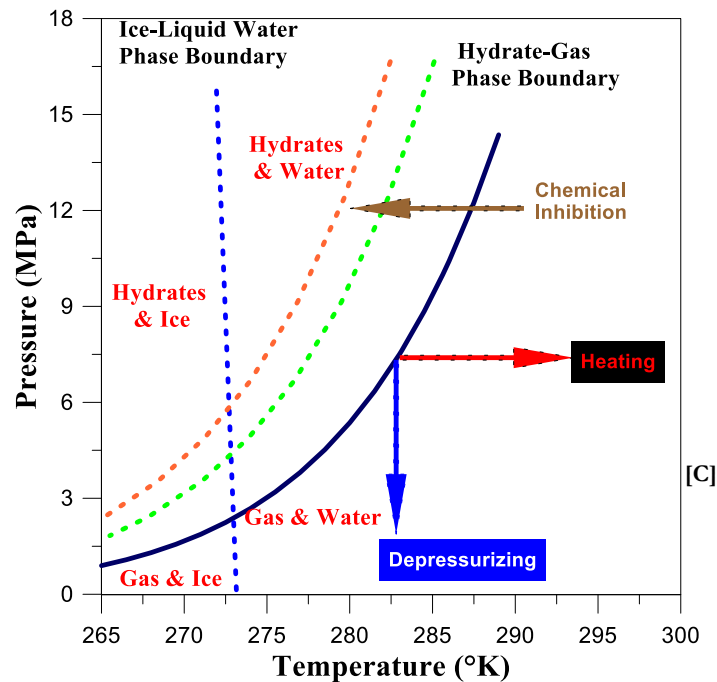


Figure 5.2 Schematic Pressure–Temperature equilibrium curves for methane–water system for hydrate formation

Changes in these conditions may induce hydrate dissociation leading to large volume expansion. Methane hydrate-bearing sediments (HBS) may destabilize spontaneously as part of geological processes, unavoidably during petroleum drilling/production operations (e.g. Briaud and Chaouch, 1997), or intentionally as part

of gas extraction from the hydrate itself (e.g. Briaud and Chaouch, 1997; and Rutqvist and Moridis, 2007).

Despite the widespread recognition of the relevance of naturally occurring gas hydrates, the understanding of key aspects associated with the behavior of HBS still remains indistinct. The response of HBS is highly complex and dependent on thermo, hydraulic and geo-chemical coupled interactions. Furthermore, HBS behavior is also affected (amongst others) by, sediment type, stress level, gas hydrate morphology and sediment history. Significant volume changes are anticipated during hydrate dissociation/formation. Those changes are basically controlled by the mechanical stability of the soil structure hosting the hydrate. Changes in porosity strongly affect the formation permeability, fluids flow (both gas and water) and the heat transfer. The intrinsic coupled nature of this problem, between the different physics and phenomena underlying HBS behavior is evident. A reliable prediction of stresses is also required for a reliable assessment of (amongst others) borehole stability and sediment integrity.

A comprehensive review on HBS properties and behavior can be found in Soga et al. (2006) and Waite et al. (2009). In particular, good correlations relating the poro-elastic properties of the sediments with its composition can be found in Waite et al. (2009). Some aspects related to HBS are summarized below.

5.2.1 Morphology of gas hydrate

The morphology of gas hydrate in sediments has a strong impact on sediment behavior. The morphology is controlled by a number of factors, including: gas availability during hydrate formation (i.e. free or dissolved gas); sediment type; size of

soil grains; porosity; hydrate concentration; and geological history (Waite et al., 2009). Some of these are discussed below.

The hydrate in a pore space can be in one of the following forms (Waite et al., 2009)

- Pore filling (i.e. in the pore space without bridging two or more particles);
- Load bearing (i.e. contributing to the mechanical stability);
- Bonding material (i.e. cementing particles at their contact points).

Figure 5.3 illustrates those three forms. The last one (i.e. cementing) is characterized by its strong influence on the HBS geomechanical behavior, even at relatively low hydrate saturation ' S_h ' (i.e. $S_h = \text{hydrate_vol}/\text{voids_vol}$).

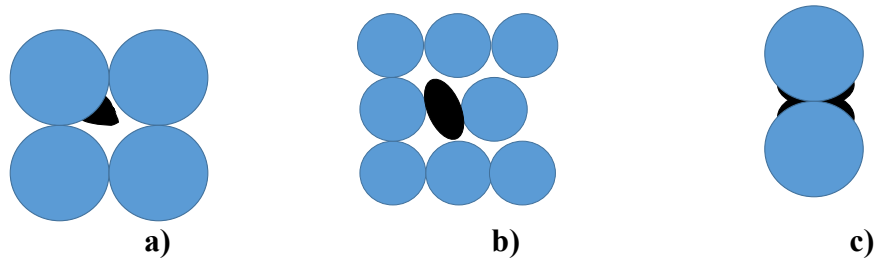


Figure 5.3 Hydrate habit in the pore space a) Pore filling b) Load bearing and c) Bonding material (Waite et al., 2009)

The formations discussed above may occur either in a natural environment or can be reconstituted in the laboratory. Studies conducted on these samples are discussed below.

Gas hydrate reservoirs in natural environment

In nature, hydrates are typically found in three general types of reservoirs (Collett et al., 2008; Waite et al., 2009): i) coarse-grained, ii) fine-grained, and iii) fracture-dominated. Coarse-grained reservoirs tend to develop gas hydrate that is present as disseminated, pore-filling, material.

In fine-grained marine sediments the occurrence of gas hydrate is associated with sub-vertical lenses (veins) or nodule-type occurrence. The formation of hydrates near fractures/fault (i.e. iii) takes place in the presence of free gas; while the hydrate formation in sediments (i.e. i and ii) is associated with dissolved aqueous phase methane (Waite et al., 2009). Undisturbed natural samples would be the ideal source to learn about the geomechanical behavior of natural HBS, however it has been hindered by inherent sampling difficulties associated with depressurization and heating during core extraction (i.e. limited testing of natural specimens). The triaxial tests performed by Masui et al. (2008), on sandy drilled cores (retrieved from mud and sand alternations), is one of the few experimental data that can be found in the open literature associated with the behavior of natural HBS.

Reconstituted/synthetic samples

Mechanical tests on reconstituted/synthetic samples of methane hydrate are limited to coarse-grained (sandy) samples (e.g. Hyodo et al., 2005; 2008; Masui et al., 2008; Yoneda et al., 2010). The preparation of reconstituted samples in the lab is

challenging due to the methane low solubility in water. The solubility is important because it controls the hydrate morphology. Four experimental techniques are typically used to reconstitute the hydrate samples in the laboratory. They are discussed in detail in Waite et al. (2009), and associated references. Some of these methodologies are discussed below

- Dissolved gas method: Water saturated with a hydrate-forming gas is circulated through the sediment at a pressure and temperature within the hydrate stability zone. This method is characterized by the long induction times, and by the fact that the hydrates growth rate tends to be limited by the concentration of hydrate former in the water. With this technique saturation S_h are generally below 60% (Waite et al., 2009).
- Partial water saturation method: grains are mixed with limited water and packed in a cell to form partially water-saturated sediment. Afterwards, the system is pressurized with methane gas and cooled into the stability field to promote hydrate formation. This technique tends to favor the presence of hydrates at contacts between the grains (Waite et al., 2009).
- The ice-seeding method: cooled grains are mixed with small ice grains. The mixture is pressurized into the hydrate stability field with methane. The pressure and temperature are then slowly changed to approach the boundary of hydrate stability (Waite et al., 2009).
- Spraying method: granular methane hydrate is prepared by spraying misted water in a pure methane gas atmosphere under phase-equilibrium conditions (Hyodo et

al., 2005; Waite et al., 2009) or by melting small ice particles in the presence of methane at high pressure (Stern, et al., 1998; Waite et al., 2009). The last three laboratory techniques are used with unconsolidated sands.

5.2.2 Behavior of HBS

Physical properties and behavior of HBS strongly depends on thermodynamic conditions. During hydrate dissociation several simultaneous coupled THMC phenomena occur. For instance, during thermal stimulation (or depressurization, or chemical stimulation) the hydrate conditions will shift to the unstable region leading to hydrate dissociation. High fluid pressure will develop due to the large volume expansion that takes place during dissociation. Gas and liquid flows are anticipated due to fluids pressure gradients. In turn, fluids pressure changes will alter the sediment effective stresses, impacting on the mechanical behavior of the sediment. Perturbations in the effective stress and strain fields will induce changes in the sediment porosity. The pore space will also be affected by the loss of solid (crystalline gas) during dissociation. Those changes in porosity will strongly affect sediment permeability, impacting on the mass transfer of both: gas and water. Furthermore, hydrate dissociation is an endothermic (self-limiting) process that strongly affects the thermal field. Most of the sediments physical properties (e.g. fluids density, viscosity) depend on temperature, so significant couplings can also be anticipated due to the variation in the thermal field. Just some of couplings between the main THMC processes that take place during hydrate dissociation/formation have been highlighted here.

Thermally controlled dissociation of methane hydrates has been recognized as a suitable methodology for releasing gas from hydrate-bearing sediments, especially for lithologically isolated deposits without mobile gas or water phases (e.g. Rutqvist and Moridis, 2007). Depressurization is another possible production technique e.g. (Rutqvist and Moridis, 2007, Makogon, 2010). Inhibitors (such as salts, alcohols, methanol and glycols) can be used to shift the equilibrium conditions by lowering the temperature and increasing the threshold pressure of the hydrates. Figure 5.2 shows, in black boxes, the three main processes that may destabilize hydrate and induce its dissociation: depressurization, heating and chemical stimulation.

Masui et al. (2008) carried tests at different saturation S_h on natural (sandy cores) and reconstituted samples. The samples were also tested without hydrate ($S_h=0$) at the same density. Figures 3 a) and b) present the results for two hydrate saturations ($S_h =7$ and 37%) only; alongside the experimental results from samples without hydrates (more result are presented in Masui et al., 2008). It is evident that the hydrate concentration has a significant impact on strength and sediment dilatancy.

Triaxial tests on synthetic (Yoneda et al., 2010): in those tests on sandy samples the presence of hydrate also affects the mechanical behavior of the soil, but its influence is less important, even at quite high S_h ($\approx 54\%$). Similar tests were performed before by Hyodo et al. (2005; 2008), with similar results. Analogue hydrates samples (Yun et al., 2007): mechanical properties of samples prepared from Tetrahydrofuran (THF) were tested in a triaxial chamber. Samples from sand, kaolin and silts were

prepared at different hydrate saturations. It was observed that the presence of hydrate increases the stiffness, strength and the dilatancy of the material.

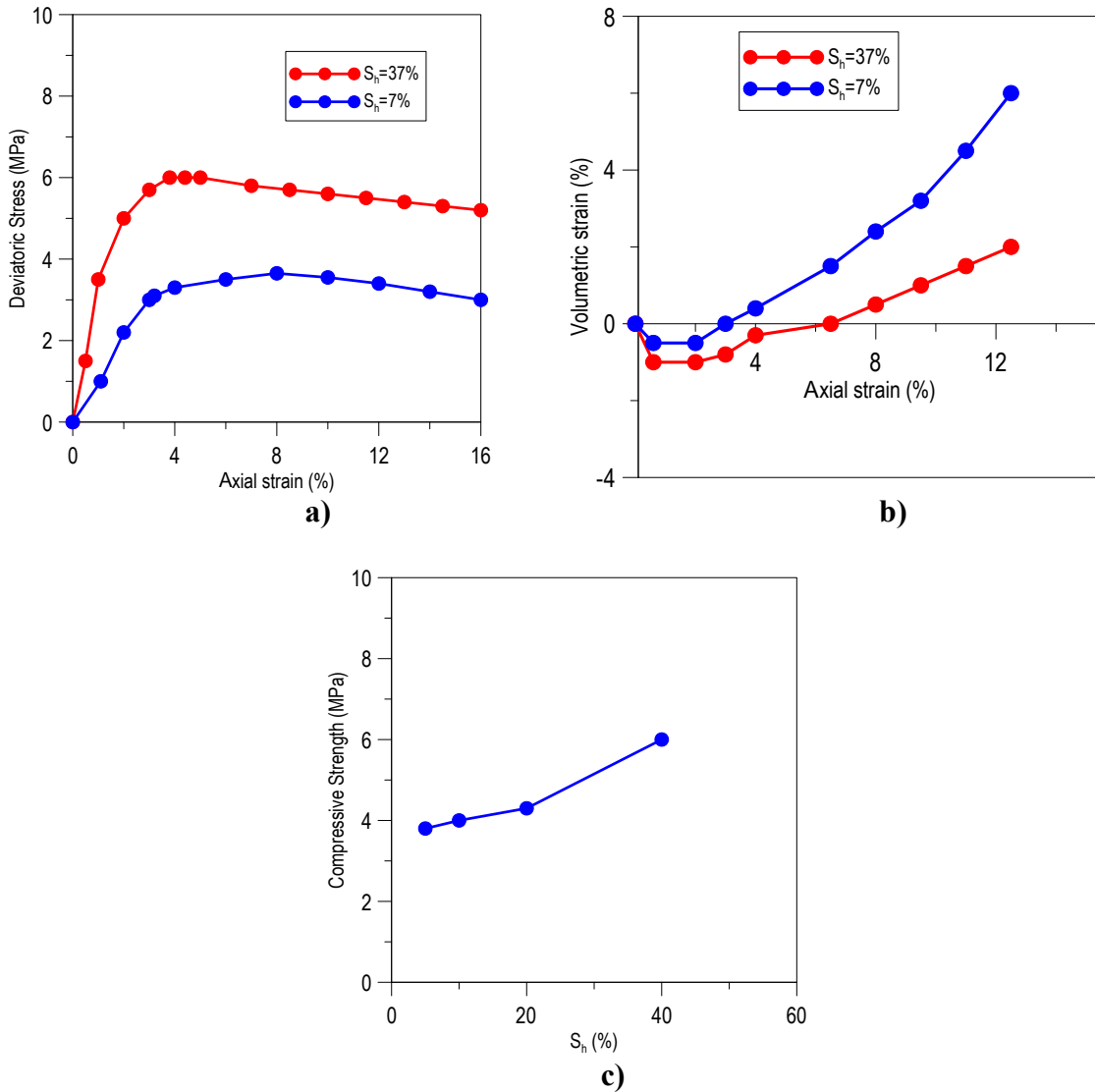


Figure 5.4 Triaxial tests conducted on HBS of different hydrate concentration a) Deviatoric stress q vs. axial strain (e_a) b) Volumetric strain vs. axial strain c) Compressive strength vs. hydrate concentration (Masui et al., 2008)

The limited experimental data associated with the mechanical behavior of HBS has been perhaps the main reason that has hindered the development of more realistic geomechanical models to describe their response. There are a number of contributions related to the geomechanical behavior of coarse-grained (sandy) sediments (e.g. Hyodo et al., 2005; 2008; Masui et al., 2008; Yoneda et al., 2010).

From above, it is evident that a reliable prediction of HBS response requires a very good understanding of its behavior and an advanced framework able to incorporate the most relevant THMC phenomena and the mutual interactions that take place during hydrate dissociation/formation. A crucial component of this framework is the mechanical model. Because it is the one that links the changes in loading conditions, fluids pressures and temperature with stress increments and deformations. In spite of its relevance, the geomechanical behavior of HBS is the one that has received (comparatively) less attention in the last few years and the one that requires further experimental investigation and modeling developments.

5.3 CONSTITUTIVE MODELING OF HBS

Several partial formulations have been developed to explore various aspects of hydrate formation and dissociation within well-defined boundary conditions (Rempel and Buffett 1997, 1998; Xu and Ruppel 1999; Davie and Buffett, 2001; Ahmadi et al., 2004; Sultan et al., 2004; Xu and Germanovich 2006; Nazridoust and Ahmadi 2007; Kwon et al., 2008). In these models, the sediment response is disregarded or handled with simple models (e.g., non-deformable rigid porous medium is assumed in Nazridoust and Ahmadi 2007, an elastic porous medium in Kwon et al., 2008; and a non-linear 1D

compression law in Garg et al., 2008). HM coupled isothermal models with more appropriate (mechanical) sediment representation include developments by Klar et al. (2010). Chemo-thermo-mechanical analyses related to ground deformation and gas production is presented in Kimoto et al. (2007, 2010). The chemical reactions considered by them are limited to gas dissociation (i.e. no dissolve salts or other chemical species are considered), no ice formation/thaw was included in those analysis. Rutqvist and Moridis (2007) and Rutqvist (2011) presented a more general THMC approach by linking (sequentially) a geomechanical code (FALC^{3D}) with a multiphase fluid and heat transport simulator TOUGHT. Our coupled THCM formulation is developed to explore gas production, rather than long-term geological formation (as in Xu and Ruppel 1999; Davie and Buffett, 2001; Garg et al., 2008).

The model mentioned above were not truly coupled THCM processes but a sequential explicit computational schemes that resolve the hydrate state separate from the sediment state at every time step (as e.g. in Rutqvist and Moridis, 2007). Sequential schemes often restrict computations to one-way coupled analysis where one can investigate, for example, the effects that changes in pressure and temperature have on the sediment mechanical response but does not account for the effect of granular strains on multiphase flow behavior.

Sanchez et al., 2014 proposed mathematical framework to analyze coupled processes that develop in hydrate bearing sediments in response to imposed changes in boundary conditions. The manuscript starts with a brief description of the formulation, including the extensive set of new constitutive equations required for the fully coupled

formulation. The approach considered hydrate dissociation with a time independent kinetic law and potential secondary hydrate and ice formation, and potential sediment failure. A brief summary of this model has been presented here.

Phases and Species – Mass densities

The pores in the granular skeleton of the hydrate bearing sediments are filled with gas, hydrate, water or ice (Figure 5.5a). The three main species mineral, water, and methane are found in five phases: solid mineral particles, liquid, gas, hydrates and ice as shown in the phase diagram Figure 5.5 b.

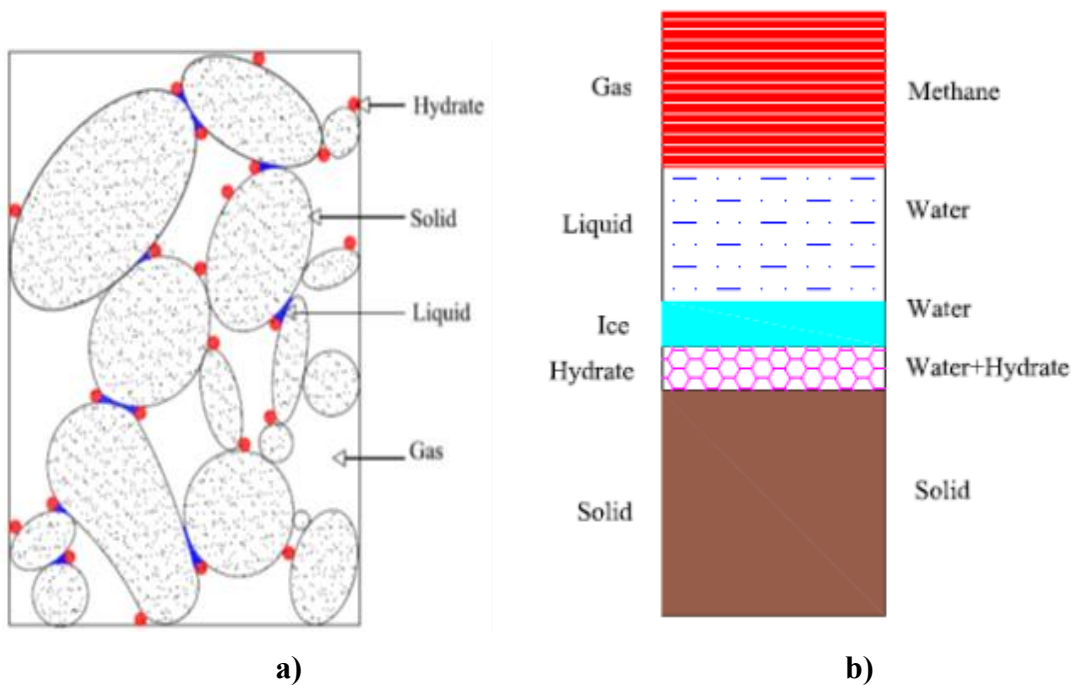


Figure 5.5 Structure of HBS a) Granular structure b) Phase diagram

These solid and the ice phases are considered single species the solid phase is made of the mineral that forms the grains, and ice is made of pure water. Their densities

are assumed constant. The hydrate phase is made of water and methane, and is assumed to be of constant density. The mass fraction of water in hydrate $\alpha=m_w/m_h$ depends on the hydration number χ for methane hydrates $CH_4\chi H_2O$. The liquid phase is made of water and dissolved gas. In the absence of hydrates, the solubility of methane in water increases with pressure and decreases with temperature and salt concentration. The opposite is true in the presence of hydrates: the solubility of CH_4 in water increases with increasing temperature and decreases with increasing pressure (Sun and Duan, 2007). In both cases, the solubility of methane in water is very low; for example, at pressure $P_\ell=10$ MPa and temperature $T=280^\circ K$, the mass fraction of methane in water is $m_m/m_w\sim 1.4\times 10^{-3}$.

The mass density of the liquid ρ_ℓ depends on temperature T [$^\circ K$] and pressure P_ℓ [MPa]. The asymptotic solution for small volumetric changes is:

$$\rho_\ell = \rho_{\ell_0} \left(1 + \frac{P_\ell}{B_\ell} \right) \left[1 - \beta_{T\ell} \left(\frac{T - 277^\circ K}{5.6} \right)^2 \right] \quad (5.1)$$

where, $\rho_{\ell_0}=0.9998 \text{ g/m}^3$ is the mass density of water at atmospheric pressure and at $T=277^\circ K$, $B_\ell=2000 \text{ MPa}$ is the bulk stiffness of water, and $\beta_{T\ell}=0.0002^\circ K^{-1}$ is the thermal expansion coefficient. This equation properly captures the thermal expansion water experiences below and above $T=277^\circ K$. All the liquid water is assumed to transform into ice at freezing temperature.

The gas phase consists of pure methane gas. The presence of water vapor in gas can be computed using the psychrometric law, to conclude that the mass fraction of water vapor in gas is very small; for example: $m_w/m_g\approx 10^{-6}$ for a gas pressure of

$P_g=10\text{MPa}$, capillary pressure $P_c=0.1\text{MPa}$, and temperature $T=280^\circ\text{K}$. Therefore, its contribution to the mass density of the gas phase and to short-duration mass transport processes is disregarded. The mass density of the gas phase is pressure P_g [MPa] and temperature T [$^\circ\text{K}$] dependent and it can be estimated using the ideal gas law. Experimental data in Younglove and Ely (1987) is used to modify the ideal gas law for methane gas in the range of interest (fitted range: $270^\circ\text{K}<T<290^\circ\text{K}$ and $0.1\text{MPa}<P_g<40\text{MPa}$):

$$\rho_g = \frac{M_m P_g}{R T} \left[1176 + 12.7 \frac{P_g}{1\text{MPa}} - 0.45 \left(\frac{P_g}{1\text{MPa}} \right)^2 \right] \quad (5.2)$$

Where, the gas constant $R=8.314$ J/(mol $^\circ\text{K}$) and the molecular mass of methane $M_m=16.042$ g/mol (example: $\rho_g=86$ g/m 3 at $T=280^\circ\text{K}$ and $P_g=10\text{MPa}$).

Volumetric relations

The total volume V_{total} is the sum of the partial volume of each β -phase V_β , where the sub-index β is one of [s, ℓ , g, h, i] for solid, liquid, gas, hydrate or ice phases, $V_{\text{total}} = \sum V_\beta$. Assuming that the solid mineral is a non-reactive phase, the total porosity is defined as the ratio of the volume of voids $V_v=1-V_s$ to the total volume V_{total} ,

$$\phi = \frac{V_v}{V_{\text{total}}} = \frac{V_g + V_\ell + V_h + V_i}{V_{\text{total}}} \quad (5.3)$$

The volume of voids V_v is occupied by the liquid, gas, hydrate and ice phases; the associated volume fractions are $S_\beta=V_\beta/V_v$ and the following volumetric restriction applies

$$S_\ell + S_g + S_h + S_i = 1 \quad (5.4)$$

Mass balance

The macroscopic balance of either mass or energy relates the rate of change per unit volume to the flux in-and-out of the volume, and takes into consideration external inputs as well. Mass balance equations are written for the three species: water w , methane m , and for the mineral M that makes the particles (no letter is required because it coincides with the solid). The mass flux in balance equations includes advective transport by the fluid and the movement of the sediment relative to a fixed reference frame. The proposed framework can also accommodate non-advective diffusive transport of species in the phases (i.e. w in g , and m in l) as discussed in Olivella et al. (1994). However, they are not included below, with the exception of the non advective solute flow (9). ‘Fickian diffusive flows’ are generally overwhelmed by advective transport in the short time scales during production.

The mass of water per unit volume of the porous medium combines the mass of water in the liquid, hydrate and ice phases. The water flux associated to the liquid, hydrate and ice phases with respect to a fixed reference system combines Darcian flow with respect to the solid phase \mathbf{q}_ℓ [m/s] and the motion of the whole sediment with velocity \mathbf{v} [m/s] relative to the fixed reference system. Then, the water mass balance can be expressed as:

$$\frac{\partial}{\partial t} \left[\underbrace{(\rho_\ell S_\ell + \alpha \rho_h S_h + \rho_i S_i)}_{\text{mass water per unit volume}} \phi \right] + \nabla \cdot \left[\underbrace{\rho_\ell \mathbf{q}_\ell + \rho_\ell S_\ell \phi \mathbf{v}}_{\text{w in liquid}} + \underbrace{\alpha \rho_h S_h \phi \mathbf{v}}_{\text{w in hydrate}} + \underbrace{\rho_i S_i \phi \mathbf{v}}_{\text{w in ice}} \right] = f^w \quad (5.5)$$

where, ρ [g/m^3] represents the mass density of phases and α is the mass fraction of water in hydrate. The external water mass supply per unit volume of the medium f^w [$\text{g}/(\text{m}^3\text{s})$] is typically $f^w=0$; however, the general form of the equation is needed to model processes such as water injection at higher temperature as part of the production strategy.

Similarly the total mass of methane per unit volume of the hydrate bearing sediment is computed by adding the mass of methane per unit volume of the gas and hydrate phases taking into consideration the volume fractions S_g and S_h , the mass fraction of methane in hydrate $(1-\alpha)$, and the porosity of the porous medium ϕ . As in the case of water balance, the flux of methane in each phase combines advective terms relative to the porous matrix and the motion of the porous medium with velocity \mathbf{v} [m/s] relative to the fixed reference system:

$$\frac{\partial}{\partial t} \left\{ \underbrace{[\rho_g S_g + (1-\alpha)\rho_h S_h]}_{\text{mass of methane per unit volume}} \phi \right\} + \nabla \cdot \left[\underbrace{\rho_g \mathbf{q}_g + \rho_g S_g \phi \mathbf{v}}_{\text{m in gas}} + \underbrace{(1-\alpha)\rho_h S_h \phi \mathbf{v}}_{\text{m in hydrate}} \right] = f^m \quad (5.6)$$

In this case, f^m [$\text{g}/(\text{m}^3\text{s})$] is an external supply of methane, expressed in terms of mass of methane per unit volume of the porous medium. Typically, $f^m=0$; however, the general expression may be used to capture conditions such as methane input along a pre-existing fault. The first term takes into consideration the methane mass exchange between the hydrate phase and the gas phase during hydrate formation-dissociation.

The mineral species is only found in the solid particles whose mass balance is given by

$$\frac{\partial}{\partial t} \underbrace{[\rho_s (1-\phi)]}_{\substack{\text{mass mineral} \\ \text{per unit volume}}} + \nabla \cdot \underbrace{[\rho_s (1-\phi) \mathbf{v}]}_{\text{m in solid}} = 0 \quad (5.7)$$

where ρ_s [g/m³] is the mass density of the mineral that makes the solid particles.

Energy balance

The energy balance equation is expressed in terms of internal energy per unit volume [J/m³], presuming that all phases are at the same temperature and in equilibrium.

In the absence of fluxes, the total energy per unit volume of the medium is

$$\frac{E}{V_{\text{total}}} = e_s \rho_s (1-\phi) + (e_\ell \rho_\ell S_\ell + e_g \rho_g S_g + e_h \rho_h S_h + e_i \rho_i S_i) \phi \quad (5.8)$$

where, e [J/g] represents the specific internal energy per unit mass of each phase. These values are computed using the specific heat of the phases c [J/(g.K)] and the local temperature T relative to a reference temperature $T_o=273^\circ\text{K}$. The selected reference temperature does not affect the calculation: the system is presumed to start at equilibrium, and energy balance is tracked in terms of “energy changes” from the initial condition. The formulation inherently captures energy changes during endothermic or exothermic processes through specific internal energies and the corresponding changes in volume fractions S_ℓ , S_g , S_h and S_i .

Momentum balance

In the absence of inertial forces, i.e., quasi-static problems, the balance of momentum for the porous medium is the equilibrium equation in terms of total stresses:

$$\nabla \cdot \boldsymbol{\sigma} + \mathbf{b} = 0 \quad (5.9)$$

where, $\boldsymbol{\sigma}_t$ [N/m²] is the total stress tensor and \mathbf{b} [N/m³] the vector of body forces. The constitutive equations for the hydrate bearing sediment permit rewriting the equilibrium equation in terms of the solid velocities, fluid pressures and temperatures.

Constitutive equations

The governing equations are finally written in terms of the unknowns when constitutive equations that relate unknowns to dependent variables are substituted in the balance equations. Note that constitutive equations capture the coupling among the various phenomena considered in the formulation. Given the complexity of the problem, simple yet robust constitutive laws are selected for this simulation.

The linear Fourier's law is assumed between the heat flow \mathbf{i}_c [W/m²] and thermal gradient. For three dimensional flow conditions and isotropic thermal conductivity,

$$\mathbf{i}_c = -\lambda_{\text{hbs}} \nabla T \quad (5.10)$$

where, λ_{hbs} [W/(m.K)] is the thermal conductivity of the hydrate bearing sediment. A non-linear volume average model is selected to track the evolution of λ_{hbs} during the simulation,

$$\lambda_{\text{hbs}} = \left[(1-\phi)\lambda_s^\beta + \phi(S_h\lambda_h^\beta + S_i\lambda_i^\beta + S_g\lambda_g^\beta + S_\ell\lambda_\ell^\beta) \right]^{1/\beta} \quad (5.11)$$

The parallel model corresponds to $\beta=1$ and the series model to $\beta=-1$. The advective flux of the liquid and the gas phases q_ℓ and q_g [m/s] are computed using the generalized Darcy's law in three-dimensions (Gens and Olivella, 2001):

$$\mathbf{q}_\alpha = -\mathbf{K}_\alpha (\nabla P_\alpha - \rho_\alpha \mathbf{g}) \quad \alpha = \ell, g \quad (5.12)$$

where, P_α is the phase pressure, and the vector \mathbf{g} is the scalar gravity $g=9.8 \text{ m/s}^2$ times the vector $[0,0,1]^T$. The second term in parenthesis captures the change in elevation in the vertical direction; the negative sign results from assuming that the vertical axis increases upwards.

The tensor \mathbf{K}_α captures the medium permeability for the α -phase in three-dimensional flow; if the medium is isotropic, \mathbf{K}_α is the scalar permeability K_α times the identity matrix. The permeability \mathbf{K}_α depends on the intrinsic permeability \mathbf{k} of the medium, the dynamic viscosity of the α -phase μ_α and the relative permeability $k_{r\alpha}$

$$\mathbf{K}_\alpha = \mathbf{k} \frac{k_{r\alpha}}{\mu_\alpha} \quad (5.13)$$

The viscosity of the liquid μ_ℓ phase varies with temperature T [$^\circ\text{K}$] (i.e. Olivella, 1994):

$$\mu_\ell [\text{Pa.s}] = 2.1 \cdot 10^{-6} \exp\left(\frac{1808.5 \text{ } ^\circ\text{K}}{T}\right) \quad (5.14)$$

While the viscosity of gases is often assumed independent of pressure, experimental data in the wide pressure range of interest shows otherwise. A pressure and temperature dependent expression for the viscosity of methane gas.

$$\mu_g [\text{Pa.s}] = 10.3 \cdot 10^{-6} \left[1 + 0.053 \frac{P_g}{\text{MPa}} \left(\frac{280 \text{ } ^\circ\text{K}}{T} \right)^3 \right] \quad (5.15)$$

The intrinsic permeability of the hydrate-bearing medium k with hydrate saturation S_h and porosity ϕ is estimated from the intrinsic permeability in the medium without hydrates k_o determined at porosity ϕ_o (Minagawa et al., 2008):

$$k = k_0 \frac{\phi^3}{(1-\phi)^2} \frac{(1-\phi_0)^2}{\phi_0^3} (1-S_h - S_i) \quad (5.16)$$

The relative permeabilities for liquid $k_{r\ell}$ and gas k_{rg} increase as the degree of saturation of each phase increases with respect to the mobile phase saturation $S_\ell + S_g$. A single parameter power function properly reproduces experimental data

$$k_{r\ell} = \left(\frac{S_\ell}{S_\ell + S_g} \right)^a = (S_\ell^*)^a \quad (5.17)$$

$$k_{rg} = \left(1 - \frac{S_\ell}{S_\ell + S_g} \right)^b = (1 - S_\ell^*)^b \quad (5.18)$$

where, $S_\ell^* = S_\ell / (S_\ell + S_g)$ is the effective liquid saturation in the hydrate bearing sediment.

The interfacial tension between liquid and gas sustains the difference between the liquid and gas pressures P_ℓ and P_g . The capillary pressure is defined as $P_c = P_g - P_\ell$. In a porous network, the capillary pressure and the effective liquid saturation S_ℓ^* are related (van Genuchten, 1978):

$$S_\ell^* = \frac{S_\ell}{S_\ell + S_g} = \left[1 + \left(\frac{P_c}{P_o} \right)^{\frac{1}{1-\lambda}} \right]^{-\lambda} \quad (5.19)$$

The variation in the compressive strength of the HBS is shown in Figure 5.4. It can be clear seen that the soil strength increase with an increase in hydrate concentration. The behavior seen in these samples indicate that the hydrate is providing a cementation to the soil grains and enhancing the mechanical properties.

To reproduce the effects of hydrate cementation on the behavior of the sediments a formulation is proposed here, analogous to the model proposed by Pinyol et al. (2007). The framework (Pinyol et al., 2007) was used to simulate the weathering effects on soft clayey rocks utilizing a damage function to describe changes in stiffness and strength during weathering process. The degradation of bonding effects was included to represent damage to bond encountered during irreversible plastic deformation. The applied external stresses on the soil are partitioned as soil grain stress and bond stress based on the damage parameter. The bond behavior was elastic and the Barcelona Basic Model (BBM) was utilized as the yield surface for the soil grains.

This concept is extended to the HBS by distinguishing the phases as solid matrix comprising of the soil grains and the void space saturated with water and the hydrate phase. The model assumes that the soil matrix cannot deform and all the deformation observed is a combination of the deformation of the saturated void space and the hydrates. The combined volumes of these two phases are characterized as the fictitious macropore space and comprise of the volume excluding the soil particles. The strain in the soil due to the change in concentration of the hydrates can be simplified as

$$\frac{\Delta V_H}{V} = C_H \varepsilon_{vol}^H \quad (5.20)$$

where, C_H is the volumetric content of hydrates in the pore space, V is the total volume and V_H is the volume of hydrates. The hydrate concentration C_H is seen to be analogous to damage coefficient proposed in Pinyol et al. 2007. The total strain ε^{ext} in

the soil described as the combination of strains occurring in the hydrates and voids given as

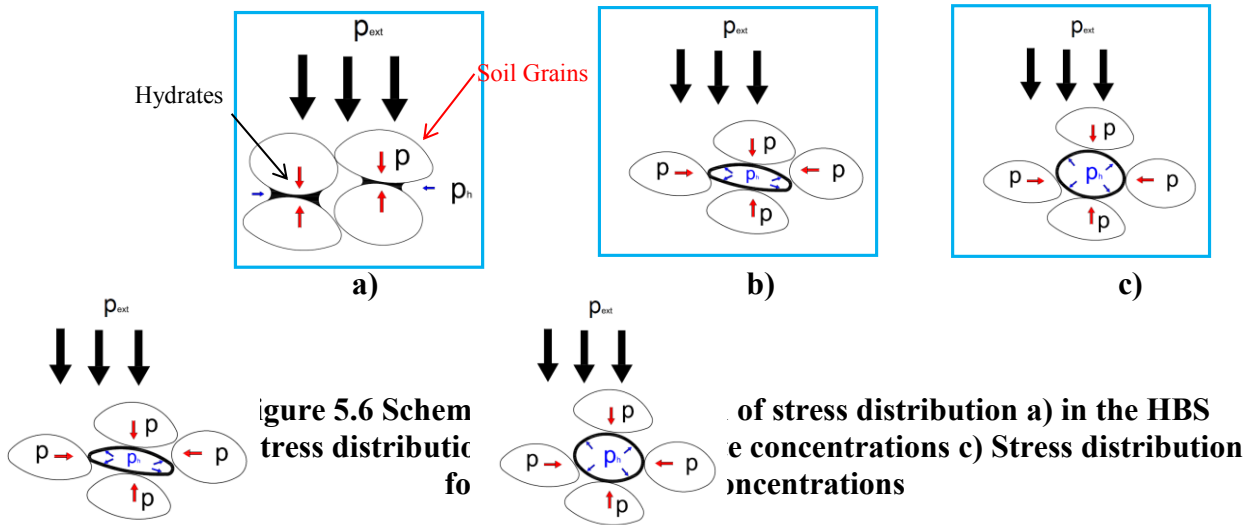
$$\varepsilon^{ext} = \varepsilon^S + C_H \varepsilon^H \quad (5.21)$$

The stresses in the system are now estimated using the principle of virtual work. A schematic of the stress redistribution between the hydrates and the soil grains is shown in Figure 5.6 a) through Figure 5.6 c).

The schematic shows external stress (p^{ext}) is applied on the HBS (Figure 5.6 a). A greater amount of stress is taken by the soil grain (Figure 5.6 b) when the concentration of the hydrates is lower while a smaller amount of stress is taken by the soil grain with low hydrate concentrations (Figure 5.6 c). This redistribution assumes the general form

$$p^{ext} = p + \left(\frac{C_H \chi}{1 + C_H \chi} \right) p^H \quad (5.22)$$

The hydrates and sediments can be modeled by using different constitute model for describing the behavior. In the initial effort the both the hydrates and the sediments were modeled elastically.



Phase boundaries - reaction kinetics

Pressure and temperature defined the phase boundary for methane hydrate and ice. The selected expression for the phase boundary of methane hydrate follows the format in Sloan and Koh (2008).

$$P_{eq-mh} [\text{kPa}] = e^{\left(40.234 - \frac{8860}{T_{eq} [^{\circ}\text{K}]}\right)} \quad (5.23)$$

The phase boundary for the ice-water transition exhibits low sensitivity to pressure. For the most common I_h ice phase, the linear fit for the pressure range between 0 MPa and 20 MPa is (based on the equation provided by Wagner et al. (2002))

$$P_{eq-ice} [\text{MPa}] = 13.0(273.16 - T [^{\circ}\text{K}]) \quad (5.24)$$

There are four distinct regions that emerge on the pressure-temperature PT-space when the hydrate stability and the ice-water boundaries are superimposed, as shown in

Figure 5.2. The presence of free gas, water, ice and hydrate in each quadrant depends on the relative mass of water and gas, and the PT trajectory. Note that the ice+gas condition $I+G$ in the c-quadrant is assumed to remain $I+G$ upon pressurization into the d-quadrant because of limited solid-gas interaction in the absence of beneficial energy conditions: the enthalpy for ice-to-hydrate transformation is $H = -48.49$ kJ/mol, i.e., an endothermic process. The simulation of these transformation demands careful attention during code development; examples are presented later in this manuscript.

Either water or free gas may be in contact with the hydrate phase at any given location. Therefore, the model compares the equilibrium pressure P_{eq-mh} or P_{eq-I} against a volume average pressure P^*

$$P^* = \frac{S_g}{S_g + S_w} P_g + \frac{S_\ell}{S_g + S_\ell} P_\ell = (1 - S_\ell^*) P_g + S_\ell^* P_\ell \quad (5.25)$$

A time independent kinetic models, was adopted here It is assumed that the rate of formation or dissociation is driven by the distance δ to the corresponding equilibrium phase boundary

$$\delta = \sqrt{\left[\delta_T (T - T_{eq}) \right]^2 + \left[\delta_P (P_{fl} - P_{eq}) \right]^2} \quad (5.26)$$

where δ_T [$^{\circ}K^{-1}$] and δ_P [MPa^{-1}] are scaling parameters; The change in hydrate or ice volume fraction applied in a given time step is a fraction β of the potential change ΔS_h or ΔS_i . The reduction factor $0 \leq \beta \leq 1.0$ is a function of the distance to the phase boundary

$$\beta = 1 - q^\delta \quad (5.27)$$

The updated hydrate or ice volume fraction at time interval $j+1$ outside the stability field is

$$S^{j+1} = S^j + \beta \Delta S \quad (5.28)$$

This flexible formulation allows us to capture different rates of reaction, relative to mass flux and drainage conditions. The preselected parameter 'q' establishes the rate of change (default value $q=0.5$). Drained conditions can be simulated by selecting high q-values so that acceptably low excess pore fluid generation is predicted throughout the medium (dissociation stops when $q=1$ and the rate of dissociation becomes $\Delta S/\Delta t=0$).

5.3.1 Numerical simulation

The mathematical formulation presented above was implemented in the finite element computer program CODE-BRIGHT (Olivella et al., 1996). It was adapted to represent all species and phases encountered in HBS and their effect on the sediment response. Details related to the code can be found elsewhere (e.g. Olivella et al., 1996, Gens et al., 2009), only the main aspects are summarized as follows: (1) The state variables are: solid velocity, \mathbf{u} (one, two or three spatial directions); liquid pressure P_l , gas pressure P_g , temperature T and chemical species concentration. (2) Small strains and small strain rates are assumed for solid deformation. (3) Thermal equilibrium between phases in a given element is assumed. (4) Kinetics in hydrate formation/dissociation as a function of the driving temperature and fluid pressure deviations was considered from the phase boundary, considering the mass fraction of methane in hydrate S_h as the associated variable. (5) All constitutive equations are modified and new equations are

added to properly accommodate for the behavior of hydrate bearing sediments and all phases involved. Point level simulations were conducted in order to ascertain the initial validity of the model and inspect the performance. The results of the modeling for two such cases namely: stress paths following a cooling and heating paths under isochoric conditions are shown in Figure 5.7 and Figure 5.8 respectively. The schematic of the stress path followed are shown in part a) of the figures. The existences of the hydrates in different states are marked by regions 1 through 4. Regions 1 and 3 marks hydrate existing in a gaseous phase with water and ice respectively while Regions 2 and 4 marks them existing in a solid phase with water and ice. The results in terms of the pressure temperature stress path and the corresponding heat flow is shown in b). The capillary stress to liquid saturation (retention curve) for the two stress paths are presented in c). The evolutions of the concentration of the different phases are shown in d).

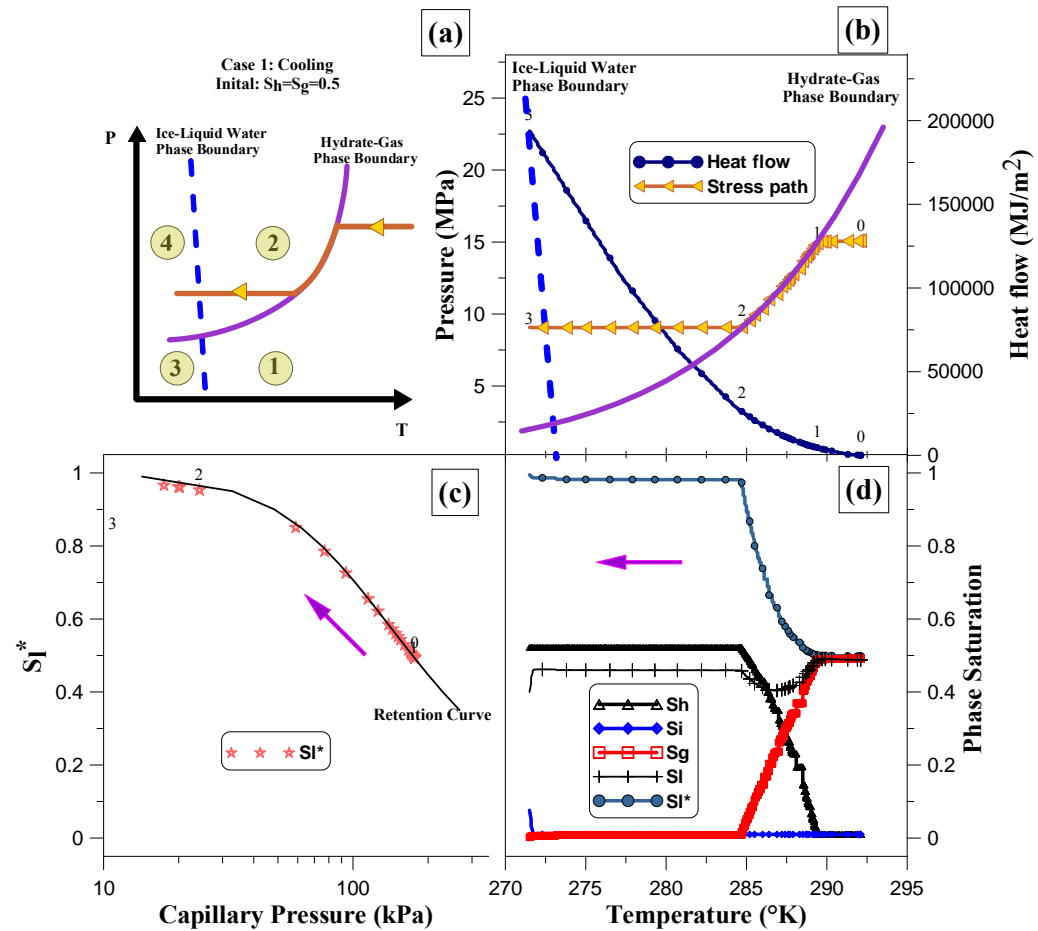


Figure 5.7 Results of hydrate formation by cooling a) Schematic of stress path b) Stress path and heat flow observed plotted along phase boundaries c) Retention curve d) Phase saturation of hydrates, water (liquid), gas and ice

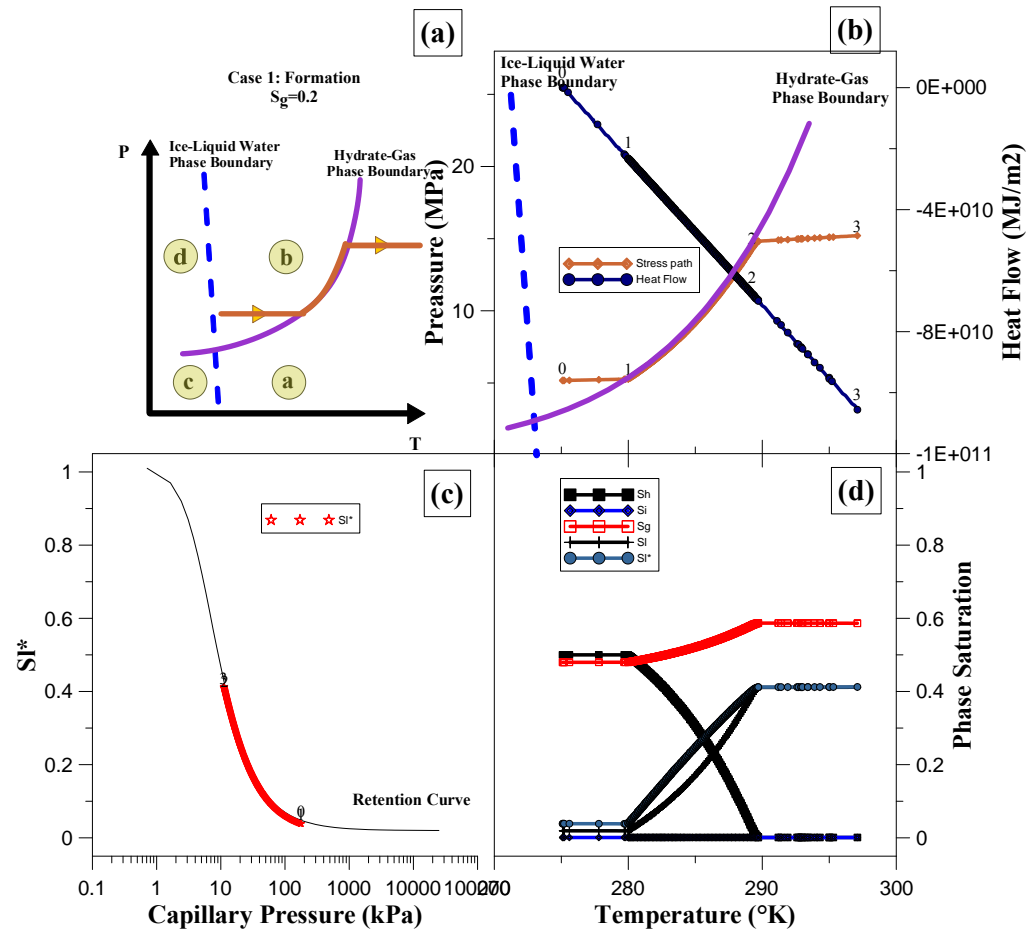


Figure 5.8 Results of hydrate formation by heating a) Schematic of stress path b) Stress path and heat flow observed plotted along phase boundaries c) Retention curve d) Phase saturation of hydrates, water (liquid), gas and ice

5.4 VALIDATION OF THE PROPOSED MODEL

The initial set of simulations conducted indicated that model was able to capture the variations in the concentration and the behavior of the hydrates for different stress path in the P-T plane. The validation of the model for established experimental work is now conducted. The experiments considered for this process is based on the work conducted by Yun et al., (2010). The validation of this work is conducted in two stages. The model is validated at d for a 2D mesh replicating the experiment. Finally the model is implemented to inspect gas production in a reservoir by heating and depressurization techniques.

5.4.1 Description of experimental work

The samples used in the experiment were part of the first Indian National Gas Hydrate Program expedition (NGHP expedition 01) which took place in the spring and summer of 2006 across the Indian Ocean shoreline. The depth of the samples recovered were in water depths ranging between 907 and 2674 m. It included 6 geophysical studies, drilling at 21 sites, logging while drilling of 12 boreholes, and the recovery of both standard and pressure cores. Five pressure cores were recovered at site NGHP-01-21, transferred into storage chambers under hydrostatic pressure, and kept at 4 °C and 13 MPa fluid pressure for characterization and analysis.

Three pressure cores were tested at an onshore facility in Singapore. The test program included the measurement of elastic wave velocity, shear strength, and electrical conductivity, followed by fast depressurization of the sub-sampled core round. A specially designed “instrumented pressure testing chamber” (IPTC) was used to

characterize the cores. The IPTC permits obtaining small-strain P-wave (using pinducers) and S-wave (using bender elements) velocities, large-strain undrained shear strength (using a cone-shaped penetrometer), electrical conductivity profile (using an electrical needle probe), and internal core temperature (using a thermocouple). The IPTC device along with the peripheral electronics horizontal displacement manipulator and X ray imaging system was housed in a 6.1 m long refrigerated container. The IPTC was used in previous studies to inspect Gulf of Mexico samples and further details are available in Yun et al., 2006. The IPTC chamber was filled with chilled water (~ 4 °C) and 13 MPa of fluid pressure was maintained. After conducting initial X-ray imaging, controlled depressurization tests were conducted on the samples. The instrumentation of the sample during the test was conducted at intervals along the length of the samples based on the points of interest ascertained through the X-ray images. The location of the instrumentation for one such sample is shown in Figure 5.9.

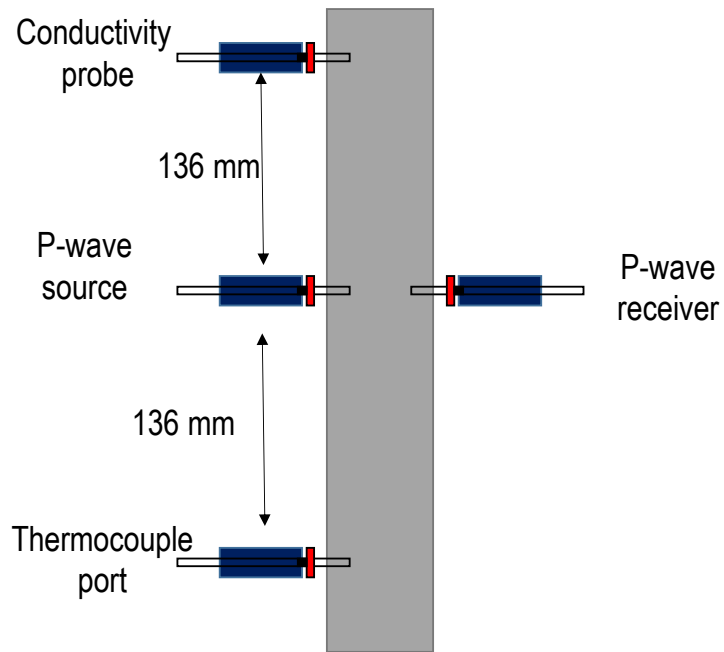


Figure 5.9 Instrumentation of the tests for sample 21C-02E (Yun et al., 2010)

The overall length of the sample tested for depressurization (Figure 5.9) was 380 mm. The fluid pressure of the IPTC chamber was slowly reduced until the fluid pressure dropped to 0. The change in the temperature p-wave velocity, electrical conductivity and the amount of gas generated was recorded. The relevant results of these tests are shown in Figure 5.10

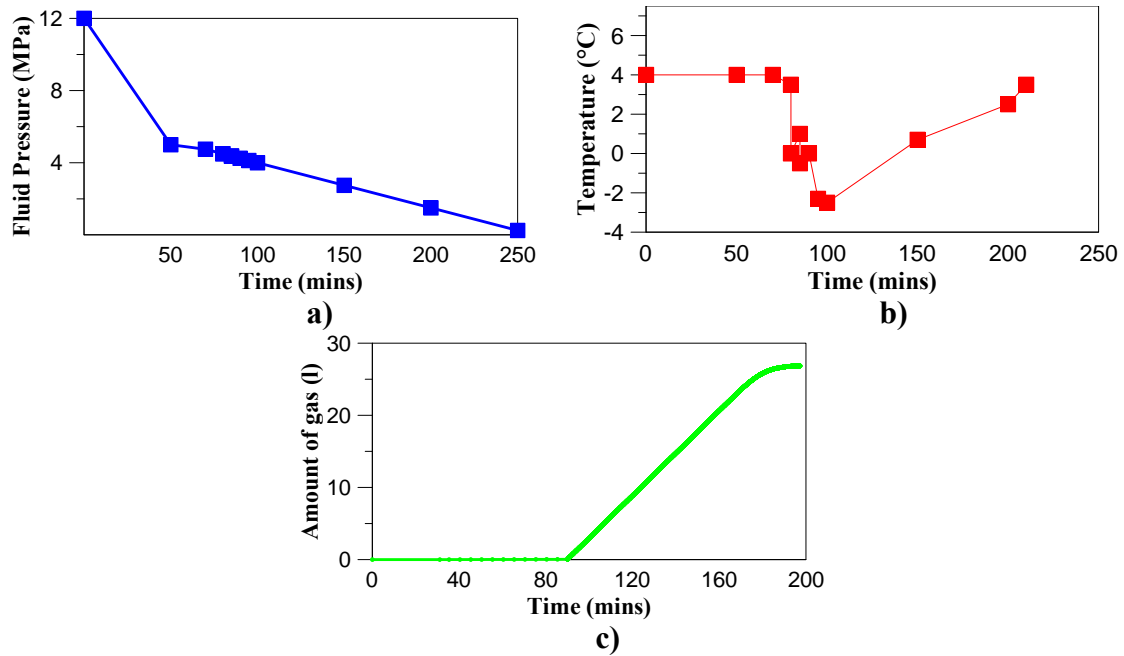


Figure 5.10 Results of controlled depressurization showing variation of a) Fluid pressure b) Temperature c) Gas Production (Yun et al., 2010)

5.4.2 Numerical modeling

Point level simulations

The numerical modeling of the experiment was conducted using the framework described in section 5.3. The finite element code `CODE_BRIGHT` modified for the HBS was utilized here. To inspect the behavior of the HBS during depressurization, point level simulations were conducted. The HBS was subjected to the same initial conditions as those in the test (Pressures of 13 MPa and temperature of 4 °C). The pressure of the sample was slowly reduced and upon reaching the hydrate-gas boundary the sample started disassociating. The results of the point level simulations is presented in Figure 5.11

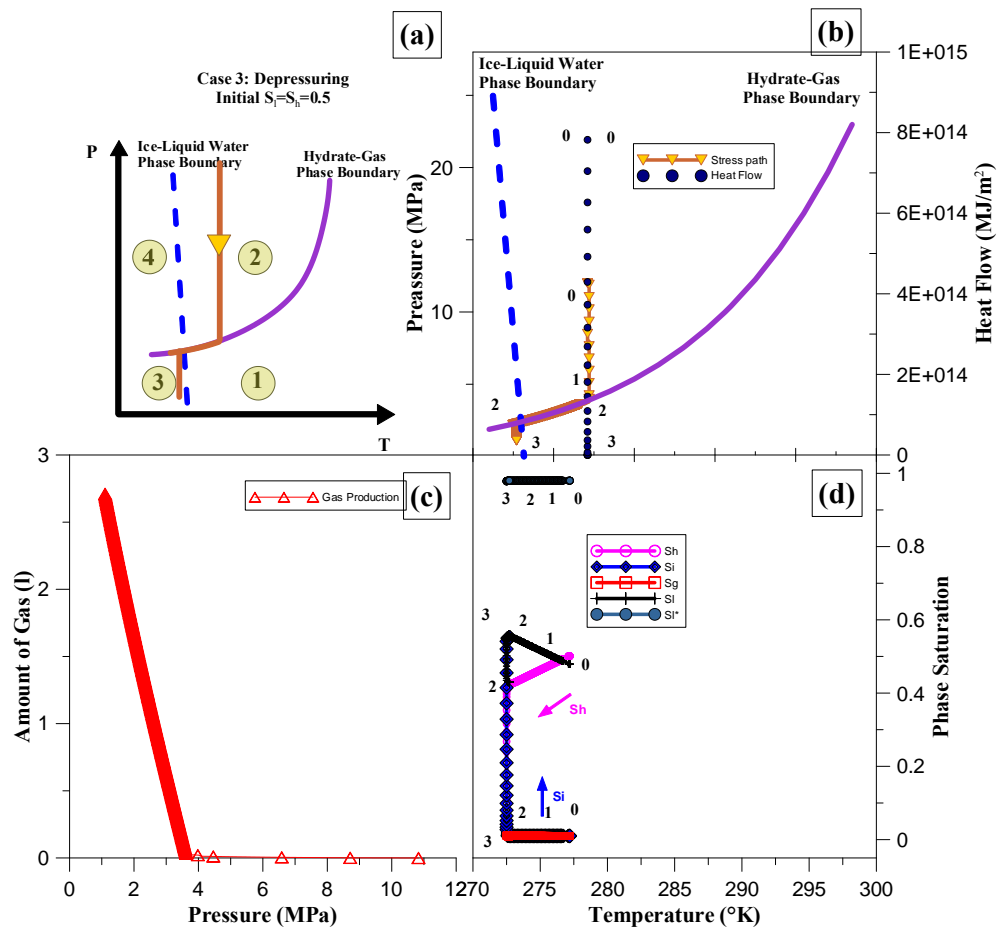


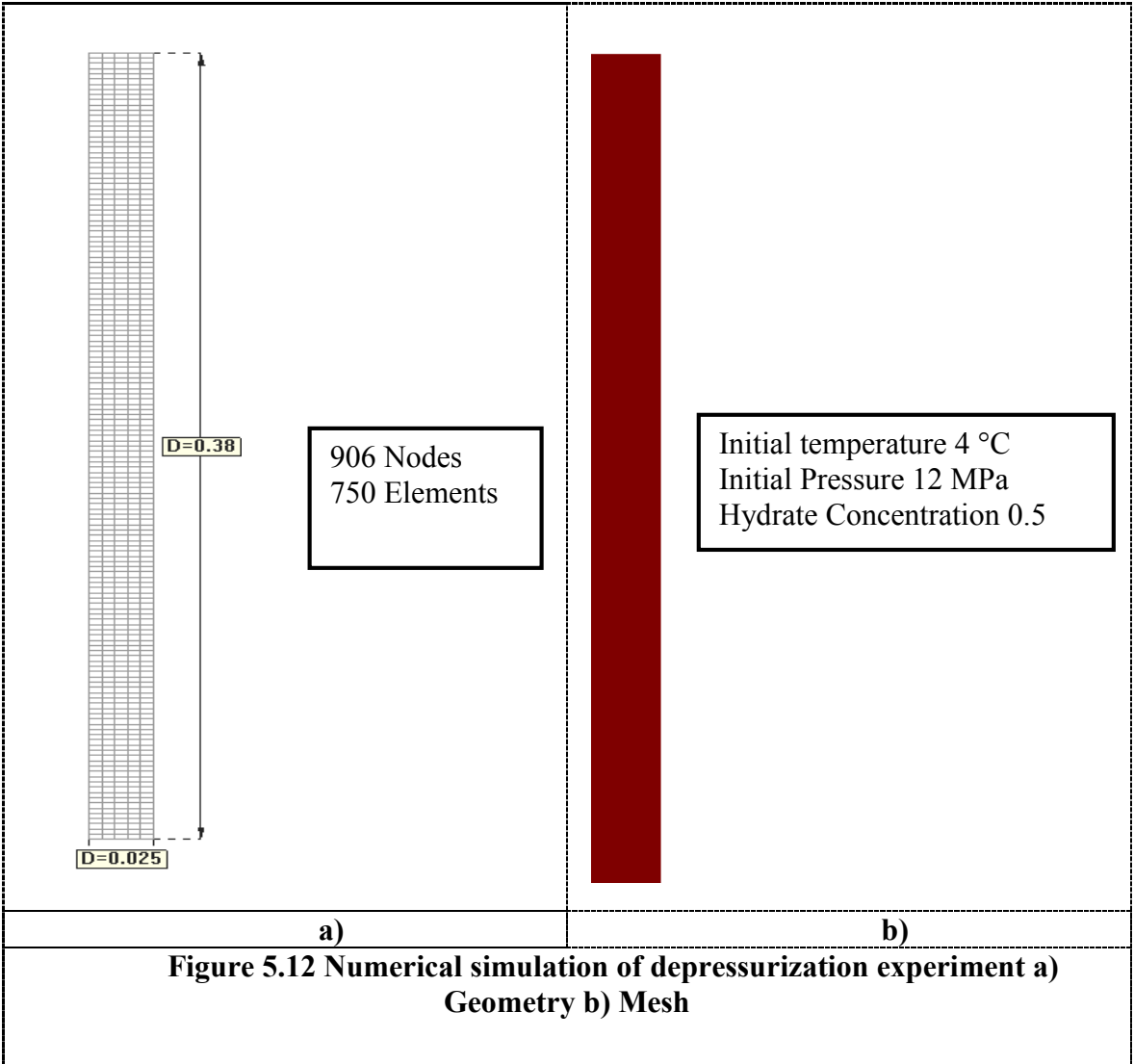
Figure 5.11 Results of hydrate formation by heating a) Schematic of stress path b) Stress path and heat flow observed plotted along phase boundaries c) Gas produced d) Phase saturation of hydrates, water (liquid), gas and ice

The stress path followed in the point level simulation is shown in Figure 5.11 a). Also marked are the four regions similar to Figure 5.7 and Figure 5.8. The stress path and the heat flow followed is shown in b), it can be seen that pressure drops at constant rate until it reaches the phase boundary (marked by step 0 to 1). At this stage the stress path follows the hydrate-gas boundary, cooling down in the process and starts to disassociate (1 to 2). This process continues until the stress path reaches ice-liquid boundary after which the pressure drops at constant temperature (2 to 3). This drop is marked by the formation of ice. The heat flow drops continuously through the entire process. The amount of gas formed during this depressurization is shown in c). As expected the gas release increases when the pressure reaches hydrate gas phase boundary. The trend in gas production is similar to experiment although, the actual amount of gas produced would not be same due to the effects of the boundary. The concentration of different phases is seen in d). This is consistent with expected result i.e. increase in ice concentration between 2 and 3; decrease in hydrate concentration between 1 and 2. It should be noted that for the point level simulation does not indicate an increase in temperature after stage 2 and remains a constant between 2 and 3. This is different from the experimental observations where there is a marked increase in temperature during this stage. This is believed to be due to effects of the surrounding soil (and boundary) that reheat the sediment after dissociation and can only be simulated with a 2D case considering the effects of the boundary.

2D simulation

Although point level simulation captured several key features of the depressurization experiment, 2D simulations were warranted in order to validate the framework. The mesh utilized for study is shown in Figure 5.12 a). The specimen dimensions are chosen based on the experimental setup. It consists of 906 nodes and 750 elements. The initial conditions of the sample are shown in Figure 5.12 b). The temperature at the boundary is kept constant at 4 °C while the depressurization is performed throughout the sample, similar to the experiment. Figure 5.13 shows the results of the simulation and when compared to the experiment. It is evident that model is able to capture the key experimental results. The comparison of the pressure of the system with respect to time is made in Figure 5.13 a). The gas production vs time for both the experiment and the model is seen in Figure 5.13 c). The model is able to replicate these 2 results extremely well. Although the simulation is able to capture the trends in the observed temperatures, there are inaccuracies (Figure 5.13 b). The experimental results drop suddenly at around 100 minutes of depressurization. The model however predicts a slower drop in the temperature values. This is mainly attributed to the heterogeneity of the sample and instrumentation made on the sample. It is mentioned in Yun et al. (2010) that the instrumentation was install at significant locations on the sample. The thermocouple used for measuring the temperature was located on hydrate lens. The disassociation of this hydrate lens would cause a rapid drop in the temperature. The saturation of the hydrate in the model however is modeled to be

a uniform value through the mesh. The dissociation takes a longer time and therefore the temperature drop is linear with time.



The amount of temperature drop predicted by the model is also lower compared to the model. It was explained at Yun et al., 2010 that the samples were recovered from the coast. The water in the sample would be of an increased salinity level. The salinity in water is known to shift the hydrate-gas boundary (Kamath and Godbole, 1987). This would result in a significantly lower temperature than what would be expected. This is one of the shortcomings of the current model and the salinity of the solution needs to be considered for accurate modeling.

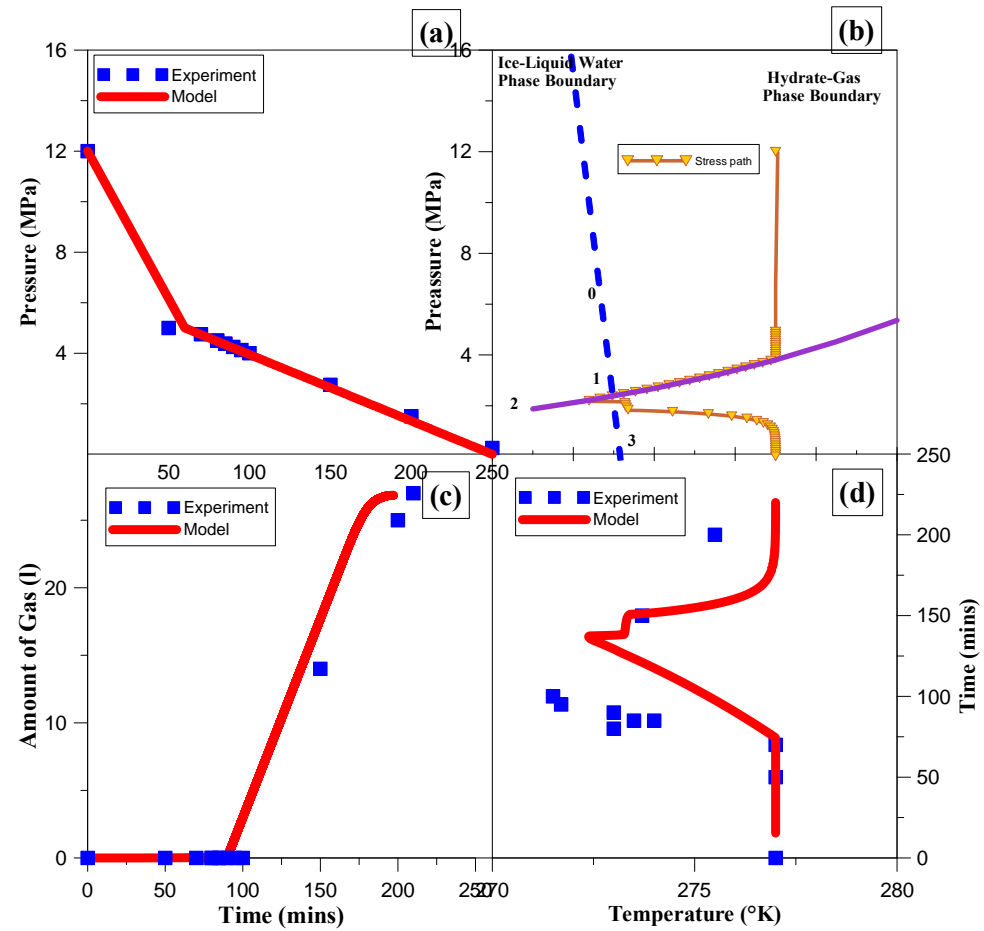


Figure 5.13 Results of the simulation compared to experimental results a) Pressure vs time b) Stress path with respect to the PT phase diagram c) Amount of gas generated with time d) Temperature of the specimen with time

5.4.3 Gas production

The framework is now implemented to inspect gas production from HBS reservoir located in the sea. Changes in pressure and temperature were used to induce disassociation. For an initial effort the same conditions are replicated in the proposed model without the inclusion of the geomechanical. The mesh and the geometry utilized in the simulation is show in Figure 5.14. The model dimensions are similar to those used in the simulations of reservoir conducted by Moridis et al. (2010). The mesh consists of 504 nodes with 460 elements. The elements are concentrated on the left end of the model where the depressurization and temperature load conditions would be applied. Such a procedure is followed as it was felt that the important changes are restricted to the edges which are loaded.

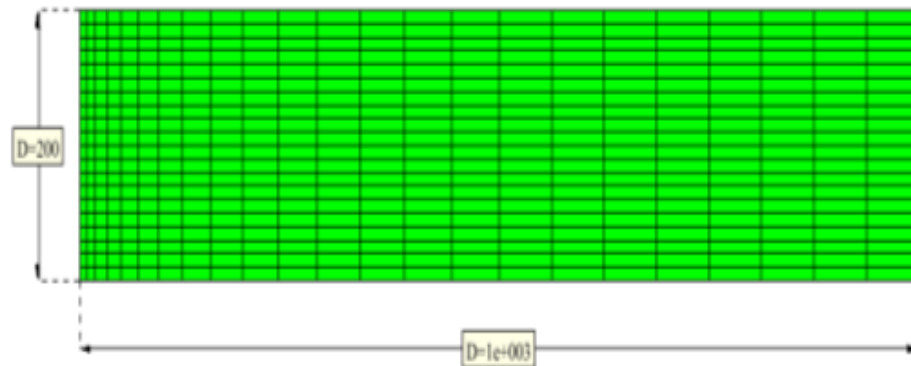


Figure 5.14 Finite element mesh used for the gas production

The initial conditions of temperature and pressure imposed are shown in Figure 5.15 . The initial pressure was calculated assuming that hydrate reservoir is around 1000 m below the sea floor subjected to hydrostatic loads. The initial temperature of 6°C

would enforce that hydrates would be remain in a solid state with little or no ice formation based on the prevalent pressure. The initial hydrate concentration was set to 30% throughout the boundary.

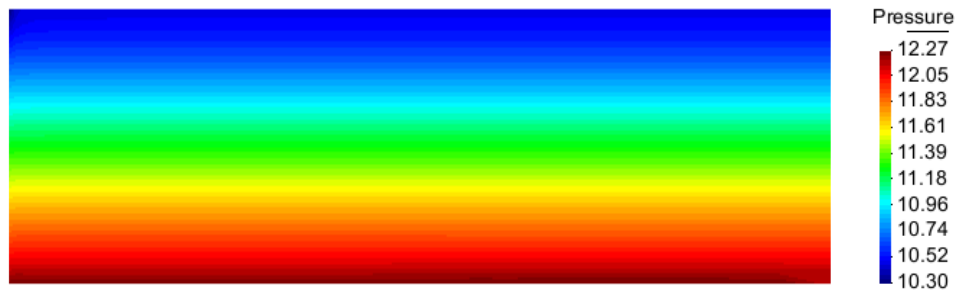


Figure 5.15 Initial conditions imposed

The depressurization induced gas production is achieved by reducing the fluid pressure to 0 MPa along the left boundary. The liquid pressure, hydrate concentration and the temperature are monitored through the depressurization process. The results of this process are shown in Figure 29. The results of the first 150 m of the mesh, where important changes are observed are shown here. It can be seen that there is a decrease in the hydrate concentration indicating gas production. The liquid pressure is seen to increase across the left front of the boundary. The temperature plots at time = 750, show that there is a decrease at the top boundary indicating the beginning of the hydrate disassociation. This region of heightened temperature moves across the boundary with time after which it returns to the initial imposed temperature of 6°C.

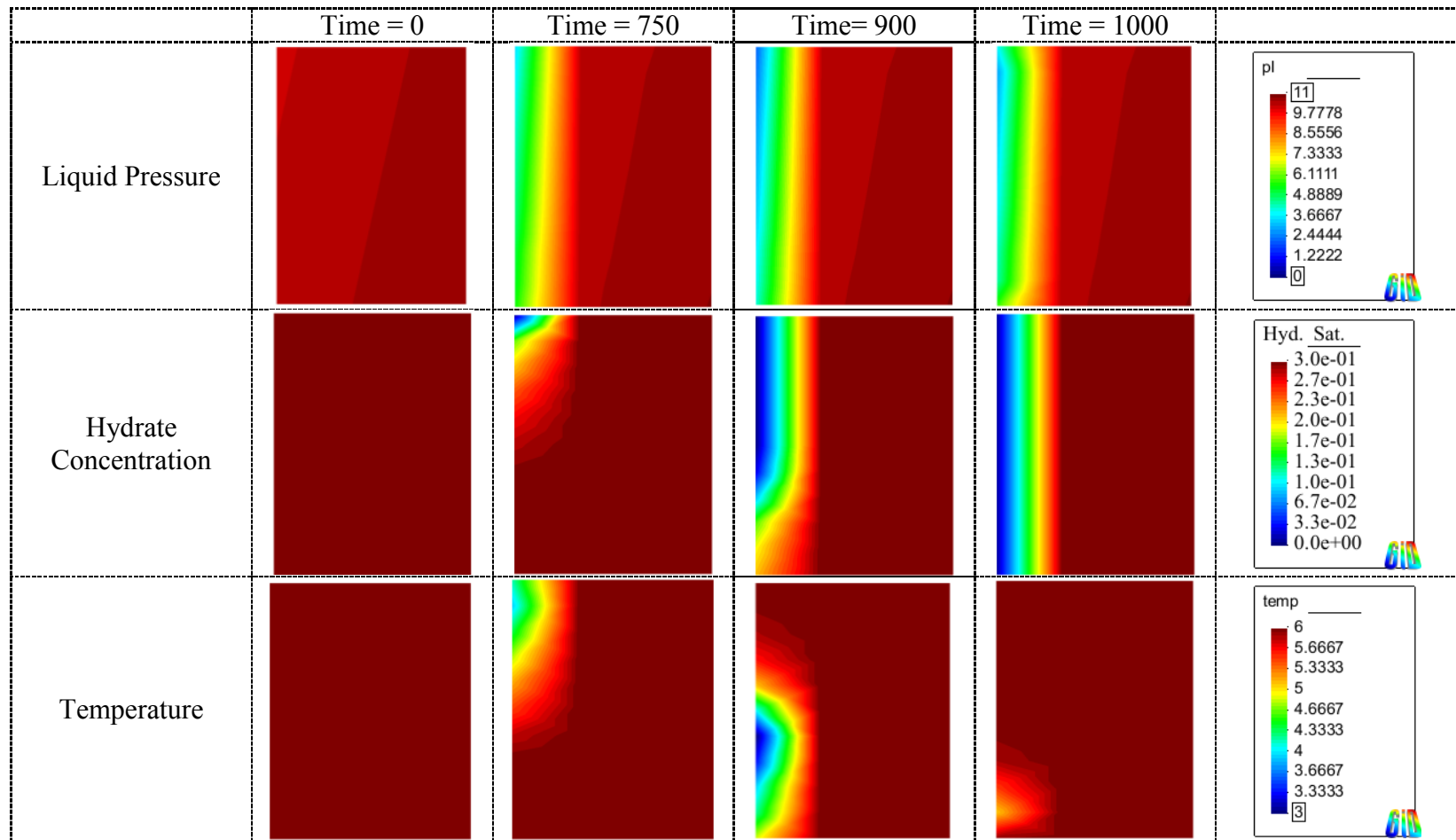


Figure 5.16 Modeling result of the depressurization

The gas production is induced by increasing the temperature at the left boundary while maintaining a constant pressure. This is performed by increasing the temperature of the left boundary from 6°C to 30°C. The results of the heating simulation is shown in Figure 5.17. The increased temperature sparks a uniform dissociation of the hydrates from top to bottom of the HBS.

The simulations of the HBS reservoir show a great deal of promise in capturing the behavior of soil in the field. With the inclusion of geomechanical and geochemical models the assessment of gas production can be made more accurately

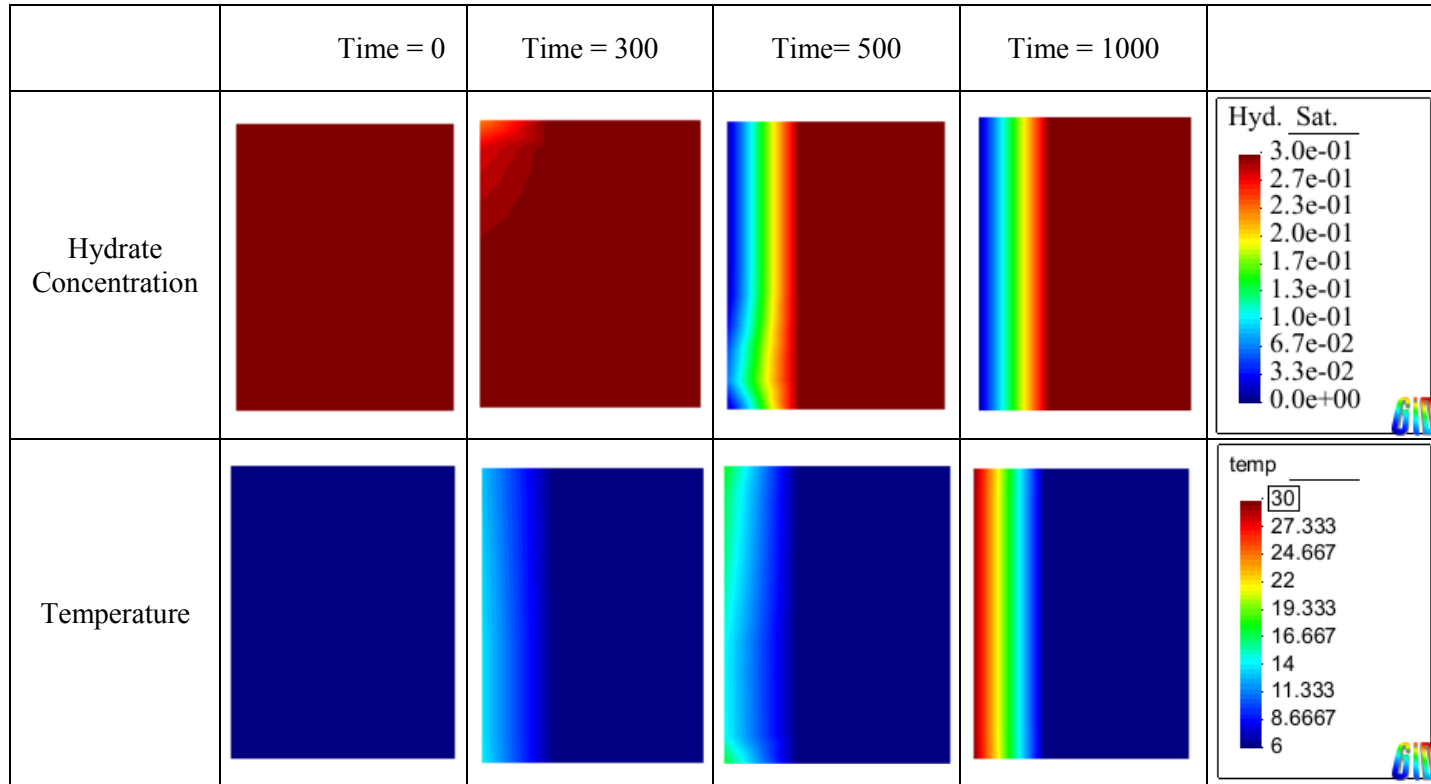


Figure 5.17 Modeling result of the heating

6 ANALYSIS OF COMPRESSED AIR ENERGY STORAGE SYSTEMS

6.1 INTRODUCTION

The rising cost of fossil fuels and the desire clean sources of energy have triggered the re-evaluation of different technologies to meet current and future energy needs. Renewable sources of energy are ideal candidates. Energy generated from wind turbines form a quintessential part in this discussion. The global wind energy is theoretically enough to satisfy the world's electricity requirements several times over (Succar and Williams, 2009). Even with the variability of wind and remoteness of high quality of wind resources it would be enough to satisfy as much as 20-30% of electricity requirements in the U.S. (Succar and Williams, 2009). However, the difference in the period between peak energy production and energy requirements become a major obstacle in considering wind power as an economic and viable option. To overcome this drawback a temporary storage of the produced energy is required, so that it can be released in times of peak energy demands.

Compressed Air Energy Storage (CAES) systems are one of such possible solutions for the storage of energy. The idea behind CAES is to compress air/gas at high pressure using the energy produced during peak wind periods and store it underground. Caverns or abandoned mines have been used for such storages. A new concept of storing the air in aquifer has been explore recently (Succar and Williams, 2009). This air is then decompressed to produce electricity during periods of high energy demand. The effects of the decompression may be magnified by burning this decompressed air along with

natural gas or coal to have higher volumetric expansions giving greater yields of electricity.

CAES requires suitable geological reservoirs for storing the compressed air. These systems are classified based on the type of geological formations into salt, hard rock and porous rock. The details of which are further discussed in the next Section 6.3. The cyclic compression and decompression of air within the reservoir would lead to changes in temperature, liquid and gas saturations and mechanical stresses. Studies of CAES are further complicated by the heterogeneity of material properties. Based on the in-situ data collected in Heath et al. 2013 the behavior for a proposed CAES project in Des Moines, Iowa is examined. The numerical modeling of this CAES facility is described in section 6.4. This case study simulates the hydraulic and mechanical behaviors of a CAES in porous rock and the influence of the heterogeneities. The conclusions and recommendations for future studies are presented at the end of the section

6.2 BACKGROUND INFORMATION

The CAES technology allows the storage of gas or air during periods of low demand to meet energy requirements at periods of high demand. This technology is one of the few systems suitable for a long-term storage of electrical energy. It also is a low cost method, where the repositories can be located in pre-existing geological formations (aquifers, caves) or abandoned caverns or salt mines which can be re-used. Furthermore, gas-turbines are relatively cheap so the energy efficiency of CAES can be boosted economically. CAES can be combined with several energy generation technologies

including nuclear and thermal power but it is an ideal partner for balancing off-peak wind energy. This last aspect is particularly relevant considering that the energy generated from wind-farms is dependent on the weather conditions and therefore it is quite difficult to anticipate. A brief history of the development of CAES, followed by the various classifications and modeling efforts to simulate the behaviors of CAES is presented the next sections.

6.2.1 Potential of CAES

CAES emerged as a promising alternative in 1970's due to the high price of fossil fuels. Due to the high demand of energy, CAES became an extremely lucrative option to be combined with an inexpensive baseload nuclear power (Stys, 1977). The technology however lost some of its momentum in the next decade due to the fall in oil prices. There has been an increased push in the wind energy sector in the recent past due to the nature of wind power which is renewable and non-polluting. The progress in the design of wind turbines in the last few years have been directly reflected in improvements the economics of wind power generation. The variability of wind output however, requires additional standby reserve capacity to ensure output during times of peak demand. This imbalance between the periods of peak production and requirements can be overcome by energy balancing (Holttinen et al., 2007).

The capital costs of various energy balancing sources are listed in Table 6.1. Alternatives to CAES include pumped hydroelectric storage (PHS) and battery technologies. PHS works on the principle that water is stored at location of higher elevation and the potential energy (associated with the conduction of the water to power

plants located at lower locations) is utilized in turbines to meet periods of high energy demand. This technique is a viable alternative to CAES, because (peak-off) wind energy is not used to storage air or gas under pressure in the ground, but to pump up water in elevated reservoirs. This idea has been explored in greater detail in the past (Schoenung, 2007; McLarnon and Cairns, 1989; Beurskens et al., 2003). It has the additional advantage that doesn't require a fuel combustion to improve efficiency. However, it requires large scale reservoirs at different elevations. One of the drawback of this technique is that has a larger negative environmental impact in terms of land use. In contrast CAES is more economical and has a broad range of already existing reservoirs with a limited surface footprint compared to PHS.

Table 6.1 Costs for various energy storage options (Sucaar and Williams, 2008)

Technology	Capital Cost for Capacity development	Capital Cost Energy Generation	Hours of Storage	Total Capital Cost
CAES	580	1.75	40	650
Pumped Hydroelectric Storage	600	37.5	10	975
Sodium Sulfur Battery	1720-1860	180-210	6-9	3100-3400

An additional reason to consider this technology is to exploit the huge onshore wind potential in the Great Plains and Midwestern states of the U.S. which account for over half the wind generation potential (Elliot et al., 1991). Wind energy capacity has

risen as much as 2000% (from 4.8 GW to 94 GW) from 1995 (Succar and Williams, 2009). Wind energy is classified based on its economic feasibility. Wind energy class greater than or equal to 4 are considered viable. Figure 6.1 shows the population density of the U.S along with 4+ class of wind power.

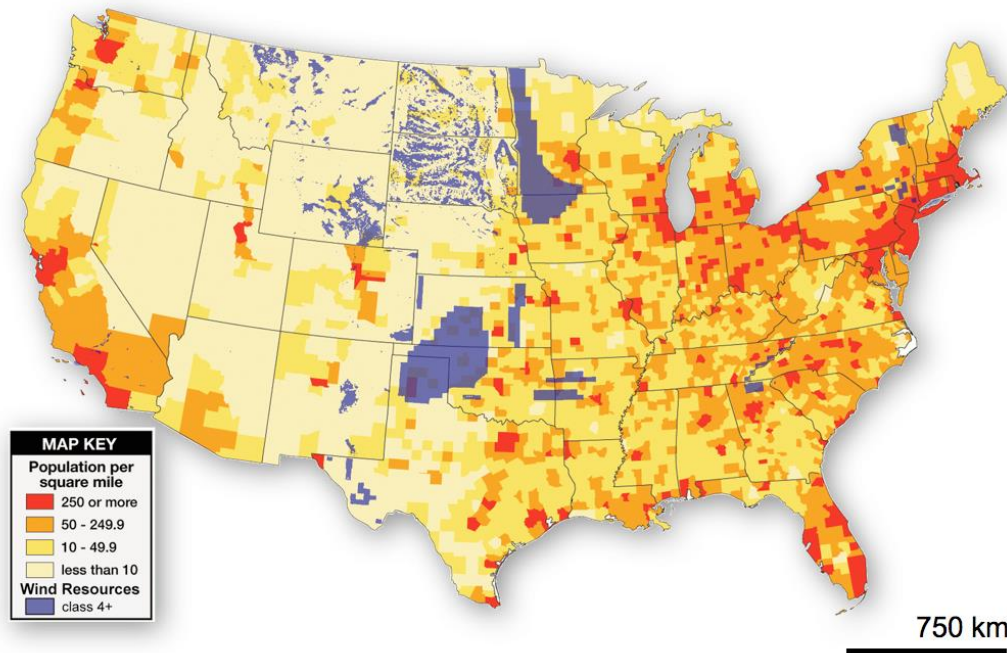


Figure 6.1 Onshore wind resource and population density of the U.S. (NREL, 2002)

6.2.2 CAES operation

The working principle of systems coupled to CAES is similar to that of gas turbines with the exception of compression and expansion cycles occurring independently and at different times. A schematic of this operation is shown in Figure 6.2. During the compression stage, electricity is used to operate a series of compressors to inject air into the storage. This injection pressure here needs to approximate the

pressure surrounding the formation. Intercoolers and aftercoolers are utilized to increase the efficiency of these compressors by reducing the temperature. During the expansion stage, the air is withdrawn and combusted with fuel such as natural gas in order to regenerate electricity. The use of this extra fuel improves the efficiency of the system by generating a greater volume of gas for the output turbines. The rise in temperature, due to the combustion, also improves operational conditions by alleviating problems with icing of the gas turbines blades, which usually results from decompression of the air.

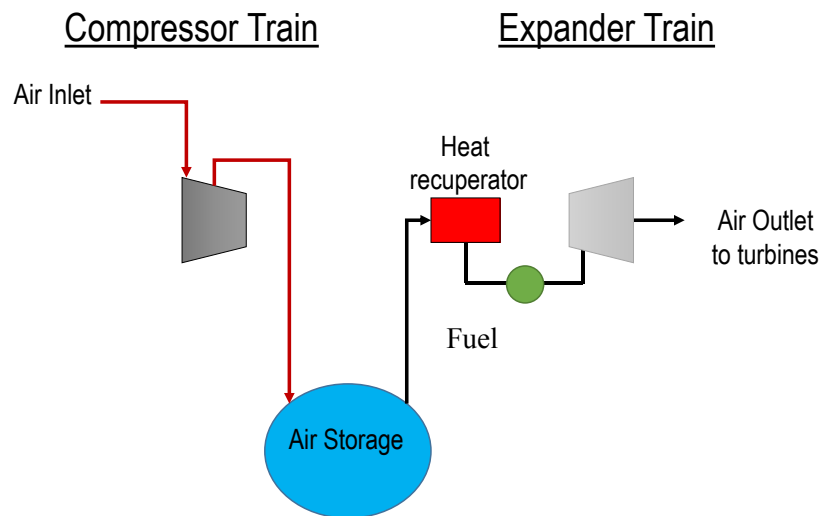


Figure 6.2 Schematic of CAES power plant

6.3 TYPES OF CAES

Based on the host rock type, CAES storage reservoirs can be classified into three categories: salt, hard rock, and porous rock. The areas that have these combined geologies account for a significant portion of the continental United States with as much

as 75% of the U.S. suitable for underground air storage (Mehta, 1992; Allen et al., 1983, Allen, 1985). These findings, preliminary in nature, do not fully estimate the potential of the proposed CAES sites, but do produce a template for identifying candidate areas for further inquiry.

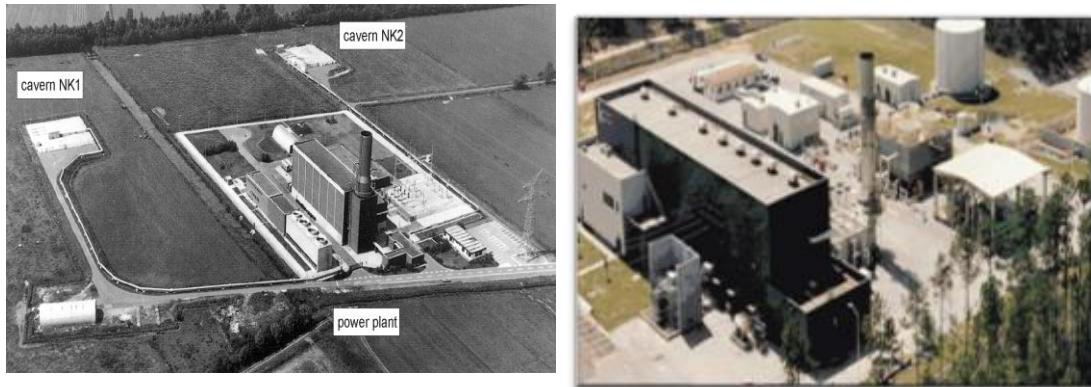
6.3.1 CAES in salt and hard rock formations

The CAES systems located in hard rock and salt mines would be stored either in existing cavities such as mines or in excavated zones in hard rock. The walls of the storage are required to have limited permeability so that air does not leak out of the rock. This can be achieved by either selecting a site where the permeability of the rock is low enough or by using liner to decrease the overall permeability. The storage system should also be stable enough to endure stresses induced during the cyclic pressurizations of the air during the operation. A brief description of the storage systems in these caverns and modeling efforts previously undertaken are discussed here.

CAES in salt mines

CAES located in used salt mines act as excellent repositories of energy. The Huntrof power plant in Germany and the McIntosh Power Plant in Alabama shown in Figure 6.3 a) and b) respectively are two such CAES plants that are already operating using solution-mined cavities in salt domes. Salt formations usually provide a straightforward approach to develop and operate a CAES. Techniques such as solution mining are utilized for creating of CAES in salt cavern by using a supply of fresh water for proper disposal of brine. These are a reliable, low cost route for developing a storage volume of the needed size, approximately \$2.00 per kWh of output from storage (Succar

and Williams, 2009). Because of the mechanical properties of the salt, the storage reservoirs pose minimal risk of air leakage (DeVries, et al., 2005).



a) b)
Figure 6.3 Existing CAES power plants a) Huntroff, Germany (Mohmeyer and Schard, 2001) b) McIntosh power plant. Alabama, U.S.A. (Epcinc, 2009)

Areas of the Central, North Central and North East United States feature large bedded repositories, while domal formations are found in the Gulf Coast Basin (DeVries, et al., 2005). Salt beds however tend to be much thinner and face problems of structural stability if they contain a high concentration of impurities. Caverns mined from salt domes can be tall and narrow with minimal roof spans as is the case at both the Huntorf and McIntosh CAES facilities. The thinner salt beds cannot support long aspect ratio designs because the air pressure must support much this large roof spans. They also suffer when facilities need to be expanded due to demand arises.

CAES in hard rock

The advantage of locating CAES repositories in hard rock is associated with the ability to reuse mines which were previously abandoned. The price for kWh is usually around 10\$ (Spila et al., 1994, Shepard and van Linden, 2001). The creation of new repositories in hard rock is usually uneconomical with prices reaching as much as \$30/kWh produced (Succar and William, 2008). The proposed Norton CAES plant (Figure 6.4), would be located in hard rock, in this case within a limestone mine. Several studies have been conducted on the behavior of CAES located in hard rock including field case studies. Test facilities for hard rock CAES have been developed in EPRI and the Luxembourg utility of Societe Electrique de l'Our using an excavated hard-rock cavern with water compensation (Lihach, 1982). Field studies have also been conducted as in the case of a 2 MW power plant in Japan using an abandoned coal mine.

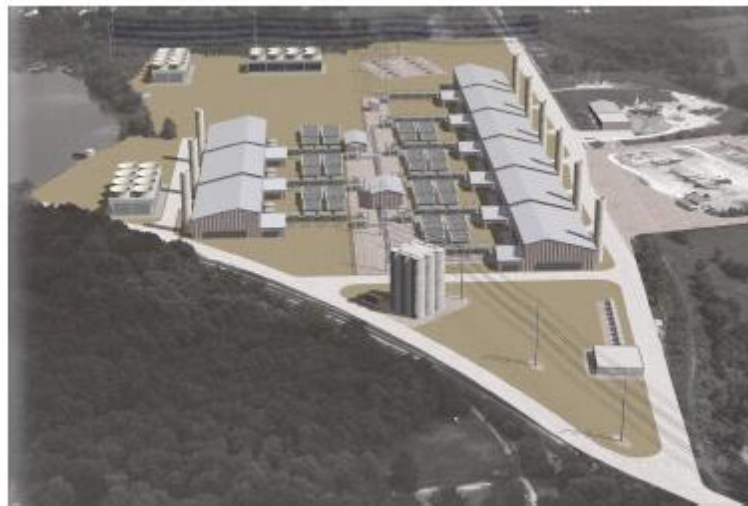


Figure 6.4 Rendering of the proposed CAES in hard rock in Norton, Ohio (OPSB, 2001)

The development costs of a CAES facility in hard rock are currently high relative to other geologies it is unlikely that this option will be the first option pursued for a large-scale deployment of CAES. Future developments in mining technology might reduce these costs, but presently other geologies offer the best opportunities for CAES development.

Modeling efforts to simulate the behavior of CAES hosts in salt and host rocks

Coupled formulations previously used in simulating the behavior of natural gas storage systems have been adopted for CAES. Different type of approaches have been proposed to model CAES system hosted in hard rock or salt caverns, amongst others: coupled TH models (e.g. Crocogino et al., 2001; Kushnir et al., 2012; Raju and Kaithan, 2012), coupled HM (e.g. Gehle, 1982; Wang et al., 2013) and over the last decade coupled THM frameworks. For example Lux, (2009) proposed a THM model for simulating the behavior of the CAES in salt caverns. The work focused on the salt caverns concentrated in Germany and discussed the practices in design, operation and abandonment of such a cavern. Experiments were conducted on the cavern material to determined key material properties. These properties were then implemented into a coupled formulation with a viscoplastic mechanical model to incorporate the effects of healing/damage of the rock. The model was then used to analyze different case studies and provide safety recommendations for operating this type of CAES sytem.

A THM framework based on the coupling of the tww codes (namely FLAC and TOUGHT) has been proposed to predict the behavior of lined caverns (e.g. Kim et al., 2011; Kim et al., 2012, Rutqvist et al., 2012). Lined rock caverns work on the same

principles of a rock cavern with the exception of possessing a liner (usually concrete) to decrease the permeability of rock in order to prevent the leakage. The framework proposed here was validated against a CAES system based on pilot test program in Korea.

A linear elastic model was used to describe the mechanical behavior of the rock. The effects of the lining consisting of a low permeability concrete liner with and without an internal synthetic seal option were examined (Rutqvist et al., 2012). The influence of the permeability of the rock and the liner, injection pressures, and temperatures were inspected on storage capacity and the leakage in the systems.

6.3.2 Porous rock

Reservoirs in porous rock provide the most economical storage option for large-scale CAES with an estimated development cost of ~\$0.11/kWh for expansion in the storage volume (EPRI-DOE, 2003). Large parts of the central US are suitable for such operations as they have large homogenous aquifers. A schematic representation of energy storage in an aquifer is shown in Figure 6.5.

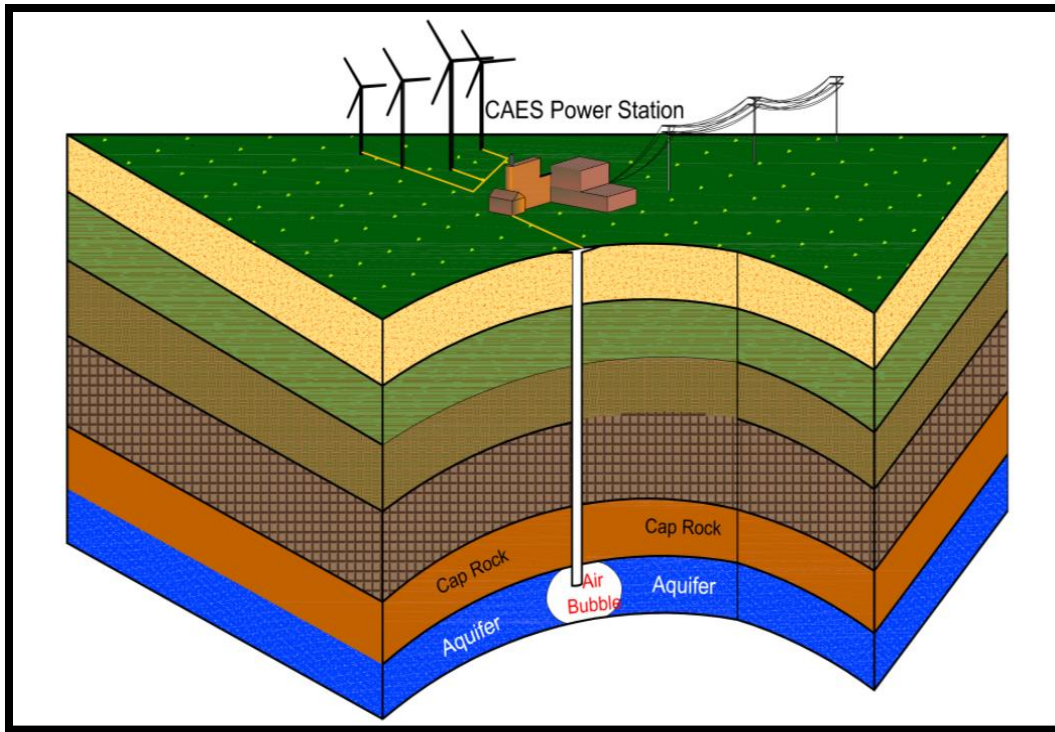


Figure 6.5 CAES storage facility in aquifer.

The concept has already been applied to store natural gas within aquifers (Moridis et al., 2007) and is now extended to storage of air. The test for such a facility was conducted in Sesta, Italy where a 25 MW facility was constructed and operated (EPRI-DOE, 2003). The first tests in the US were conducted by the US Department of Energy in the porous sandstone formation in Pittsfield, Illinois (Succar and Williams, 2009). The test was conducted in an effort to characterize the nature of aquifers to produce an economical storage system. These requirements were used study the feasibility of setting an aquifer based CAES facility at Dallas center, Iowa.

The design and operation of a CAES in porous rocks is based on the concept of multiple barriers to airflow used in reservoir engineering. A typical schematic of such a reservoir is shown in Figure 6.6

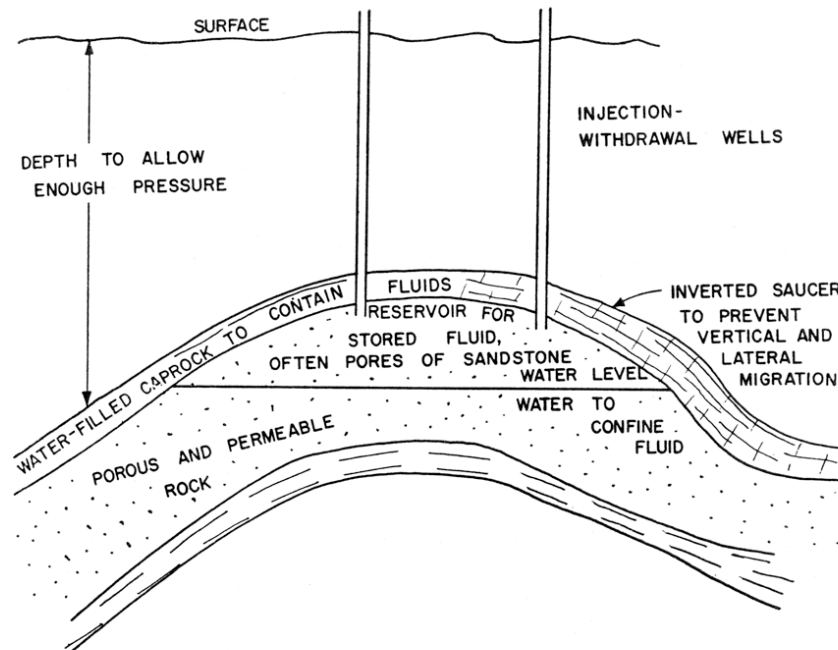


Figure 6.6 Schematic of Gas Storage (Succar and Williams, 2009)

A preferable reservoir should comprise of a dome like cap rock overlying the permeable rock where the air would be stored. The reservoir should be deep enough to accommodate the air storage required for the power generation. The permeability of the reservoir should be in a range so as to create the required storage space while not allowing major leakage of the stored air. The cap rock and the aquifer rock must be strong enough to resist fracturing when the air is introduced into the reservoir.

The operation of the reservoir is conducted in two stages:

- (i) Gas Bubble formation
- (ii) Cyclic injection and withdrawal operations.

During the formation of the gas bubble air is continuously pumped in the ground at a desired rate/pressure for a designated period of time. The rate/pressure depends on the structural stability of the aquifer while the period of pumping is dictated by required storage space. A very large injection pressure needs to be avoided as it could lead to fingering effects wherein the more mobile fluid (i.e. air) displaces the water and results in high gas saturation bands. These gas bands penetrate deep into the water zone leading to heterogeneous distribution of air saturation in the subsurface.

The daily operations of the system are conducted by cyclic injection and withdrawal of the air. This is performed by application of cycles of fluxes. The injection pressure should not exceed the natural lithospheric stresses and the withdrawal pressure should not cause any instability of the storage system. An ideal pressure range should also be within the working range of the compressor and gas turbines they are connected to. The bubble formed in the previous stage must be held steady and the water production during these cycles must be minimal.

These requirements suggest the need for extensive field and material testing at selected sites as well as strong numerical modeling to ensure that CAES is viable and sustainable.

Modeling efforts

The concept of CAES systems in porous rocks have been explored in greater detail only in the last five years. The guidelines for establishing such a facility has been

published some time back (Doerthy et al., 1982). Because of the similarities in storage of air and natural gas, the principles of reservoir engineering are utilized in modeling these facilities. However, in a CAES system coupled with a wind plant the switch between compression and generation will happen at least once a day (and perhaps several times a day), while the natural gas storage may be cycled as infrequently as once a year. The changes in the physical and chemical properties of the air compared to natural gas are also deviation which needs to be considered. The Department of Energy (DOE) along with the HYDROdynamics Group^{LLC} studied the feasibility of a CAES plant in a sandstone aquifer at Dallas Center in Iowa (Moridis et al., 2007). The initial feasibility study included the simulation of the CAES based on the data of the nearby Redfield aquifer. The Redfield aquifer currently houses a natural gas storage system and the properties were expected to be similar to the candidate site at Dallas. The sandstone found in these regions was expected to act as an excellent host material that could be used for the storage of compressed air. Based on the initial survey and the power requirements, the aquifer would be located at a depth of about 900m from the surface and would be 30m deep with a reservoir radius of nearly 1000m. A minimum of thirteen wells would be required to supply the necessary air flow rate. Based on the geophysical survey the aquifer rock was divided into 4 layers considering the rock porosities (ranging between 0.16 to 0.17) and the thicknesses (ranging between 5 to 15m). The simulation of the storage during the operational stage was conducted by injecting and withdrawing air into the aquifer with daily cycles. A simple capillary pressure model along with relative permeability model was used to analyze the behavior of the CAES system. The

parameters for the model were obtained from the Redfield storage facility. The details of the simulation are published elsewhere (Moridis et al., 2007).

Although the initial study recommended the site for establishing a CAES facility a much detailed characterization of the properties of the rock at the Dallas center site revealed that the initial study had several shortcomings (Heath et al., 2013). The average porosity of the Dallas center site was around 0.13, which is much lower than the one prevailing at Redfield site. This significantly changes the injection and operational volumes of the reservoir. The distribution of the porosity was also found to be heterogenous in nature and the rock could no longer be simply classified into four layers. The study also did not consider the mechanical response of the aquifer due to the changing fluid pressures during the working of the CAES. These shortcomings led to the abandonment of this site as a potential site. However it did provide valuable data and an opportunity to study how this kind of facility operates. The work done in this dissertation focus on a better understanding on how a CAES system in porous rock behaves based on actual data.

The following sections are organized as follows. First the formal approach used in the numerical analyses is presented; afterwards, information about the actual site adopted in this study is briefly introduced and finally the main outcomes of the numerical analyses are discussed. Two types of simulations were performed, in the first one pressure cycles were applied to learn about the maximum injection rates that can be used during the operation of the CAES system. Based on this study, an injection rate was adopted to simulate the response of the CAES during 30 years.

6.4 NUMERICAL APPROACH TO THE CASE STUDY

The fully coupled THM approach proposed by Olivella et al. (1996) was adopted to simulate the CAES in the Dallas-Center site. The formulation utilized here is similar to the formulation mentioned in the previous Section. The details of this general framework are presented in Appendix. The framework is formulated using a multi-phase, multi-species approach with three phases: solid(s), liquid(l) and gas(g), and three species: mineral(m), water(w) and air(a). The liquid phase may contain water and dissolved air, and the gas phase is a mixture of dry air and vapor. The approach is composed of: i) balance equations, ii) constitutive equations and iii) equilibrium restrictions. The balance equations considered in the formulation are: mass balance of species, balance of internal energy and balance of momentum.

The equation associated with the mass balances of water is:

$$\frac{\partial}{\partial t} (\theta_l^w S_l \phi + \theta_g^w S_g \phi) + \nabla \cdot (\mathbf{j}_l^w + \mathbf{j}_g^w) = f^w \quad (6.1)$$

In a similar manner the mass balance of air is defined. Thermal equilibrium between phases is assumed; consequently only one equation (balance of internal energy) is required for the thermal problem:

$$\frac{\partial}{\partial t} (E_s \rho_s (1 - \phi) + E_l \rho_l S_l \phi + E_g \rho_g S_g \phi) + \nabla \cdot (\mathbf{i}_c + \mathbf{j}_{Es} + \mathbf{j}_{El} + \mathbf{j}_{Eg}) = f^E \quad (6.2)$$

The formulation also includes the momentum balance (Olivella et al., 1996) and the transport of reactive species (Guimaraes et al., 2006). It was assumed that the sandstone behaves elastically.

The constitutive equations and the equilibrium restrictions establish the link between the main (state) variables (e.g. \mathbf{u} , P_b , P_g , T) and the dependent variables (e.g. $\boldsymbol{\sigma}$, S_l , S_g , \mathbf{i}_c). Based on the above coupled formulation, the finite element program CODE_BRIGTH was developed (Olivella et al., 1996). All the equations are solved in a fully coupled way, the Newton-Raphson method is used to solve the non-linear problem.

The operational stage of injection and withdrawal of air is generally simulated by applying gas flux at the injection points in the aquifer (Moridis et al., 2007). The gas flux rate imposed needs be so that it would not compromise the geology. One approach of determining the right air flux would be to conduct the simulation by applying compression and decompression cycles of pressures which is below the lithospheric conditions (Lux, 2009).

The distribution of the materials at different depths including the ‘Eau-Claire’ formation, the Mount Simon sandstone, and ‘Red-clastics’ formation; alongside with the estimated values of permeability and porosity (Heath et al., 2012) is shown in Figure 6.7. The first formation is a dolomite (which would act as a cap-rock); the second one is the aquifer, with four sub-divisions (A-D); and the third one is a very low permeability rock. A strong heterogeneity characterizes the results from subdivisions C-D.

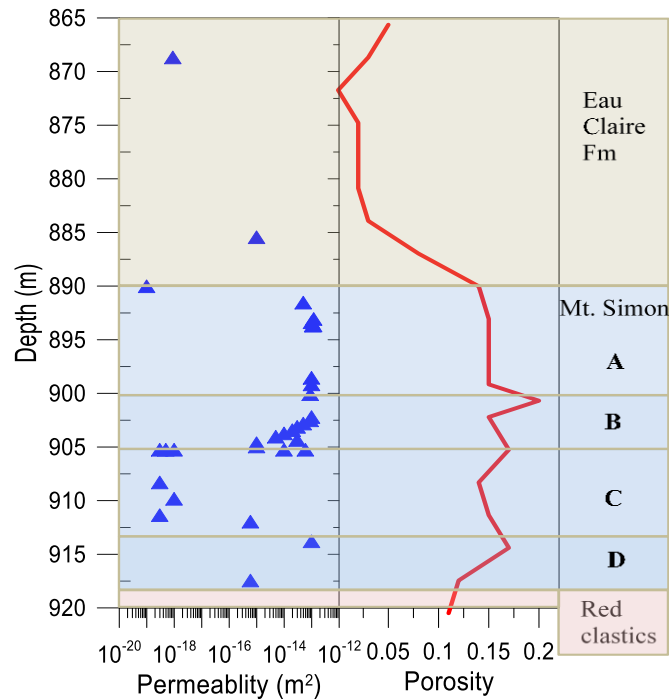


Figure 6.7 Distribution of the properties of the sandstone with depth

It can be clearly observed that value of the permeability has an extremely high variability. Figure 6.8 presents the experimental results of the main constitutive laws used in this study. The relationship between the porosity and the permeability using Kozeny's law (Equation 6.1) is shown in Figure 6.8 a). Similarly, the water retention behavior and the relative permeability described using the van Genuchten relationship (equations 6.5) are shown in Figure 6.8 b) and Figure 6.8 c) respectively.

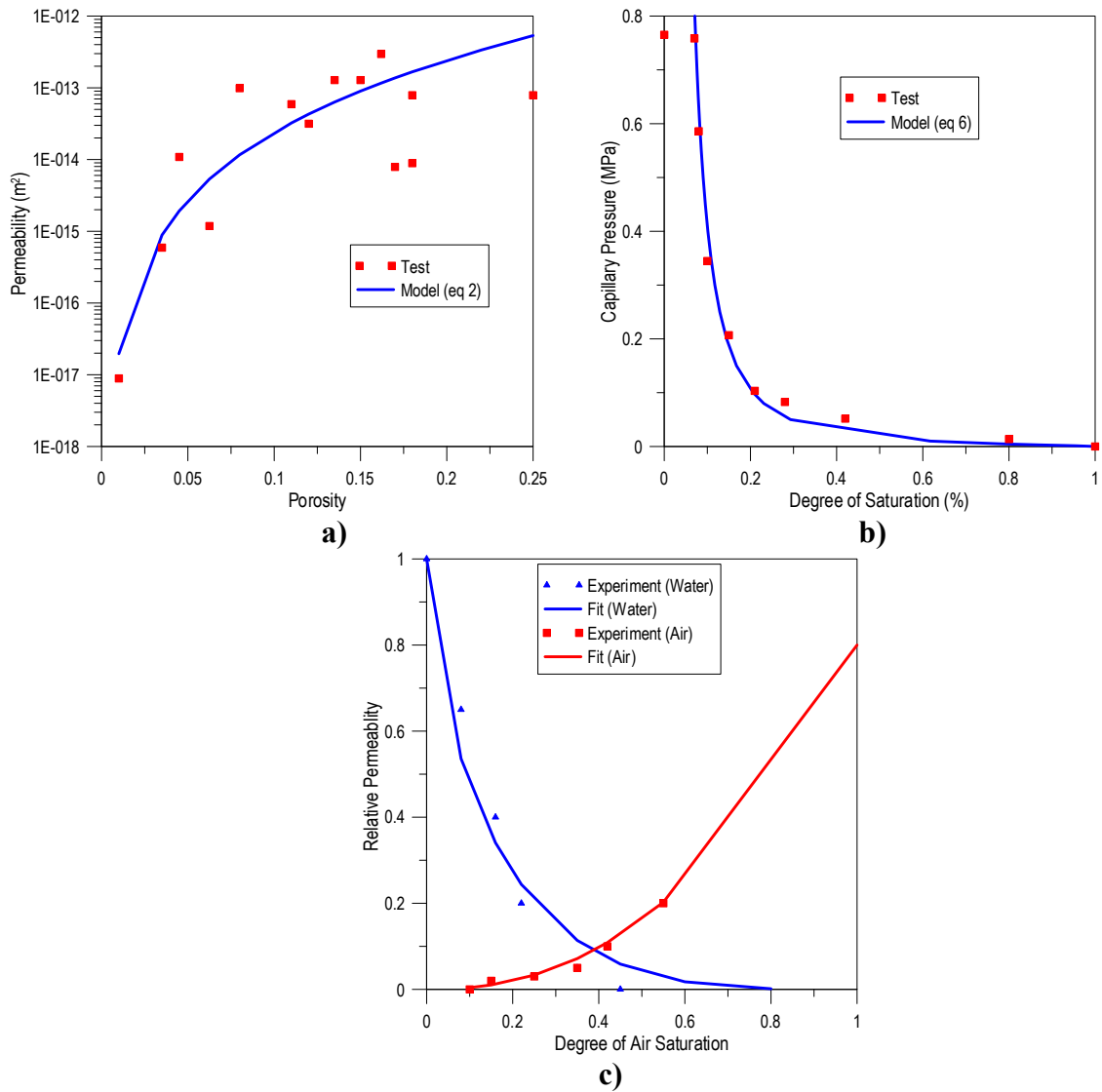


Figure 6.8 Results of the main constitutive laws used in this study a) Variation of the porosity with permeability b) Water retention curve c) Relative permeability of water and gas

The summary of the constitutive equations and the equilibrium restrictions along with the parameter used in the model are tabulated in Table 6.2

Table 6.2 Summary of Constitutive Laws and Equilibrium Restrictions

Equation	Variable name	Equation	Parameter relationships	Parameters	Equation number
Constitutive equations ($\alpha = l, g$ $i = w, a$)					
Darcy' laws	Liquid and gas advective flux	$\mathbf{q}_\alpha = -\mathbf{k} \frac{k_{r\alpha}}{\mu_\alpha} (\nabla P_\alpha - \rho_\alpha \mathbf{g})$	$\mathbf{k} = k_0 \frac{\phi^3}{(1-\phi)^2} \frac{(1-\phi_0)^2}{\phi_0^3} \mathbf{I}$	*) $k_0=6.5 \text{ m}^2$ $\phi_0 = 0.13e^{-14}$	(6.1)
Relative permeability	Liquid relative permeability	$k_{rl} = \sqrt{S_e} \left(1 - \left(1 - S_e^{1/\lambda} \right)^\lambda \right)^2$ $S_{rl} \sim 0.073$ *)		*) $\lambda=0.65$	(6.2)
Relative permeability	Gas relative permeability	$k_{rg} = AS_{eg}^\lambda$		*) $\lambda=2.3; A=0.8$	(6.3)
Fick's law	Vapor and air non advective flux	$\mathbf{i}_\alpha^i = -\mathbf{D}_\alpha^i \nabla \omega_\alpha^i =$ $\mathbf{D}_\alpha^i = (\phi \rho_\alpha S_\alpha \tau D_m^i \mathbf{I} + \rho_\alpha \mathbf{D}_\alpha^i)$	$D_m^w = d \frac{(273,15+T)^{2.3}}{P_g}$ $d = 5.9 \times 10^{-12}$	$\tau = 1$	(6.4)
Retention curve	Phase degree of saturation	$S_e = \left[1 + \left(\frac{P_c}{P_0} \right)^{\frac{1}{1-\lambda}} \right]^{-\lambda}$	$S_e = \frac{S_l - S_{lr}}{S_{ls} - S_{lr}}$ $S_l = 1 - S_g$	*) $\lambda=0.34$ $P_0=0.0047$ $P_0: [\text{MPa}]$	(6.5)

Table 6.2. Continued

Mechanical constitutive model	Linear Elastic Stress	$\dot{\boldsymbol{\sigma}}' = \mathbf{D} \dot{\boldsymbol{\varepsilon}}$ $A = \frac{E}{(1+\nu)(1-2\nu)}$ $C = \frac{(1-2\nu)}{2}$	$\mathbf{D} = A \begin{bmatrix} 1-\nu & \nu & \nu & 0 \\ \nu & 1-\nu & \nu & 0 \\ \nu & \nu & 1-\nu & 0 \\ 0 & 0 & 0 & C \end{bmatrix}$	$\begin{matrix} **) \\ E = 10 \text{ GPa} \\ \nu = 0.3 \end{matrix}$	(6.6)
Phase density	Gas density Liquid density	$\rho_g = \theta_g^a + \theta_g^w$ $\rho_l = 1002.6 \exp(4.5 \times 10^{-4} (P_l - 0.1) - 3.4 \times 10^{-4} T)$		$\begin{matrix} ***) \\ T_0 = 45 \text{ }^\circ\text{C} \end{matrix}$	(6.7)
Phase viscosity	Liquid viscosity Gas viscosity	$\mu_l = 2.1 \times 10^{-12} \exp\left(\frac{1808.5}{273.15 + T}\right)$ $\mu_g = 1.48 \times 10^{-12} \exp\left(\frac{(273.15 + T)^{1/2}}{1 + \frac{119}{(273.15 + T)}}\right)$			(6.8)
Equilibrium restrictions					
Henry's Law	Air dissolved mass fraction	$\theta_l^a = \omega_a' \rho_l = \frac{P_a}{H} \frac{M_a}{M_w} \rho_l$			(6.9)
Psychometric Law	Water vapor dissolved mass fraction	$\theta_g^w = (\theta_g^w)^0 \exp\left(\frac{-(p_g - p_l) M_w}{R(273.15 + T) \rho_l}\right)$	$(\theta_g^w)^0 = \frac{M_w P_v(T)}{R(273.15 + T)}$		(6.10)

6.5 NUMERICAL ANALYSES

The numerical analyses were conducted in two stages. A fully coupled THM analysis was performed first on the CAES reservoir by imposing air pressure. Air pressure was imposed in the two main stages considered in this study: i) air bubble formation, ii) cycles of air pressure associated with the CAES plant operation. . The temperature during the injection and withdrawal stage was calculated by assuming the system was polytropic (Zheng et al., 2010) in nature. This analysis was done primarily for two reasons namely: (i) to estimate the maximum air flow rate that can be imposed for a safe operation of the reservoir (as mentioned in section 6.4); and (ii) to analyze the effects of temperature on the behavior of the reservoir. The second study focused on the hydro-mechanical response of the reservoir when an air flow rate is imposed. This is kind of analysis is closer to actual operation conditions because in this kind of system the variable that is controlled by the air pumps is the air flow rate. . The simulation of these two analyses are described in Sections 6.5.1 and 6.5.2

6.5.1 THM analyses of CAES storage imposing air pressure

A 2-D axisymmetric section was adopted to model the 30m thick aquifer with the four layers A to D presented in Figure 6.9Figure 6.7. Figure 6.9 a) shows the finite element mesh used in the analysis consisting of 1048 elements. A denser mesh was adopted within the 200 meters from the well to properly capture the high hydraulic gradients anticipated in this region. Figure 6.9 b) presents the adopted geostatic initial stresses.

A critical operational aspect of a CAES facility in a porous-rock is the development of the initial air-bubble, generated by the air injection that displaces the natural water simultaneously. It is recommended to develop a large air-bubble in the aquifer to operate the CAES with injection/production cycles without significant changes in the reservoir pressure. Furthermore, the pressure cycles must be around the hydrostatic pressure to maintain a net change in the reservoir volume (Moridis et al., 2007). Based on the field data, the initial mean liquid pressure can be estimated around 10.5 MPa. The minimum decompression pressure is dictated by the gas-turbines coupled to CAES facility (typically the minimum operation pressure is around 6 MPa). A minimum pressure of 7 MPa was adopted in this study. The maximum compression pressure of 14 MPa was selected in order to have a pressure cycle around the hydrostatic pressure. This pressure was also satisfies the recommendations that the maximum pressure applied in the reservoir was not to exceed the lithospheric pressure (Moridis et al., 2007). To develop the initial air-bubble air was injected at a constant safe designated pressure of 14 MPa for about six months.

Figure 6.9 c) illustrates the applied air pressure at the borehole position (i.e. throughout the whole aquifer thickness), together with the initial liquid pressure (P_l) field. Based on field data (Heath et al., 2013), a hydrostatic initial P_l distribution was adopted. Impermeable top and bottom boundaries were considered to simulate the cap-rock. After the period of constant air pressure (i.e. air-bubble formation), the compression/decompression cycles during three years by imposing an injection/withdrawal pressures were simulated.

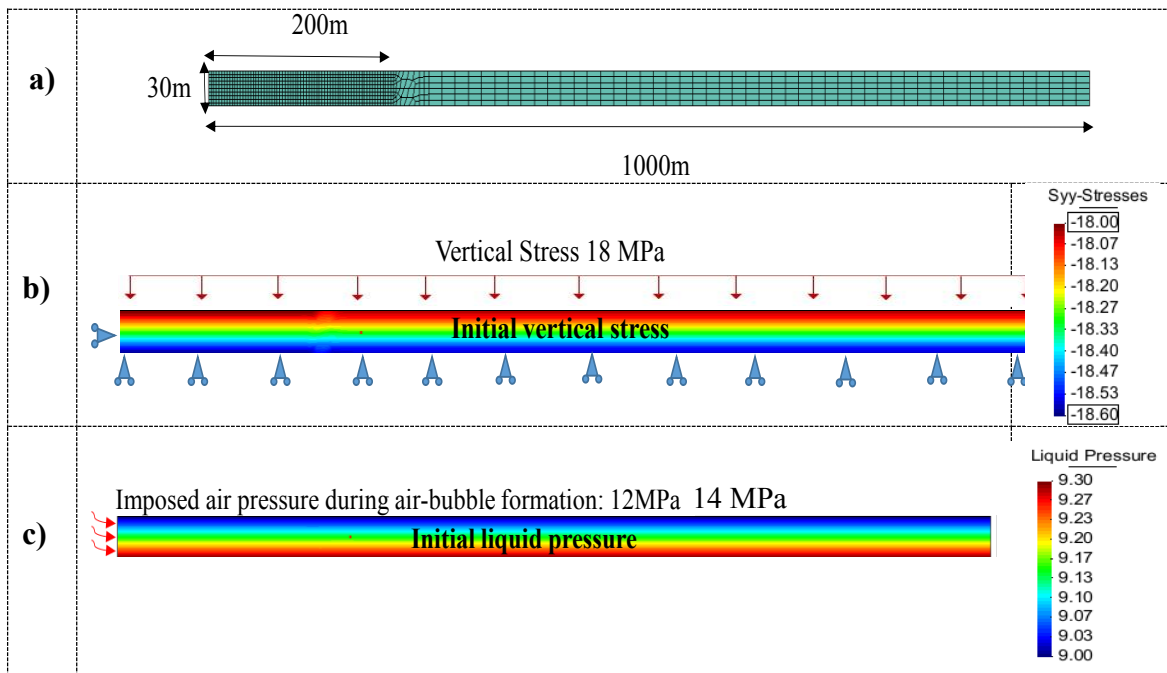
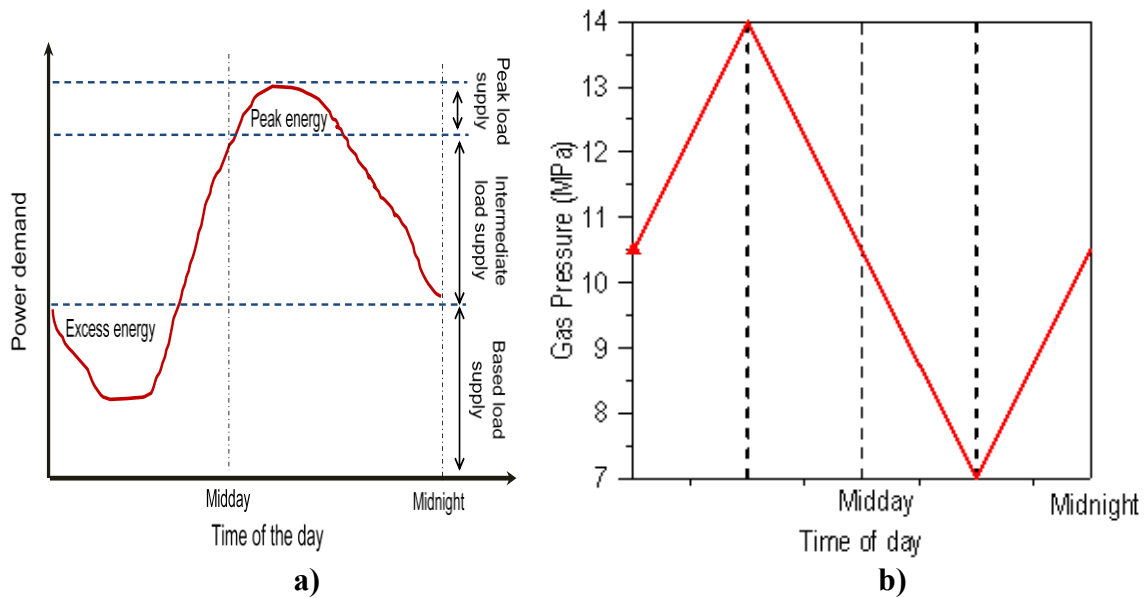


Figure 6.9 Geometry, initial and boundary conditions: a) Geometry and adopted finite element mesh b) Initial stresses and mechanical boundary conditions c) Initial liquid pressure and imposed air pressure during the air-bubble formation stage

A typical daily variation of energy demand is presented in Figure 6.10 a). Figure 6.10 b) presents the adopted pressure cycle attempting to use off-peak energy to supply energy at high demand hours. A ground temperature of 10°C and a thermal gradient of 0.03°C/m were adopted, resulting in a temperature of 40°C and 41°C at the top and bottom of the aquifer, respectively. The effect of pressure changes on temperature was calculated assuming that the gas injection/release process is polytropic in nature, resulting in a $\Delta T \sim 5^\circ\text{C}$. The polytropic coefficient calculated for the pressure and temperature range was 1.69



a)
b)
Figure 6.10 Variations of the daily demand and applied load a) Typical demand of energy (Kushnir et al., 2012) b) Applied gas pressure to match the demand

The pressure cycles as indicated in Figure 6.10 b) were applied for a period of 3 years. Figure 6.11 presents the computed gas flow for this period. For illustration, the detailed cyclic variation of air flow-rate between 800 and 820 days is presented at the bottom right of the figure. It can be seen that the gas flux of $2E-3$ Kg/s is an optimal rate of injection/withdrawal without increasing the pressure beyond the designated range. The gas flux computed here is used in the HM case in the next Section.

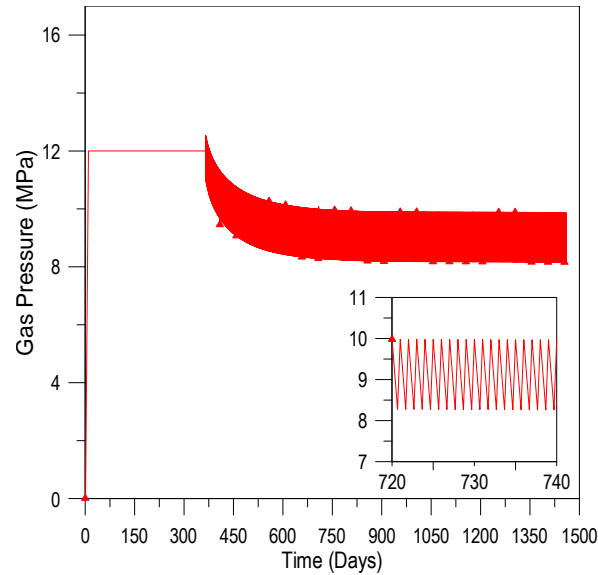


Figure 6.11 Computed gas flow rate

The domain used in the contour plots is shown in Figure 6.12. The contour plots of gas pressure, gas saturation temperature and vertical stresses, at three different times: end of bubble formation, 16, and 32 months are seen in Figure 6.13 and Figure 6.14. The results are presented at the maximum and minimum pressures. At end of the P-constant period the bubble involve around 30 meters only. This can be attributed to the relatively low permeability of the aquifer for a CAES project. The growing of the bubble during the subsequent P-T cycles implies that equilibrium with the prevailing formation conditions was not achieved after 3 years. The results at maximum and minimum pressures indicate that the effect of the cyclic load concentrates around the borehole mainly. The development of a non-uniform bubble is related to the buoyancy effects included in Darcy equation (Table 6.2). It can also be observed that the influence of

temperature limits to a quite narrow area. The operation of the CAES also impact remarkably on the stress field.

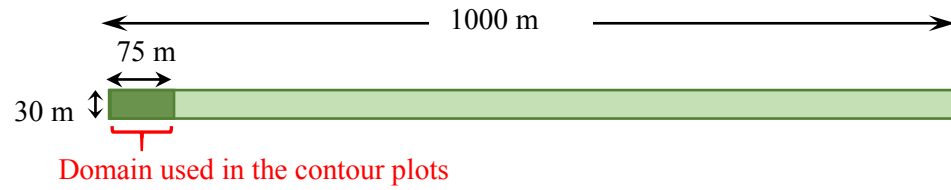
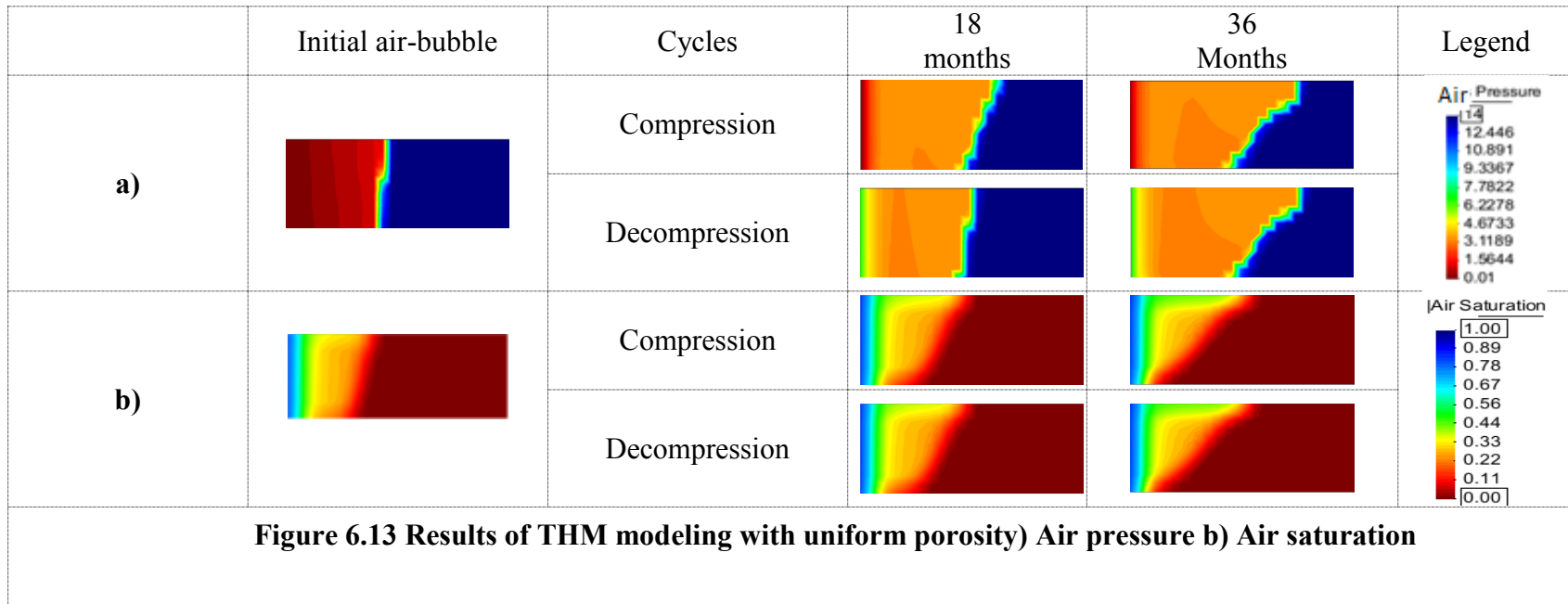


Figure 6.12 Domain used in the contour plots



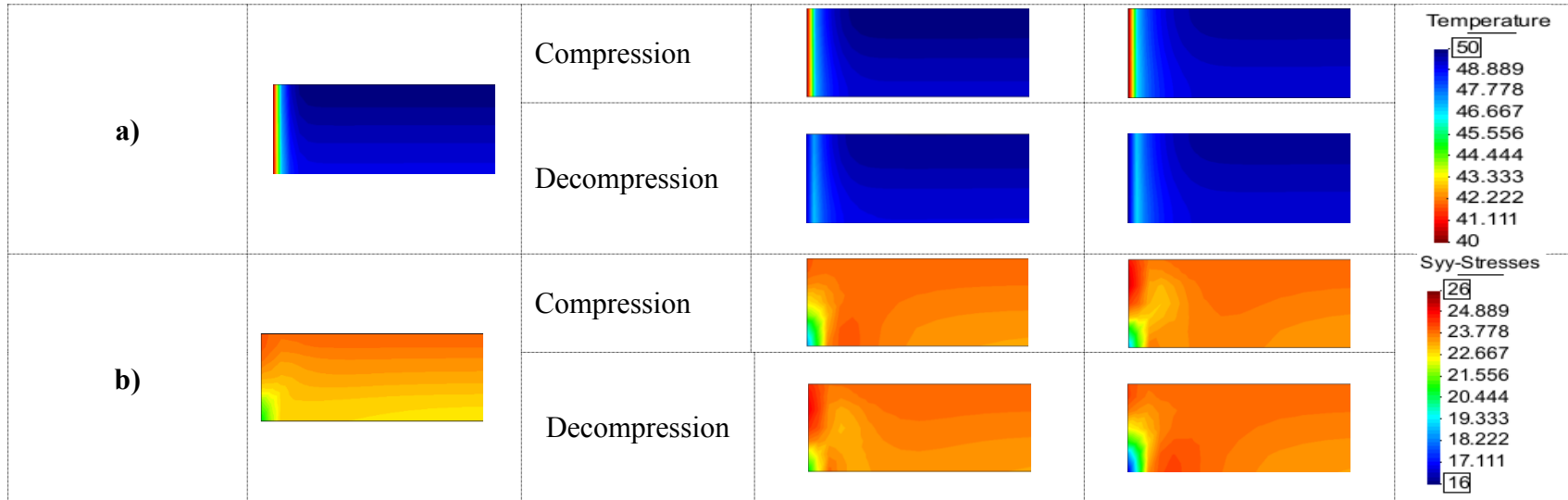
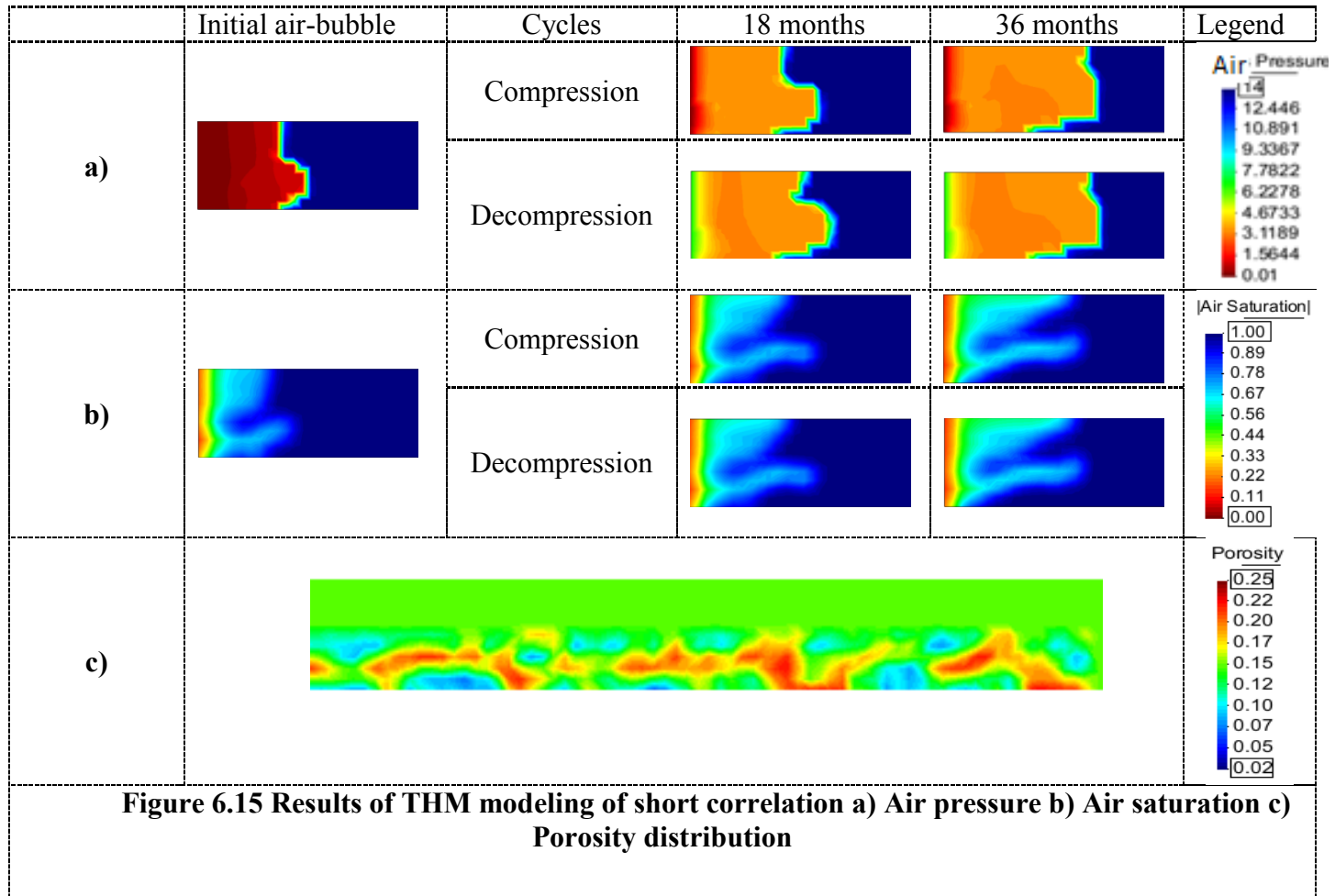
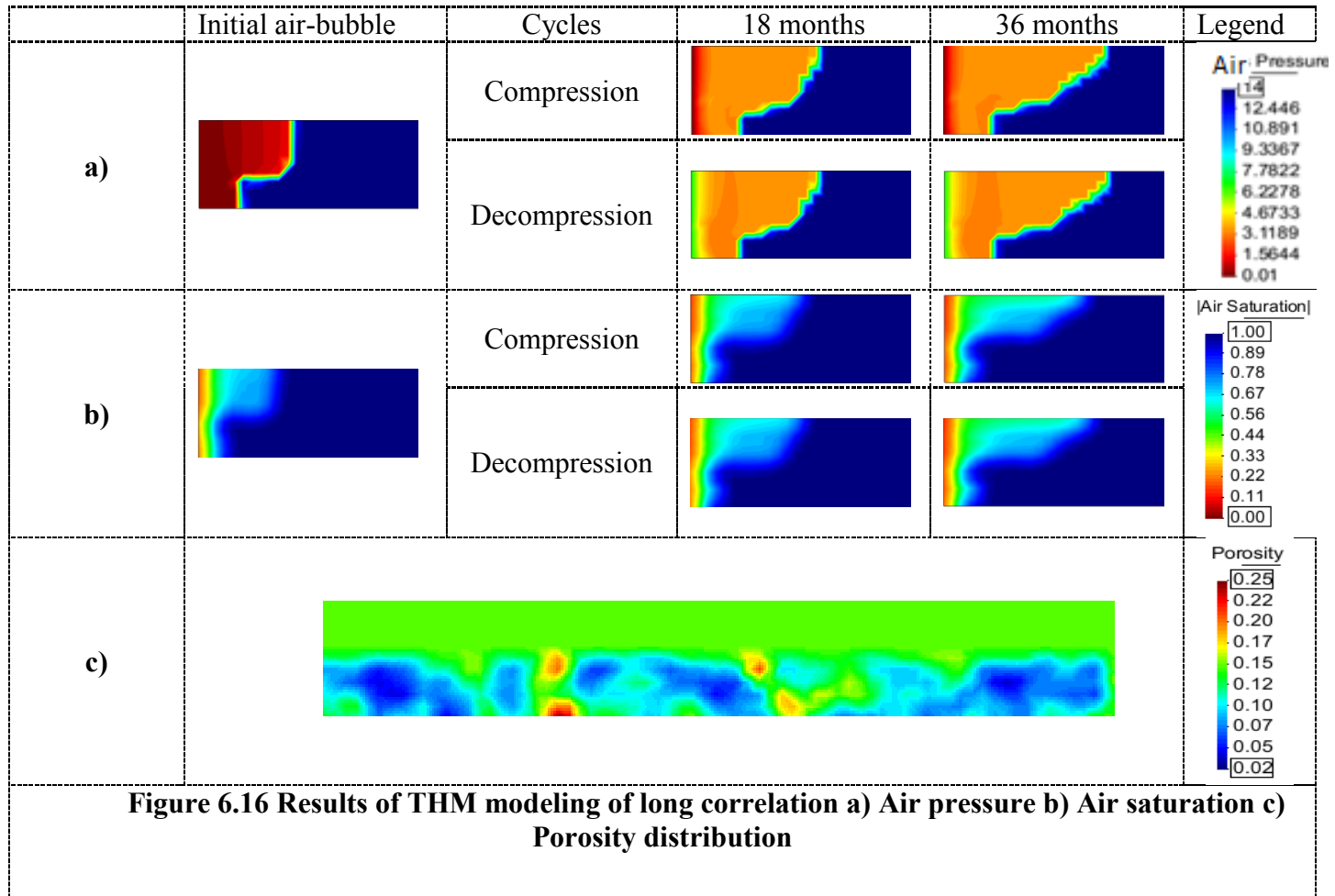


Figure 6.14 Results of THM modeling with uniform porosity) Temperature b) Vertical Stress

One of the reasons to abandon this project was the heterogeneous permeability of the reservoir, in particular layers C-D (Heath et al., 2013). The available field information is limited, but still useful to explore the impact that possible random distributions of porosity may have on the CAES performance. Two plausible scenarios corresponding to short and long correlation lengths were explored. To generate the random porosity fields we adopted the procedure proposed by Le et al. (2011, 2013). This method combines local average subdivision (Fenton and Griffiths, 2008) with a Markovian correlation function. Porosity is assumed to follow a log-normal distribution with constant mean equal to 0.13, standard deviation of 0.075 and correlation length ranging between 3 and 100 m. The impact of porosity on permeability is contemplated through equation (6.2).

Figure 6.15 and Figure 6.16 presents the results for the short and long correlation cases in term of gas pressure and saturation, alongside with the adopted porosity fields respectively. Temperature and stress plots are omitted. For the long correlation length, the presence of low porosity zones dominates the performance of the system delaying the flux of air. It is noticeable that for the case of short correlation length, layers CandD act as a preferential flow path for the air.





The impact of heterogeneities is also evident when looking at the cumulative injected air in the reservoir after 3 years (Figure 6.17a). The water production is another key aspect to be studied in a CAES project; it has to be very low to prevent problems with the gas-turbine (Succar and Williams, 2009). Figure 6.17b) shows that heterogeneities are unfavorable in this regard as well.

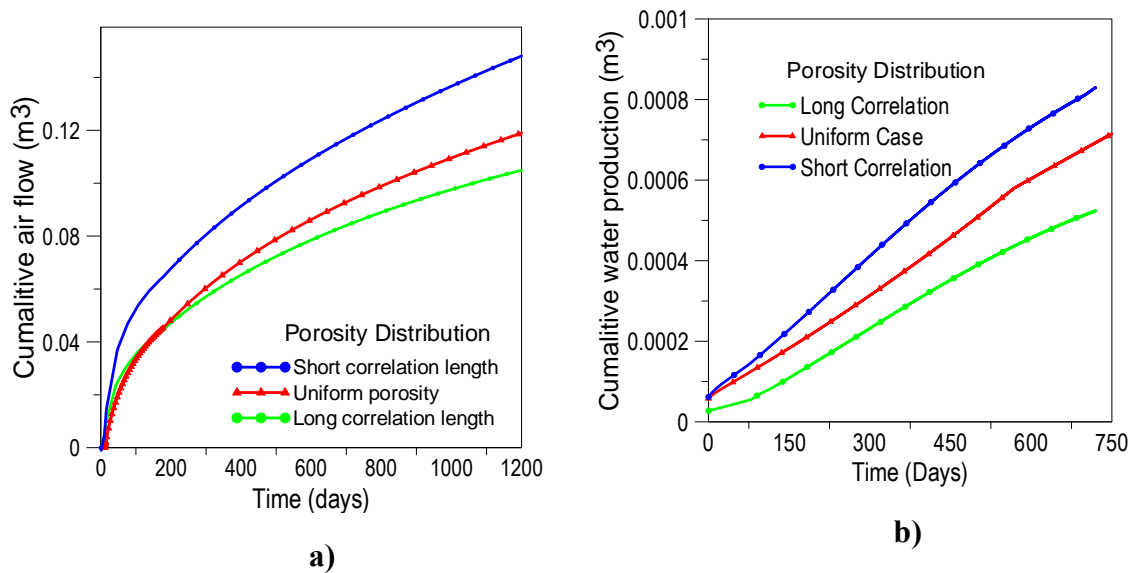


Figure 6.17 Impact of heterogeneities a) Cumulative air inflow b) Cumulative water production

6.5.2 HM analyses of CAES system imposing air flow rate

The finite element mesh is the same as the one used in THM analysis explained in section 6.5.1. To develop the initial air-bubble air was injected at a constant pressure of 12 MPa for one year. This pressure chosen is a noted drop from one which was used in the earlier model. This was done so that the maximum pressure would not exceed the designated safe pressure of 14 MPa during the operational stage of the reservoir. The

time period here was also increased as it was felt that bubble formed might have been insufficiently formed. Figure 6.18 c) illustrates the applied air pressure at the borehole position (i.e. throughout the whole aquifer thickness), together with the initial liquid pressure (P_l) field. Based on field data (Heath et al., 2013), a hydrostatic initial P_l distribution was adopted. After the period of constant air pressure (i.e. air-bubble formation), the compression/decompression cycles during three years by imposing an injection/withdrawal air flow-rates were simulated. Figure 6.18 d) shows the injected/produced air flow-rates alongside the distribution of air saturation at the end of the air-bubble formation.

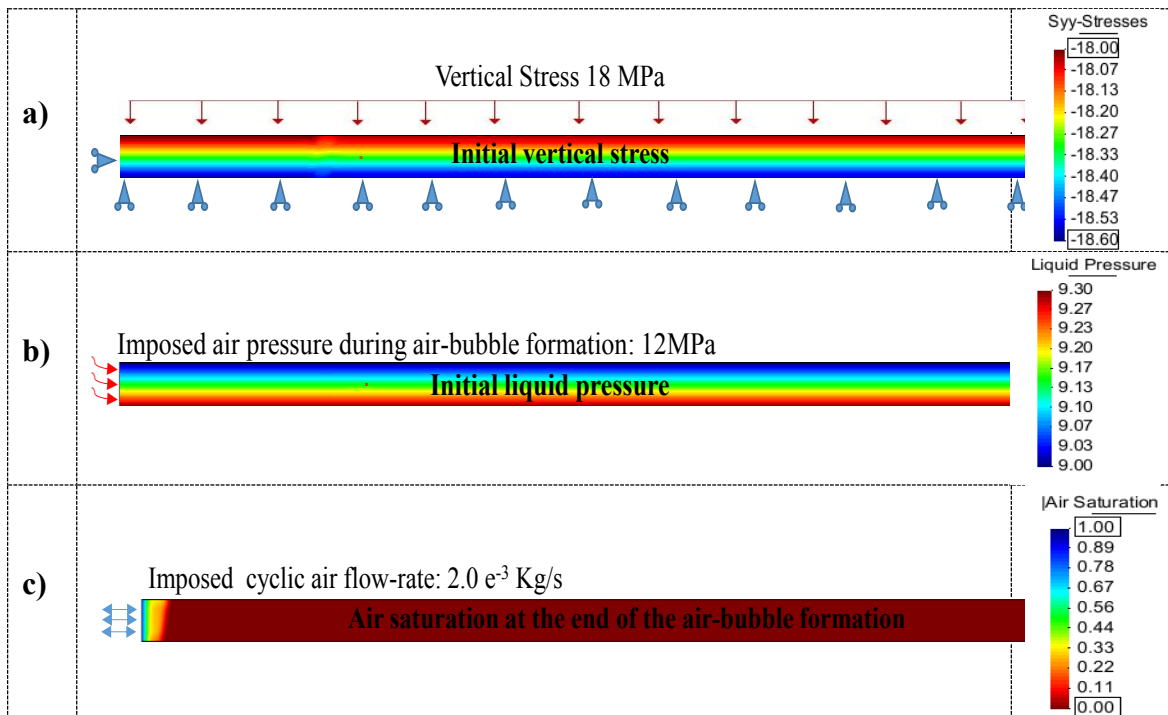


Figure 6.18 Geometry, initial and boundary conditions: a) Initial stresses and mechanical boundary conditions b) Initial liquid pressure and imposed air pressure during the air-bubble formation stage c) Air saturation of the end of air-bubble formation and imposed cyclic air flow-rate

Figure 6.19 shows the adopted gas flux cycles that attempts to use off-peak energy to supply energy at high demand hours. The daily variation of air compression/decompression was simulated by injecting air at a constant rate for 12 hours, and then producing air at a constant rate during other 12 hours. An air injection rate of $2.0\text{E-}3$ Kg/s was calculated as the optimal rate from the THM analysis described in the previous section. The adopted boundary conditions lead to a balanced pressure cycles around the hydrostatic pressure.

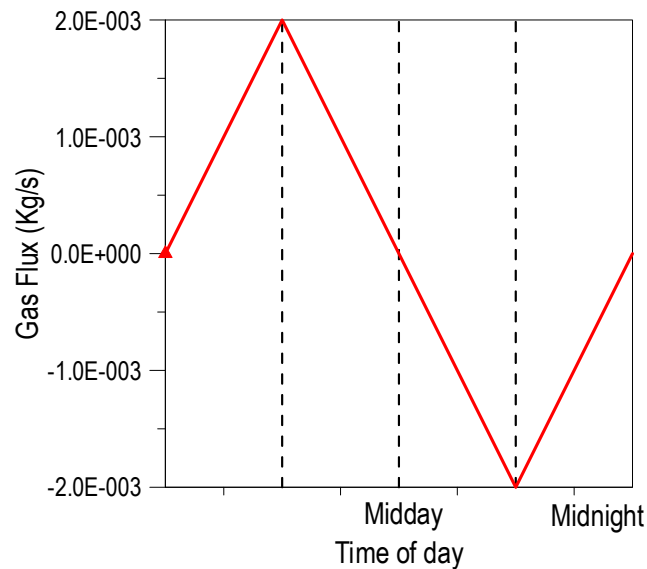


Figure 6.19 Variations in the applied load

The results of the analysis considering a constant porosity distribution are presented first (i.e. $\phi=0.13$). Figure 6.20 shows the evolution of P_a for both stages (i.e. air-bubble formation and injection/withdrawal cycles). A detailed cyclic variation of P_a between 720 and 740 days is presented at the bottom right of the figure. The computed

P_a decreases just after the bubble formation period and then oscillates around the hydrostatic P_l .

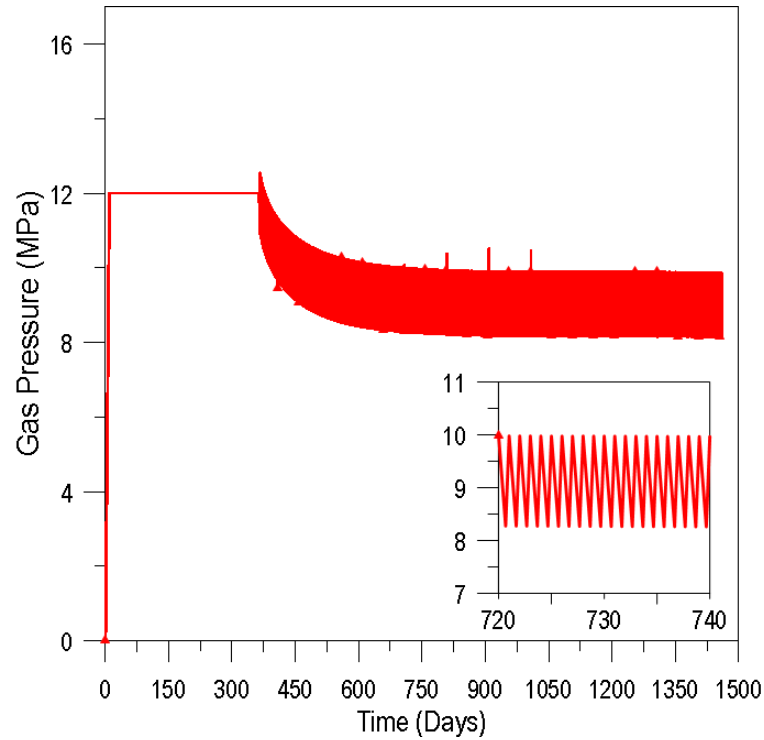


Figure 6.20 Evolution of gas pressure for the uniform case

The results of the modelling are shown in Figure 6.22 and Figure 6.23. The domain used in the contour plots is shown in Figure 6.21. The P_a (Figure 6.22 a), air saturation (Figure 6.22 b), horizontal stress (Figure 6.23 a), vertical stress (Figure 6.23 b), and porosity (Figure 6.23 c). The results are presented at three different injection periods: end of the bubble formation, 18 months, and 36 months. Contours plots at the end of injection and withdrawal stages are shown for each of these periods. The size of the bubble does not change significantly during the compression/decompression cycles.).

Note that to facilitate the air inflow/outflow in the aquifer irreducible water saturation (i.e. $S_{ri} \sim 0.073$ for this rock, Heath et al., 2013) should prevail in the air-bubble to lead to maximum air permeability. However, in this analysis S_{ri} was only observed in a quite tiny volume around the well. The operation of the CAES also changes the stress and porosity fields. The perturbations are more noticeable near the injection zone; nevertheless they are quite small due to the high-stiffness of the host-rock. The impact of heterogeneities is once again inspected using the same methodology used in Section 6.5.1. The randomly distributed porosities is reused from the THM analysis. Figure 6.24 presents the evolution of air pressure for the four years of analysis and for the two extreme random fields studied in this work.

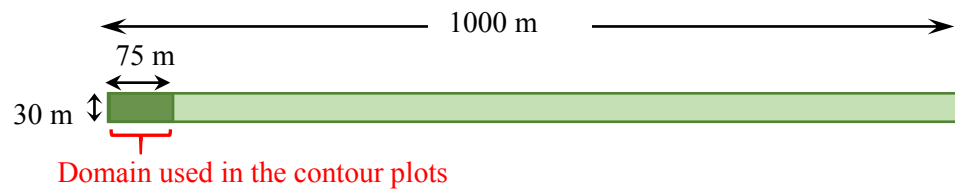
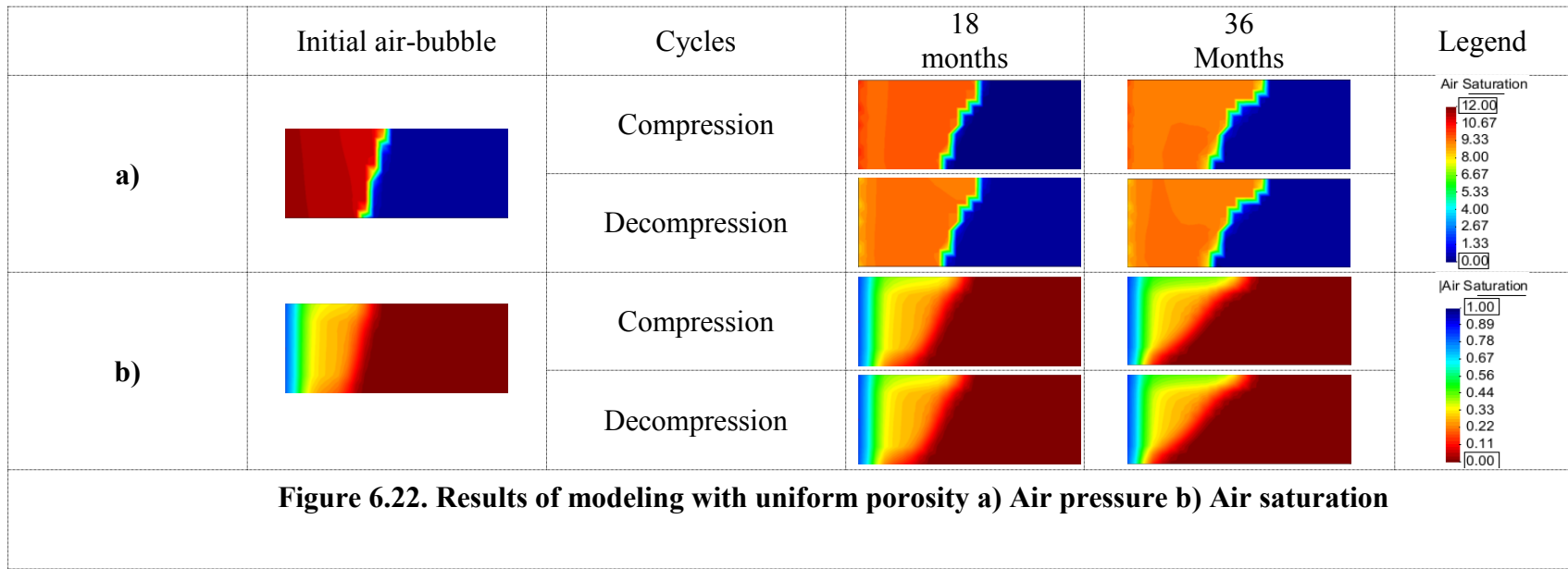


Figure 6.21 Adopted geometry and domain used in the contour plots



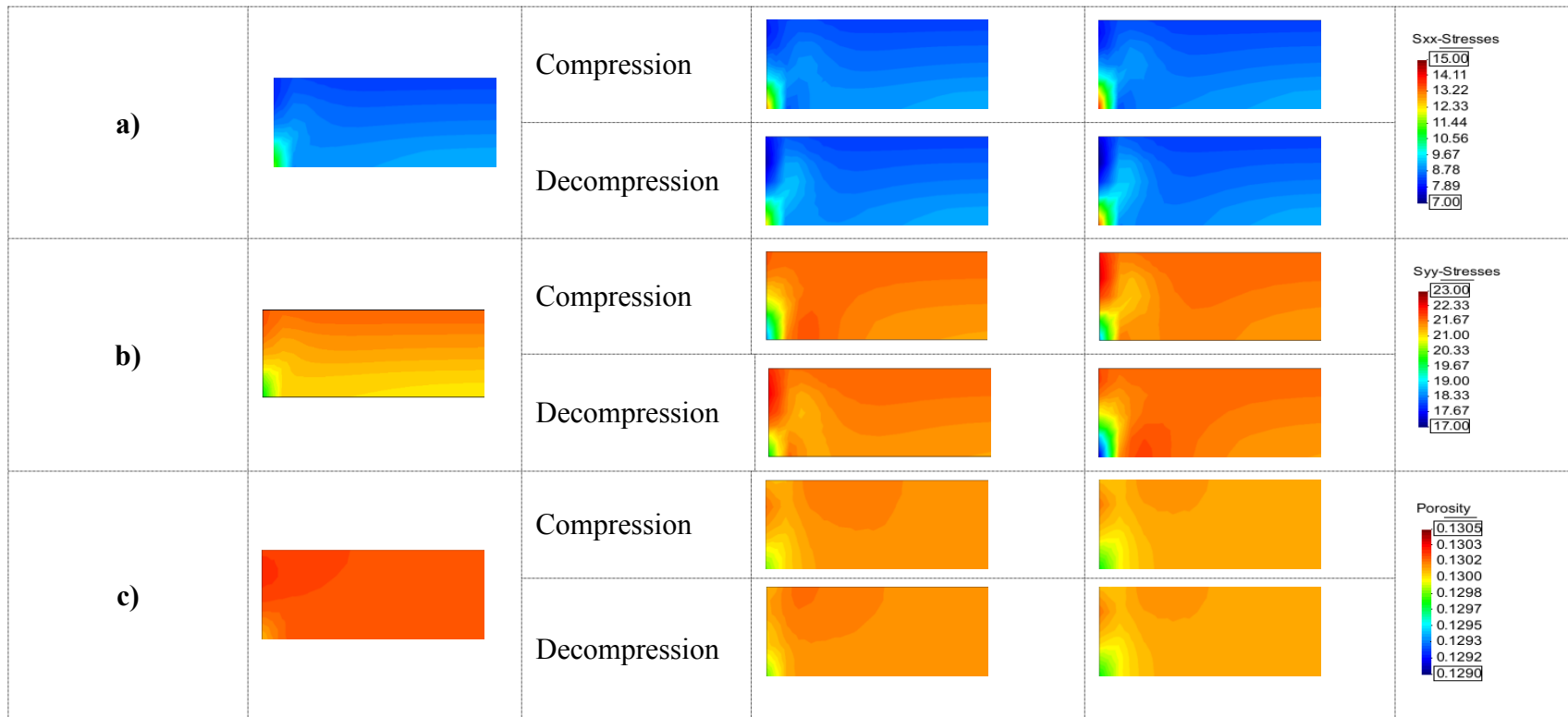


Figure 6.23 Results of modeling with uniform porosity a) Horizontal Stress b) Vertical Stress c) Porosity

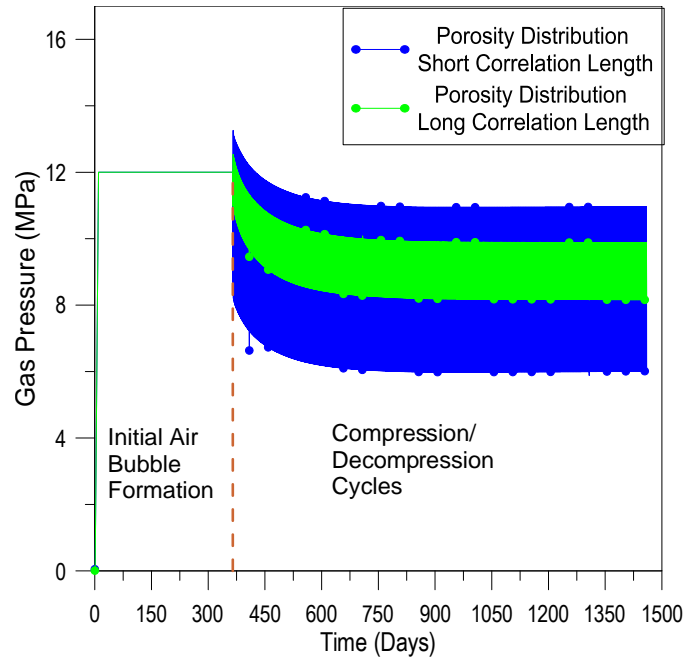
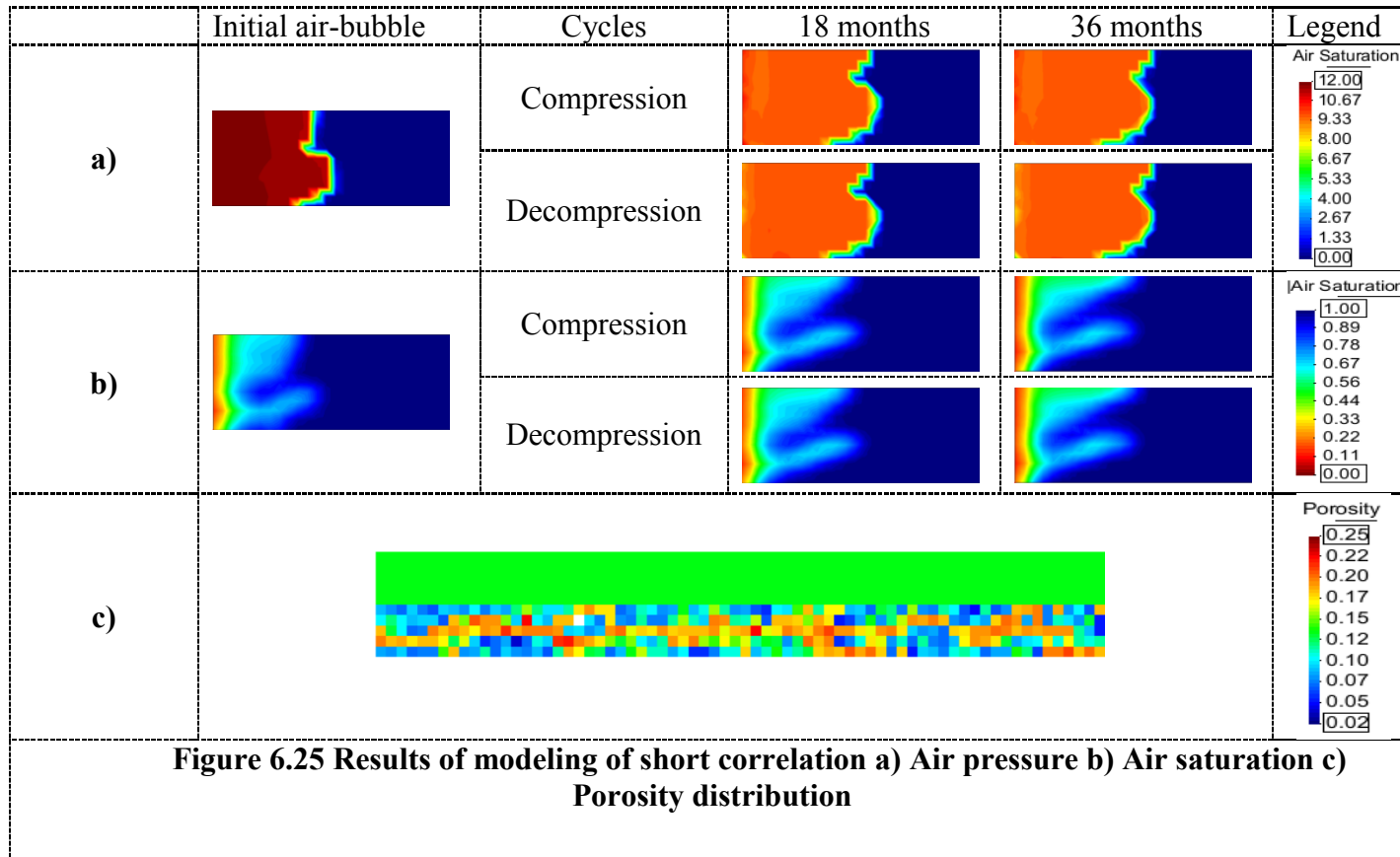
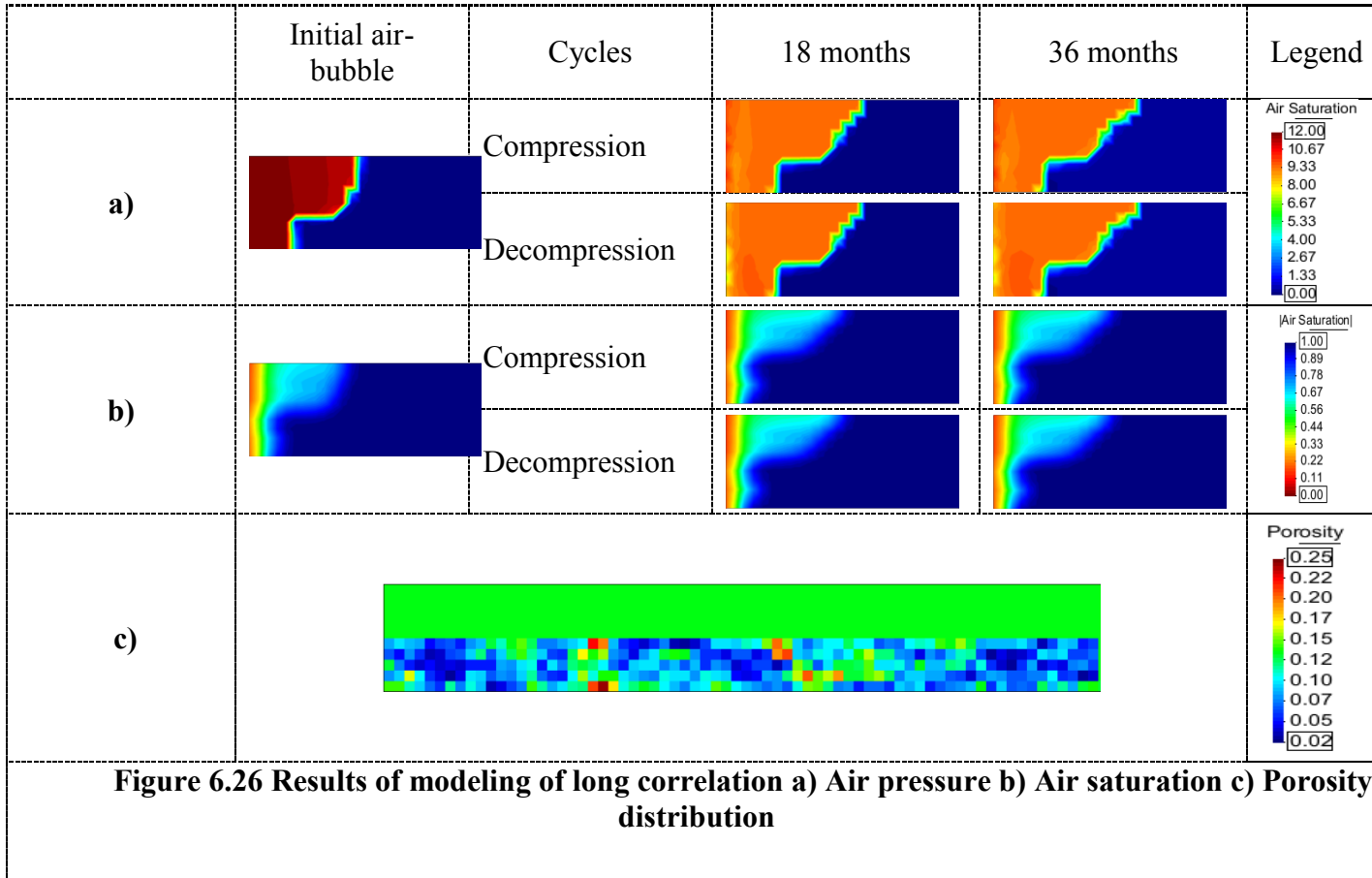


Figure 6.24 Evolution of the gas pressures for the long and short correlations

Figure 6.25 and Figure 6.26 presents the numerical results in terms of air pressure and air saturation for the short and long correlation porosity fields respectively. For the long correlation length, the presence of low porosity zones dominates the performance of the system, delaying the flux of air (e.g. compare the air-bubble formation Figure 6.26 b) and Figure 6.22 b). As for the short correlation length, the model predicts the presence of undesirable fingering effects, leading to air-flow pathways that do not fill the entire structure (Figure 6.25b).





The impact of heterogeneities is also evident when looking at the cumulative injected air during the first year (Figure 6.27 a). The air injected in the short correlation length case is around three times higher than the one computed in the uniform porosity case, evidencing the presence of air pathways. The water production is another key aspect to be studied in a CAES project. It has to be very low to prevent problems with the gas-turbine (Succar and Williams, 2009). The water produced in the short correlation analysis is the highest computed one (Figure 6.27 b), nevertheless the amount of water produced is quite small.

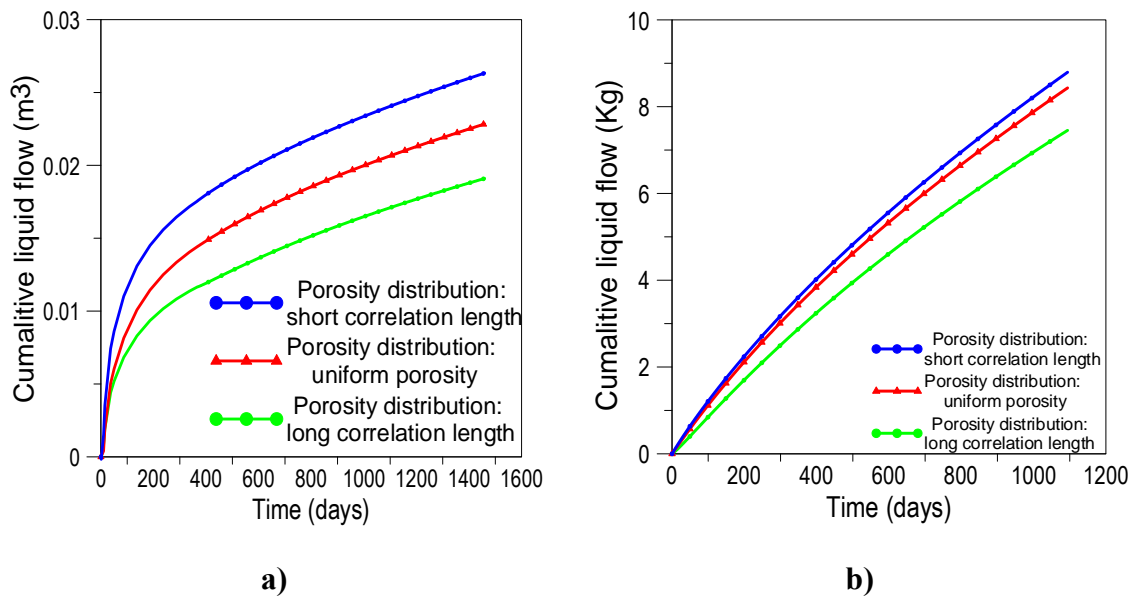


Figure 6.27 Liquid flow in the aquifer a) Cumulative air flow intake during the one year period of air injection at constant pressure (i.e. formation of air-bubble) b) Cumulative water production during the subsequent three years of compression/decompression cycles

7 SUMMARY AND SCOPE FOR FURTHER WORK

7.1 SUMMARY

Three distinct topics have been covered in this Thesis, concerning various aspects of the interaction between soils and the environment: frozen soils; hydrate bearing sediments; storage of compressed air in underground aquifers. In most of them the classical soil mechanics formulation has been generalized to account for a broader range of phenomena and soil behavior. This has been done by:

- Introducing new variables such as cryogenic suction and subzero temperature.
- Enhancing the balance equations as required by the formulation: water/air/gas mass balance and equilibrium (momentum balance). This has allowed the performance of coupled analyses of increasing degree of complexity, namely: TH, HM and THM.
- Extending generalized constitutive laws to account for complex soil behavior.
- Demonstrating the application of the formulations proposed to case studies in order to illustrate the usefulness of the developments described.

It is possible to perceive several common themes, present in classical soil mechanics, inspiring the advances presented.

- Materials are multiphase with phase changes affecting the soil behavior greatly.
- The relevant phenomena are generally strongly coupled with mutual interactions.
- Soil behavior features are often closely linked, and may be understood in an integrated manner.

- Microstructure plays a significant role in soil behavior.

7.2 CONCLUSIONS AND SCOPE FOR FUTURE WORK

The major conclusions drawn and scope of improvements have identified in this section. They have been described based on the topic covered here.

Frozen soils

The work conducted in this Thesis constitutes an effort to explore further the behavior of frozen soils and to explore the capabilities of a THM formulation to simulate their behavior under varying temperatures and mechanical conditions. The mechanical framework chosen in this is based on Barcelona Basic Model modified to include the effects of low temperature and cryogenic suction. The cryogenic suction, calculated from Clausius-Clapeyron equation, increases with a decrease in temperature under conditions of constant liquid pressure. Hydraulic behavior of the reconstituted samples was examined. Mechanical behaviors of natural and reconstituted samples were examined using the coupled THM model. The finite element program CODE_BRIGHT was used in the simulations. The results of the modeling are in close agreement with the experimental results. The model was then used to simulate collapse compression behaviors observed in failure of foundation and pipelines. The major conclusion are:

- The behavior of frozen soils was found to be similar to that of unsaturated soils in qualitative terms.
- The isotropic tests reveal that the variation of the mean stress with the voids ratio is negligible in the elastic zone and decreases with a decrease in decrease in temperature post yielding.

- The hydrostatic tests also indicate an increase in the apparent pre-consolidation pressure with a decrease in temperature.
- An increase in the maximum strength of the soil is observed with the decrease in temperature.
- The strength increases with an increase in confining pressure.
- The proposed model is able to incorporate the main tendencies of frozen soil behavior quoted above and it is also a reliable tool to simulate the collapse behavior which takes place post thawing, as it was demonstrated with the case studies presented in Section 3.

The THM model for frozen soils however, was not able to account for the volumetric changes observed during cyclic freeze and thaw. After an intensive search in the open literature, it was found that the available information on freeze-thaw behavior was quite scarce for closed systems and in particular for fine grained soils. An experimental campaign was then undertaken to understand the behavior of the clayed soils subjected to freeze/thaw cycles. The experimental campaign revealed the clay behavior with different OCR experience similar behaviors as previously observed in samples made up of coarse grained soils with different densities. Based on all the available data (i.e. already published experimental data and new tests performed in this Thesis) it was observed that:

- The microstructure of soils subjected to freeze/thaw cycles has a significant impact on the final macroscopic response of these soils.

- It was observed that loose soils developed a net contraction while dense soils showed a net expansion after subjecting them to cycles of freezing and thawing temperatures.
- After a few cycles the soils attained a fairly constant or 'residual' state, wherein the plastic deformations observed due to freezing would equal those observed during thawing, resulting in a net zero volume change at the end of the freeze-thaw cycle.

Based on these observations an elastoplastic mechanical model was proposed in this Thesis extending the previously proposed THM model for frozen soils to account now for the changes in soils during freeze-thaw cycles. The proposed model incorporates a couple of interaction functions which determines the amount of plastic deformation accumulated during the phase transition of water to ice during freezing and ice to water during thawing. The concept of the equilibrium point allows accounting for the residual state achieved after a certain number of cycles.

The experimental procedure suggested here seems appropriate to study the behavior of clayed soils subjected to freeze/thaw cycles. Although repeated tests need to be performed on greater number of samples and soil structures to reaffirm the expected behavior, the results obtained in this Thesis represent a progress respect to the current state of the art. The constitutive model perhaps requires a larger amount of data that for a comprehensive validation. However the data used in this Thesis can be considered appropriate for a partial validation of the model; and also satisfactory to check the ability

of the model to simulate the main patterns observed in soils subjected to freeze/thaw cycles.

As future work, it is suggested to perform more experiments to increase the available test data in this area. The model also requires a more in deep validation involving, for example, more case studies associated with actual problems involving freeze/thaw cycles.

Hydrate bearing sediments

A general mathematical formulation was developed to analyze coupled THMC problems involving gas hydrate bearing sediments (Sanchez et al., 2014). It takes into consideration thermal processes (conduction, phase transformation), hydraulic processes (multiphase flow), effective-stress dependent sediment response and the change in sediment properties in the presence of hydrates.

This formulation was upgrade to consider the behavior of HBS at low temperatures and the effect of water salinity Simulation results compare favorably with published results with well-defined boundary conditions; this corroborates the validity of the implementation. The model properly captures the complex interaction between water and gas, and kinetic differences between ice and hydrate formation. Therefore, it permits exploring the development of phases along the various Pressure-Temperature trajectories that may take place in field situations. Results show the pronounced effect of hydrate dissociation on pore fluid pressure generation.

A more advanced model for the mechanical behavior of the HBS is recommended. The corresponding validation needs to be performed for both established

laboratory experiments as well as established field studies to fully understand the impact of hydrate disassociation on stability of the HBS.

Compressed air energy storage

A coupled formulation was adopted to analyze the behavior of CAES in an aquifer. The model was based on field and laboratory information of an actual site contemplated for a CAES project in Iowa. The analysis was conducted in two distinct stages. The first, was understanding the performance of the reservoir by applying the gas pressure during the operational stage. The analysis was conducted for case considering heterogeneities in the host rock for this case. Based on the result obtained here, a secondary analysis was conducted by applying a suitable gas flux calculated from the results of the first analysis. The simulation of the operational stage was redone with this gas flux during the operational stage with heterogeneous distribution of the properties. The analysis has confirmed that the site is not adequate for a CAES plant. The relatively low permeability of the natural rock prevents the development of a large and the stable air-bubble necessary to maintain required volume of air for the turbo-generator. Furthermore, the heterogeneous character of the aquifer has on strong negative impact on both the amount of air injected and water produced.

The impact of the heterogeneity of the various features needs to be studied by conducting a more robust set of simulations. The cap-rock was modeled as an impervious boundary but in reality it might not be so impervious. The impact of fissures and mechanical behavior of the cap-rock needs to be incorporated into the model.

Despite these shortcomings this is a preliminary study into the behavior has shown a great potential in replicating the behavior of a porous rock CAES.

7.3 CONCLUDING REMARKS

The requirement for complex frameworks to describe the behavior of soil is best quoted by Dr. Antonio Gens “Problems facing geotechnical engineers are complex and this often leads to complex formulations. It is possible, however, to reduce the risk of drowning in complexity (Biot, 1963). Although it will never be possible (or even sensible) to avoid the use of empirical rules based on experience, it is advisable, when dealing with new and complex problems, to base the formulations and theoretical approaches on sound physical principles as much as is practicable.” (Gens, 2009)

To conclude, it can be stated that the extension of classical soil mechanics, conducted with the same underlying spirit and approach, can assist to a better understanding and provides the tools that are required to tackle current and future challenges coupled problems in geotechnical engineering. The possibilities exist, and they will come into increasing use in the future.

REFERENCES

- Ahmadi, G., Ji, C., and Smith, D.H. 2004. Numerical solution for natural gas production from methane hydrate dissociation. *Journal of Petroleum Science and Engineering* 414, 269-285.
- Allen, K. 1985. CAES: the underground portion. *IEEE Transactions on Power Apparatus and Systems*, PAS-104, 809-12.
- Allen, R. D., Doherty, T. J., Erikson, R. L., and Wiles, L. E. 1983. Factors affecting storage of compressed air in porous-rock reservoirs. Pacific Northwest Lab., Richland, WA USA.
- Andersland, O.B., and Ladanyi, B. 2004. *Frozen ground engineering*. John Wiley and Sons Inc. New Jersey. USA
- Arenson, L.U., and Springman, S.M. 2005. Mathematical descriptions for the behavior of ice-rich frozen soils at temperatures close to 0°C. *Canadian Geotechnical Journal*, 422, 431-442.
- Beskow, G. 1935. Tjälbildningen och tjällyftningen med särskild hänsyn till vägar och järnvägar. [English translation: Soil freezing and frost heaving with special application to roads and railroads Translated by J. O. Osterberg. Evanston, Illinois, Technological Institute, Northwestern University, [1947.]
- Biot, M. A. 1941. General theory of three-dimensional consolidation. *Journal of Applied Physics*. 12, 155–164.
- Biot, M. A. 1963. Are we drowning in complexity? *Mechanical Engineering*. 85, 26–27.
- Briaud, J. L., and Chaouch, A. 1997. Hydrate melting in soil around hot conductor. *Journal of Geotechnical and Geoenvironmental engineering*, 1237, 645-653.
- Briaud, J.L. 2013. *Geotechnical Engineering: Unsaturated and Saturated Soils*, John Wiley and Sons. New Jersey. USA
- Calontiw, S. 2013. Facts about Wind Energy for Kids <<http://technologygreenenergy.blogspot.com/2013/11/facts-about-wind-energy-for-kids.html>>
- Chamberlain, E. J., and Gow, A. J. 1979. Effect of freezing and thawing on the permeability and structure of soils. *Engineering Geology*, 131, 73-92.

- Chatti, I., Delahaye, A., Fournaison, L., and Petitet, J.P. 2005. Benefits and drawbacks of clathrate hydrates: a review of their areas of interest. *Energy Conversion and Management*; 46:1333–1343.
- Collett, T. S., Johnson, A. H., Knapp, C. C., and Boswell, R. 2008. Indian National Gas Hydrate Program Expedition 01 initial reports: Expedition 01 of the Indian National Gas Hydrate Program from Mumbai, India to Chennai, India; Sites NGHP-01-01 through NGHP-01-21, April 2006–August 2006, Dir. Gen. of Hydrocarbons, Ministry of Petroleum And Natural Gas, Noida, India.
- Côté, J., and Konrad, J.M. 2005. A generalized thermal conductivity model for soils and construction materials. *Canadian Geotechnical Journal*, 422, 443-458.
- Coussy, O., 2005. Poromechanics of freezing materials. *Journal of the Mechanics and Physics of Solids*, 538, 1689-1718.
- Crotogino, F., Mohmeyer, K. U., and Scharf, R. 2001. Huntorf CAES: More Than 20 Years of Successful Operation, in Solution Mining Research Institute Meeting Orlando, Florida, USA.
- Davie, M.K., and Buffett, B.A. 2001. A numerical model for the formation of gas hydrate below the seafloor. *Journal of Geophysical Research*, 106B1, 497-514.
- DOE (Department of energy), 1999. Frozen Soil Barrier, Report number EM-0483
- DeVries, K. L., Mellegard, K. D., Callahan, G. D., and Goodman, W. M. 2005. Cavern Roof Stability For Natural Gas Storage In Bedded Salt, United States Department of Energy National Energy Technology Laboratory Topical Report RSI-1829, DE-FG26-02NT41651, June 2005.
- Dickens, G., Paull, C., and Wallace, P. 1997. Direct measurement of in situ methane quantities in a large gas-hydrate, *Nature* 385:426-428.
- EPRI-DOE, 2003. Handbook of Energy Storage for Transmission and Distribution Applications, EPRI, DOE, Palo Alto, CA, Washington, DC.
- Everett, D. 1961. The thermodynamics of frost damage to porous solids. *Transactions of the Faraday Society*, 57, 1541-1551.
- Fredlund, D.G., and Morgenstern, N.R. 1977. Stress state variables for unsaturated soils. *American Society of Civil Engineers*, 103, GT5, 447-446.
- Gens, A. 2010. Soil–environment interactions in geotechnical engineering. *Geotechnique*, 60(1), 3-74.

- Gens, A., and Olivella, S. 2000. Non-isothermal multiphase flow in deformable porous media: coupled formulation and application to nuclear waste disposal. In *Developments in theoretical geomechanics: The John Booker Memorial Symposium* D. W. Smith and I. P. Carter, 619–640. Rotterdam: A. A. Balkema.
- Gens, A., and Alonso, E. E. 1992. A framework for the behaviour of unsaturated expansive clays. *Canadian Geotechnical Journal*, 29, 1013–1032.
- Gens, A., and Nova, R. 1993. Conceptual bases for a constitutive model for bonded soils and weak rocks. In *Geotechnical Engineering of Hard Soils–Soft Rocks*, 1, . 485–494. Rotterdam: Balkema.
- Gens, A., and Alonso, E.E. 1992. A framework for the behavior of unsaturated expansive clays. *Canadian Geotechnical Journal*, 29, 1013–1032.
- Gens, A., and Nova, R. 1993. Conceptual bases for a constitutive model for bonded soils and weak rocks. In: Agagnostopoulos, A. et al. Eds., *Proceedings of the Symposium on Geotechnical Engineering of Hard Soils – Soft Rocks*. Balkema, 485–493.
- Gens, A., Garcia, M.A., Olivella, S., Alonso, E.E., and Huertas, F. 1998. Analysis of a full scale in-situ test simulating repository conditions. *International Journal for Numerical and Analytical Methods in Geomechanics*, 22, 515–548.
- Gens, A., Sánchez, M., Guimarães, L., Lloret, A., Olivella, S., and Alonso, E. 2009. A full scale in situ heating test for high level nuclear waste disposal. Observations, analysis and interpretation. *Géotechnique*. May, 59, 377–399. doi: 10.1680/geot.2009.59.4.377.
- Gens, A., Vaunat, J., Garitte, B., and Wileveau, Y. 2007. In situ behaviour of a stiff layered clay subject to thermal loading: observations and interpretation. *Geotechnique*, 572, 207-228.
- Gens, A., Valleján, B., Sánchez, M., Imbert, C., Villar, M., and Van Geet, M. 2010. Hydromechanical behaviour of a heterogeneous compacted soil: experimental observations and modelling. *Geotechnique*, 615, 367-386.
- Gilpin, R., 1980. A Model for the Prediction of Ice Lensing. *Water Resources Research*, 165, 918-930.
- Guimarães, L., Gens, A., Sánchez, M., and Olivella, S. 2006. THM and reactive transport analysis of expansive clay barrier in radioactive waste isolation. *Communications in Numerical Methods in Engineering*, 22 8: 849–859.

- Guimarães L., 2002. Análisis multi-componente no isoterma en medio poroso deformable no saturado. PhD thesis, Universitat Politècnica de Catalunya, Spain.
- Guimarães L., Gens, A. and Olivella, S. 1999. THM and reactive transport coupling in unsaturated porous media. Proc. 7th Int. Symp. on Numerical Models in Geomechanics, Graz, 303–308.
- Guimarães, L., Gens, A., and Olivella, S. 2007. Coupled thermo-hydro-mechanical and chemical analysis of expansive clay subjected to heating and hydration. *Transport in Porous Media*, 66, 341–372.
- Guymon, G. L., and Luthin, J. N. 1974. A coupled heat and moisture transport model for arctic soils. *Water Resource*, No 10, 995–1001.
- Hanna, A., Saunders, R., Lem, G., and Carlson, L. 1983. Alaska Highway Gas Pipeline Project Yukon Section Thaw Settlement Design Approach. Proc., Proceedings: 4th International Conference on Permafrost, Fairbanks, Alaska.
- Hansson, K., and Lundin, L.C. 2006. Equifinality and sensitivity in freezing and thawing simulations of laboratory and in situ data. *Cold Regions Science and Technology*, 44, 20–37.
- Hansson, K., Simunek, J., Mizoguchi, M., Lundin, L.-C. and van Genuchten, M. Th. 2004. Water flow and heat transport in frozen soil: numerical solution and freeze-thaw applications, *Vadose Zone Journal* 3, 693–704.
- Harlan, R., 1973. Analysis of coupled heat-fluid transport in partially frozen soil. *Water Resources Research* 95, 1314-1323.
- Haug, M. D., and Wong, L. C. 1992. Impact of molding water content on hydraulic conductivity of compacted sand-bentonite. *Canadian Geotechnical Journal*, 292, 253-262.
- Hawkes, I., and Mellor, M. 1972. Deformation and fracture of ice under uniaxial stress. *Journal of Glaciology*, 11, 103-131.
- Heath, J., Bauer, S.J., Broome, S.T., Dewers, T., and Rodriguez, M. 2013. Petrologic and petrophysical evaluation of the Dallas Center Structure, Iowa, for compressed air energy storage in the Mount Simon Sandstone. Sandia National Laboratories SNL-NM, Albuquerque, NM United States.
- Hyodo, M., Nakata, Y., Yoshimoto, N., and Ebinuma, T. 2005. Basic research on the mechanical behavior of methane hydrate-sediments mixture. *Soils and Foundations*, 451, 75-85.

- Hyodo, M., Nakata, Y., Yoshimoto, N., and Yoneda, J. 2008 Shear Strength of methane hydrate bearing sand and its deformation during dissociation of methane hydrate. In: Proceedings of the 4th International Symposium on Deformation Characteristics of Geomaterials, 549–556
- Jamaluddin, A., Kalogerakis, N., and Bishnoi, P. 1991. Hydrate plugging problems in undersea natural gas pipelines under shutdown conditions. *Journal of Petroleum Science and Engineering*, 5, 323-335.
- Jame, Y. W., and Norum, D.I. 1980. Heat and mass transfer in a freezing unsaturated porous medium. *Water Resource Research*, 164, 811-819.
- Jessberger, H.L. 1981. A state-of-the-art report. Ground freezing: mechanical properties, processes and design. *Engineering Geology*, 18, 5–30.
- Johnson, L., Yarmak, E., and Long, E. 2000. Cryogenic Barrier Demonstration Project. Final Report. Arctic Foundations, Inc., Anchorage, AK (US).
- Kamath, V., and Godbole, S. 1987. Evaluation of hot-brine stimulation technique for gas production from natural gas hydrates. *Journal of Petroleum Technology*, 3911. 1379-1388.
- Kayen, R., and Lee, H. 1991. ‘Pleistocene slope instability of gas hydrate-laden sediment’. *Marine Geotechnology*; 10:125-141
- Kiger, P J. 2013 Can an Ice Wall Stop Radioactive Water Leaks from Fukushima <<http://news.nationalgeographic.com/news/energy/2013/08/130819-japan-ice-wall-for-fukushima-radioactive-leaks/>>
- Kim, H.-M., Rutqvist, J., Ryu, D.-W., Choi, B.-H., Sunwoo, C., and Song, W.-K. 2012. Exploring the concept of compressed air energy storage CAES in lined rock caverns at shallow depth: a modeling study of air tightness and energy balance. *Applied Energy*, 92, 653-667.
- Klar, A., Soga, K., and Ng, M. 2010. Coupled deformation—flow analysis for methane hydrate extraction. *Geotechnique*, 6010, 765-776
- Konrad, J. M., and Duquennoi, C. 1993. A model for water transport and ice lensing in freezing soils. *Water Resources Research*, 299, 3109-3124.
- Konrad, J. M. and Morgenstern, N.R., 1980. A mechanistic theory of ice lens formation in fine-grained soils. *Canadian Geotechnical Journal*, 174, 473-486.
- Konrad, J.-M. 1989. Physical processes during freeze-thaw cycles in clayey silts. *Cold Regions Science and Technology*, 163, 291-303.

- Konrad, J.M. 2010. Hydraulic conductivity changes of a low-plasticity till subjected to freeze thaw cycles. *Geotechnique*, 609, 679-690.
- Konrad, J.M., and Morgenstern, N.R. 1981. The segregation potential of a freezing soil. *Canadian Geotechnical Journal*, 184, 482-491.
- Konrad, J.M., and Morgenstern, N.R. 1984. Frost heave prediction of chilled pipelines buried in unfrozen soils. *Canadian Geotechnical Journal*, 211, 100-115.
- Konrad, J.-M., and Samson, M. 2000. Hydraulic conductivity of kaolinite-silt mixtures subjected to closed-system freezing and thaw consolidation. *Canadian Geotechnical Journal*, 374, 857-869.
- Konrad, J.M., and Shen, M. 1996. 2-D frost action modeling using the segregation potential of soils. *Cold Regions Science and Technology*, 243, 263-278.
- Kushnir, R., Dayan, A., and Ullmann, A. 2012. Temperature and pressure variations within compressed air energy storage caverns. *International Journal of Heat and Mass Transfer*, 55, 5616-5630.
- Kwon, T.H., Cho, G.C., and Santamarina, J.C., 2008. Gas hydrate dissociation in sediments: Pressure-temperature evolution. *Geochemistry, Geophysics, Geosystems* 93, Q03019.
- Ladanyi, B., and Johnston, G. 1974. Behavior of circular footings and plate anchors in permafrost. *Canadian Geotechnical Journal* 114, 531-553.
- Le, T., Gallipoli D., Sánchez, M., and Wheeler, J. 2013. Rainfall-induced differential settlements of shallow foundations on heterogeneous unsaturated soils. *Géotechnique*, 63, 1346–1355.
- Le, T. Gallipoli, D., Sánchez, M., Wheeler, J. 2011. Stochastic Analysis of unsaturated seepage through randomly heterogeneous earth embankments. *International Journal for Numerical and Analytical Methods in Geomechanics*, 36, 1056–1076.
- Lee, M.Y., Fossum, A., Costin, L. S., and Bronowski, D. 2002. Frozen soil material testing and constitutive modeling. Report No. SAND2002-0524, Sandia National Laboratory, USA.
- Lihach, N. 1982. Breaking New Ground With Caes, *EPRI Journal*, 7, 17-21.
- Liu, Z., and Yu, X. 2011. Coupled thermo-hydro-mechanical model for porous materials under frost action: theory and implementation. *Acta Geotechnica*, 1-15.
- Loch, J.P.G. 1978 Thermodynamic equilibrium between ice and water in porous media. *Soil Science*, 1262: 77D80

- Makogon, Y. 2010. 'Natural gas hydrates – A promising source of energy' *Journal of Natural Gas Science and Engineering*, 2, 49–59
- Makogon, Y. 1966. Peculiarities a Gas-Field Development in Permafrost. Nedra, Moscow.
- Makogon, Y. F. 1965. Hydrate formation in the gas-bearing beds under permafrost conditions. *Gazovaia Promyshlennost*, 5, 14-15.
- Masui, A., Haneda, H., Ogata, Y, and Aoki, K. 2005. 'The effects of saturation degree of methane hydrate on the shear strength of synthetic methane hydrate sediments'. *Proceedings of the Fifth International Conference on Gas Hydrates*, June 12-16, Trondheim, Norway.
- Masui, A., K. Miyazaki, H. Haneda, Y. Ogata, and K. Aoki. 2008. 'Mechanical characteristics of natural and artificial gas hydrate bearing sediments', paper 5697 presented at the 6th International Conference on Gas Hydrates, Chevron, Vancouver, B. C., Canada, 6–10 July.
- Mehta, B., 1992. CAES geology, *EPRI Journal*, 17, 38-41.
- Mellor, M., and Cole, D. M. 1982. Deformation and failure of ice under constant stress or constant strain-rate. *Cold Regions Science and Technology*, 53, 201-219.
- Michalowski, R. L., and Zhu, M., 2006. Frost heave modelling using porosity rate function. *International Journal for Numerical and Analytical Methods in Geomechanics*, 308, 703-722.
- Michel, B., and Ramseier, R. 1971. Classification of river and lake ice. *Canadian Geotechnical Journal*, 81, 36-45.
- Miller, R. D. 1978. Frost heaving in non-colloidal soils. *Third International Conference on Permafrost Natural Resources*. Council of Can.Edmonton, Alta.
- Miller, R., Loch, J., and Bresler, E. 1975. Transport of water and heat in a frozen permeameter. *Soil Science Society of America Journal*, 396, 1029-1036.
- Moridis, G., Collett, T., Boswell, R., Kurihara, M., Reagan, M., Koh, C., and Sloan, E. 2008. Toward production from gas hydrates: current status, assessment of resources, and simulation-based evaluation of technology and potential. *SPE Reservoir Evaluation and Engineering*, 125, 745-771.
- Moridis, G., Silpngarmert, S., Reagan, M., Collett, T., and Zhang, K. 2010. Gas production from a cold, stratigraphically bounded hydrate deposit at the Mount Elbert site, North Slope, Alaska. *Marine and Petroleum Geology*, 30, 1-18.

- Mortrench.2011.Peripheral-freezing.
<http://www.moretrech.com/services.articles.php?Peripheral-Freezing->
- Multon, S., Sellier, A., and Perrin, B. 2012. Numerical analysis of frost effects in porous media. Benefits and limits of the finite element poroelasticity formulation. *International Journal for Numerical and Analytical Methods in Geomechanics*, 364, 438-458.
- Nakano, Y. 1997. A mathematical model called M1 and the Gilpin model of soil freezing. *Proceedings of the international symposium on ground freezing and frost action in soils, Lulea*, 139–146.
- NSIDC (National Snow and Ice Data Center). 2013 All about sea ice/ Ice formation <
<http://nsidc.org/cryosphere/seaice/characteristics/formation.html>>
- Nazridoust, K., and Ahmadi, G. 2007. Computational modeling of methane hydrate dissociation in a sandstone core. *Chemical Engineering Science*, 6222, 6155-6177.
- Newman, G.P., and Wilson, G.W. 1997. Heat and mass transfer in unsaturated soils during freezing. *Canadian Geotechnical Journal*, 341, 63-70.
- Nishimura, S., Gens, A., Olivella, S., and Jardine, R. 2009. THM-coupled finite element analysis of frozen soil: formulation and application. *Geotechnique*, 593, 159-171.
- Nixon, J. 1990. Effect of climatic warming on pile creep in permafrost. *Journal of cold Regions Engineering*, 41, 67-73.
- Nixon, J.F. 1978. Foundation design approaches in permafrost areas. *Canadian Geotechnical Journal* 15, 96–112.
- O’Neill, K., and Miller, R.D. 1985. Exploration of a rigid ice model of frost heave. *Water Resources Research*, 213, 281-296.
- Olivella, S., Gens, A., Carrera, J., Alonso, E.E. 1996. Numerical formulation for a simulator CODE-BRIGHT for the coupled analysis of saline media. *Engineering Computations*, 137, 87–112.
- Olivella, S., Gens, A., Carrera, J., and Alonso, E.E. 1994. Nonisothermal multiphase flow of brine and gas through saline media. *Transport in Porous Media*, 15, 271-293.
- Parameswaran, V. 1980. Deformation behaviour and strength of frozen sand. *Canadian Geotechnical Journal*, 171, 74-88.

- Parameswaran, V., and Jones, S. 1981. Triaxial testing of frozen sand. *Journal of Glaciology*, 2795, 147-155.
- Parry, M., Canziani, O., Palutikof, J., Van der Linden, P., and Hanson, C. 2007. IPCC, 2007: climate change 2007: impacts, adaptation and vulnerability. Contribution of working group II to the fourth assessment report of the intergovernmental panel on climate change. Cambridge University Press, Cambridge.
- Paudel, B., and Wang, B. 2010. Freeze-thaw effect on consolidation properties of fine grained soils from the Mackenzie valley, Canada. In *Proceedings: GEO2010-63rd Canadian Geotechnical Conference*, Calgary Canada.
- Pinyol, P, N.M., Vaunat, J., and Alonso, E. 2009. A constitutive model for soft clayey rocks that includes weathering effects. *Geotechnique*, 57, 137–151.
- Pusch, R. 1979. Unfrozen water as a function of clay microstructure. *Engineering Geology*, 131, 157-162.
- Qi, J., Hu, W., and Ma, W. 2010. Experimental study of a pseudo-preconsolidation pressure in frozen soils. *Cold Regions Science and Technology*, 603, 230-233.
- Rekacewicz, P. 2005. Permafrost distribution in the Arctic <<http://maps.grida.no/go/graphic/permafrost-distribution-in-the-arctic>>
- Raju, M., and Khaitan, S. 2012. Modeling and simulation of compressed air storage in caverns: a case study of the Huntorf plant. *Applied Energy*, 891, 474-481.
- Rempel, A., and Buffett, B. 1997. Formation and accumulation of gas hydrate in porous media. *Journal of Geophysical Research*, 102.
- Romanovsky, Vladimir E. 2010. How rapidly is permafrost changing and what are the impacts of these changes? http://www.arctic.noaa.gov/essay_romanovsky.html.
- Rutqvist, J. 2011. Status of the TOUGH-FLAC simulator and recent applications related to coupled fluid flow and crustal deformations. *Computers and Geosciences* 376, 739-750.
- Rutqvist, J., and Moridis G. 2007. Numerical studies of geomechanical stability of hydrate-bearing sediments. *Offshore Technological Conference*, Houston, U.S.A.; OTC 18860.
- Rutqvist, J., Kim, H.-M., Ryu, D.-W., Synn, J.-H., and Song, W.-K. 2012. Modeling of coupled thermodynamic and geomechanical performance of underground compressed air energy storage in lined rock caverns. *International Journal of Rock Mechanics and Mining Sciences*, 52, 71-81.

- Sanchez, M., 2010. Transport in Porous Media. Class notes Texas A&M University.
- Sanchez, M., Gens, A., Guimaraes, L.N., and Olivella, S. 2005. A double structure generalized plasticity model for expansive materials. *International Journal of Numerical Analysis Methods in Geomechanics*, 29, 751–787.
- Sanchez, M., Gens, A., Guimaraes, L. do N. and Olivella, S. 2008. Implementation algorithm of a generalised plasticity model for swelling clays. *Computers and Geotechnics*, 35, 860–871
- Sayles, F. H. 1973. Triaxial and creep tests on frozen Ottawa sand. Proc., Proceedings of the North American Contribution to the 2nd International Permafrost Conference, Yakutsk, USSR National Academy of Sciences, Washington, DC, 384-391.
- Schoeneich, P., Dall’Amico, M., Deline, P., Zischg, A. 2011. Hazards related to permafrost and to permafrost degradation. PermaNET project, state-of-the-art report 6.2. On-line publication ISBN 978-2-903095-59-8.
- Schulson, E. M. 2004. Compressive shear faults within arctic sea ice: Fracture on scales large and small. *Journal of Geophysical Research: Oceans* 109C7.
- Shepard, S., and van der Linden, S. 2001. Compressed air energy storage adapts proven technology to address market opportunities, *Power Engineering Barrington, Illinois*, 105, 34-37.
- Shoop, S., Affleck, R., Haehnel, R., and Janoo, V. 2008. Mechanical behavior modeling of thaw-weakened soil. *Cold Regions Science and Technology*, 522, 191-206.
- Simms, D. A., Schreck, S., Hand, M., and Fingersh, L. 2001. NREL unsteady aerodynamics experiment in the NASA-Ames wind tunnel: a comparison of predictions to measurements, National Renewable Energy Laboratory Colorado, USA.
- Sinha, N. K. 1989. Elasticity of natural types of polycrystalline ice. *Cold Regions Science and Technology*, 172, 127-135.
- Sloan, E.D. 1998. *Clathrate Hydrates of Natural Gases*. 2nd Edition. Marcel Dekker Inc New York
- Soga, K., Lee, S.L., Ng, M.Y.A., and Klar A. 2006. Characterisation and Engineering Properties of Methane Hydrate Soils. 2nd International Workshop on Characterisation and Engineering Properties of Natural Soils. Singapore.

- Stern, L. A., Kirby, S. H., and Durham, W. B. 1998. Polycrystalline methane hydrate: Synthesis from superheated ice, and low-temperature mechanical properties. *Energy and Fuels*, 122, 201-211.
- Stys, Z. S. 1977. Compressed air storage for load leveling of nuclear power plants, in *Proceedings of the 12th Intersociety Energy Conversion Engineering Conference*. II Washington, DC, USA: American Nuclear Soc, 1023-30.
- Succar, S., and Williams, R. H. 2008. Compressed air energy storage: Theory, resources, and applications for wind power. Princeton Environmental Institute Report.
- Sultan, N., Foucher, J. P., Cochonat, P., Tonnerre, T., Bourillet, J. F., Ondreas, H., Cauquil, E., and Grauls, D. 2004. Dynamics of gas hydrate: case of the Congo continental slope. *Marine Geology*, 2061-4, 1-18.
- Sun, R., and Duan, Z. 2007. An accurate model to predict the thermodynamic stability of methane hydrate and methane solubility in marine environments. *Chemical geology*, 2441-2, 248-262.
- Taber, S. 1929. Frost heaving. *The Journal of Geology*, 428-461.
- Thomas, H., Cleall, P., Li, Y., Harris, C., and Kern-Luetschg, M. 2009. Modelling of cryogenic processes in permafrost and seasonally frozen soils. *Geotechnique* 593, 173-184.
- Tice, A. R., Anderson, D. M., and Banin, A. 1976. The prediction of unfrozen water contents in frozen soils from liquid limit determinations. In *Proceedings Symposium on Frost Action on Roads, Paris 1976*.
- Tice, A., Black, P., and Berg, R. 1988. Unfrozen water contents of undisturbed and remolded Alaskan silt. *Cold Regions Science and Technology*, 172, 103-111.
- Vaughan, P. R. 1999. Special lecture: Problematic soil or problematic soil mechanics *Proceedings of the international symposium on problematic soils, Sendai*, 2, 803–814.
- Viklander, P. 1998. Permeability and volume changes in till due to cyclic freeze/thaw *Canadian Geotechnical Journal*, 35, 471–477
- Varani, A. 2001. Frozen soils and climate systems <http://earthobservatory.nasa.gov/Features/FrozenSoils/>
- Wagner, W., and Prub, A. 2002. The IAPWS formulation 1995 for the thermodynamic properties of ordinary water substance for general and scientific use. *Journal of Physical and Chemical Reference Data*, 312, 387-535.

- Weeks, W.F. 1998. *Physics of Ice-Covered Seas*, ed. M. Leppäranta Helsinki: Helsinki University Printing House, 1998, 1-24 and 25-104
- Watson, G. H., Slusarchuwk, A., and Rowley, K. 1973. Performance of a warm-oil pipeline buried in permafrost. In *Proceedings. 2nd, Int. Conf. Permafrost, North American Contributions*. National Academy of Science. 759-776
- White, K. D. 1999. Hydraulic and physical properties affecting ice jams. DTIC Document.
- Williams, P. J. 1964. Unfrozen water content of frozen soils and soil moisture suction. *Geotechnique*, 143, 231-246.
- Xu, W., and Ruppel, C. 1999. Predicting the occurrence distribution and evolution of methane gas hydrate in porous marine sediments. *Journal of Geophysical Research* 104B3, 5081-5095.
- Xu, W., Germanovich, L.N. 2006. Excess pore pressure resulting from methane hydrate dissociation in marine sediments: A theoretical approach. *Journal of Geophysical Research* 111B1 B01104.
- Xu, X., Wang, J., Zhang, L., Deng Y. 1999, *Mechanisms of Frost Heave and Salt Expansion of Soils*. Science Press.
- Yasufuaku, N., and Springman, S. 1999. Stress-Strain Relationship of Frozen Sand at Small Strain as a Composite Material Bericht Nr. I 463 Zurich.
- Yoneda, J., Hyodo, M., Nakata, Y., and Yoshimoto, N. 2010. Triaxial Shear Characteristics of Methane Hydrate-bearing Sediment in the Deep Seabed, *Journal of Geotechnical and Geoenvironmental Engineering*, 66, 742-756 in Japanese
- Yun, T., Santamarina, J. C., and Ruppel, C. 2007. ‘Mechanical properties of sand, silt, and clay containing synthetic hydrate’. *Journal of Geophysical Research*, doi:10.1029/2006JB004484
- Yun, T. S., Fratta, D., and Santamarina, J. C. 2010. Hydrate-Bearing Sediments from the Krishna– Godavari Basin: Physical Characterization, Pressure Core Testing, and Scaled Production Monitoring. *Energy & Fuels*, 2411, 5972-5983.
- Zeimusu, 2008. Gas hydrates 1996. <http://en.wikipedia.org/wiki/Methane_clathrate>
- Zheng, B., Zhang, J., and Qin, Y. 2010. Investigation for the deformation of embankment underlain by warm and ice-rich permafrost. *Cold Regions Science and Technology* 602, 161-168.

Zhukov, V. 1990. Basic causes of deformation of buildings constructed on permafrost.
Soil Mechanics and Foundation Engineering, 274, 174-178

APPENDIX

The appendix lists the basic constitutive and balance equations used in the dissertation.

A.1 BALANCE EQUATIONS

Mass balance equations were established following the compositional approach, which consists of balancing the species rather than the phases. Water is present in liquid and gas phases. The total mass balance of water is expressed as (Olivella et al. 1994):

$$\frac{\partial}{\partial t}(\theta_l^w S_l n + \theta_g^w S_g n) + \nabla \cdot (\mathbf{j}_l^w + \mathbf{j}_g^w) = f^w \quad (\text{A1})$$

The main variable associated with this equation is the liquid pressure (P_l). A similar equation can be written for the mass balance of air (Olivella et al. 1994), however this equation has not been used in this analyses as a constant gas pressure has been assumed (Gens et al., 2009). Thermal equilibrium between phases has been assumed; consequently only one equation is required to establish energy balance. The total internal energy per unit volume of porous media is obtained adding the internal energy of each phase corresponding to each medium. Applying the balance equation to this quantity, the following equation is obtained:

The main variable associated with this equation is the liquid pressure (P_l). A similar equation can be written for the mass balance of air (Olivella et al. 1994), however this equation has not been used in this analyses as a constant gas pressure has been assumed (Gens et al., 2009). Thermal equilibrium between phases has been assumed; consequently only one equation is required to establish energy balance. The total internal energy per unit volume of porous media is obtained adding the internal

energy of each phase corresponding to each medium. Applying the balance equation to this quantity, the following equation is obtained:

$$\frac{\partial}{\partial t} (E_s \rho_s (1-n) + E_l \rho_l S_l n + E_g \rho_g S_g n) + \nabla \cdot (\mathbf{i}_c + \mathbf{j}_{E_s} + \mathbf{j}_{E_l} + \mathbf{j}_{E_g}) = f^E \quad (\text{A2})$$

The temperature (T) is the main variable associated with this equation. The balance of momentum for the porous medium reduces to the equilibrium equation in total stresses:

$$\nabla \cdot \boldsymbol{\sigma} + \mathbf{b} = 0 \quad (\text{A3})$$

Through an adequate constitutive model (presented in the next section), the equilibrium equation is transformed into a form expressed in terms of solid velocities and fluid pressures. The assumption of small strain rate is also made. The displacement field (\mathbf{u}) is the main variable associated with this equation. In addition, the mass balance of solid is established for the whole porous medium and it is used to update the porosity (Olivella et al. 1996).

A.2 CONSTITUTIVE EQUATIONS

The main constitutive laws are presented in the following sections.

A.2.1 Mechanical constitutive model

The BBM was developed in a effort to provide an integrated and a consistent framework for reproducing the behavior of unsaturated soils. The framework needed to be established on parameters which would be easily identifiable in a laboratory environment and possess a flexible base for future developments of the complex

behavior of the unsaturated soils. The details of the model was published in Alonso et al. (1990) where the authors describe the use of a two-stress variable namely; the net stress and the suction, based on similar work of Coleman (1962); Bishop and Blight, (1963) and Fredlund and Morgenstern, (1977). The net stress σ was defined as the excess of total stress σ_t over the gas pressure p_g (Gens, 2010)

$$\sigma = \sigma_t - p_g I \quad (A4)$$

This model was developed in an elastoplastic framework similar to those used in saturated soil mechanics which is dominated largely by critical state soil mechanics. The bulk modulus (K) for changes in mean stress is evaluated with the following law:

$$K = \frac{(1+e)}{\kappa} p \quad (A5)$$

The bulk modulus for changes in suction is computed according to the following law:

$$K_s = \frac{(1+e)(s + p_{atm})}{\kappa_s} \quad (A6)$$

The yield surface of the ellipse of the modified cam clay is adopted. The equation of the yield surface is given by

$$F = \left[p_n - \left(\frac{p_{n0} - ks}{2} \right) \right]^2 + \frac{q}{M^2} - \left(\frac{p_{n0} - ks}{2} \right)^2 \quad (A7)$$

and flow rule is dictated by,

$$\frac{d\varepsilon_s^p}{d\varepsilon_v^p} = \frac{2q\alpha}{M^2(2p + p_s + p_0)} \quad (A8)$$

where M is the slope of the critical state line, κ is the parameter describing the increase in cohesion due to suction, α is the parameter related to the non-associative flow rule and q is the deviatoric stress given by $q = \sqrt{\left(\frac{3}{2} s_{ij}s_{ij}\right)}$, $s_{ij} = \sigma_{ij} - p\delta_{ij}$

The description of the soil assumes that it is saturated at zero suction. The results of an idealized consolidation test conducted at different degrees of saturation therefore different values of suction are as shown in Figure A1 a) and Figure A1 b).

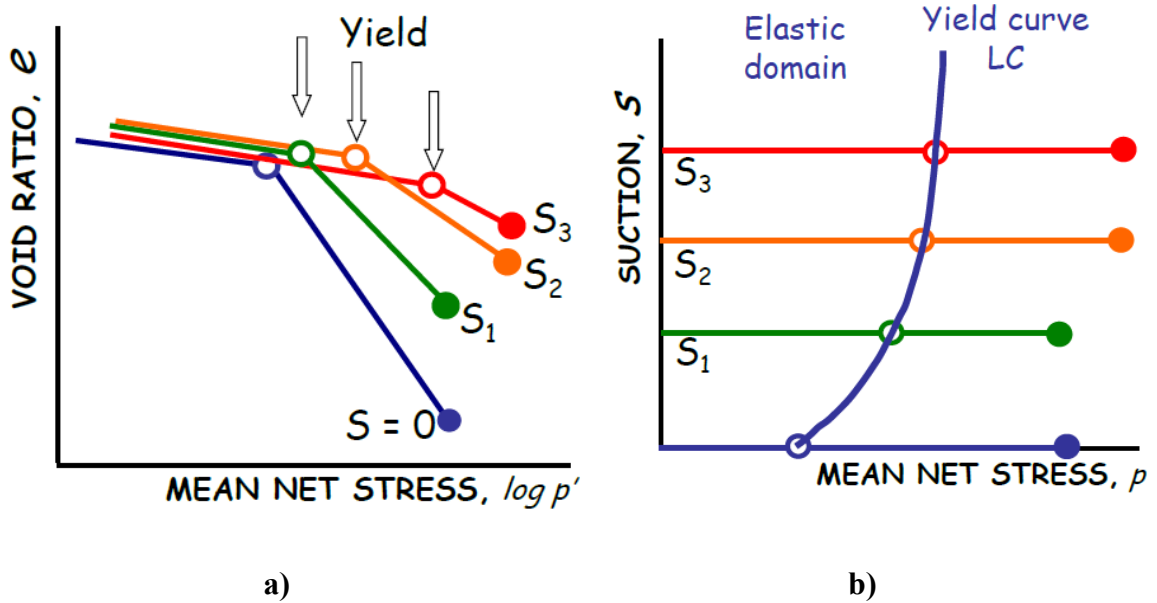


Figure A1. Feature of BBM model a) Idealized consolidation curves at different suction b) LC yield curve in p-s plane (Sanchez et al., 2010)

The apparent preconsolidation pressures are considered as a yield points beyond which irreversible deformations occur in the soil. It is easy to observe that this yield point increases with an increase in suction. The combination of the suction and net stress causing the yield, results in a yield curve in p-s (mean net stress – suction plane). This

curve is termed as the Load-Collapse (LC) curve which causes the yielding of the soil. In consistency with the modified cam clay model, the plastic strains ε_v^p encountered beyond this was determined using

$$d\varepsilon_v^p = \frac{\lambda_0 - \kappa}{(1+e)} \frac{dp_0^*}{p_0^*} \quad (\text{A9})$$

where, λ_0 is the slope of the saturated (suction, $s = 0$) virgin consolidation curve, κ is the slope of the unloading and reloading line, p_0^* is the apparent preconsolidation pressure at saturation and e is the voids ratio. The expression for the LC reduces to,

$$p_0 = p^c \left(\frac{p_0^*}{p^c} \right)^{\frac{\lambda_0 - \kappa}{\lambda_s - \kappa}} \quad (\text{A10})$$

where,

$$\lambda_s = \lambda_0 [r + (1-r)\exp(-\beta s)] \quad (\text{A11})$$

and p_0 is the mean yield stress, λ_s is the slope of consolidation curve at suction s , β and r are model parameters.

The assumption of the increase in cohesion with suction is accommodated by extending the yield surface of the left to give rise to the ps curve. The composite yield surface in the p - s plane is shown in Figure A2

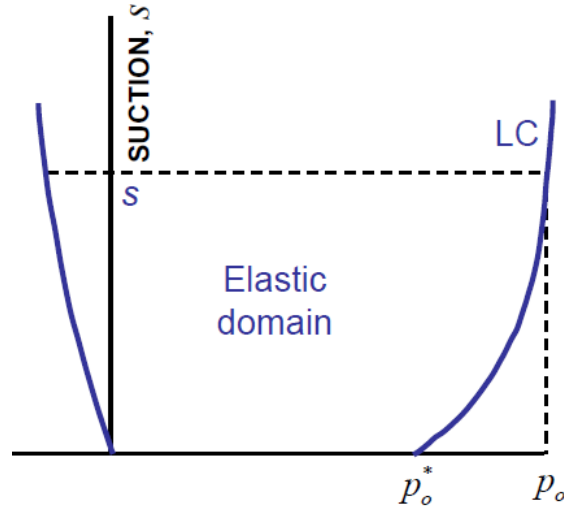


Figure A2 BBM yield surface in the mean stress suction (p-s) plane

A.2.2 Thermal constitutive model

Conductive heat flow is assumed to be governed by Fourier's law:

$$\mathbf{i}_c = -\lambda \nabla T \quad (\text{A12})$$

where, λ is the global thermal conductivity of the porous medium and S_l is the volumetric liquid fraction. The following law has been adopted for the overall thermal conductivity

$$\lambda = \lambda_{sat}^{S_l} \lambda_{dry}^{(1-S_l)} \quad (\text{A13})$$

The internal energy for the medium is computed assuming that it is additive in relation to the phase (Olivella et al., 1994).

$$E = E_s \rho_s (1 - \phi) + E_l \rho_l S_l \phi + E_g \rho_g S_g \phi \quad (\text{A14})$$

where, E_s , E_l and E_g are the specific internal energies corresponding to each phase, i.e., the internal energy per unit mass of phase. ρ_s , ρ_l , ρ_g , are the densities of the three phases, ϕ is the porosity and S_g is the gas fraction with respect to the pore volume.

The gas phase energy is usually expressed as (Olivella et al., 1994):

$$E_g \rho_g = (E_g^w \omega_g^w + E_g^a \omega_g^a) \rho_g = E_g^w \theta_g^w + E_g^a \theta_g^a \quad (\text{A15})$$

where, E_g^w and E_g^a are the specific internal energies of species (respectively water and air), that is, internal energy per unit of mass of species. ω_g^w and ω_g^a are the mass fraction of water and air species in gas phase, respectively. This additive decomposition is admissible for the gaseous phase in the assumption of mixture of gasses.

It is not so direct that the same decomposition is also valid for the liquid phase, however the same assumption will be made since the significance of the internal energy of dissolved air is small (Olivella et al., 1994; Gens and Olivella, 2001):

$$E_l \rho_l = (E_l^w \omega_l^w + E_l^a \omega_l^a) \rho_l = E_l^w \theta_l^w + E_l^a \theta_l^a \quad (\text{A16})$$

It can be noted that the specific internal energy of the vapour (water in gas phase) contains an additional term that represents the latent heat in vapour. The thermal consequences of evaporation/condensation are therefore taken into account in a straightforward way (Gens and Olivella, 2001).

A.2.3 Hydraulic constitutive model

Advective fluxes are computed using generalized Darcy's law, expressed as (Gens and Olivella, 2001):

$$\mathbf{q}_\alpha = -\mathbf{K}_\alpha (\nabla P_\alpha - \rho_\alpha \mathbf{g}); \quad \alpha = l, g \quad (\text{A17})$$

where, P_α is the phase pressure. \mathbf{K}_α is the permeability tensor of α phase and \mathbf{g} is the gravity vector. The permeability tensor is not constant but, in turn it, depends on other variables:

$$\mathbf{K}_\alpha = \mathbf{k} \frac{k_{r\alpha}}{\mu_\alpha}; \quad \alpha = l, g \quad (\text{A18})$$

where, \mathbf{k} is the intrinsic permeability tensor, μ_α is the dynamic viscosity of the α phase. Finally, $k_{r\alpha}$ is the α phase relative permeability.

The dependence of intrinsic permeability on pore structure is considered in terms of porosity. Two different laws were used in the analysis. In the first one the intrinsic permeability of the bentonite depends on porosity according to:

$$\mathbf{k} = k_0 \frac{\phi^3}{(1-\phi)^2} \frac{(1-\phi_0)^2}{\phi_0^3} \mathbf{I} \quad (\text{A19})$$

where, k_0 is the reference permeability at the reference porosity ϕ_0 . The other model that can be potentially used corresponds to an exponential law, presented as follows:

$$\mathbf{k} = k_0 \exp[b(\phi - \phi_0)] \mathbf{I} \quad (\text{A20})$$

Where, k_0 is the intrinsic permeability at the reference porosity ϕ_0 , and b is a model parameter.

The relative permeabilities of liquid and gaseous phases are made dependent on the degree of saturation according to:

$$a) k_{rl} = S_{el}^n; \quad b) k_{rg} = (1 - k_{rl}) \quad (\text{A21})$$

where:

$$S_{el} = \frac{S_l - S_{lr}}{S_s - S_{lr}} \quad (\text{A22})$$

where, S_{lr} , S_{ls} and n are model parameters. Equation (A39) considers the reduction of hydraulic permeability as the degree of saturation decreases. This variation is very difficult to determine directly and it is necessary to resort to indirect means of estimation.

The retention curve relates the degree of saturation of the material with suction.

The law adopted is the following:

$$S_{el} = \left[1 + \left(\frac{s}{P_0} \right)^{\frac{1}{1-\lambda_0}} \right]^{-\lambda_0} f_d \quad (\text{A23})$$

where:

$$f_d = \left(1 - \frac{s}{P_d} \right)^{\lambda_d} \quad (\text{A24})$$

where, P_o and λ_o are model parameters. The function f_d is included in order to model properly the high suction range. Similar functions were proposed previously by other authors (i.e. Romero, 1999). Here P_d is related with the suction at 0 degree of saturation and λ_d is a model parameter. When $\lambda_d = 0$ the original model (i.e. Gens et al., 1998) is recovered.

Non-advective fluxes of species inside the fluid phases are computed through Fick's law, which expresses them in terms of gradients of mass fraction of species through a hydrodynamic dispersion tensor that includes both molecular diffusion and mechanical dispersion (i.e. Olivella et al., 1994; Gens and Olivella 2001):

$$\mathbf{i}_\alpha^i = -\mathbf{D}_\alpha^i \nabla \omega_\alpha^i; \quad i = w, a; \quad \alpha = l, g \quad (\text{A25})$$

where, \mathbf{D}_α^i is the dispersion tensor of the medium.

For vapour diffusion, the following expression for the hydrodynamic dispersion tensor is adopted (i.e. Olivella, 1995):

$$\mathbf{i}_g^w = -\mathbf{D}_g^w \nabla \omega_g^w = -\left(\phi \rho_g S_g \tau D_m^w \mathbf{I} + \rho_g \mathbf{D}'_g\right) \nabla \omega_g^w \quad (\text{A26})$$

where, \mathbf{D}_g^w is the dispersion tensor, τ is the tortuosity, D_m^w is the dispersion coefficient corresponding to molecular diffusion of vapour in air and \mathbf{D}'_g is the mechanical dispersion tensor. The tortuosity takes into account the fact that the vapour diffusion takes place inside the voids of a porous media. A value of $\tau = 0.8$ has been adopted

(Lloret et al., 2001). The molecular diffusion coefficient is given by (i.e. Olivella, 1995 and Gens and Olivella, 2001):

$$D_m^w = 5.9 \times 10^{-12} \frac{(273.15 + T)^{2.3}}{P_g} \quad (\text{A27})$$

where, D_m^w is in m^2/s , P_g is in MPa and T in $^\circ\text{C}$. It can be noted that in vapour diffusion, the *THM* couplings are evident: effect of temperature through the variation of molecular diffusion with temperature; hydraulic effect through the influence of degree of saturation; and mechanical effects due to porosity changes (Gens and Olivella, 2001).

A usual expression for the mechanical dispersion is (i.e. Olivella, 1995 and Gens and Olivella, 2001):

$$\mathbf{D}'_g = -\mathbf{q}_g \mathbf{I} + (d_l - d_t) \frac{\mathbf{q}_g \mathbf{q}_g^t}{|\mathbf{q}_g|} \quad (\text{A28})$$

where, d_t and d_l are transversal and longitudinal dispersivities respectively. In this case it has been assumed that the molecular diffusion is dominant and the mechanical dispersion of vapour has been neglected. So, the equation (A28) has been presented for completeness of the formulation only.

The same consideration can be made regarding diffusion of air in the liquid phase:

$$\mathbf{i}'_l = -\mathbf{D}'_l \nabla \omega_l^a = -(\phi \rho_l S_l \tau D_m^a \mathbf{I} + \rho_l \mathbf{D}'_l) \nabla \omega_l^a \quad (\text{A29})$$

A.3 EQUILIBRIUM RESTRICTIONS

It is assumed that phase changes are rapid in relation to the characteristic times typical of the problem under consideration. So, they can be considered in local equilibrium, giving rise to a set of equilibrium restrictions that must be satisfied at all times. The vapour concentration in the gaseous phase is governed by the psychrometric law and the amount of air dissolved in water is given by Henry's law (Olivella et al. 1994; 1996).

A.3.1 Equilibrium restrictions

It is assumed that phase changes are rapid in relation to the characteristic times typical of this problem. So, they can be considered in local equilibrium, giving rise to a set of equilibrium restrictions that must be satisfied at all times (Olivella, 1995 and Gens and Olivella, 2001).

The vapour concentration in the gaseous phase is governed by the psychrometric law, which can be expressed as (i.e. Gens and Olivella, 2001):

$$\theta_g^w = (\theta_g^w)^0 \exp\left(\frac{\Psi M_w}{R(273.15 + T)\rho_l}\right) \quad (\text{A30})$$

where, θ_g^w is the vapour concentration in the gas phase; $(\theta_g^w)^0$ is the vapour concentration in the gas phase in equilibrium with a liquid at flat surface (at the sample temperature); Ψ is the total water potential of the water (excluding gravity terms), in this case it is related to suction ($\Psi = P_l - P_g$); M_w is the molecular mass of the water (0.018 kg/mol) and R the gas constant (8.314 J/mol/°K). The gases law relates vapour density and vapour pressure (i.e. Olivella, 1995):

$$(\theta_g^w)^0 = \frac{M_w P_{v(T)}}{R(273.15 + T)} \quad (\text{A31})$$

For pure water the vapour pressure has been approximate as (i.e. Olivella, 1995):

$$P_{v(T)} = 136075 \exp\left(\frac{-5239.7}{273.15 + T}\right) \quad (\text{A32})$$

To define the amount of air dissolved in water, Henry's law is adopted. This law expresses a linear relationship between the concentration of air in dissolution and the partial pressure of air (P_a) in the gaseous phase:

$$\theta_l^a = \omega_a^l \rho_l = \frac{P_a}{H} \frac{M_a}{M_w} \rho_l \quad (\text{A33})$$

where, M_a is the molecular mass of the air (0.02895 kg/mol), and H is Henry's constant (1000 MPa).

A.3.2 Phase physical properties

The properties of the fluid phase appear in the balance equations and in the constitutive laws. In general, they depend on the composition of the phase and on the state variables (temperatures and pressures). Some of them are introduced below.

The function of density for the liquid phase can be expressed as (i.e. Olivella, 1995 and Gens and Olivella, 2001):

$$\rho_l = 1002.6 \exp\left(4.5 \times 10^{-4} (P_l - 0.1) - 3.4 \times 10^{-4} T\right) \quad (\text{A34})$$

where, T is expressed in °C, P_l in MPa and in ρ_l kg/m³. This expression must have a cut-off for large negative liquid pressures; if not, unrealistic low liquid density is obtained.

The air density is obtained from the law of ideal gases:

$$\theta_g^a = \frac{M_a P_a}{R(273.15 + T)} \quad (\text{A35})$$

The density of the gas phase is obtained adding the partial densities of the two species:

$$\rho_g = \theta_g^w + \theta_g^a \quad (\text{A36})$$

Finally, the viscosity of the liquid and gas phase are, respectively (i.e. Olivella, 1995):

$$\mu_l = 2.1 \times 10^{-12} \exp\left(\frac{1808.5}{273.15 + T}\right) \quad (\text{A37})$$

$$\mu_g = 1.48 \times 10^{-12} \exp\left(\frac{(273.15 + T)^{1/2}}{1 + \frac{119}{(273.15 + T)}}\right) \quad (\text{A38})$$

where, T is expressed in °C and μ_α in MPa.s.